



The
University
Of
Sheffield.

CAMIRA: Correction Advances for Myocardial Imaging using Registration Algorithms

By:
Shelley Redgate

A thesis submitted in partial fulfilment of the requirements
for the degree of Doctor of Philosophy

The University of Sheffield
Faculty of Medicine
Department of Infection, Immunity and Cardiovascular
Disease

Jan 2018

Contents

Abstract.....	iv
Nomenclature.....	vi
List of Figures.....	x
List of Tables.....	xxii
Summary.....	xxvi
Acknowledgments.....	xxvii
1 – Introduction.....	1
1.1 – Coronary Artery Disease.....	1
1.2 – Solid State Dedicated Cardiac Imaging.....	1
1.3 – Patient Motion.....	2
1.4 – Respiratory Motion.....	3
1.5 – Research Question.....	4
1.6 – Overview of Thesis.....	6
1.7 – Thesis Exclusions.....	7
1.8 – Summary.....	8
2 – Literature Review.....	9
2.1 – Coronary Artery Disease.....	9
2.2 – Cardiac Imaging.....	9
2.3 – Myocardial Perfusion Imaging Acquisition.....	11
2.4 – Motion on Anger Gamma Cameras.....	26
2.5 – Motion on the Discovery 530c Dedicated Cardiac Camera.....	42
2.6 – Summary.....	53
3 – Effect of Motion on the Discovery 530c Dedicated Cardiac Camera.....	55
3.1 – Introduction.....	55
3.2 – Mathematical Model.....	55
3.3 – Statistical Analysis.....	61
3.4 – Labelling Convention.....	62
3.5 – Clinical Imaging and Processing.....	64
3.6 – Phantom Simulation Patient Motion.....	65
3.7 – Comparison to Mathematical Model.....	84
3.8 – Respiratory Motion.....	87
3.9 – Summary.....	89
4 – Motion Estimation on the Discovery 530c Dedicated Cardiac Camera.....	90

4.1	– Introduction	90
4.2	– Motion Estimation Technique.....	90
4.3	– Pinhole Collimation	94
4.4	– Initial Evaluation of Motion Estimation Technique.....	97
4.5	– Software Development.....	102
4.6	– Summary	105
5	– Patient Motion Estimation and Correction: Phantom Validation and Patient Application.....	107
5.1	– Introduction	107
5.2	– Phantom Evaluation	107
5.3	– Application to Patient Studies.....	118
5.4	– Summary	128
6	– Respiratory Motion Estimation and Correction Technique.....	129
6.1	– Introduction	129
6.2	– Initial Adaptations to the Patient Motion Estimation Techniques	129
6.3	– Motion Estimation using Principal Component Analysis.....	130
6.4	– Initial Evaluation of the Technique.....	131
6.5	– Motion Correction Technique	136
6.6	– Software Development.....	136
6.7	– Optimisation of Technique: Phantom Acquisitions	140
6.8	– Summary	150
7	– Respiratory Motion Estimation and Correction: Validation and Patient Application.....	152
7.1	– Introduction	152
7.2	– Patient Cohort.....	152
7.3	– Respiratory Effort Transducer.....	153
7.4	– Signal Post Processing	154
7.5	– Patient Validation.....	158
7.6	– Quality Index.....	175
7.7	– Patient Application.....	178
7.8	– Summary	193
8	– Summary and Discussion.....	194
8.1	– Effect of Motion.....	194
8.2	– Patient Motion Estimation.....	196
8.3	– Respiratory Motion Estimation.....	199

8.4	– Motion Correction.....	201
8.5	– Patient Studies.....	204
8.6	– Principal Component Analysis.....	206
8.7	– Limitations	208
9	– Conclusion and Further Work.....	209
9.1	– Conclusion.....	209
9.2	– Further Work.....	210
	References.....	212
	Appendix A – Data Driven Motion Estimation.....	I
	Appendix B – Respiratory Motion Patient Results.....	VII
	Appendix C – Publications	X
	Appendix D – Permissions	XII

Abstract

Introduction: Myocardial perfusion imaging uses a gamma camera to image the perfusion of the heart to evaluate the presence of coronary artery disease. The Discovery NM 530c dedicated solid state cardiac gamma camera (DNM 530c) is an inherently three-dimensional imaging system that is different in design, and uses different acquisition parameters, compared to Anger gamma cameras.

Aim: To determine the extent and frequency of patient and respiratory motion artefacts on myocardial perfusion images acquired on the DNM 530c and develop data driven motion estimation and correction techniques that utilise the three-dimensional nature of the system.

Method: The effect of motion on myocardial perfusion images acquired on the DNM 530c was evaluated on phantom studies, and planar and three-dimensional techniques implementing image registration were developed for patient motion estimation. The technique was adapted to incorporate principal component analysis to facilitate the measurement of respiratory motion. Validation was performed on phantom simulations and explored through patient studies. Motion correction was applied by registering reconstructed binned data.

Results: Patient motion $\geq 10\text{mm}$ that is present for $\geq 17\%$ of the acquisition introduced significant motion artefacts. There was no significant difference ($P=0.258$) between the planar and three-dimensional patient motion estimation techniques. Motion correction removed artefacts from 9/10 phantom simulations. Cranio-caudal motion $\geq 8\text{mm}$ was measured on 10% of patient studies and 5% were affected by motion. No significant patient motion was identified in the lateral or ventral-dorsal directions. A strong correlation was demonstrated between the respiratory motion signal generated using the respiratory motion estimation technique and measured using an external device for two out of eight validation patients, with one patient demonstrating motion artefacts. Significant cranio-caudal respiratory motion was identified on 45% of patient images, with 4% demonstrating motion artefacts. Respiratory motion $\geq 15\text{mm}$ introduced artefacts. A quality index of

≥ 0.7 can be used to identify images that would benefit from motion correction; this would result in 1 in 3 patients undergoing correction.

Conclusions: Data driven motion estimation techniques for both patient and respiratory motion on the DNM 530c have been developed. It has been demonstrated that patient motion $\geq 10\text{mm}$ that is present for $\geq 17\%$ of the acquisition and respiratory motion $\geq 15\text{mm}$ can introduce artefacts into clinical scans.

Acknowledgements: This report is independent research arising from a NIHR/CSO Healthcare Scientist Doctoral Research Fellowship supported by the National Institute for Health Research. The views expressed in this publication are those of the author(s) and not necessarily those of the NHS, the National Institute for Health Research or the Department of Health.

Nomenclature

Acronyms

AC	- Attenuation Correction
ARSAC	- Administration of Radioactive Substances Advisory Committee
ASIC	- Application-Specific Integrated Circuit
ASNC	- American Society of Nuclear Cardiology
BHT	- Breath Hold Triggering
BNMS	- British Nuclear Medicine Society
CAD	- Coronary Artery Disease
CAMIRA	- Correction Advances for Myocardial Imaging using Registration Algorithms
CCTA	- Coronary Computed Tomographic Angiography
CMR	- Cardiac Magnetic Resonance Imaging
CPP	- Counts Per Pixel
CSO	- Chief Scientific Officer
CTA	- Computed Tomography Angiography
CZT	- Cadmium Zinc Telluride
DRL	- Diagnostic Reference Level
DNM 530c	- Discovery NM 530c Dedicated Solid State Cardiac Camera
EANM	- European Association of Nuclear Medicine
ECG	- Electrocardiogram
EDV	- End Diastolic Volume
ESV	- End Systolic Volume
FBP	- Filtered Back Projection
FFR	- Fractional Flow Reserve
FWHM	- Full Width Half Maximum
GE	- General Electric
HPD	- Heart-to-Pinhole Distance
IR	- Image Registration
LE	- Laplacian Eigenmaps
LLH	- Low Likelihood
LV	- Left Ventricle

LVEF	- Left Ventricle Ejection Fraction
MC	- Motion Correction
MCAT	- Mathematical Cardiac Torso
MDC	- Alcyone Motion Detection and Correction
MIBI	- Sestamibi
MLEM	- Maximum-Likelihood Expectation Maximization
MPD	- Myocardial Perfusion Defect
MPI	- Myocardial Perfusion Imaging
MRI	- Magnetic Resonance Imaging
MSE	- Mean Square Error
NAC	- Non-Attenuation Corrected
NCAT	- NURBS-based Cardiac-Torso
NICE	- National Institute for Health and Care Excellence
NIHR	- National Institute for Health Research
OSEM	- Ordered-Subset Expectation Maximization
OSL	- One-Step-Late
PCA	- Principal Component Analysis
PCA(C1)	- First Normalised Coefficient from Principal Component Analysis
PCA+IR.	- Registration of the Principal Component Analysis Smoothed Images
PDD	- Pinhole-to-Detector Distance
PET	- Positron Emission Tomography
PMT	- Photomultiplier Tubes
PSF	- Point Spread Function
QFOV	- Quality Field Of View
QGS	- Quantitative Gated SPECT
QI	- Quality Index
QPS	- Quantitative Perfusion SPECT
ROI	- Region Of Interest
RR	- Resolution Recovery
SD	- Standard Deviation
SDS	- Summed Difference Score
SG	- Savitzky-Golay
SHIRT	- Sheffield Image Registration Toolkit
SNM	- Society of Nuclear Medicine

SPECT	- Single Photon Emission Computed Tomography
SRS	- Summed Rest Score
SSS	- Summed Stress Score
STH	- Sheffield Teaching Hospitals NHS Foundation Trust
TF	- Tetrafosmin
TPD	- Total Perfusion Deficit
US	- United States

Symbols

T_n – Numbering system for triplets of detectors, where n is the triplet number

c – Standard deviation of the Gaussian in the mathematical model, section 3.2

a – Maximum of the Gaussian in the mathematical model, section 3.2

t – Scaling factor representing the percentage of the total time spent at a position due to motion, section 3.2

b – The position of the maximum of the Gaussian in the mathematical model, section 3.2

s – The magnitude of simulated motion in the mathematical model, section 3.2

$f(\max)$ – The maximum of the profile generated by summing two Gaussians in the mathematical model, section 3.2

T – Myocardial thickness measured from images of the heart

P – Probability value

r – Pearson's correlation coefficient

x, y – Motion relative to the detector, figure 3-5

X, Y, Z – Motion relative to the patient, figure 3-5

$\mathbf{X, Y, Z}$ – Motion relative to the reoriented axes of the heart, figure 3-5

h_x – The shift of the heart

dx – The shift of the image of the heart on the detector

f – Frame length of a Savitzky-Golay filter

k – Polynomial order of a Savitzky-Golay filter

List of Figures

Figure 1-1 – A short axis representation of the left ventricle, (a) patient and respiratory motion is primarily a vector that translates the position of the heart, (b) cardiac motion is primarily radial motion about a central point. 8

Figure 2-1 – Examples of myocardial perfusion studies showing, (a) normal myocardial uptake on the stress image and therefore no evidence of significant coronary artery disease, (b) reduced uptake on the stress image which reverses at rest (indicated by arrows) suggesting myocardial ischaemia and (c) matched reduced uptake at stress and rest (indicated by arrows) suggesting either attenuation artefacts or myocardial infarction. 12

Figure 2-2 – (a) A dual headed camera in the ‘L Mode’ configuration used for myocardial perfusion imaging, (b) schematic diagram of an Anger gamma camera, A - γ rays parallel to collimator pass through and interact with the crystal, B - γ rays at an angle to the collimator are absorbed and do not interact with the crystal. The X,Y (location) and Z (energy) signals are used to produce an image of the radioactivity distribution in the patient..... 13

Figure 2-3 – Cardiac gating involves dividing the data acquired for each R-R interval into 8 or 16 bins. The data in each bin is summed and reconstructed, to give 8 or 16 three-dimensional images of the left ventricle at different points in the cardiac cycle. Viewing these as a sequence facilitates visualisation of the motion and thickening of the myocardial walls. ECG – Electrocardiogram, QGS – Quantitative Gated SPECT. 15

Figure 2-4 – (a) Polar plots are a two-dimensional representation of the left ventricle, (b) Quantitative Perfusion SPECT displays the perfusion (%) on the segmented polar map. 16

Figure 2-5 – (a) The DNM 530c is a fixed system with no movement of the gantry during the acquisition, (b) a schematic diagram showing the pinhole collimators focused on the quality field of view (QFOV); at each angle there is a set of detectors, denoted T_n , with the number of detectors in each set alternating between 1 and 3, (c) the solid state cadmium zinc telluride (CZT) detector modules convert gamma ray energy straight into an electrical signal, A - γ rays incident on the pinhole are

detected, B - γ rays that are not incident on the pinhole are absorbed by the collimator. ASIC – application-specific integrated circuit 18

Figure 2-6 – A patient scan performed on an Anger camera. (a) Motion is visible between projections, (b) reconstructed short axis slices before and (c) after motion correction. Motion artefacts are indicated by the arrows. 31

Figure 2-7 – The results from a phantom study showing artefacts are barely apparent with 1cm simulated motion and clear with 2cm and 3 cm simulated motion. This research was originally published in *The Journal of Nuclear Medicine*, (Pitman et al., 2002), <http://jnm.snmjournals.org/content/43/9/1259.full>. Reproduced with written permission of the rights holder. © by the Society of Nuclear Medicine and Molecular Imaging, Inc. 35

Figure 2-8 – Different methods of gating the respiratory signal; (a) Time gating divides each respiratory cycle into an equal number of time bins (in this example 4) and then sums the images from corresponding bins, (b) Amplitude gating divides the overall amplitude of the signal into an equal number of bins (in this example 4) and then sums the data in each bin. 37

Figure 2-9 - The results of a patient study showing the segmented endocardium boundaries at end expiration and inspiration, motion is clearly visualised between the two phases of the respiratory cycle and this is reduced following motion correction. The short axis slices of the reconstructed study show anterior and inferior wall defects which are reduced following correction. This research was originally published in *The Journal of Nuclear Medicine*, (Kovalski et al., 2007), <http://jnm.snmjournals.org/content/48/4/630.full?related-urls=yes>48/4/630. Reproduced with written permission of the rights holder. © by the Society of Nuclear Medicine and Molecular Imaging, Inc. 39

Figure 2-10 – (a) Phantom study showing artefacts from 2cm inferior motion, dorsal motion and motion to the left and removal of the artefacts following motion correction. (b) Patient study of sub-optimal quality due to motion, with the proportion of the scan with motion discarded and after being rescanned. This research was originally published in *Medical and Biological Engineering and Computing*, (Kennedy and Strauss, 2016), <https://link.springer.com/article/10.1007/s11517-016-1548-z>.

Reproduced with permission of Springer Nature. © International Federation for Medical and Biological Engineering 2016. 47

Figure 2-11 – A patient study on the DNM 530c showing the respiratory signal and patient images before and after respiratory motion correction. This research was originally published in The Journal of Nuclear Cardiology, (Ko et al., 2015), <https://link.springer.com/article/10.1007/s12350-014-9963-8>. Reproduced with permission of Springer. © American Society of Nuclear Cardiology 2014. 52

Figure 3-1 – (a) The radioactivity distribution in a short axis slice of the left ventricle, (b) a radial profile from the centre of the left ventricle can be approximated to a square function, (c) this is then blurred due to cardiac motion and (d) convolved with the point spread function of the imaging system. PSF – point spread function. 56

Figure 3-2 – (a) A long axis representation of the left ventricle, (b) Quantitative Perfusion SPECT segments of the endocardial boundary to define the myocardium using 65% of the inner standard deviation of a Gaussian fitted across the wall of the left ventricle, c - standard deviation of the Gaussian, T - myocardial thickness..... 56

Figure 3-3 – (a) The profile of the left ventricle is simplified to a symmetrical Gaussian function, (b) motion half way through the scan can be simulated using two functions shifted relative to each other, (c) summing these functions models the left ventricle with motion imposed and (d) the model can be adapted to demonstrate motion for a proportion of the scan time. FWHM – full width half maximum, c – standard deviation, a - maximum of the Gaussian, t – scaling factor representing the percentage of the total time spent at the position, f(max) – maximum of the profile generated by summing two Gaussians, b – the x position of the maximum, s - magnitude of simulated motion..... 57

Figure 3-4 – The amount of motion, S_{lim} , required to reduce the maximum of two summed Gaussian profiles to 70% of the maximum without motion, as measured myocardial thickness increases. The grey dashed line represents a typical myocardial thickness as measured on a patient image on the DNM 530c. The percentage values represent the proportion of the acquisition time affected by motion. 59

Figure 3-5 – The labelling convention used throughout the thesis, (a) relative to the plane of the detector, (b) relative to the planes of the patients, (c) relative to the plane of the heart. 63

Figure 3-6 – The Data Spectrum anthropomorphic phantom used for the simulations. 66

Figure 3-7 – Projection images of the heart from (a) a patient image and (b) the phantom image. 67

Figure 3-8 – Stationary phantom acquisitions acquired at different X, Y and Z positions. (a) Starting with the heart in the centre of the QFOV the imaging bed was moved in the Z direction (perpendicular to the plane of the paper). (b) Starting with the heart central in the QFOV the gantry is moved out (motion is approximately 45° to the X and Y axes); the gantry shift is calculated from the required X motion using Pythagoras Theory and the bed is then moved up by the same amount. This keeps the heart at the same Y position in the QFOV and changes the X position. (c) Starting with heart at an X position of 20mm the imaging bed was moved up to acquire images at different Y positions. (d) Demonstrates where all the images were acquired within the QFOV. QFOV – Quality Field of View. 68

Figure 3-9 – Thirty second images from acquisitions at different positions in the quality field of view were added to simulate three types of motion; step, bounce (with three durations) and creep. The duration of the images was varied according to equation 3.9 to facilitate simulation of creep motion. 69

Figure 3-10 – Flow chart outlining how images acquired at different positions in the QFOV were combined to simulate phantom images with motion. The original images were reconstructed, and reframed, summed and reconstructed for comparison purposes. 71

Figure 3-11 - Short axis images for different amounts and directions of simulated step motion..... 74

Figure 3-12 – (a) The y profiles for short axis slices and (b) the FWHM of the profiles for different amounts of Z motion. Note: the FWHM of peak 2 increases at a faster rate than peak 1 due to the close proximity to and reducing separation between the inferior wall and the sub-diaphragmatic activity as the magnitude of the motion increases..... 75

Figure 3-13 – Polar plots showing (a) uptake and (b) severity for different amounts of step motion in the Z direction..... 76

Figure 3-14 – The TPD values calculated for all the simulated images (a) Z direction, (b) Y direction and (c) X direction. The red horizontal dashed line on each graph represents the cut off limit of a TPD \geq 5.5% for the identification of motion artefacts; TPD values above this indicate significant patient motion artefacts. 77

*Figure 3-15 – Confidence in the report by both reporters for the different types of simulated motion. * Studies where the stress images appeared to have improved uptake in the basal infero-lateral region..... 78*

Figure 3-16 – (a) Myocardial perfusion imaging reporting screen and (b) polar plots for 12mm step motion in the Z direction. A - Improved basal infero-lateral perfusion at stress (with motion) compared to rest (no motion). B - Improved anterior and infero-apical perfusion at rest (no motion) compared to stress (with motion). 80

Figure 3-17 – The maximum of the profile expressed as the percentage of the maximum when no motion is present, for different durations of motion, calculated using the mathematical model and measured on phantom simulations. (a) 50% (b) 8% (c) 17% and (d) 25% of the acquisition affected by motion. A value for c of 8.7 was used for the model. The error bars are based on the variation in the FWHM measured on the phantom simulations. The red and blue lines represent the values measured on two different slices of the phantom image. The limit for significant motion artefacts, point at which the maximum count is 70%, is represented by the limit line. 85

Figure 3-18 – A graphical representation of (a) step and (c) creep cranio-caudal (Z) patient motion, and (e) cranio-caudal respiratory motion. The histograms for (b) step, (d) creep and (f) respiratory motion represent the amount of time spent by the heart at different positions. 88

Figure 4-1 – A diagrammatic representation of the technique used for motion estimation throughout this thesis. (a) The myocardial perfusion image is divided into a time series of images; any shift in the heart (represented by the black dot) may be visualised between the images. (b) Each image in the series is registered to the first image in the series generating a registration mapping (black arrows). (c) The

<i>mappings from the registrations are extracted and plotted to estimate the motion present during the study.</i>	92
<i>Figure 4-2 – (a) An image is acquired on the DNM 530c, resulting in 19 projection images of the heart. (b) The list mode data is divided into a time series, with 19 projections of the heart associated with each time interval. (c) The images from each projection are combined to give 19 time series or (d) the images at each time point are reconstructed to give a series of three-dimensional images over time. Motion on the images (planar or three-dimensional), is then assessed as described in figure 4.1.</i>	93
<i>Figure 4-3 - (a) A schematic diagram showing the heart-to-pinhole distance (HPD) and pinhole-to-detector distance (PDD). (b) The HPD changes as the position of the heart changes in the QFOV. (c) The shift of the image of the heart measured on the detector (dx) will depend on the true shift of the heart (hx) and the ratio of the HPD to PDD; in this example the shift of the heart is the same but the HPD and hence the shift of the image on the detector is different.</i>	95
<i>Figure 4-4 – Transaxial images of the heart for two patients showing the variation in the position of the heart in the QFOV.</i>	97
<i>Figure 4-5 – Images from detector number 9 with different durations.</i>	100
<i>Figure 4-6 – The mean absolute error (+/- 1SD) of the measured shift for (a) planar and (b) reconstructed images. * Due to the noise on the 1s images no sensible registration mask could be drawn.</i>	100
<i>Figure 4-7 – (a) The background corrected counts per pixel (CPP) for each detector measured on phantom images and normalised to detector 8, Δ - lateral detectors, O - ventral detectors. (b) The numbering convention of detectors. (c) The detectors used for patient motion estimation are highlighted by red boxes.</i>	104
<i>Figure 5-1 – (a) The errors on the measured Z motion on phantom simulations for the two methods of motion estimation and (b) the measured motion using both techniques plotted against the applied motion for simulations with Z motion.</i>	111
<i>Figure 5-2 – The TPD values for the phantom simulations with motion, before and after application of the motion correction algorithm.</i>	112

Figure 5-3 – (a) Polar plots for 15mm step Z motion, before and after motion correction, the arrows indicate motion artefacts that are corrected following motion correction. (b) Vertical long axis slices for 20mm Y 90s bounce motion, before and after motion correction, and the stationary acquisition acquired at the baseline Y position ($X = 20\text{mm}$, $Y = 0$, $Z = 0$). This is the only study where motion correction did not reduce the TPD value to $\leq 5.5\%$ and the images have residual motion artefacts on the motion corrected image in the inferior-basal wall, as indicated by the arrows. 113

Figure 5-4 – (a) Phantom images with 12mm simulated Z motion before and after motion correction, the arrows highlight the area that was identified as a motion artefact; this was the only study where the artefact was not fully corrected by the motion correction software. (b) Phantom images with 6mm simulated Z motion before and after motion correction, compared to the phantom image with no motion; the arrows highlight the artefact introduced by motion correction (see the discussion for further analysis of this artefact). 114

Figure 5-5 – (a) Motion measured on 96 patient images using the three-dimensional technique, * statistically significant difference and (b) motion measured for a patient that did not demonstrate significant motion. 120

Figure 5-6 – Patient 6 rest study. (a) Motion measured in the Z direction using the planar and three-dimensional techniques and (b) a comparison of the motion and motion corrected images. 122

Figure 5-7 – Patient 7 rest study. (a) Motion measured in the Z direction using the planar and three-dimensional techniques and (b) a comparison of the motion and motion corrected images, the arrows show areas of reversibility identified by the reporters..... 123

Figure 5-8 – Patient 13 stress study. (a) Motion measured in the Z direction using the planar and three-dimensional techniques and (b) a comparison of the motion and motion corrected images, the arrows show areas of reversibility identified by the reporters..... 124

Figure 5-9 – Patient 25 stress study. (a) Motion measured in the Z direction using the planar and three-dimensional techniques and (b) a comparison of the motion and motion corrected images. 125

Figure 6-1 – Projection 8 of a phantom acquisition (a) 360s data, (b) 20s data and (c) 1s data. 132

Figure 6-2 – The first 3 sets of normalised coefficients, mean, C1 and C2, generated from PCA analysis of 20s images from a phantom acquisition with simulated sinusoidal motion, compared to the motion that was simulated on the images. Note: the magnitudes of the signals have been displayed to allow comparison with the simulated motion. 133

Figure 6-3 – The signals measured using three different techniques: Image Registration (IR), the first set of normalised coefficients from principal component analysis (PCA(C1)) and PCA smoothing of the images combined with image registration (PCA+IR), (a) PCA+IR 20s images, (b) PCA C1 20s images, (c) IR 20s images, (d) PCA+IR 1s images, (e) PCA C1 1s images and (f) IR 1s images. Note: only part of the signal from the 1s images has been included for comparison purposes. 134

Figure 6-4 – A diagrammatic representation of the proposed motion correction technique. The motion curve is measured using the PCA+IR or PCA(C1) motion estimation technique. The data are then divided into bins based on the amplitude of the measured motion. The data from each bin are reconstructed. The reconstructed images are registered together to remove motion. PCA+IR – Principal component analysis smoothing with image registration, PCA(C1) – the first set of normalised coefficients from principal component analysis. 137

Figure 6-5 – Flowchart showing the steps for planar and three-dimensional patient motion and planar respiratory motion estimation and correction. PCA(C1) – 1st normalised coefficient from principal component analysis (PCA), PCA+IR - Image registration of the PCA images. 138

*Figure 6-6 – The process of estimating and correcting for respiratory motion can be divided into seven steps performed on the Link Medical and Xeleris workstations. * This was implemented through the Sheffield Image Registration Toolkit (ShIRT). PCA(C1) – the first normalised coefficient from principal component analysis (PCA), PCA+IR – Image registration of the PCA smoothed images. 139*

Figure 6-7 - (a) The moving platform (Darwesh et al., 2013) used to simulate motion in three dimensions, i - phantom drive system, ii - controls, iii - cardiac insert, and (b) the cardiac insert..... 141

Figure 6-8 – (a) The signals generated for motion in the Z direction through registration of reconstructed images (three-dimensional patient motion estimation technique) for different image durations, (b) the Fourier transform of the signals. 142

Figure 6-9 – (a)The counts per pixel (CPP) in the myocardium measured for each detector and normalised to detector 8, (b) the difference between the counts in the heart and background activity varies between detectors..... 144

Figure 6-10 – The normalised MSE when the motion signal measured on multiple detectors is averaged. PCA(C1) – the first normalised coefficient from principal component analysis (PCA), PCA+IR - Image registration of the PCA smoothed images. Av – Average with equal weights applied to each detector, WAv – Weighted average determined by the counts per pixel measured in the myocardium..... 146

Figure 6-11 – Three consecutive central short axis slices of the phantom, with and without motion and motion corrected with different numbers of bins..... 148

Figure 6-12 – Images 0.5s in duration from detector 8 of (a) the phantom acquisition and (b) a patient acquisition. 151

Figure 7-1 – (a) Respiratory effort transducer on an elastic strap, (b) the elastic strap and transducer are fitted around the thorax, (c) these are connected to a MP45 data acquisition system, (d) which is connected to a computer that displays the measured respiratory signal in mV..... 153

Figure 7-2 – The signal detected by the respiratory motion detection software, the baseline signal after two passes of a moving mean filter and the patient motion signal measured using the software developed in chapter 4, (a) Patient PAT40E (b) PAT46E. The error bars represent the error measured on the patient motion signal in chapter 4 (mean error \pm 3SD). 156

Figure 7-3 – The Fourier transform of the signal from PAT40E for (a) 1s and 0.5s images without post processing, (b) 0.5s images with and without post processing and a section of the signal from PAT40E with and without post processing. SG - Savitzky-Golay 157

Figure 7-4 – (a) The magnitude of the respiratory motion was measured from the signal generated by the external device (method 1), (b) the magnitude of the respiratory and patient motion combined was measured from the signal generated by the motion estimation technique using methods 2 and 3..... 160

Figure 7-5 – A flowchart showing the processing steps (grey lines) and comparisons (coloured lines) made between the signals generated using the motion estimation technique and the external device. 161

Figure 7-6 – A comparison of the respiratory signals from (a) the motion estimation technique and (b) the external device, for patient PAT40E. Regular markers have been added to aid comparison. (c) A correlation plot for both respiratory signals with a trend line added..... 163

Figure 7-7 – A comparison of the respiratory signals from (a) the motion estimation technique and (b) the external device, for patient PAT46E. Regular markers have been added to aid comparison. (c) A correlation plot for both respiratory signals with a trend line added..... 164

Figure 7-8 – A comparison of the respiratory signals from (a) the motion estimation technique and (b) the external device, for patient PAT43E. Regular markers have been added to aid comparison. (c) A correlation plot for both respiratory signals with a trend line added..... 165

Figure 7-9 – A comparison of the respiratory signals from (a) the motion estimation technique and (b) the external device, for patient PAT44E. Regular markers have been added to aid comparison. (c) A correlation plot for both respiratory signals with a trend line added..... 166

Figure 7-10 – Fourier transforms of the respiratory signals, (a) and (c) PAT40E from the external device and motion estimation technique respectively, (b) and (d) PAT46E from the external device and motion estimation technique respectively.. 167

Figure 7-11 – Fourier transforms of the respiratory signals, (a) and (c) PAT43E from the external device and motion estimation technique respectively, (b) and (d) patient PAT44E from the external device and motion estimation technique respectively.. 168

<i>Figure 7-12 - The correlation between the motion estimation technique and external device, against the motion measured using method 1. Data for all patients are included. x - Insignificant correlation value.</i>	171
<i>Figure 7-13 – The difference in sub-diaphragmatic activity between studies demonstrated on detector 9 for (a) PAT40E and (b) PAT41E.</i>	172
<i>Figure 7-14 – The average first normalised coefficients against the signal from the motion estimation technique. (a) PAT40E, $r = 0.96$, $P < 0.01$ (b) PAT41E, $r = 0.08$, $P = 0.03$.</i>	176
<i>Figure 7-15 – The relationship between the external device and motion estimation technique correlation, and the quality index. Only values where both correlations were significant have been included.</i>	177
<i>Figure 7-16 – A flowchart showing the processing steps applied to the clinical images and the selection criteria for motion correction.</i>	179
<i>Figure 7-17 – The magnitude of respiratory motion across the 55 clinical images in the patient cohort. The measurements from the validation patients are not included.</i>	182
<i>Figure 7-18 – The magnitude of the motion, the Fourier transform scores and visual motion assessment scores for 63 patient images, consisting of 47 clinical images, 8 repeat clinical images and 8 additional images acquired with an external device.</i>	183
<i>Figure 7-19 – The images for PAT6 corrected using data binned according to the motion estimation signal. The arrows represent areas of reversibility identified by both reporters.</i>	186
<i>Figure 7-20 – The images for PAT17 corrected using data binned according to the motion estimation signal. The arrows represent areas of reversibility identified by both reporters.</i>	186
<i>Figure 7-21 – The images for PAT46E corrected using data binned according to the motion estimation signal. The arrows represent areas of reversibility identified by both reporters.</i>	187
<i>Figure 7-22 – The (a) magnitude of motion measured using method 2, (b) magnitude of motion measured using method 3, (c) quality index, categorised according to</i>	

images that did not meet the criteria for motion correction, as defined in figure 7.16, (n = 30), images that did meet the criteria but no significant difference was reported before and after motion correction (n = 23), and for images where a significant difference was identified between the images with and without respiratory motion correction by both reporters (n = 2). Values for the quality index that were not significant and patient data acquired using the external device have not been included..... 189

Figure 7-23 – The association between the quality index and the average counts per pixel across the detectors ($r = 0.56, P < 0.01$) and in a region around the heart ($r = 0.42, P = 0.01$), for the detectors used for motion estimation. CPP – counts per pixel. 189

Figure 8-1 – Polar plots of a phantom study reconstructed from the whole dataset and through summing reconstructed images from data divided into different duration images. TPD - total perfusion deficit. 202

Figure i – A very simple representation of an image. The object is identified by pixel values of 1. The imaging plane consists of 36 pixels, with a coordinate system (x,y) that references the centre of the pixel, for example (1,1) is referencing the centre of the bottom left pixel. (a) original image, (b) a second image after the object has moved.....I

Figure ii – (a) The original data, M, (b) the data normalised by subtract of the mean, (c) the data projected onto the principal component axes, (d) the original data and data regenerated from the first and second components (PC1 and PC2).....VI

List of Tables

*Table 2.1 – Key performance parameters measured for the DNM 530c and a dual headed dedicated cardiac camera, Ventri™ by Bocher et al., (2010). * Male Phantom, + Centre of the Quality field of View. 20*

Table 2.2 – Literature comparing the performance of the DNM 530c to Anger cameras, reconstruction parameters for Anger cameras are supplied when specified. CAD – coronary artery disease, CTA – coronary computed tomography angiography, DNM 530c - Discovery NM 530c solid state dedicated cardiac camera, MIBI - sestamibi, OSEM - ordered subset expectation maximisation, RR – resolution recovery, SSS – summed stress score, SRS – summed rest score and SDS – summed difference score, S-R – stress-rest, R-S – rest-stress, TF – tetrofosmin... 23

Table 2.3 – Literature comparing the performance of the DNM 530c to coronary angiography. AC – attenuation correction, MIBI – sestamibi, S-R – stress-rest, R-S – rest-stress, TF – tetrofosmin..... 24

Table 2.4 – A summary of the literature on patient motion on Anger cameras. Unless otherwise stated imaging was with the heads configured at 90° with imaging performed over 180° using a 64 x 64 matrix with no attenuation or scatter correction. Dual / single refers to the number of heads on the camera. The duration of each projection is given in seconds (s). MIBI - sestamibi, TF - tetrofosmin, FBP - filtered back projection, OSEM - ordered-subset expectation maximisation, RR – resolution recovery, AC – attenuation correction, LLH CAD - low likelihood coronary artery disease, Recon - reconstruction. Where parameters are not included these were not specified..... 30

Table 2.5 - The cranio-caudal displacement of the heart and diaphragm as reported in the literature. MRI – magnetic resonance imaging, PET – positron emission tomography. 34

Table 2.6 - A summary of published research on patient motion on the DNM 530c. MPI – myocardial perfusion imaging, FFR – fractional flow reserve, TF – tetrofosmin, MIBI – sestamibi, TPD – total perfusion defect, CZT– cadmium zinc telluride. 45

<i>Table 2.7 - A summary of published research on respiratory motion on the DNM 530c. MPI - myocardial perfusion imaging, FFR – fractional flow reserve, TF – tetrafosmin, TPD – total perfusion defect, LV – left ventricle, AC – attenuation corrected, NAC – non-attenuation corrected, BHT – breath hold triggering, LVEF – left ventricular ejection fraction, FWHM – full width half maximum, MPD – myocardial perfusion defect.....</i>	<i>50</i>
<i>Table 3.1 – The look-up table used to describe the association between two continuous variables.....</i>	<i>62</i>
<i>Table 3.2 – Stationary images were acquired at different positions in the quality field of view. * Images could only be acquired one side of the central position as motion was restricted by the physical dimensions of the camera. ** Images were acquired at a lateral position of 20mm due to the physical restrictions of the camera. The bold numbers represent the images used to compile the normal database.</i>	<i>67</i>
<i>Table 3.3 – A total of 54 images with simulated motion were generated.....</i>	<i>70</i>
<i>Table 3.4 – The artefact extent and mean severity scores calculated from blinded reporting of the images by 2 experienced reporters. * Studies where the stress images appeared to have improved uptake in the basal infero-lateral region. The shaded cells represent no consensus report required.</i>	<i>79</i>
<i>Table 3.5 – The limit at which motion artefacts occur as determined by different methods. + - Linear interpolation was used to find limits that fell between acquired data points. >20 - Limit not reached for the measured range of 0 - 20mm. NM – Not measured. NMA – No motion artefacts as the maximum count never falls below 70% regardless of the magnitude of the motion.....</i>	<i>86</i>
<i>Table 4.1 – The mean and standard deviation of the scaling factors calculated to convert the shift measured on planar detector images into the true shift of the heart. Error HM is the error on a true heart motion of 10mm that would be introduced due to measurement uncertainties in the calculated scaling factor based on a 1SD error.</i>	<i>96</i>
<i>Table 5.1 – A subset of the phantom simulations discussed in section 3.6, table 3.3, were used to evaluate the errors on the motion estimation and correction software.</i>	<i>108</i>

<i>Table 5.2 – Images identified as appearing to have improved perfusion at stress (simulated motion or motion corrected image) compared to the rest image (no motion).</i>	110
<i>Table 5.3 – The studies that were identified to have ≥ 8mm motion identified by either the planar or three-dimensional technique.</i>	121
<i>Table 6.1 – The phantom acquisitions acquired using the moving platform. A frequency of 20 cycles/minute gives a respiratory cycle duration of 3s, representing the average respiratory frequency during myocardial perfusion imaging.</i>	140
<i>Table 6.2 – The frequency of the measured signal for different frame durations.</i> ...	143
<i>Table 6.3 – The grey boxes indicate the detectors averaged for each simulation. CPP - counts per pixel.</i>	145
<i>Table 6.4 – The motion measured on the study from registration of the reconstructed binned data for different numbers of bins.</i>	149
<i>Table 7.1 - The average Pearson correlation coefficient between the signal from the motion estimation technique (patient motion subtracted) and the external device.</i>	155
<i>Table 7.2 – The Pearson correlation coefficients, frequency and magnitude of motion for all eight patients. * Further details on the motion measurements are included in section 7.5.1 and figure 7.4. + The respiratory signal was not detected by the software, as demonstrated by no significant or a weak correlation with the external device, therefore these measurements are not a meaningful measure of the motion on the study.</i>	169
<i>Table 7.3 – The predicted correlation between the motion estimation technique and external device for different quality indices.</i>	177
<i>Table 7.4 - The images identified as having areas of reversibility by both reporters, the location of the reversibility and the significance.</i>	185
<i>Table 8.1 - The mean absolute errors for the patient motion estimation techniques developed in this thesis compared to the mean absolute errors measured by Van-Dijk et al., (2016).</i>	197
<i>Table i – The results from the respiratory motion patient cohort, section 7.2. The shaded rows represent images identified as having significant respiratory motion,</i>	

defined by the criteria in section 7.7. Method 2 and Method 3 represent the measures of motion as described in section 7.5.1.....IX

Summary

The work contained within this thesis is solely the work of the author, unless otherwise stated below.

- The research nurses, Sally Fleming and Bridget Billingham, provided guidance on obtaining research authorisation and ethics approval (REC reference number: 10/H1308/24), and consented patients.
- The clinical technologists at Sheffield Teaching Hospitals NHS Foundation Trust scanned the patients; the author set up the external device for the eight validation patients.
- Michael Hanney and Jonathan Taylor reported the myocardial perfusion images.
- Prof Alan C Perkins, Radiological Sciences, University of Nottingham & Medical Physics and Clinical Engineering, Nottingham University Hospitals NHS Trust provided the dynamic platform (Darwesh et al., 2013) for the respiratory phantom acquisitions.
- GE Healthcare provided technical support with respect to the camera and Xeleris processing software.
- Dr A Al-Mohammad was the clinical advisor for the study.
- Prof David Barber developed the Sheffield Image Registration Toolkit (ShIRT) software that was used in the study.
- Dr Peter Metherall originally developed and adapted the in-house JView software to facilitate blinded reporting.
- Feedback on the study was provided to the cardiovascular patient and public involvement panel. This was organised by the Sheffield Teaching Hospitals NHS Foundation Trust cardiology research coordinator.

Acknowledgments

There have been many people who have supported me both academically and personally. I would like to thank my supervisors Dr John Fenner, Prof David Barber and Prof Wendy Tindale for their continued support, academic input, scientific advice and discussion. Without the support of Prof Wendy Tindale and Anna Hallam, encouraging me to apply for the NIHR fellowship and practically facilitating my reduction in working hours, this thesis would never have got underway. I would also like to thank Dr Abdallah Al-Mohammad for all his support; the project evolved from an idea of Dr Al-Mohammad's and for that idea I am extremely grateful.

I would like to thank all the staff within the Nuclear Medicine Department at Sheffield Teaching Hospitals NHS Foundation Trust for their support, specifically Philip Hillel, Dr Peter Metherall, Sally Fleming, Bridget Billingham, Jonathan Taylor and Michael Hanney. I would also like to thank the nuclear medicine clinical technologists for embracing the extra cardiac scanning within their clinical workloads.

I would like to thank the National Institute for Health Research (NIHR) for the opportunity to undertake a fellowship and for funding this research, along with training opportunities and the means to present this work at conferences, GE Healthcare for their technical support, scientific advice and discussion and Prof Alan Perkins and Dr Reem Darwesh for their support with and loan of the dynamic platform.

Throughout, I have had the support of many family members and friends. I would like to thank my parents and sister for their encouragement and friends for their understanding and childcare offers. I would like to thank Oliver for his constant smiles and cuddles. Finally, I would have never survived without the support of my partner Chris, who has provided endless practical and emotional support.

1 – Introduction

1.1 – Coronary Artery Disease

In the UK there were 102,000 new cases of angina and 187,000 heart attacks, along with 69,000 deaths from coronary heart disease in 2014 (Townsend et al., 2015). Coronary heart disease cost the NHS £1.6 billion in 2013 (Townsend et al., 2014) and statistics published in 2009 suggest that coronary heart disease costs £10 billion per year from production losses and informal care of people with the disease (Townsend et al., 2012). Myocardial perfusion imaging (MPI) is a scintigraphic diagnostic test to identify patients with ischaemic heart disease.

MPI offers advantages over stress echocardiography due to improved sensitivity, (Heijenbrok-Kal et al., 2007), particularly for some sub-groups of patients. The cost and availability of MPI makes it an attractive alternative to some of the other non-invasive modalities used to diagnose coronary artery disease (CAD) such as positron emission tomography (PET), computed tomography angiography (CTA) and cardiac magnetic resonance imaging (CMR). However, there is a decline in the competitiveness of MPI with these modalities due to the patient inconvenience, inferior spatial resolution and radiation doses associated with MPI (Duvall and Henzlova, 2015). The administered activity and therefore radiation dose in the UK is limited by the Administration of Radioactive Substances Advisory Committee (ARSAC, 2017) to 800MBq (6mSv) at stress and rest for a standard weight patient (70kg). On a per patient basis the administered activity is adjusted based on the patient's weight. The mean radiation dose from MPI is 8.0mSv in Europe (Lindner et al., 2016) and 10.9mSv in the US (Mercuri et al., 2016). Recent US guidelines recommend working to a target of ≤ 9 mSv in at least 50% of studies (Henzlova et al., 2016).

1.2 – Solid State Dedicated Cardiac Imaging

Traditionally myocardial perfusion imaging has been performed on Anger gamma cameras. The Discovery NM 530c dedicated cardiac camera (DNM 530c) is one of a

new generation of solid state cameras that are transforming myocardial perfusion imaging.

“Recent technological advances (new software and advent of high-efficiency cameras) present the field an opportunity to emerge into the twenty-first century reinvigorated” (Duvall and Henzlova, 2015)

The hardware improvements on these systems allow the imaging time to be significantly reduced, with 2 minute acquisitions reported in the literature (Slomka et al., 2010). It is suggested that using these systems with a standard acquisition time of 15 minutes could reduce the radiation burden of the test to 2-3mSv (Slomka et al., 2012). Recent studies are also assessing reduced dose imaging in parallel with reduced imaging times (Sharir et al., 2015).

“The current health care environment will favor technological advances that will be at the same time cost saving, diagnostically accurate and mindful of radiation burden” (Slomka et al., 2012)

1.3 – Patient Motion

Artefacts can be introduced into myocardial perfusion images if patient motion occurs during the scan; this could be physical patient movements, or relaxation of the patient resulting in a gradual change in the position of the heart. The effect of patient motion on myocardial perfusion images acquired using traditional Anger cameras is well understood and documented. The camera design, acquisition parameters and processing algorithms used on the DNM 530c are very different to those used on traditional Anger systems and these differences have been discussed in many review articles (Garcia and Faber, 2009; Slomka et al., 2009; Garcia et al., 2011; DePuey; Slomka et al., 2012; Agostini et al., 2016; Ben-Haim et al., 2016; Henzlova and Duvall, 2016; Sharir et al., 2016)

“Shorter study times promote easier scheduling, higher patient satisfaction, and, importantly, less patient motion during acquisition, which translates to higher-quality images” (Garcia et al., 2011)

“Shorter acquisition times made possible by the newer detector designs should reduce the frequency of motion artefacts, but it will not eliminate them. Detectors that acquire information three-dimensionally still will be blurred by “upward creep” of the heart as the diaphragm relaxes” (Garcia and Faber, 2009)

It is assumed that patient motion on the DNM 530c will be reduced compared to Anger systems, due to shorter imaging times and consistent angular data (Garcia and Faber, 2009). However, the effect of patient motion on the DNM 530c is not well documented and software for motion estimation and correction is limited.

“CZT camera software is suboptimal for detecting motion” (Agostini et al., 2016)

“The most glaring omissions of the new CZT cameras are inferior detection of motion” (Henzlova and Duvall, 2016)

Motion detection and correction on Anger systems was limited by the camera design to two dimensions however, the design of the solid state systems offers the potential for three-dimensional motion estimation and correction.

“Inherent tomographic imaging may potentially enable 3D patient motion correction” (Bocher et al., 2010)

1.4 – Respiratory Motion

It has also been demonstrated that respiratory motion can introduce artefacts into myocardial perfusion imaging on Anger cameras and respiratory gating has been shown to improve the appearance of artefacts, although this remains challenging and has not been adopted clinically. Respiratory gating involves measuring the respiratory signal using either an external device or deriving the signal from the image data, which is termed data driven motion correction. Respiratory gating corrects for motion by limiting the reconstructed data to one gated bin or by aligning

the gated bins. The success of the latter using translational corrections is limited as respiration also deforms and rotates the heart.

“Respiratory gating has remained challenging due to the step-and-shoot acquisition mode with SPECT gamma cameras with rotating detectors”
(Buechel et al., 2010b)

Solid state cameras offer improved resolution over Anger systems, however the full benefit of this is not being realised as the resolution of MPI images is limited by respiratory and cardiac motion. There is limited work investigating respiratory motion correction on the DNM 530c.

“More precise gated acquisition with more and hence shorter gate intervals may allow the algorithmic creation of de-blurred perfusion images free of both respiratory motion and cardiac motion artefacts. Such de-blurring is an essential preliminary step before any hardware improvement of spatial resolution can become effective” (Bocher et al., 2010)

“We also envision that in the near future increased resolution will be a key factor as nuclear cardiology matures within molecular imaging” (Bocher et al., 2010)

The work in this thesis contributes to a body of evidence on patient and respiratory motion on the DNM 530c. In the future this may contribute to creating a myocardial perfusion image of the heart “frozen in time”, that utilises the recent hardware advances of the imaging systems to improve resolution, thus improving the ability of MPI to compete with other imaging modalities.

1.5 – Research Question

“To what extent does patient and respiratory motion introduce artefacts on myocardial perfusion imaging (MPI) on the Discovery NM 530c dedicated solid state cardiac camera (DNM 530c) and can the inherently 3D nature of this system be utilised for three-dimensional motion estimation and correction?”

To address this, the thesis is divided into two parts; patient motion and respiratory motion. A sub-set of questions is addressed in each part.

1.5.1 – Patient Motion

1. What magnitude of patient motion during MPI on the DNM 530c introduces significant image artefacts?
2. Can the inherently three-dimensional nature of the imaging system be utilised to develop patient motion estimation techniques?
3. What is the magnitude of patient motion in our patient population?
4. What percentage of patients' myocardial perfusion images are visually affected by patient motion artefacts?

1.5.2 – Respiratory Motion

1. Can the motion estimation technique developed for patient motion be adapted to detect respiratory motion?
2. How does the respiratory motion signal compare to the signal measured using an external device?
3. What is the magnitude of respiratory motion in our patient population?
4. What percentage of patients' myocardial perfusion images are visually affected by respiratory motion artefacts?

The work also considers correction, using the motion data to support motion correction algorithms. Together, these results inform priorities for future work.

1.6 – Overview of Thesis

	<p>Chapter 2 – Literature Review</p> <p>A review of the literature related to: Myocardial perfusion imaging • Anger gamma cameras • DNM 530c • Patient motion • Respiratory motion • Motion estimation and correction</p>
	<p>Chapter 3 – Effect of Motion on the DNM 530c</p> <ul style="list-style-type: none"> • One-dimensional mathematical model of motion • Phantom study to determine the magnitude and duration of patient motion that introduces motion artefacts on the DNM 530c • Relevance of phantom results to respiratory motion
Patient Motion	<p>Chapter 4 – Motion Estimation on the DNM 530c</p> <ul style="list-style-type: none"> • Proposed motion estimation technique • Pinhole collimation • Initial evaluation of technique • Development of software
	<p>Chapter 5 – Phantom Validation and Patient Application</p> <ul style="list-style-type: none"> • Phantom evaluation of the technique and software • Application to a patient cohort
Respiratory Motion	<p>Chapter 6 – Respiratory Motion Estimation and Correction</p> <ul style="list-style-type: none"> • Adaptation of the patient motion estimation technique to include principal component analysis • Initial evaluation of the technique • Motion correction technique • Development of software • Dynamic phantom evaluation and optimisation
	<p>Chapter 7 – Validation and Patient Application</p> <ul style="list-style-type: none"> • Signal post processing • Validation of the technique and software against an external device • Development of a quality index • Application to a patient cohort
	<p>Chapter 8 – Summary and Discussion</p>
	<p>Chapter 9 – Conclusions and Further Work</p>

1.7 – Thesis Exclusions

For the purpose of this thesis it is important to identify three types of motion that are present during MPI:-

- Low frequency motion such as patient motions and upward creep, which can be grouped together as “*patient motion*”
- *Respiratory motion*
- *Cardiac motion*

This thesis focuses on patient and respiratory motion on the DNM 530c. Cardiac motion has not been addressed for the following reasons;

Geometry of the Motion: Patient and respiratory motion both primarily involve translation of the heart, figure 1.1a. The techniques developed in this thesis to estimate and correct for patient and respiratory motion are based around the principle of measuring the translation of the heart at specified times throughout the MPI study. Cardiac motion is a different type of motion, primarily involving radial motion of the heart muscle around a central point, with limited overall translation of the heart, figure 1.1b. Therefore, a different approach or significant adaptations to the developed techniques should be explored for cardiac motion correction.

Commercially Available Software: At the start of this work there were no commercially available software packages for patient and respiratory motion estimation and correction on the DNM 530c and no published literature on adaptation or development of techniques for this system. The methods used clinically on Anger cameras could not be directly translated for use on the DNM 530c without adaptations. Acquiring cardiac gated images is standard practice on both Anger cameras and the DNM 530c and there is commercially available software (cardiac morphing, Xeleris workstation, GE Healthcare) that warps cardiac gated images to the end-diastolic position, limiting blurring due to cardiac motion.

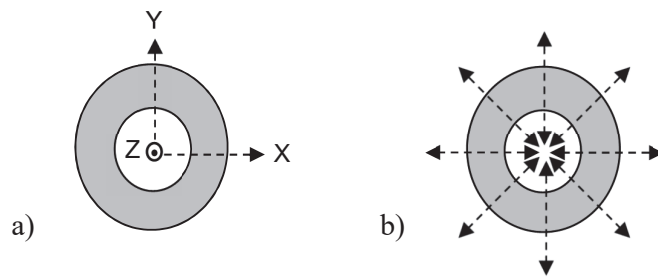


Figure 1-1 – A short axis representation of the left ventricle, (a) patient and respiratory motion is primarily a vector that translates the position of the heart, (b) cardiac motion is primarily radial motion about a central point.

This PhD began by investigating patient motion and extension of the developed methods naturally accommodated respiratory motion. The above clarifies why different methods are required for cardiac motion and consequently this can be considered beyond the scope of this thesis.

1.8 – Summary

This chapter has introduced the background to the research problem, identified how the research problem will be approached, outlined the format of the thesis and explained why correction for cardiac motion has not been included.

2 – Literature Review

2.1 – Coronary Artery Disease

Coronary artery disease (CAD) is a result of plaque build-up on the walls of the blood vessels that supply the myocardium of the heart with blood and therefore oxygen. This causes narrowing of the blood vessels resulting in chest pain on exertion, also known as ischaemic heart disease (angina), as the oxygen supply to the myocardium cannot meet demand. Untreated this can lead to heart failure, myocardial infarction or stroke. Once diagnosed, the blood supply to the myocardium can be increased by performing angioplasty, to widen the blood vessels, or coronary artery bypass grafting. The diagnostic tests available to assess for CAD are invasive coronary angiography, stress echocardiography, myocardial perfusion imaging, cardiac magnetic resonance imaging, cardiac positron emission tomography and coronary computed tomographic angiography (NICE, 2017)

2.2 – Cardiac Imaging

Non-invasive diagnostic investigations for myocardial ischemia can be divided into anatomical and functional imaging. Coronary computed tomographic angiography (CCTA) is an anatomical imaging technique that involves intravenous administration of contrast and computed tomography to image blood flow through the coronary arteries. Occlusions of the vessels can be categorised in terms of the percentage stenosis, with the National Institute for Health and Care Excellence (NICE) guidelines (NICE, 2017) stating that significant coronary artery disease is a $\geq 70\%$ stenosis of at least one major epicardial artery segment or $\geq 50\%$ stenosis of the left main coronary artery.

Functional imaging compares images of the heart at rest and during stress, which can be exercise or pharmacologically induced, to assesses the functional significance of narrowed coronary arteries. Functional imaging includes myocardial perfusion imaging, positron emission tomography (PET), stress echocardiography, first pass contrast enhanced magnetic resonance perfusion and magnetic

resonance imaging for stress induced wall motion abnormalities. Myocardial perfusion imaging involves intravenous injection of a radioisotope (Tc^{99m} or Tl^{201}), a fraction of the radioisotope is distributed in the myocardium in proportion to perfusion and perfusion can then be imaged with a gamma camera. Differences in perfusion of the myocardium between stress and rest suggest ischemia, this is described in more detail in section 2.3. PET imaging works in a similar way to myocardial perfusion imaging using radioisotopes that decay via positron emission (O^{15} , N^{13} , Rb^{82}) and using a system designed for coincidence imaging. Perfusion defects can also be identified using intravenous contrast magnetic resonance imaging as areas with diminished and/or delayed contrast enhancement compared with normal myocardium, with coronary artery disease defined as perfusion defects that are present at stress and not at rest (Wolff et al., 2004). Stress echocardiography compares ultrasound images of the heart and ischemia is characterised by new or worsening wall motion abnormalities induced by exercise (Marwick, 2003). Stress induced wall motion abnormalities can also be evaluated using magnetic resonance imaging.

The NICE Guidelines (NICE, 2017) recommend diagnostic investigations for myocardial ischemia. The guidelines recommend 64 slice CCTA as the first line diagnostic test. Non-invasive functional investigations are recommended as second line diagnostic tests, where the results from CCTA are of uncertain functional significance or non-diagnostic. Invasive coronary angiography is recommended as the third line investigation for myocardial ischemia. These are UK guidelines and in other countries, such as the US, myocardial perfusion imaging is classified as an appropriate first line diagnostic investigation. The differences in guidelines between NICE and the Appropriate Use Criteria in the US (Wolk et al., 2014) are discussed by Udelson and Hoffmann, (2017), with a possible explanation for the differences attributed to the different goals of the guidelines in terms of diagnosis, prognostic assessment and patient management.

2.3 – Myocardial Perfusion Imaging Acquisition

2.3.1 – SPECT Imaging

Single Photon Emission Computed Tomography (SPECT) myocardial perfusion imaging is a well-established and non-invasive imaging technique for the investigation of CAD. The tracers used are, Tc^{99m} labelled tetrofosmin¹ or sestamibi², or Tl²⁰¹. Uptake of tracer in the myocardium is related to perfusion of the myocardium. Three-dimensional images of the left ventricle of the heart are generated through imaging on an Anger gamma camera or dedicated cardiac cameras. Two scans are usually performed; a rest and stress scan. Stressing of the heart is performed through exercise or pharmaceutically. The images are aligned along the heart axes, to produce short axis, horizontal and vertical long axis images of the left ventricle, figure 2-1a.

Uniform uptake in the left ventricle on the stress images, often described as a “doughnut appearance” on short axis images, represents normal myocardial uptake, figure 2-1a. Normal stress images are associated with a <1% annual probability of a major cardiac event (Chowdhury et al., 2014). Myocardial ischaemia is characterised by areas of reduced uptake on stress images that reverse at rest, figure 2-1b. Myocardial infarction is characterised by the presence of one or more areas of matched reduced tracer uptake on the rest and stress images, figure 2-1c. In the absence of attenuation correction, matched reduced tracer uptake may also be the result of attenuation artefacts, however this can often be distinguished from infarction through the assessment of wall motion and thickening on cardiac gated images, section 2.3.4.

¹ Brand name Myoview (GE Healthcare)

² Commonly referred to as MIBI, brand name Cardiolite (Lantheus Medical Imaging), generic versions are available.

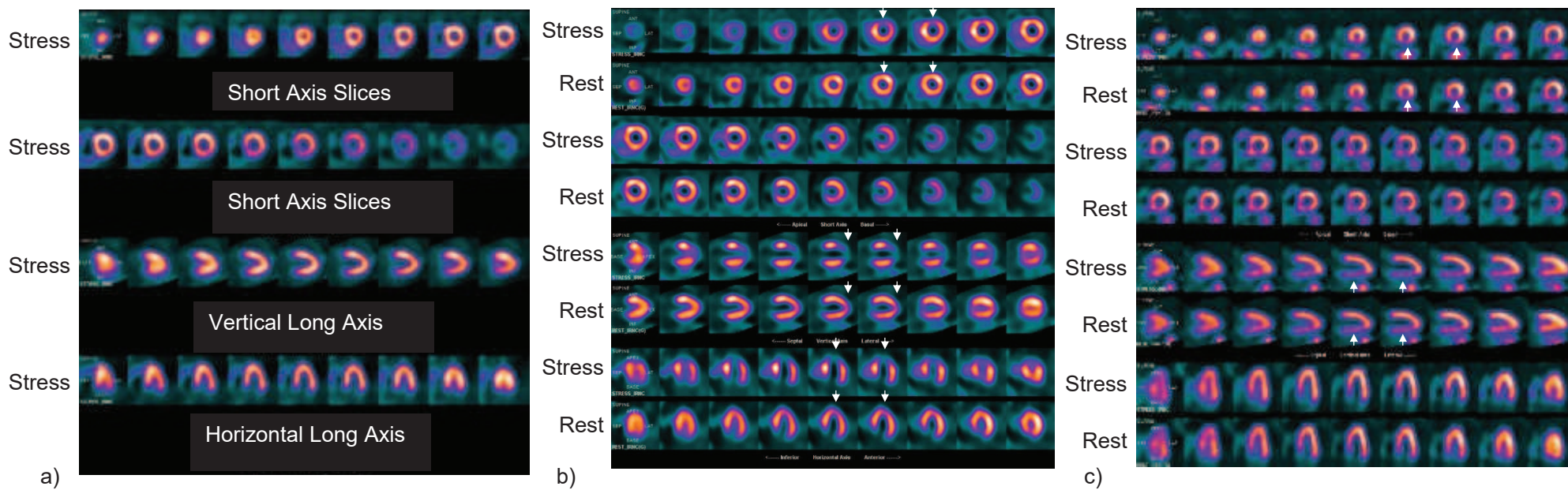


Figure 2-1 – Examples of myocardial perfusion studies showing, (a) normal myocardial uptake on the stress image and therefore no evidence of significant coronary artery disease, (b) reduced uptake on the stress image which reverses at rest (indicated by arrows) suggesting myocardial ischaemia and (c) matched reduced uptake at stress and rest (indicated by arrows) suggesting either attenuation artefacts or myocardial infarction.

2.3.2 – Anger Gamma Cameras

Conventionally single or dual headed Anger gamma cameras with parallel hole collimators have been used for myocardial perfusion imaging, figure 2-2a. The collimator lies in front of a NaI(Tl) crystal coupled to an array of photomultiplier tubes (PMT). The PMT signals are analysed to determine the energy and location of the gamma ray interaction in the crystal, producing an image of the radioactivity distribution within the patient, figure 2-2b. The heads of the camera rotate around the patient collecting projection images at different angles. The projection images are reconstructed to produce a three-dimensional image of the perfusion of the left ventricle. Procedure guidelines for radionuclide myocardial perfusion imaging (Arumugam et al., 2012; Verberne et al., 2015; Henzlova et al., 2016) recommend imaging at 15-60 minutes post injection from right anterior oblique angle of 45° to a left posterior oblique angle of 45° . For a dual headed gamma camera this is achieved with the heads in an 'L mode' configuration, figure 2-2a.

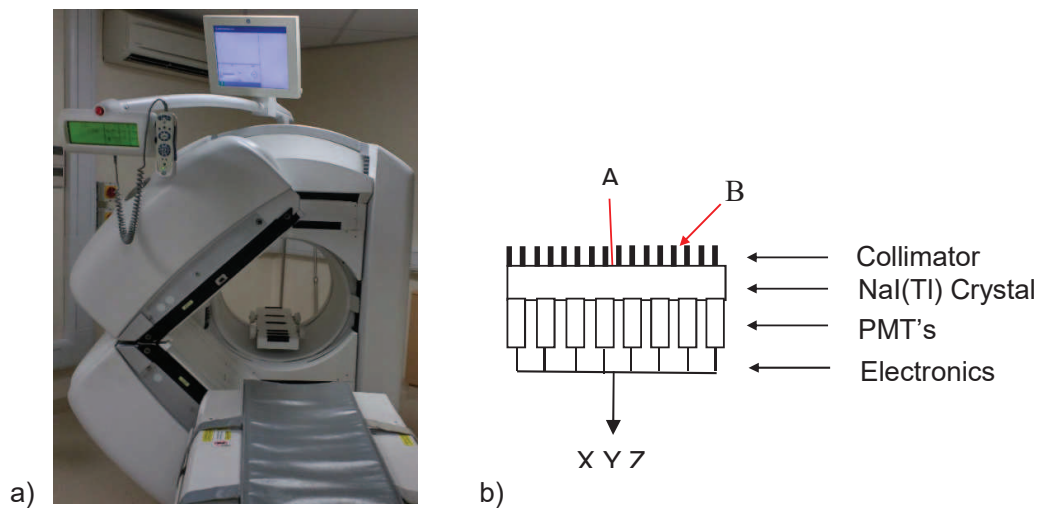


Figure 2-2 – (a) A dual headed camera in the 'L Mode' configuration used for myocardial perfusion imaging, (b) schematic diagram of an Anger gamma camera, A - γ rays parallel to collimator pass through and interact with the crystal, B - γ rays at an angle to the collimator are absorbed and do not interact with the crystal. The X,Y (location) and Z (energy) signals are used to produce an image of the radioactivity distribution in the patient.

2.3.3 – SPECT Reconstruction and Image Quality

Reconstruction techniques have evolved over time from filtered back projection to iterative reconstruction. Projecting images taken at different angles around an object back through the object space provides an approximation of the original object, however this also introduces star artefacts that blur the reconstructed image. Filtered back projection combines back projection with a ramp filter to reduce this blurring. A commonly used iterative reconstruction algorithm is maximum-likelihood expectation maximization (MLEM). MLEM assumes an initial estimate of the object and then forward projects this estimate to get estimated projections. The estimated projections are compared to the measured projections and the difference is used to update the initial estimate of the object. This process is then repeated for a fixed number of iterations, converging on a solution. Ordered subset expectation maximisation (OSEM) divides the projections into groups, with each group containing a subset of projections that are equally distributed around the object. An iteration is complete when the MLEM algorithm has been applied to each subset. OSEM accelerates convergence compared to the MLEM algorithm (Bruyant, 2002). MLEM and OSEM use a system matrix to model the probabilities that photons from specific voxels will be detected by specific detector pixels. Attenuation, scatter and depth dependent resolution can be incorporated into the system matrix improving the accuracy of iterative reconstruction algorithms (Hutton, 2011; DePuey, 2013).

The quality of SPECT images can be affected by many factors including; collimator type, spatial resolution, energy resolution, non-uniformities, centre of rotation errors, multi-detector alignment, noise, partial volume effects, activity outside the organ of interest, patient and organ motion, attenuation, scatter, depth dependent resolution, type of reconstruction, reconstruction parameters, noise regularisation and filtering (DePuey, 1994; Rosenthal et al., 1995; Case and Bateman, 2013). The resolution of a SPECT study depends mainly on the isotope and collimator used, the type of reconstruction, corrections applied and post filtering parameters. Correction for non-uniformities and some forms of patient motion can be applied before reconstruction. Attenuation can be corrected using CT images, or cardiac gating can be used to distinguish between attenuation artefacts and fixed perfusion defects.

2.3.4 – Cardiac Gating

Cardiac gating, figure 2-3, is a technique that often forms part of routine myocardial perfusion imaging. The acquisition is gated with the electrocardiogram (ECG) of the patient to isolate parts of the cardiac cycle. Each cardiac cycle is usually gated into 8 or 16 bins. Viewing the cine of the reconstructed bins shows motion and thickening of the myocardial walls. Attenuation can produce artefacts, often in the anterior wall in females and the inferior wall in males. It has been demonstrated that viewing cardiac gated data alongside perfusion images increases specificity by identifying fixed perfusion defects with normal function as attenuation artefacts (DePuey and Rozanski, 1995).

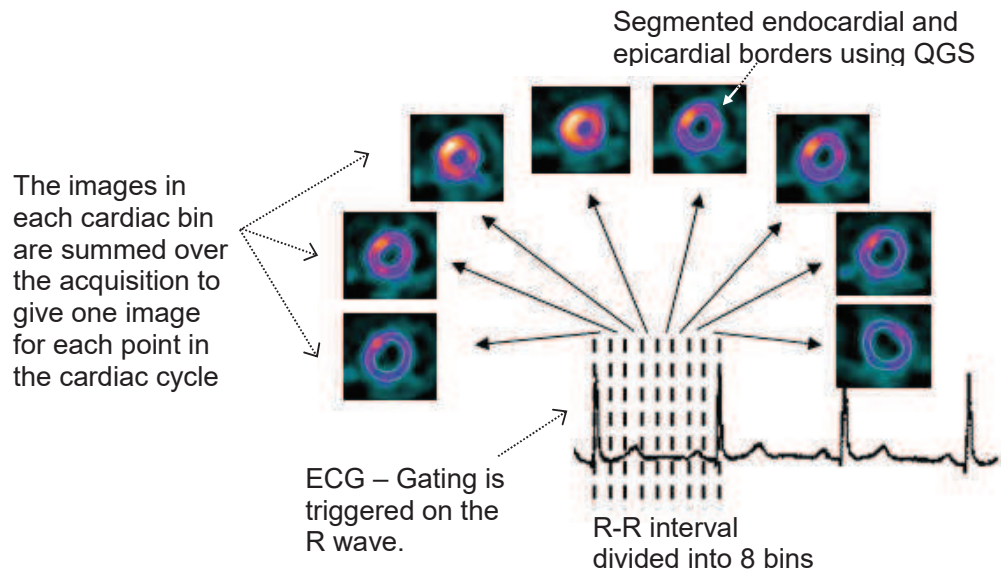


Figure 2-3 – Cardiac gating involves dividing the data acquired for each R-R interval into 8 or 16 bins. The data in each bin is summed and reconstructed, to give 8 or 16 three-dimensional images of the left ventricle at different points in the cardiac cycle. Viewing these as a sequence facilitates visualisation of the motion and thickening of the myocardial walls. ECG – Electrocardiogram, QGS – Quantitative Gated SPECT.

2.3.5 – Quantification of Myocardial Perfusion Images

Semi-quantitative assessment is often performed by reviewing the images using a discrete color scale normalised to the maximum pixel value in the myocardium with 100%–70% representing normal perfusion and 69%–50%, 49%–30%, 29%–10% and 9%–0% representing mild, moderate, severe and absent perfusion respectively, (Kapur et al., 2002).

Quantitative Perfusion SPECT (QPS, Cedars-Sinai Medical Centre, Los Angeles, CA) produces several quantitative measures of myocardial perfusion by comparison of patient images to a normal database (Germano et al., 2007). The left ventricle is segmented using the techniques described in Germano et al., (2000) and pixel based polar maps, which are a two-dimensional representation of the left ventricle, with the centre of the plot corresponding to the apex and the outer part of the plot corresponding to the base are produced, figure 2-4. Measures of perfusion (%), defect extent (%) and defect severity (0-10SD) are displayed on the segmented polar maps. QPS can also generate segmental scores, defined as the summed stress score (SSS), summed rest score (SRS) and summed difference score (SDS) based on the perfusion of each segment at stress or rest and the difference between the two.

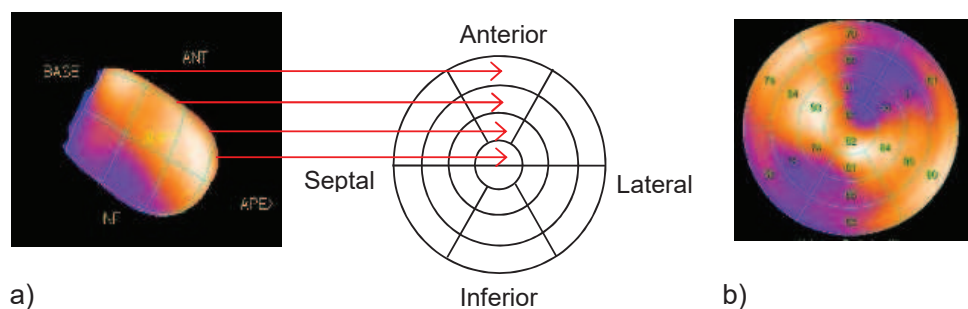


Figure 2-4 – (a) Polar plots are a two-dimensional representation of the left ventricle, (b) Quantitative Perfusion SPECT displays the perfusion (%) on the segmented polar map.

The improved quantification module of Quantitative Perfusion SPECT (PFQ, Cedars-Sinai Medical Centre, Los Angeles, CA) calculates the total perfusion deficit (TPD) from equation 2.1, where a and p are radial coordinates of the polar plot, A and P are the maximum number of points in each direction and $score(a, p)$ is the score at polar plot location (a, p) , (Slomka et al., 2005). The scores assigned to each polar plot pixel are defined by how much the perfusion fell below the normal limit. The TPD is therefore a figure reflecting the extent and severity of the overall perfusion defect.

$$TPD = 100 \times \sum_{a=0}^{a<A} \sum_{p=0}^{p<P} score(a, p) / (4AP) \quad \text{Equation 2-1}$$

Quantitative Gated SPECT (QGS, Cedars-Sinai Medical Centre, Los Angeles, CA) aids reporting of cardiac gated studies by segmenting the left ventricle in each cardiac gated bin and producing polar plots showing wall motion and thickening. Functional parameters such as the left ventricular ejection fraction, end diastolic volume and end systolic volume are also calculated.

2.3.6 – Discovery 530c Dedicated Cardiac Camera

The focus of this thesis is the Discovery NM 530c solid state dedicated cardiac camera (DNM 530c). The DNM 530c, figure 2-5a, has 19 detector modules positioned at different angles around the patient, from a right anterior oblique position to a left posterior oblique position. These are arranged around the patient as an alternating sequence of triplets and single cadmium zinc telluride (CZT) detector modules, creating 19 images of the heart, figure 2-5b. These all focus on a quality field of view (QFOV). This is nominally described as a 19cm sphere, however the results from one study suggest it is an ellipsoid of less than 18 x 16 x 16 mm (Aarsvold et al., 2012).

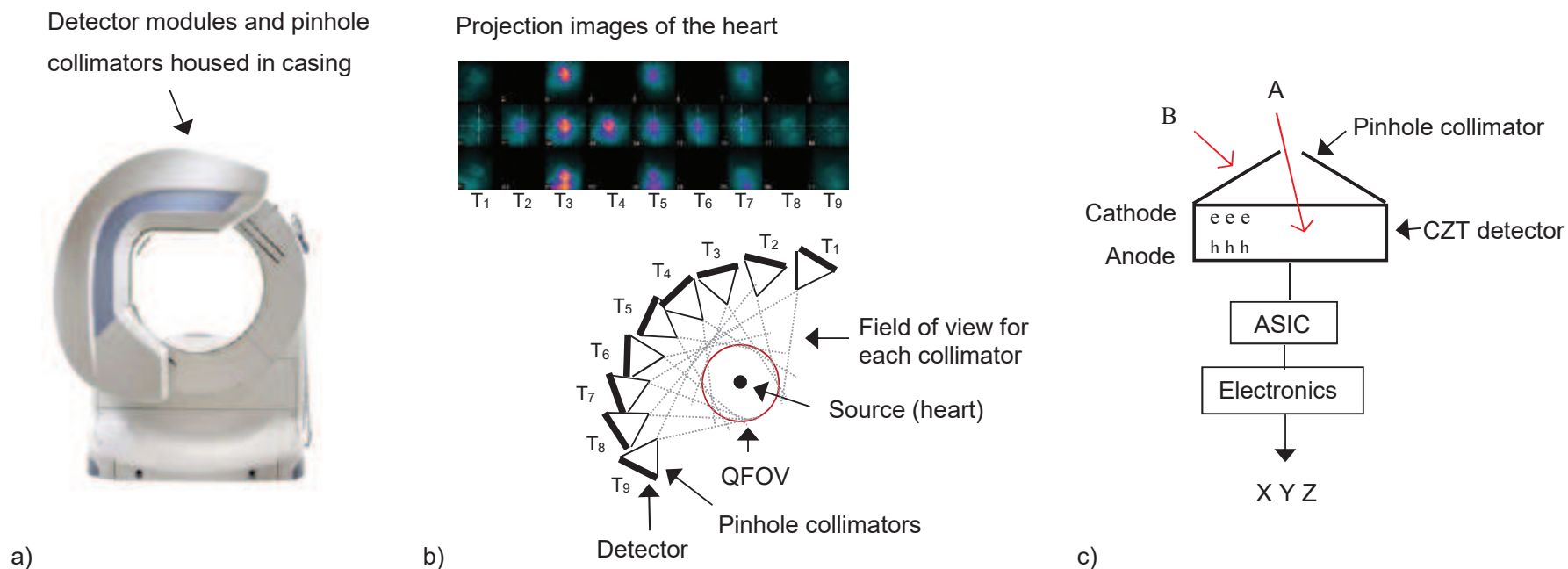


Figure 2-5 – (a) The DNM 530c is a fixed system with no movement of the gantry during the acquisition, (b) a schematic diagram showing the pinhole collimators focused on the quality field of view (QFOV); at each angle there is a set of detectors, denoted T_n , with the number of detectors in each set alternating between 1 and 3, (c) the solid state cadmium zinc telluride (CZT) detector modules convert gamma ray energy straight into an electrical signal, A - γ rays incident on the pinhole are detected, B - γ rays that are not incident on the pinhole are absorbed by the collimator. ASIC – application-specific integrated circuit.

Each detector module has a tungsten pinhole collimator, with an approximate diameter of 4.8 – 5.1mm (Jansen et al., 2010; Aarsvold et al., 2012; Kennedy et al., 2014; Agostini et al., 2016), to produce an inverted miniaturised image of the heart on the detector. Images acquired on the DNM 530c are reconstructed using a maximum likelihood expectation maximisation (MLEM) iterative reconstruction technique that models the system geometry including collimator response, with an adaptation of OSL Green's prior (Green, 1990) to control smoothness of the reconstruction and a Butterworth 3D post filter (Bocher et al., 2010).

2.3.7 – Comparison of Performance

The key differences between an Anger gamma camera and the DNM 530c are listed below:

Solid State Detector Technology: The lower energy required by solid state detectors to create an electron-hole pair (3–6eV) compared to the energy required to create a photon (~30eV) in a NaI(Tl) scintillation crystal, and direct conversion, which eliminates the losses and statistical variations associated with indirect conversion, results in increased energy and spatial resolution (GE Healthcare, Alcyone Technology White Paper ; Garcia et al., 2011).

Focused Collimation: Pinhole collimation used on the DNM 530c increases the efficiency of the system. The focused nature of the pinhole collimation facilitates the use of smaller detectors allowing multiple detectors to acquire images simultaneously at different angles, without any moving parts, therefore increasing detection sensitivity (Slomka et al., 2009).

One of the first papers to be published on the performance of the DNM 530c (Bocher et al., 2010) compared key performance parameters between the DNM 530c and a dual-head dedicated cardiac camera (Ventri™, GE Healthcare). This demonstrated that for Tc^{99m} the DNM 530c has three times the sensitivity, twice the energy resolution, a higher spatial resolution and linear count rate performance, table 2.1. For shorter acquisitions, 5 and 3 minutes on the DNM 530c compared to

12.5 and 10 minutes on the dual headed camera, the uniformity and defect contrast were comparable or better for the DNM 530c.

Parameter	DNM 530c	Ventri™
Sensitivity (c/s/MBq)	657 ⁺	206
Tc ^{99m} Energy Resolution (%)	5.4	9.4
Tc ^{99m} Spatial Resolution (mm)	6.1 ⁺	10.9
Maximum Count Rate (Kc/s)	612	320
Normalised Standard Deviation (%)*	12.5	13.6
Effective Contrast Lateral Wall (%)*	38.5	30.5

*Table 2.1 – Key performance parameters measured for the DNM 530c and a dual headed dedicated cardiac camera, Ventri™ by Bocher et al., (2010). * Male Phantom, + Centre of the Quality field of View.*

These parameters have also been assessed in another publication with similar results; average spatial resolution $6.9 \pm 1.0\text{mm}$, sensitivity $460 \pm 190\text{ c/s/MBq}$ and a linear count rate performance with a maximum count rate of 418 Kc/s (Kennedy et al., 2014). Although these measurements demonstrate the differences between the different types of technology, they do not represent a direct comparison between the systems. For example, NEMA guidelines recommend spatial resolution measurement with filtered back projection (FBP), however as FBP is not an option for the DNM 530c the dedicated iterative reconstruction algorithm was used (Bocher et al., 2010). Also, these results are not necessarily representative of the clinical scenario as clinically relevant reconstruction parameters and voxel sizes were not used for some of the measurements (Bocher et al., 2010), or in cases where clinical reconstruction parameters were used post reconstruction filtering was excluded (Kennedy et al., 2014). During acceptance testing of the DNM 530c at Sheffield Teaching Hospitals NHS Foundation Trust (STH) using clinical reconstruction and post filtering parameters, the spatial resolution was measured to be 12.7mm and 13.8mm at the centre and edge of the QFOV respectively, the energy resolution was 7% and there was a linear count rate performance (Hillel et al., 2011).

Since the introduction of the DNM 530c into clinical practice, there have been an increasing number of original papers assessing the performance of the DNM 530c. These can be divided into two categories: -

Comparison with dual headed Anger gamma cameras (table 2.2): A number of studies performed sequential scanning on both systems. These used reduced imaging times on the DNM 530c compared to dual headed Anger gamma cameras, demonstrating that imaging times can be reduced by a factor of 2.4 – 7.5, with comparable diagnostic performance and improved image quality. Three studies retrospectively compared groups of patients scanned on both cameras showing that the number of abnormal scans on the DNM 530c was reduced compared to Anger cameras, resulting in significantly less need for rest imaging or coronary angiography. The prognostic value in terms of future events (death, non-fatal myocardial infarction and revascularisation) was shown to be similar for both cameras despite lower administered activities and/or shorter acquisition times.

Comparison to coronary angiography (table 2.3): Many studies compared the results from the DNM 530c to coronary angiography. These demonstrated sensitivity, specificity and accuracy figures for the DNM 530c of 72-95%, 37-79%, 69-83% respectively. Loong and Anagnostopoulos, (2004) reviewed 89 studies, showing the sensitivity and specificity for Anger cameras to be 64-100% and 28-100% respectively.

Table 2.2 and table 2.3 clearly highlight the multiple variables across studies, including but not limited to; radiopharmaceutical; imaging protocol; administered activity; imaging time; dose; reconstruction method; supine or prone imaging and attenuation correction. The literature is biased towards a one-day protocol. The British Nuclear Medicine Society guidelines (Arumugam et al., 2012) recommend a two-day protocol on the basis of superior image quality. Only one of the studies reviewed used a two-day protocol.

Reference	Tracer	Protocol	Patients	Method	Results
Esteves et al., (2009)	Tc ^{99m} TF	One day, R-S, 370MBq and 1110MBq. Exercise or adenosine or dipyridamole stress.	168 multicentre trial	DNM 530c, 4 and 2 minute acquisitions. Dual headed 14 and 12 minute acquisitions. Scanned sequentially on both systems. Visual identification of perfusion defects compared.	DNM 530c had comparable per patient diagnostic performance for significantly reduced imaging times and improved image quality.
Herzog et al., (2010)	Tc ^{99m} TF	One day, S-R, 300-350MBq and 2.5-3 times stress dose. Adenosine stress.	20 consecutive	DNM 530c, 6 minute list data acquisition, rebinned into 1, 2, 3, 4, 5 and 6 minute images. Dual headed 15 minute both images (OSEM). Scanned sequentially on both systems.	Minimum required scan times for the DNM 530c were 3 minute for low dose and 2 minute for high dose acquisitions.
Buechel et al., (2010a)	Tc ^{99m} TF	One day, S-R, Mean dose: 337MBq and 948MBq. Adenosine stress.	75 consecutive	DNM 530c, 3 and 2 minute acquisitions. Dual headed 15 minute both images (OSEM). Scanned sequentially on both systems. Clinical agreement assessed.	DNM 530c allows fivefold reduction in scan time and provides equivalent per patient clinical information.
Gimelli et al., (2011)	Tc ^{99m} TF	One day, S-R, 370MBq and 740MBq. Exercise or dipyridamole stress.	34 consecutive	DNM 530c, 5 and 4 minute acquisitions. Dual headed 20 and 18 minutes (OSEM). Scanned sequentially. Qualitative and quantitative analysis performed.	DNM 530c equivalent diagnostic confidence on a per patient basis. Improved diagnostic confidence on a per-vessel basis.
Duvall et al., (2011a)	Tc ^{99m} MIBI	One day, R-S, 185 and 555MBq. Exercise or pharmacologic stress.	131 over 7 weeks	DNM 530c, rest 5 and 8 minute acquisitions, stress 3 and 5 minutes. Dual headed 15 minutes (MLEM). Scanned sequentially. Image quality comparison and clinical follow-up.	No difference in image quality between longer and shorter scans. Compared to the dual headed scanner diagnostic accuracy preserved.

Mouden et al., (2012)	Tc ^{99m} TF	One day, S-R, 370MBq and 740MBq. Adenosine or dobutamine stress.	456 consecutive without known CAD	DNM 530c, 5 and 4 minute acquisitions (255 patients). Dual headed 12 and 15 minute acquisitions (231 patients). 1-year clinical follow-up.	DNM 530c significantly reduced rest imaging and CTA. Identical clinical outcomes after 1 year.
Tanaka et al., (2013)	Tc ^{99m} MIBI or TF	One day, S-R, 296-370MBq and 740MBq. Exercise or adenosine stress.	150 consecutive Japanese patients	DNM 530c, 5 and 3 minute acquisitions. Triple headed 5 minutes both images. Scanned sequentially. Image quality graded. Visual evaluation images and segmental scoring.	DNM 530c image quality rated as good or excellent. Strong positive correlation between SSS, SRS, SDS and function parameters.
Lima et al., (2016)	Tc ^{99m} MIBI	Group1: Two day, S-R, 370-444 and 555-666MBq. Group 2: One day, R-S, 185 and 555MBq. Exercise or dipyridamole or dobutamine stress.	3554 patients. Two matched groups, 1777 in each	Group 1: Dual headed 6 minute acquisitions. Group 2: DNM 530c, 6 and 3 minute acquisitions (OSEM-RR). Classified normal or abnormal. Perfusion scores calculated. Clinical follow-up.	Group 1 had more abnormal scans and higher scores than group 2. Lower prevalence of hard events in patient's normal scan on DNM 530c. Similar prognostic results for patients with CAD.
Oldan et al., (2016)	Tc ^{99m} TF	One day, R-S, 370-444 and 777-1332MBq. Exercise or regadenoson or dipyridamole or dobutamine stress.	1993 Patients	DNM 530c, 5 and 3 minute acquisitions (1128 patients). Dual headed 15 and 10 minute acquisitions (865 patients, FBP). Clinical follow-up.	Similar prognostic results between cameras.

Table 2.2 – Literature comparing the performance of the DNM 530c to Anger cameras, reconstruction parameters for Anger cameras are supplied when specified. CAD – coronary artery disease, CTA – coronary computed tomography angiography, DNM 530c - Discovery NM 530c solid state dedicated cardiac camera, MIBI - sestamibi, OSEM - ordered subset expectation maximisation, RR – resolution recovery, SSS – summed stress score, SRS – summed rest score and SDS – summed difference score, S-R – stress-rest, R-S – rest-stress, TF – tetrofosmin.

Reference	Tracer	Protocol	Patients	Results
Duvall et al., (2011b)	Tc ^{99m} MIBI or Tl ²⁰¹	One day, R-S (185 and 555MBq, 5 and 3 minutes) or S-R (463MBq, 5minute) or stress-redistribution (93MBq, 5minute). Supine and prone imaging. Exercise or pharmacologic stress. No AC.	230 Patients over one year who had coronary angiography within 2 months.	Sensitivity 95% Specificity 37% Accuracy 69%
Fiechter et al., (2011)	Tc ^{99m} TF	One day, S-R (mean doses: 335MBq and 980MBq, 3 and 2 minutes), adenosine or dobutamine stress. AC.	66 Patients who had coronary angiography within 3 months.	Sensitivity 87% Specificity 67% Accuracy 83%
Gimelli et al., (2012)	Tc ^{99m} TF	One-day, S-R (185-222 and 370-444MBq, 7 and 6 minutes). Exercise or dipyridamole stress. Supine imaging. No AC.	137 who had coronary angiography within 1 month.	Sensitivity 95% Specificity 77%
Chowdhury et al., (2014)	Tc ^{99m} TF	Two-day protocol (550MBq, 200-600 seconds dependent on weight). Adenosine stress. Supine imaging. No AC.	Retrospective analysis of 165 patients who had angiography within 8 weeks.	Sensitivity 84% Specificity 79% Accuracy 82%
Esteves et al., (2013)	Tc ^{99m} TF	One day, R-S (222 and 740MBq, 5 and 3 minutes), exercise or regadenoson stress. Supine only. AC.	55 Patients who had coronary angiography within 2 months.	Sensitivity 79-92% Specificity 44-75%
Barone-Rochette et al., (2015)	Tc ^{99m} MIBI and Tl201	Tl201 stress (74-111MBq, 5 minute) and Tc ^{99m} MIBI rest (300-450MBq, 5 minute). Exercise or dipyridamole or dobutamine stress. Supine and prone imaging.	55 Patients who had coronary angiography within 3 months.	Sensitivity 94% Specificity 50% Accuracy 83%
Sharir et al., (2015)	Tc ^{99m} MIBI	One day, S-R, low dose (185 and 555MBq, 5 minute) and standard dose (333 and 925MBq, 5-7 minute). Exercise or dipyridamole stress. Supine and prone imaging.	128 standard dose and 156 low dose, coronary angiography within 60 days.	Sensitivity 86-91% Specificity 77-78% Accuracy 81-84%

Table 2.3 – Literature comparing the performance of the DNM 530c to coronary angiography. AC – attenuation correction, MIBI – sestamibi, S-R – stress-rest, R-S – rest-stress, TF – tetrofosmin.

It has been shown in the literature, table 2.2, that using the DNM 530c allows a significant reduction in scan time. However, scan time can be extended in order to facilitate a reduction in MPI doses. Oddstig et al., (2013) divided patients into 3 subgroups, with 4, 3 and 2.5MBq/kg administered at stress and three times the stress activity at rest. Imaging time was increased in proportion to the decreased activity, resulting in scan times of 300s – 475s. They demonstrated that the dose could be decreased from 9.3mSv to 5.8mSv with no significant difference in image quality. Sharir et al., (2015) divided patients into two groups; low dose, 185 and 555MBq stress-rest, 5 minute imaging and standard dose, 333 and 925MBq stress-rest, 5-7 minute imaging. There were 156 and 128 patients in the low and standard dose groups respectively and all patients had coronary angiography within 60 days of the MPI scan. The study demonstrated that the dose could be reduced from 11.7mSv to 6.9mSv with no significant difference in sensitivity, specificity or accuracy. Duvall et al., (2013) calculated the sensitivity and specificity using both visual and automated quantitative analysis for different patient groups on the DNM 530c and demonstrated that visual and quantitative assessment both provide a similar diagnostic accuracy when compared to angiography.

There is increasing interest in the cumulative doses received from diagnostic imaging and dose reduction. The mean effective dose from MPI SPECT is 8.0mSv in Europe (Lindner et al., 2016) and 10.9mSv in the US (Mercuri et al., 2016). The American Society for Nuclear Cardiology (ASNC) published recommendations for reducing radiation exposure from MPI, including the recommendation that *“high sensitivity SPECT geometries should be used wherever available and considered at the time of new equipment purchase”* (Cerqueira et al., 2010). The ARSAC DRL for myocardial perfusion imaging is 800MBq each for stress and rest imaging, resulting in an effective dose of 11.9mSv (ARSAC, 2017).

The DNM 530c can be supplied with CT for attenuation correction; however, in many centres this option is not available. Attenuation is known to introduce artefacts into MPI and one method of assessing for artefacts is through the use of cardiac gating, section 2.3.4. An additional technique that can be used on the DNM 530c is prone imaging in addition to supine imaging. Attenuation artefacts will change with patient position and therefore when supine and prone imaging is performed a scan

is only classified as abnormal when reduced perfusion is identified in the same regions on both images. It has been demonstrated that combined supine-prone imaging reduces the number of inferior wall artefacts and significantly increases the specificity and accuracy compared to supine only imaging, therefore reducing the number of rest images and coronary angiography investigations performed (Duvall et al., 2013; Goto et al., 2014; Nishiyama et al., 2014; Stathaki et al., 2015; Howard et al., 2016). It has also been demonstrated that the risk of cardiac death and myocardial infarction in patients with reduced perfusion on supine imaging, that was not apparent on prone imaging, is comparable to the risk to patients with no perfusion abnormalities (Worden et al., 2015). Quantitative perfusion SPECT (QPS) can calculate combined prone-supine TPD values based on the three-dimensional registration of prone and supine image (Germano et al., 2007).

It has been demonstrated that gated studies on the DNM 530c have increased end diastolic volume (EDV) and end systolic volume (ESV) and decreased left ventricular ejection fraction (LVEF) values compared to Anger cameras due to the increased spatial and energy resolution of the systems (Miao et al., 2015). Good correlation has been demonstrated between the EDV, ESV and LVEF values calculated on the DNM 530c and compared to MRI (Claudin et al., 2016).

2.3.8 – List Mode Data

In addition to producing projection images, some cameras, both dedicated and Anger, also store acquisitions in list mode. List mode records the detected events as a list, along with parameters such as the location, energy and time associated with each event.

2.4 – Motion on Anger Gamma Cameras

Motion is a source of artefacts in myocardial perfusion imaging. This may be physical movement of the patient, organ motion (upward creep or respiratory motion) and cardiac contraction. Motion comparable with the SPECT resolution of a system will blur the images. Patient and respiratory motion blurring is position dependent and leads to apparent variations in the intensity of the left ventricular

wall, which could mimic true perfusion defects. Small local defects could also be obscured by motion blurring.

Patient motion arises due to gross patient movements, such as moving on the imaging couch. Upward creep of the heart is associated with a gradual change in the diaphragm position, resulting in a gradual creep upwards in the position of the heart throughout the acquisition. This can occur following exercise, a change in the body position from erect to supine or as a result of relaxation of the patient during the scan. Both patient motion and upward creep usually involve a change in the position of the heart that can be visualised between projection images on Anger cameras. From this point onwards any references to patient motion will include upward creep of the heart, as the same principles apply to both types of motion.

The duration of a myocardial perfusion scan on a standard Anger camera is a compromise between improved count statistics and an increased likelihood of patient motion. The recommended MPI scan time is 20-30 minutes which equates to 10-30s projections (Hesse et al., 2005).

Respiratory motion is movement of the heart due to diaphragm and internal organ motion during respiration. This has a higher frequency than patient motion, with multiple respiratory cycles occurring within projection images. Alternative approaches are therefore required for respiratory motion estimation and correction. Respiratory motion is discussed further in sections 2.4.3 and 2.4.4.

2.4.1 – Patient Motion

Physical movements of a patient and relaxation during myocardial perfusion imaging on Anger cameras is inevitable with imaging times of 20 – 30 minutes and is routinely seen in clinical practice. The British Nuclear Medicine Society (BNMS), European Association of Nuclear Medicine (EANM) and the Society of Nuclear Medicine (SNM) guidelines (Anagnostopoulos et al., 2003; Hesse et al., 2005; Strauss et al., 2008) recommend routinely assessing images for patient motion before the patient leaves the department. The European guidelines (Hesse et al., 2005) recommend that ≥ 2 pixels of patient motion justifies motion correction.

The effect of patient motion on Anger cameras is well documented and relevant findings from these studies are summarised in table 2.4. A majority of the studies are for Tl^{201} , exercise stressing and filtered back projection (FBP). There are a few more recent studies that investigate Tc^{99m} tracers, OSEM reconstruction and pharmaceutical stressing. The ROBUST study (Kapur et al., 2002) found that there were less motion artefacts with Tl^{201} than with either of the Tc^{99m} tracers, but there was no difference between sestamibi and tetrofosmin. The main points to note from the literature are that;

- Artefacts vary depending on the position and number of projection images affected and the extent of the displacement.
- Artefacts were observed in the anterior and inferior walls of the left ventricle for cranio-caudal translations and in the septal and lateral walls for horizontal translations between projection images.
- Artefacts were more significant with dual headed cameras, as a single occurrence of motion affects twice the number of projections compared to a single headed camera. For upward creep the maximum motion occurs between the first frame of the second detector and the last frame of the first detector, which corresponds to a point with relatively high myocardial counts (Matsumoto et al., 2001).
- Quantitative results showed an increase in defect severity with improved image reconstruction techniques.

An example of a patient motion artefact is shown in figure 2-6. Patient motion can also cause blurring of cardiac gated bins, which can affect the accuracy of measurements made on the gated images (Asit and Hani, 2004).

Reference	Tracer	Patient	Stress Test	Acquisition Parameters	Recon	Method	Results
Mukherjee et al., (2010)	Tl ²⁰¹	66 patients (110 studies)	Exercise Dipyridamole	Dual, 68 projections, 102° configuration.	OSEM- ACRR	Motion measured using a visual tracking system.	Motion 3-6mm and >6mm for >4 minutes for 23% and 5% studies respectively.
Zakavi et al., (2006)	Tc ^{99m} MIBI	Simulations on 6 normal studies	Not stated	Single, 32 x 30s projections.	FBP OSEM	Simulated 3 pixel returning and non-returning motion on normal studies.	No difference in image reports. Defect severity increased with OSEM reconstruction.
Karacalioglu et al., (2006)	Tc ^{99m} MIBI	200 patients	Treadmill Exercise	Dual, 64 x 28s projections.	FBP	Patients split into 5 minute bed rest and no rest post stress. Upward creep compared.	Creep reduced for 5 minute bed rest after stressing; 53-55% compared to 89-86%. Motion 1.4-22.3mm.
Wheat and Currie, (2004)	Tc ^{99m}	400 patients	3 protocols across 3 sites		----	Motion assessed visually for the type and location of motion.	36% visually detectable motion. Multiple bounce most common type.
Kapur et al., (2002)	Tc ^{99m} Tl ²⁰¹	2560 patients	Adenosine	Dual, 64 x 20-25s projections.	FBP	Patients randomised to MIBI, TF or Tl. Number of pixels motion assessed.	Significantly more motion artefacts with Tc ^{99m} tracers. No difference MIBI and TF.
Matsumoto et al., (2001)	Dual MIBI Tl ²⁰¹	130 patients	Exercise	Dual, 64 projections.	FBP	Motion simulated to represent single and dual headed cameras on 8 normal patients. Motion artefacts assessed on all patients.	Defect size depends on position of motion. Artefacts increased for dual headed cameras. Patient motion 63% bounce, 26% creep, 11% other.
Prigent et al., (1993)	Tl ²⁰¹	164 patients	Treadmill Exercise	Single, 32 x 40s projections.	----	Motion pixel area (MOPA) used to quantify motion on patients <5% LLH CAD.	Motion in 26% of patients studies, with motion causing defects in 4%.

Botvinick et al., (1993)	Tl ²⁰¹	165 patients	Treadmill Exercise	Single, 32 x 40s projections.	FBP	Motion simulated on 6 normal studies. Motion artefacts assessed in clinical review.	Artefacts vary depending on the displacement, position, and number of projections affected. Detectable motion in 25% of patients, with motion causing defects in 5%.
Cooper et al., (1992)	Tl ²⁰¹	Simulations on normal studies	Treadmill Exercise	Single, 32 x 40s projections.	FBP	Motion simulated on normal studies. Bulls-eye plots compared to a normal database.	6.5mm (1 pixel) motion visible not clinically significant, 13mm motion clinically significant.
Mester et al., (1991)	Tl ²⁰¹	100 patients	Exercise	Single, 32 x 30s projections.	FBP	Motion assessed by measuring the shift in the bottom/top of the heart between projections.	1, 2 and 3 pixels of upward creep found in 16, 4 and 3 patients. Motion ≥ 2 pixels gave antero-septal defects and ≥ 3 pixels gave false-positive diagnostic results.
Friedman et al., (1989)	Tl ²⁰¹	102 and 45 patients	Exercise	Single, 32 x 30s projections.	FBP	Group 1 -102 consecutive patients. Group 2 – 45 patients <5% LLH CAD patients.	Group 1 - 29% had creep ≥ 2 pixels. Group 2 - 38% ≥ 2 pixels motion. One and three pixels motion resulted in defects in 10% and 100% of cases respectively

Table 2.4 – A summary of the literature on patient motion on Anger cameras. Unless otherwise stated imaging was with the heads configured at 90° with imaging performed over 180° using a 64 x 64 matrix with no attenuation or scatter correction. Dual / single refers to the number of heads on the camera. The duration of each projection is given in seconds (s). MIBI - sestamibi, TF - tetrofosmin, FBP - filtered back projection, OSEM - ordered-subset expectation maximisation, RR – resolution recovery, AC – attenuation correction, LLH CAD - low likelihood coronary artery disease, Recon - reconstruction. Where parameters are not included these were not specified.

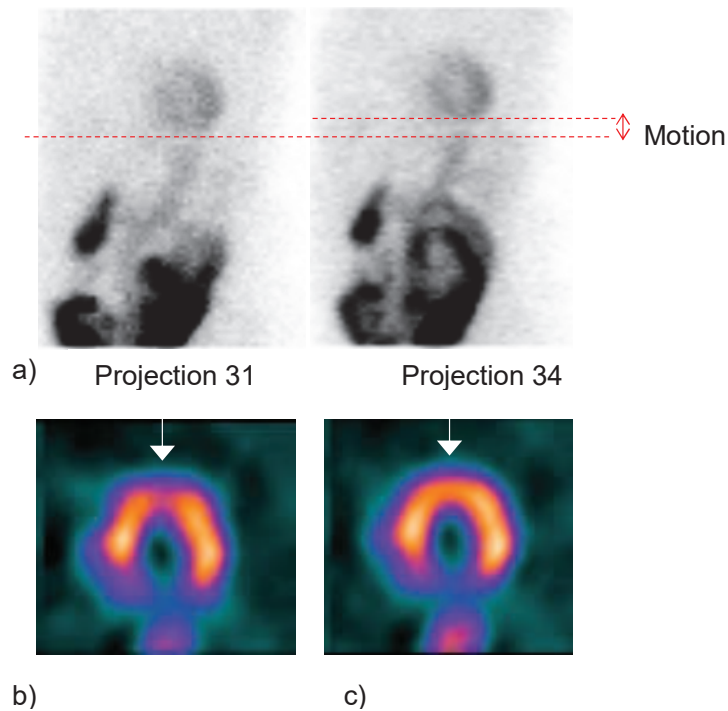


Figure 2-6 – A patient scan performed on an Anger camera. (a) Motion is visible between projections, (b) reconstructed short axis slices before and (c) after motion correction. Motion artefacts are indicated by the arrows.

There is a complex relationship between diaphragmatic motion, sub-diaphragmatic activity in the upper abdominal organs and image artefacts. When sub-diaphragmatic activity is present artefacts are dependent on the activity ratio between the inferior wall and sub-diaphragmatic activity, and the amplitude of the diaphragm (Pitman et al., 2005). It has been demonstrated on Anger cameras that inferior wall uptake is increased when MPI data is confined to end inspiration compared to end expiration, due to increased distance and reduced overlap between the inferior wall and sub-diaphragmatic activity (Cho et al., 1999).

2.4.2 – Patient Motion Detection and Correction

On Anger cameras projection images are acquired sequentially, therefore movement of the heart can be visualised as a shift in the heart position between projections. Early methods on Anger cameras involved detecting motion between projection images and correcting for motion prior to reconstruction by translating the projection images to remove the motion. Sinogram and linogram displays of the acquired data are tools to assess horizontal and vertical motion respectively. A

sinogram displays a stack of the same row of pixels or the sum of selected rows of pixels and a linogram displays the same column of pixels or the sum of columns over a selected region, selective linogram (Wallis, 1995), throughout the acquisition. A sinogram appears as a smooth spiral with horizontal motion appearing as discontinuities in the spiral and a linogram as a smooth line, with vertical motion appearing as discontinuities in the line, (Fitzgerald and Danias, 2001).

The techniques available for motion correction can be categorised as cross-correlation, diverging squares algorithm, two-dimensional fit, projection re-projection and manual shift (Fitzgerald and Danias, 2001). Matsumoto et al., (2001) found that in patient studies 27% of abnormal segmental scores determined using the QPS software were reclassified as normal following motion correction with the projection re-projection motion correction algorithm. This type of algorithm works well for all types of patient motion (Fitzgerald and Danias, 2001). Frame-to-frame cross correlation techniques (Eisner et al., 1987) are known to depend on the successive planar images being truly correlated and adequate signal to background counts in the heart. These are good at detecting sudden displacements between projections but are less sensitive to gradual displacements (Eisner et al., 1987; Fitzgerald and Danias, 2001). The diverging squares algorithm assumes accurate identification of the heart centre, which may be affected by activity outside the heart overlapping the heart on projection images. This technique can correct for both sudden and gradual changes in the heart position, however its success is limited when heart uptake relative to the surrounding background structures is low (Geckle et al., 1988). Manual techniques allow the operator to shift the projection images manually, using a reference marker or a sinogram and linogram for guidance. The limitation of these techniques is that motion detection and correction is restricted to translational motion in the plane of the projection.

Beach et al., (2004) demonstrated that patient motion could be measured by the Polaris motion-tracking system, an external device that uses infrared reflection from small spheres to provide real-time position data. This was tested with the cardiac insert from a Data Spectrum phantom, using the motion data to correct the projection images. The motion signal from similar visual tracking systems utilising near infrared (McNamara et al., 2009) or visible retroreflective spheres (Bruyant et

al., 2005) have also been used for motion correction. Motion measured using external tracking devices can be used to correct the position coordinates in the list mode data prior to OSEM reconstruction (Bruyant et al., 2005) or to split projections into motion groups, facilitating registration based estimation of the transform between the groups and therefore motion estimation solely from the data (Mukherjee et al., 2013). A signal determined solely from the data is termed a “data driven” signal. Motion measured using external tracking devices or data driven techniques can be incorporated into OSEM reconstruction for simultaneous motion and activity estimation of cardiac SPECT imaging (Boening et al., 2004; Mukherjee et al., 2013). This facilitates correction of rigid body motion with six degrees of freedom. Pretorius et al., (2016) applied OSEM reconstruction with motion correction using the signal from a visual tracking system to 64 patient studies. The patients agreed to undergo a second scan, with 48 performing a predefined motion and 16 remaining still. The diagnostic outcome changed between the first and second scan for 43.8% of patients; this reduced to 14.1% after motion correction.

2.4.3 – Respiratory Motion

Respiratory motion of organs results from movement of the diaphragm and thorax during respiration; this affects the internal anatomy, resulting in movement of the heart. MPI artefacts resulting from this motion are termed respiratory motion artefacts. The main directional component of respiratory motion is in the cranio-caudal direction, with smaller movements in the ventral-dorsal and lateral directions. Many studies have evaluated the extent of diaphragm or heart displacement during respiration, each consisting of different patient groups, types of breathing, imaging modalities and measurement techniques, table 2.5.

Across the studies in table 2.5 the heart displacement in the cranio-caudal direction was in the range of 2 - 24mm. Movement of the diaphragm in the cranio-caudal direction was in the range of 7 - 28mm for quiet free breathing, and up to 59mm for breath hold techniques and deep breathing. The ratio of diaphragm motion to heart motion in a cranio-caudal direction measured in the literature varied between 0.26 and 0.99, with studies reporting a large inter-subject variability (Wang et al., 1995; Danias et al., 1999; McLeish et al., 2002; Shechter et al., 2004; Livieratos et al., 2006).

Reference	Diaphragm Motion		Cranio-Caudal Heart Motion		Subjects and Method
	Average (mm)	Range (mm)	Average (mm)	Range or $\pm 1SD$ (mm)	
Korin et al., (1992)	13	-----	-----	-----	15 volunteers, MRI, normal breathing.
Davies et al., (1994)	12	7 - 28	-----	-----	9 healthy volunteers, ultrasound, quiet breathing.
	43	25 - 56	-----	-----	Deep inspiration.
Wang et al., (1995)	20	-----	13	9 - 17	10 healthy volunteers, MRI, breath hold techniques.
Holland et al., (1998)	13	7 - 22	-----	-----	10 healthy volunteers, MRI, free breathing.
Danias et al., (1999)	13	± 5	9	± 3	12 healthy volunteers, MRI, free breathing.
Mageras et al., (2001)	14	7 - 21	-----	-----	6 lung cancer patients, fluoroscopy, free breathing.
Keegan et al., (2002)	12	9 - 14	-----	-----	8 healthy subjects, MRI, free breathing.
McLeish et al., (2002)	30	9 - 59	12	4 - 24	8 healthy volunteers and 10 patients, MRI, breath hold.
Shechter et al., (2004)	-----	-----	5	2 - 8	10 patients, cine-angiogram, free breathing.
Livieratos et al., (2006)	-----	-----	9	5 - 17	6 patients, PET, free breathing.
Kovalski et al., (2007)	-----	-----	9	4 - 13	8 MPI patients, free breathing.
Martinez-Moller et al., (2007)	-----	-----	5	± 2	12 patients, PET, free breathing.
Kovalski et al., (2009b)	-----	-----	7	± 3	34 MPI patients, free breathing.
Bitarafan et al., (2015)	-----	-----	11	8 - 17	26 MPI patients, free breathing.

Table 2.5 - The cranio-caudal displacement of the heart and diaphragm as reported in the literature. MRI – magnetic resonance imaging, PET – positron emission tomography.

To a lesser extent than in the cranio-caudal direction, respiratory motion can translate the heart in the ventral-dorsal and lateral directions, as well as rotate the heart in all three planes (Shechter et al., 2004). Deformation of the heart during respiration can also occur with the inferior wall moving further than the anterior wall (Martinez-Moller et al., 2007). Motion of the heart in the cranio-caudal direction during MPI was 4 - 17mm.

Phantom studies have been conducted to look at the effect of respiratory motion on myocardial perfusion imaging. Pitman et al., (2002) simulated heart displacements in the cranio-caudal direction of 10, 20 and 30mm using a dynamic anthropomorphic phantom. Motion artefacts were barely apparent with 10mm of motion, clearly visible with 20mm of motion and gross with 30mm of motion, figure 2-7. Tsui et al., (2000) used the 4D spline-based mathematical cardiac torso (MCAT) phantom (Segars et al., 1999) to model the effects of upward creep and respiratory motion with an extent of 2cm. They demonstrated that this introduces a regional decrease in count density in the inferior wall.

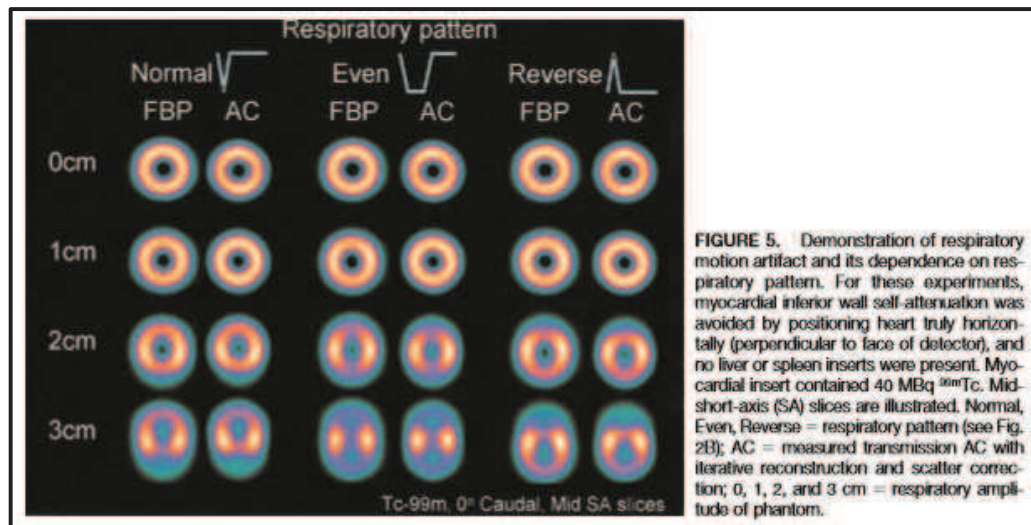


Figure 2-7 – The results from a phantom study showing artefacts are barely apparent with 1cm simulated motion and clear with 2cm and 3 cm simulated motion. This research was originally published in *The Journal of Nuclear Medicine*, (Pitman et al., 2002), <http://jnm.snmjournals.org/content/43/9/1259.full>. Reproduced with written permission of the rights holder. © by the Society of Nuclear Medicine and Molecular Imaging, Inc.

2.4.4 – Respiratory Motion Detection and Correction

The average respiratory cycle is 10 cycles/minute for slow deep breathing, 20 cycles/minute for normal breathing and 40 cycles/minute for shallow breathing (Marieb, 2004). Projection images are usually approximately 20-30s in duration. Therefore, techniques for patient motion estimation and correction that shift the projections to remove motion prior to reconstruction are unable to correct for respiratory motion, as there are many respiratory cycles averaged over each projection image.

Many studies have investigated the use of respiratory gating as a method of removing the effects of respiratory motion. Using similar techniques to cardiac gating section 2.3.4, the respiratory signal from the patient is used to limit the signal that is acquired to a specific part of the respiratory cycle or to divide the acquired data from each projection into groups of similar displacement, referred to as bins, based on either the time or amplitude of the respiratory signal, (Abdelnour et al., 2007), figure 2-8.

Time gating has the advantage of being unaffected by changes in the baseline of the signal and produces gated images with similar count statistics. However, amplitude gating does not make assumptions about the periodicity of the respiratory signal. Data from one of the respiratory gated bins can be reconstructed, removing some of the respiratory motion but reducing the signal-to-noise ratio or the gated bins can be aligned to reduce the motion whilst maintaining count statistics.

The respiratory signal is often recorded using an external device. The types of external gating devices that can be used are elasticised belts (Kovalski et al., 2007; Martinez-Moller et al., 2007), pneumatic bellows (Beach et al., 2004), ECG derived signals (Konik et al., 2011) or more complex visual tracking systems, such as those used for patient motion correction discussed in section 2.4.2. Elasticised belts measure the expansion of the chest using a transducer, for example they can incorporate a coiled fine flexible wire, which measures the change in inductance of the coil as the strap is stretched (Livieratos et al., 2005; Livieratos et al., 2006).

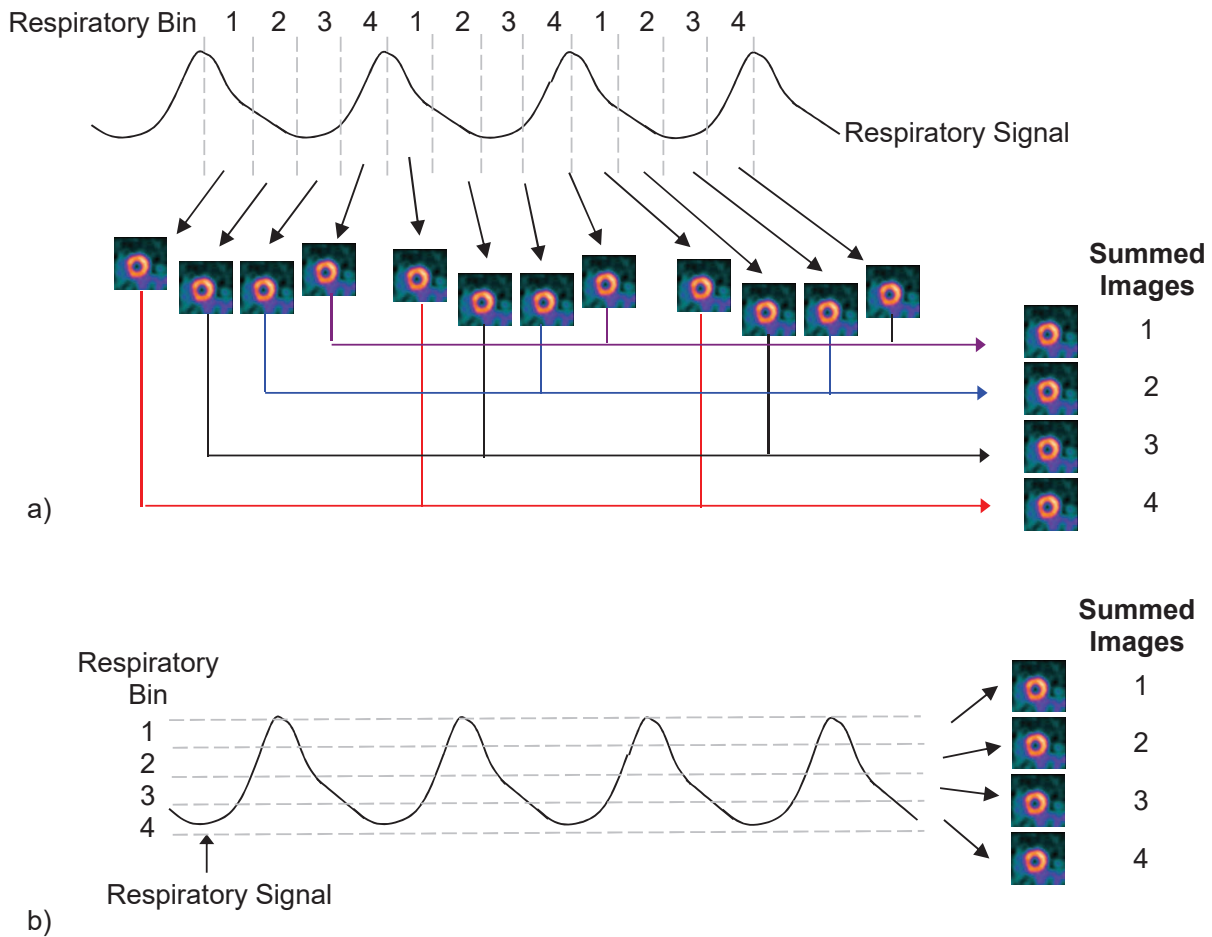


Figure 2-8 – Different methods of gating the respiratory signal; (a) Time gating divides each respiratory cycle into an equal number of time bins (in this example 4) and then sums the images from corresponding bins, (b) Amplitude gating divides the overall amplitude of the signal into an equal number of bins (in this example 4) and then sums the data in each bin.

Segars and Tsui, (2002) studied the effectiveness of respiratory gating using the 4D NURBS-based cardiac-torso (NCAT) phantom, a software phantom based on data from the Visible Human Project (Ackerman and Banvard, 2000). They used this to generate projection data for MPI on an Anger gamma camera, simulating a respiratory cycle of 5s, with 4cm motion over the respiratory cycle and a cardiac cycle of 1s. The respiratory cycle was divided into 16, 8 and 4 bins. Each reconstructed bin was assessed for artefacts due to respiratory motion. They found that respiratory artefacts are significantly reduced if the extent of respiratory motion

within a bin is $\leq 1\text{cm}$ during a gated time period. Therefore, although eliminating respiratory motion entirely may be difficult, provided that a motion correction technique can reduce motion within the bins to less than the resolution of the camera, significant artefacts can be avoided.

The success of removing respiratory motion by limiting the data collected to a specific part of the respiratory cycle has been demonstrated in clinical studies (Cho et al., 1999). Using just one of the respiratory bins results in a significant amount of discarded data and reduces the counts in the final image, which in itself could affect image quality and the ability to distinguish defects. Techniques have therefore been developed using gating that do not reduce the count statistics in the final image. Kovalski et al., (2007) simulated 5, 8 and 18mm respiratory motion by oscillating a cardiac phantom placed in an oblique orientation to simulate axial and horizontal shifts. The segmentation algorithm which forms part of the Myovation software (Xeleris workstation, GE Healthcare) produces an ellipsoid fitted to the left ventricle. This ellipsoid was fitted to each of the respiratory gated bins reconstructed with FBP, figure 2-9, after reorientation into the standard short axis, vertical and horizontal long axis slices. Motion was identified as the shift between the centres of the ellipsoids. The first respiratory bin was used as a reference and vectors corresponding to motion relative to this reference image were projected from the short axis orientation to the transaxial orientation. These were then used to shift the projection images vertically and horizontally to correct for respiratory motion. The shifted projections were summed and reconstructed to give one final motion corrected image. This technique will depend on the robustness of the segmentation software to fit an ellipsoid to the left ventricle. Kovalski et al., (2007) applied this technique to eight patients attending for myocardial perfusion imaging and the average shift on the images in the cranio-caudal direction reduced from 9mm before motion correction to 0.5mm post correction. Clinically significant differences were seen in the anterior and inferior walls of the myocardium on bulls-eye plots before and after motion correction, figure 2-9.

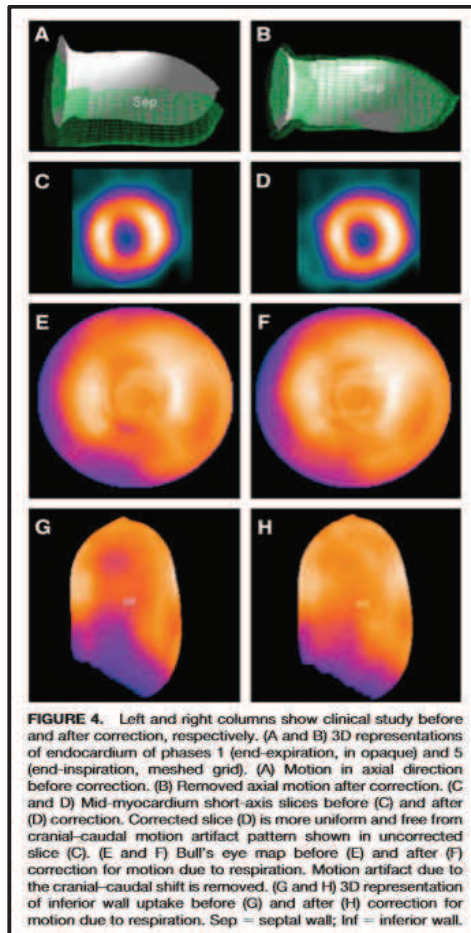


Figure 2-9 - The results of a patient study showing the segmented endocardium boundaries at end expiration and inspiration, motion is clearly visualised between the two phases of the respiratory cycle and this is reduced following motion correction. The short axis slices of the reconstructed study show anterior and inferior wall defects which are reduced following correction. This research was originally published in *The Journal of Nuclear Medicine*, (Kovalski et al., 2007), <http://jnm.snmjournals.org/content/48/4/630.full?related-urls=yes>48/4/630. Reproduced with written permission of the rights holder.

© by the Society of Nuclear Medicine and Molecular Imaging, Inc.

Kovalski et al., (2007) extended their work to images reconstructed using iterative reconstruction techniques. Iterative techniques are preferred for MPI as they reduce noise and more accurately model the physical processes (Hesse et al., 2005; Strauss et al., 2008). Kovalski et al., (2009a) demonstrated in a study of myocardial perfusion imaging in 34 patients that there is a noticeable difference in the segmental perfusion scores for images with and without motion correction in 2% of patients when reconstruction with FBP is used, 10% of patients when iterative reconstruction with resolution recovery is used and 20% of patients when corrections for scatter and attenuation are also included. This demonstrates that as reconstruction techniques become more sophisticated, and more of the physical processes are included in the iterative reconstruction algorithms, the quality and resolution of the images are improved and the effect of respiratory motion on the images becomes more significant. Dividing the projection data into bins and

incorporating motion correction into the reconstruction, in a similar way to patient motion as described in section 2.4.2, has also been explored (Dey and King, 2009). Other studies have investigated data driven techniques for respiratory motion correction of MPI, removing the need for an external device. Bruyant, (2002) simulated Tc^{99m} MIBI projection data using the MCAT phantom with 15mm motion in the cranio-caudal direction. Each projection was divided into a series of images with 24 time frames per respiratory cycle. The images in each projection were thresholded to isolate the liver, heart and spleen and then shifted to align the centre of mass of the thresholded regions along the axial axis, relative to a reference frame. It was demonstrated using polar plots that respiratory motion introduced artefacts into the anterior and inferior regions and these artefacts were no longer present after motion correction. This study only simulated one component of respiratory motion, in the cranio-caudal direction, and the simulations assume that the heart, liver and spleen have the same periodic translations due to respiration. It is therefore not clear which organ is driving motion correction or how successful this technique would be in patient studies if there were differences in the motion of the heart, liver and spleen or if other hot structures were close to these organs. Redgate et al., (2013) used a similar technique on data generated using the NCAT phantom. Each projection was divided into a series of 1s images and image registration was used to align the images in each projection prior to reconstruction, demonstrating that motion artefacts improved following correction.

Recent studies have shown that dimensionality reduction using either principal component analysis (PCA) or Laplacian eigenmaps (LE) can provide a data driven respiratory signal and a significant correlation has been demonstrated between these data driven signals and an external device (elastic belt with a pressure sensor) on 14 patient studies (Sanders et al., 2015).

2.4.5 – Cardiac Motion

Cardiac contraction of the heart as visualised on cardiac gated images is an important diagnostic tool, as discussed in section 2.3.4, however this will also blur the stress and rest images used for reporting. Correction for cardiac motion has been achieved by detecting the endocardial and epicardial wall boundaries on selected cardiac gated SPECT images. Nonlinear image warping can be used to

warp the images to the end diastolic bin (Slomka et al., 2004; Germano et al., 2007; Suzuki et al., 2008). This technique improved the detection of CAD in obese patients (Suzuki, Slomka et al. 2008).

2.4.6 – Dual Motion Correction

The ‘ideal’ myocardial perfusion image would not only be corrected for the physical characteristics of the imaging system but also for all types of motion, including patient, respiratory and cardiac motion to create a motion free image of the heart.

Patient and Respiratory Motion: Mitra et al., (2007) measured patient and respiratory motion using an infrared visual tracking system, divided each projection into 100ms frames and incorporated rigid body and respiratory motion correction into the OSEM reconstruction. The success of this technique was demonstrated using a Data Spectrum anthropomorphic phantom.

Respiratory Motion and ECG Gating: Respiratory motion correction has been performed whilst maintaining ECG gating (Daou et al., 2007; Bitarafan et al., 2008). Respiratory motion affected the results of cardiac gated analysis with a significant difference in the left ventricular ejection fraction observed before and after respiratory motion correction (Bitarafan et al., 2015).

Respiratory and Cardiac Motion: Kovalski et al., (2009a) extended their work on respiratory motion correction discussed in section 2.4.4 to include correction for cardiac motion. Respiratory and cardiac gated bins were generated for each projection of 48 myocardial perfusion scans (Kovalski et al., 2009b). Respiratory motion was detected using the segmentation method described (Kovalski et al., 2007; Kovalski et al., 2009a) and correction for respiratory motion was applied to all the cardiac gated bins with the same respiratory phase. The images were corrected for cardiac contraction by segmenting the cardiac gated bins and morphing all the bins to match the end diastolic bin. Comparing the segmental differences between bulls-eye plots for the different types of correction showed that there was a noticeable discrepancy in 2% of patients corrected for respiratory motion, 15% that were corrected for cardiac contraction and 25% that were corrected for both

respiratory and cardiac motion. This demonstrates that correcting for cardiac motion and hence increasing the resolution of the final images, reduces the amount of respiratory motion that has a significant effect on the images and artefacts introduced by respiration increase.

2.5 – Motion on the Discovery 530c Dedicated Cardiac Camera

At the start of this work in 2010 there was very limited published work on patient or respiratory motion on the DNM 530c. There was no documented attempt to measure either type of motion during clinical imaging and therefore no way, other than patient observation, to determine if the image quality may have been degraded by motion artefacts. This section will explore the effect of patient and respiratory motion on the DNM 530c.

2.5.1 – Patient Motion

Many review articles on the DNM 530c have stated that patient motion will be reduced on this system due to reduced imaging times and temporally consistent data.

Reduced Imaging Times: The length of time over which data are acquired correlates with the likelihood for motion (Fitzgerald and Danias, 2001). It is therefore suggested that as imaging times can be reduced on the DNM 530c, *'patient motion itself and its consequential artefacts may be reduced because of increased patient comfort and cooperation during the short acquisitions'* (Bocher et al., 2010; Schillaci and Danieli, 2010).

Temporal Consistency: During iterative reconstruction, the algorithm is converging on a solution that produces forward projected images that agree with the measured projections. When motion is present on a dual headed camera, converging on the solution will be affected by the fact that there are temporal differences between the images of the heart on each projection. There is therefore no solution that will produce estimated projections that will agree with the measured projections. On the

DNM 530c, as images are acquired from all angles simultaneously, there will be no temporal differences due to motion, the images at all angles will be blurred by the motion. Therefore, the estimated solution from iterative reconstruction will be blurred to account for motion, but there will be a solution that produces agreement between the estimated and measured projections. The argument presented in the literature is that using stationary detectors to provide consistent angular data and eliminate view-to-view inconsistencies will reduce artefacts induced by patient motion (Garcia and Faber, 2009; Garcia et al., 2011).

The suggestion that motion will be reduced due to short scan times is only applicable for gradual patient motion or upward creep. High frequency patient motion, which is often visualised as the heart 'bouncing' up and down, will not be reduced by the shorter acquisition time. In contrast, aspects of the design of the DNM 530c may result in motion artefacts increasing.

Resolution and Reconstruction Algorithms: It has been demonstrated for Anger systems that as image reconstruction techniques become more sophisticated, the severity of motion defects increase. The DNM 530c has increased spatial and energy resolution and iterative reconstruction techniques that include modeling of the system and noise regularisation which may increase the severity of any artefacts that are present.

Reduced Imaging Times: For Anger cameras motion artefacts were more significant with dual headed cameras, as a single occurrence of motion affected twice the number of projections compared to a single headed camera (Matsumoto et al., 2001). If this theory is applied to the DNM 530c a single occurrence of motion will affect all 19 detectors and as imaging times can be reduced by a factor of 2.5 – 7.5, a greater percentage of the acquisition time will be affected by short periods of motion. A single occurrence of motion would therefore constitute a larger proportion of the overall scan time and the effect of this motion may be more significant than the same occurrence of motion on a dual headed camera.

The studies that have been published to date on patient motion on the DNM 530c are summarised in table 2.6. The publication resulting from chapters 3 - 5 of this thesis is shown for comparison purposes (Redgate et al., 2016).

Reference	Study Type (phantom / patient)	Acquisition Parameters	Methodology	Results
Abstract: Kim et al., (2010)	100 stress studies	900MBq, TF, 8 minute image duration	Patients divided equally into age groups, <50, 50-60, 60-70 and >70. Motion measured between 1 minute images reconstructed from the list mode data.	Significant motion was seen in 10% of patients after 4 minutes of imaging. There was a significant increase in motion after 6-7 minutes. No difference between age groups.
Redgate et al., (2016)	Anthropomorphic Phantom	8MBq, 360s image duration	Step, creep and bounce motion between 0-20mm simulated in three planes.	Significant artefacts visible for ≥ 10 mm motion that persists for ≥ 60 s.
Editorial: Benz and Buechel, (2016)	40 patient studies	500MBq, TF, 2-day protocol, 6 minute image duration	Motion assessed on phantom and patient data through registration of 30s planar and reconstructed images.	Significant cranial-caudal motion (≥ 8 mm) identified for 10% patients and 5% had visible motion artefacts. No significant lateral or ventral-dorsal motion.
Van-Dijk et al., (2016)	Cardiac Insert in Jaszczak Phantom™	20MBq, 180s image duration	Table moved every 20s to simulate patient motion. Phantom and patient list mode data binned into 20s images. Motion measured and corrected using	Mean error, lateral -1.1 ± 0.8 , ventral-dorsal 0.9 ± 0.9 and cranio-caudal 0.0 ± 1.0 mm.
Editorial: Benz and Fuchs, (2016)	83 patients undergoing MPI and FFR	370MBq stress, 740MBq rest, 8 minute image duration	the manufacturer's software (MDC for Alcyone, GE Healthcare). Difference between simulated and measured motion calculated. Diagnostic outcomes compared to FFR measurements.	Mean (maximum) error, lateral 0.9 ± 0.2 (2.4 ± 0.8), ventral-dorsal 1.0 ± 0.2 (2.8 ± 0.9) and cranial-caudal 1.2 ± 0.5 (3.4 ± 1.5) mm. Overall mean and maximum errors were 2.1 ± 0.4 and 4.5 ± 1.3 respectively. No change in outcome for any patients.

Kennedy and Strauss, (2016)	Cardiac phantom (Model ECT/CAR/I, Data Spectrum Corp)	26MBq in cardiac insert, 5 minute image duration	Acquisition paused after 2.5 minutes and phantom moved 0, 5, 10, 15, or 20mm in the lateral, ventral-dorsal, cranio-caudal directions. Motion assessed by dividing list mode data into 10s frames. The change in the centre of mass for each projection was calculated. Images visually assessed for artefacts and quantitatively assessed using TPD values. Correction performed by rejecting data with a motion index >2 pixels.	Significant artefacts, (TPD, >5 %) observed when motion ≥ 1.5 cm, figure 2-10a. No artefacts observed after removal of data above motion index limit. The TPD changed from $24.3 \pm 5.2\%$ to $0.6 \pm 0.5\%$ after correction.
	1 Patient Example	296MBq stress 925MBq rest, MIBI, 5 and 3 minute image durations		Motion visually apparent on 10s projection images. Correction reduced blurring due to motion, figure 2-10b.
(Salvadori et al., 2018)	Cardiac phantom (Biodex Medical Systems)	10MBq in cardiac insert,	Images acquired on dedicated cardiac cameras with CZT detectors, DNM 530c and DSEPCT (Spectrum Dynamics), and on an Anger camera, Symbia T2, with astigmatic and parallel hole collimators. Phantom scanned with no motion and with 5 and 10mm simulated motion. Abnormal segments defined as <65% uptake on a 17 segment model.	The CZT cameras were found to be less vulnerable to small cardiac motions than Anger cameras due to differences in the pre-existing homogeneity. The results were highly dependent on the reconstruction parameters used.

Table 2.6 - A summary of published research on patient motion on the DNM 530c. MPI – myocardial perfusion imaging, FFR – fractional flow reserve, TF – tetrofosmin, MIBI – sestamibi, TPD – total perfusion defect, CZT– cadmium zinc telluride.

The abstract by Kim et al., (2010), table 2.6, concluded that patient motion correction may be necessary on the DNM 530c. Although this was never published as a full paper, this was the first evidence, amongst assumptions of reduced motion due to shorter imaging times, that patient motion on this system may have an impact on MPI. The limitation of this study was that the magnitude for significant patient motion artefacts was assumed to be the same as for Anger cameras, $\geq 12\text{mm}$ (3 pixels). Although this is not an unreasonable assumption, as the resolution obtained under the conditions used for clinical imaging is similar between the two systems, the systems have very different designs and therefore using this limit to identify significant motion artefacts requires validation.

The studies by Van-Dijk et al., (2016) and Kennedy and Strauss, (2016) described in table 2.6 use data driven techniques to measure motion. The manufacturer's motion detection and correction software (MDC for Alcyone, Xeleris workstation, GE Healthcare) released clinically during the course of this work was evaluated by Van-Dijk et al., (2016). The motion detection and correction software (MDC for Alcyone, Xeleris workstation, GE Healthcare) and the technique used by Kennedy and Strauss, (2016), use centre of mass analysis to estimate motion between reframed images. They both take steps to exclude sub-diaphragmatic activity, however the number of projections used differs, with the motion detection and correction software (MDC for Alcyone, Xeleris workstation, GE Healthcare) using data from five projections and Kennedy and Strauss, (2016) using all 19 projections. Another difference is the duration of the images that the list data are reframed into, with Van-Dijk et al., (2016) using 20s images and Kennedy and Strauss, (2016) using 10s images. Both studies approached motion correction differently with the motion detection and correction software (MDC for Alcyone, Xeleris workstation, GE Healthcare) incorporating motion correction into the reconstruction and Kennedy and Strauss, (2016) discarding data with motion.

Salvadori et al., (2018) identified abnormal segments on phantom studies on the DNM 530c for 10mm simulated motion. The phantom study by Kennedy and Strauss, (2016) also found that $>1\text{cm}$ motion introduces significant motion artefacts and they presented a clinical example where motion had degraded the quality of an MPI study, figure 2-10. Van-Dijk et al., (2016) measured patient motion in a cohort of 83 patients concluding that the maximum motion averaged across all patients was

4.5 ± 1.3 mm and there was limited value to patient motion correction. These are contrasting results, with one group finding a patient scan that has clearly been negatively affected by patient motion and the other group not identifying any examples of significant motion in a cohort of 83 patients. More work is therefore required to assess the effect of patient motion on different groups of patients scanned on the DNM 530c.

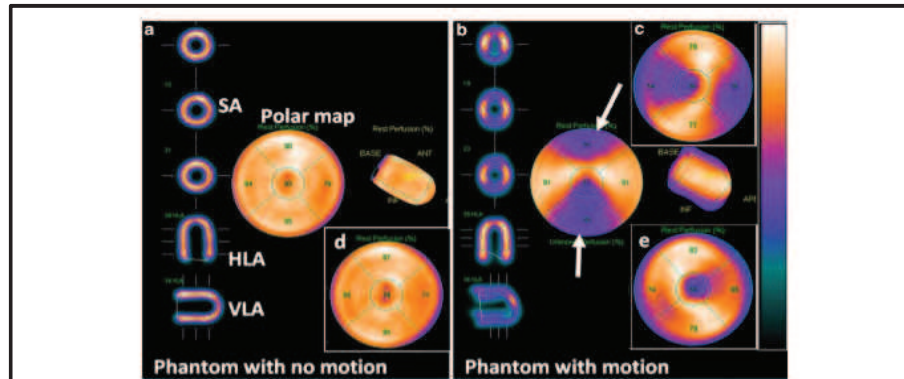


Fig. 2 In the phantom acquisition with no motion, the uptake distribution appears approximately homogeneous (a) in the short axis (SA), horizontal long axis (HLA), and vertical long axis (VLA) views as well as in the projection of this data onto a polar map. For the phantom with a 2-cm inferior motion half way through the acquisition (b), the reconstructed images show artifactual deficits

in uptake in the anterior and inferior walls (arrows). Dorsal motion induces artifacts in the septal and lateral walls (c), and motion to the left causes apical thinning (e). These artifactual deficits have been removed by eliminating the data acquired after the motion (d). The uptake distribution appears approximately homogeneous as for the case with no motion in (a)

a)

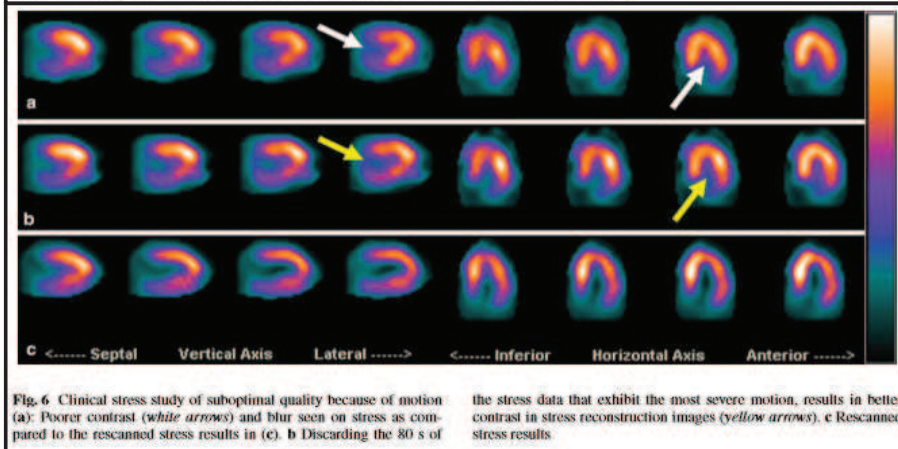


Fig. 6 Clinical stress study of suboptimal quality because of motion (a): Poorer contrast (white arrows) and blur seen on stress as compared to the rescanned stress results in (c). b Discarding the 80 s of

the stress data that exhibit the most severe motion, results in better contrast in stress reconstruction images (yellow arrows). c Rescanned stress results

Figure 2-10 – (a) Phantom study showing artefacts from 2cm inferior motion, dorsal motion and motion to the left and removal of the artefacts following motion correction. (b) Patient study of sub-optimal quality due to motion, with the proportion of the scan with motion discarded and after being rescanned. This research was originally published in *Medical and Biological Engineering and Computing*, (Kennedy and Strauss, 2016), <https://link.springer.com/article/10.1007/s11517-016-1548-z>. Reproduced with permission of Springer Nature. © International Federation for Medical and Biological Engineering 2016.

2.5.2 – Respiratory and Cardiac Motion

Cardiac gating is incorporated into acquisitions on the DNM 530c. It is suggested that some of the count sensitivity gained by the DNM 530c could be traded for respiratory gating (Garcia et al., 2011). Respiratory gating on an Anger camera requires the counts along the angular dimension to be normalised to ensure consistency between corresponding respiratory bins (Kovalski et al., 2007). This would not be necessary on the DNM 530c, as images at all angles are acquired simultaneously. The studies that have been published to date on respiratory motion on the DNM 530c are summarised in table 2.7.

The techniques used in table 2.7 can be described as breath hold techniques (Buechel et al., 2010b; Clerc et al., 2017) and data driven techniques. The data driven techniques can be subdivided into centre of mass tracking; one in-house developed (Ko et al., 2015) and one by the manufacturer (MDC for Alcyone, Xeleris workstation, GE Healthcare) which was evaluated by Van-Dijk et al., (2016), and the REGAT software (Daou et al., 2017b; Daou et al., 2017c). The REGAT software is described as *“a curve generation technique based on a statistical method specifically adapted to handle low signal-to-noise ratio data”*, however there is limited information on the underlying theory of the REGAT technique, only examples of its application. Motion correction was incorporated into the reconstruction in the motion detection and correction software (MDC for Alcyone, Xeleris workstation, GE Healthcare) and into in-house developed software (Ko et al., 2015), or was achieved by summing reconstructed gated images (Daou et al., 2017b).

Reference	Study Type (phantom / patient)	Acquisition Parameters	Methodology	Results
Buechel et al., (2010b)	40 patient studies	TF, 1-day protocol, 3 and 2 minute image durations for stress and rest.	Scanned on Anger camera with AC and twice on DNM 530c, once with normal breathing and once with breath hold triggering (BHT).	On the Anger camera 19 areas were identified as artefacts. Nineteen and 6 were apparent on free breathing and BHT images respectively. BHT increases the specificity for discriminating true defects from artefacts.
Buechel et al., (2010c)	28 patients			Significant change in left ventricular volume, stroke volume and regional wall motion. No significant change in LVEF.
Ko et al., (2015)	Cardiac insert	7.4 MBq, Tl ²⁰¹ , 120s image duration.	2.5 – 25 mm axial motion simulated using a moving platform. Phantom and patient data divided into 0.5s frames. Motion determined from centre of mass.	Correlation between the simulated and measured axial shifts, r=0.999, P=0.001, with errors <1mm. Significant motion artefacts for ≥ 15mm axial motion.
	552 patients	111 MBq, Tl ²⁰¹ , 180 and 240s image durations.	Motion correction incorporated into reconstruction.	12.0 ± 4.3 and 10.4 ± 4.0 mm motion for the treadmill and dipyridamole stress. Reduced tracer activity, increased wall thickness and decreased volume for ≥15 mm axial. This improved after motion correction. Significant respiratory motion in 8% of patients.
Van-Dijk et al., (2016)	Cardiac Insert	20MBq	Table moved every 20s to simulate motion. List data reframed into 1s images. Motion measured and corrected using the manufacturer's software (MDC for Alcyone, GE Healthcare).	Difference between measured and simulated cranial-caudal motion, mean 0.9 ± 2.4 and absolute mean 2.1 ± 1.6mm.
Editorial: Benz and Fuchs, (2016)	83 patients	370MBq stress, 740MBq rest, 8 minute image duration.	Outcomes compared to FFR.	Mean and maximal motion 2.5 ± 0.4 and 10 ± 2.0mm. Correction changed interpretation in 11% patients, with 5% agreeing with FFR. Concluded that there is limited value to correction.

Daou et al., (2017b) Editorial: Benz and Buechel, (2017), 'Images that Teach' Daou et al., (2017a)	18 patients	2 MBq/kg stress, 6 MBq/kg rest, one-day protocol, TF, 5 minute image duration, mainly prone imaging.	List data binned into 0.5s frames and processed with REGAT software which produces respiratory motion gated volumes. These are summed without and with realignment. LV counts and FWHM walls compared.	Motion at stress and rest was, lateral 1.4 ± 1.3 and 1.7 ± 2.2 , ventral-dorsal 1.4 ± 1.2 and 2.2 ± 1.5 and cranial-caudal 9.7 ± 6.2 and 10.7 ± 4.3 mm. There was a significant difference in the maximum and minimum LV counts and FWHM of the inferior and anterior walls between non-corrected and corrected images. Cranial-caudal motion was ≥ 10 mm in 50% studies.
Daou et al., (2017c) Editorial: Giannopoulos and Buechel, (2017)	25 patients (different ones to above)		Processed as above. Severity and extent of segment scores assessed before and after correction.	Motion at stress and rest was, septal-lateral 1.9 ± 1.0 and 1.7 ± 1.2 , apical-basal 3.1 ± 2.7 and 2.9 ± 2.0 and anterior-inferior 9.4 ± 4.9 and 9.9 ± 4.4 mm. Anterior-inferior motion ≥ 10 mm in 55% studies, with 26% showing a change in MPD severity or extent, and ≥ 15 mm in 10% studies, with 60% showing a change in MPD severity or extent.
Clerc et al., (2017)	40 patient studies	TF, 1-day protocol, 3 and 2 minute image durations for stress and rest.	Images were acquired with free- breathing and deep inspiration BHT. Four images reconstructed: (1) Free breathing NAC, (2) BHT NAC, (3) Free breathing AC, (4) BHT AC. Images were blindly reported.	Frequency of normal scans: (1) 10%, (2) 21%, (3) 38%, (4) 51%. The best image quality and inter-observer correlation was found for BHT-AC.

Table 2.7 - A summary of published research on respiratory motion on the DNM 530c. MPI - myocardial perfusion imaging, FFR – fractional flow reserve, TF – tetrafosmin, TPD – total perfusion defect, LV – left ventricle, AC – attenuation corrected, NAC – non-attenuation corrected, BHT – breath hold triggering, LVEF – left ventricular ejection fraction, FWHM – full width half maximum, MPD – myocardial perfusion defect.

Breath hold triggering (BHT) on the DNM 530c was investigated by Buechel et al., (2010b). This acquires data at inspiration while the patient holds their breath and a decrease in the number of motion artefacts was observed. It is difficult in this study to isolate the cause of artefact reduction, as the gold standard AC Anger images were not corrected for respiratory motion. Breath hold techniques are not tolerated on Anger cameras due to the long scan time. This technique was most effective in patients with sub-diaphragmatic tracer activity and in obese patients with attenuation artefacts in the right coronary artery territory. This suggests that the differences are mainly due to changes in diaphragmatic attenuation and increased separation between the heart and sub-diaphragmatic activity with breath hold techniques. The number of studies reported as normal increased from 10% with free breathing no attenuation correction to 51% with attenuation corrected breath hold acquisitions (Daou et al., 2017c).

The studies in table 2.7 all measured similar values for the average cranial-caudal respiratory motion, despite the different techniques and patient groups. The average motion measured across the studies was 12.0 ± 4.3 and 10.4 ± 4.0 mm for exercise and pharmacological stress respectively (Ko et al., 2015), 10 ± 2.0 mm (Van-Dijk et al., 2016) and 9.4 - 10.7mm across stress and rest groups over 2 studies (Daou et al., 2017b; Daou et al., 2017c). One of these studies was performed with the patients in the prone position, suggesting that respiratory motion doesn't change with imaging position, however considering that some centres perform both supine and prone scanning, direct comparison is warranted.

Ko et al., (2015) concluded that ≥ 15 mm axial motion introduced significant motion artefacts. A clinical example from this study is shown in figure 2-11. Daou et al., (2017c) found that 10% of patients had ≥ 15 mm motion, with a change in the extent or severity of myocardial perfusion defects observed for 60% of these patients. From comparison of the images pre and post motion correction respiratory motion artefacts were identified in 8% of scans (Ko et al., 2015) and 11% of patients (Van-Dijk et al., 2016). There are limited data on how these motion artefacts change the diagnostic outcome through comparison to other measures of CAD. Van-Dijk et al., (2016) concluded that motion correction was of limited value as only 5% of the 11%

of scans that had changed interpretation following motion correction agreed with the fractional flow reserve. This needs further evaluation in more studies.

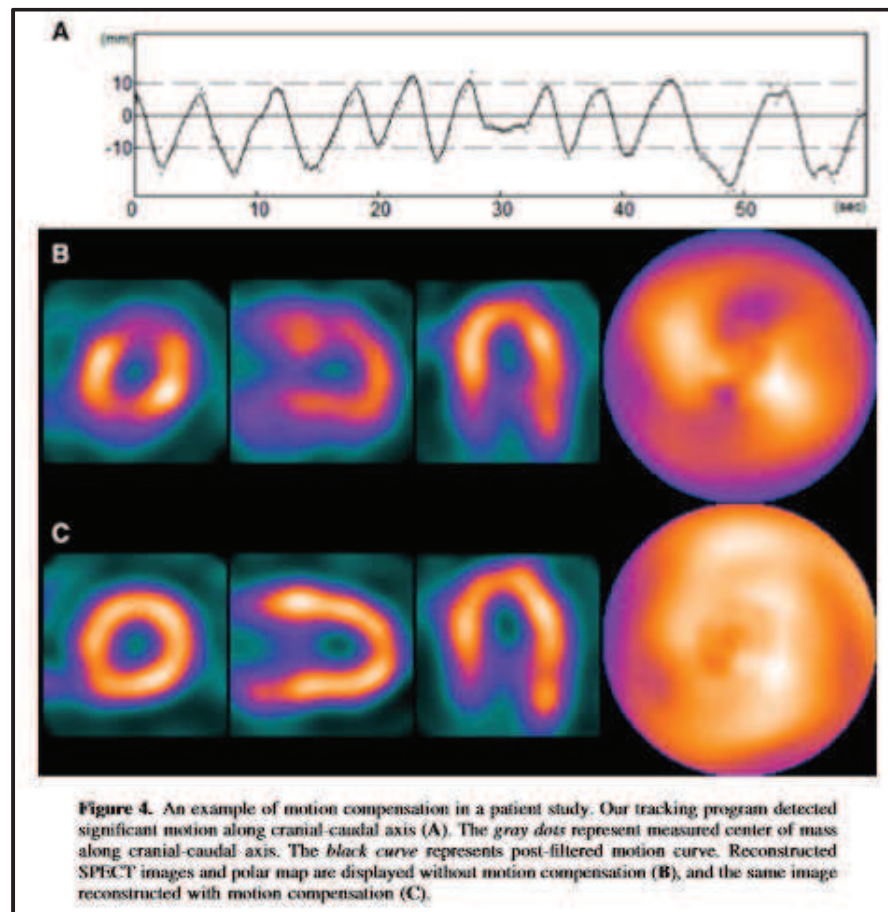


Figure 2-11 – A patient study on the DNM 530c showing the respiratory signal and patient images before and after respiratory motion correction. This research was originally published in The Journal of Nuclear Cardiology, (Ko et al., 2015), <https://link.springer.com/article/10.1007/s12350-014-9963-8>. Reproduced with permission of Springer. © American Society of Nuclear Cardiology 2014.

Some correlations with patient characteristics were assessed across these studies. A positive correlation was found on multivariate analysis between the magnitude of motion and patient height and weight (Ko et al., 2015) and the magnitude of motion and gender (Daou et al., 2017c).

The major drawback of breath hold techniques is the additional burden placed on the technologist and patient. There will also be variations between the breath holds, which may result in residual respiratory motion on the study. A common limitation amongst all the studies using data driven techniques is that no comparison was made to an external tracking system, although for the REGAT software this has been performed on Anger cameras (Daou et al., 2015). All of the data driven correction techniques utilise all the data to form the final motion corrected image, either through incorporating correction into the reconstruction (Ko et al., 2015; Van-Dijk et al., 2016) or summing aligned reconstructed bins (Daou et al., 2017b), therefore maintaining count statistics. The disadvantage of summing reconstructed bins is that this is not the same as reconstructing the whole dataset as one, due to non-linear reconstruction, and this may therefore result in changes in image quality between the original and motion corrected images.

2.6 – Summary

Myocardial perfusion imaging is a diagnostic test to identify coronary artery disease. Image artefacts may be present on Anger cameras due to patient or organ motion that is greater than the resolution of the imaging system (~1cm). Patient motion and upward creep are routinely estimated and corrected before patients leave the department, in line with procedural guidelines. The methods that can be used to reduce the effect of respiratory motion are listed below;

Respiratory Gating using External Devices: This increases the burden of the test for both the patient and technologist performing the scan and has not gained widespread clinical acceptance for SPECT myocardial perfusion imaging, although this is routinely used in other imaging modalities.

Breath Hold Triggering: Breath hold triggering relies on the heart returning to the same position for each breath hold, which may not necessarily be the case. It also depends on patient compliance and increases the burden of the test for the patients and technologists.

Data Driven Techniques: The advantage of data driven techniques is that they facilitate motion estimation and correction without increasing the burden of the test.

It is suggested that motion artefacts on the DNM 530c will be reduced due to shorter acquisition times and temporal consistency. However, where sudden short movements, such as bounce, have negligible effect on Anger cameras, these will affect a greater percentage of the acquisition time on the DNM 530c and may produce more significant artefacts. Gradually, literature on motion on DNM 530c is accumulating but as yet, no guidance has been published on the need to assess for motion on this system and uncertainty remains over the diagnostic value of motion correction.

There is a constant strive to reduce the dose from imaging and one approach is to reduce the administered activity and increase the scanning time, which risks increasing motion artefacts. The increased sensitivity of the DNM 530c is currently utilised to reduce radiation exposure or imaging time, with conservative improvements in spatial resolution; however, an alternative approach could be taken to prioritise image quality. Bocher, Blevis et al. (2010) describe the removal of respiratory and cardiac motion as the next step in improving myocardial perfusion imaging, as until this is possible the advantages of the improved spatial resolution of the DNM 530c cannot be realised.

3 – Effect of Motion on the Discovery 530c Dedicated Cardiac Camera

3.1 – Introduction

Chapter 2 introduced myocardial perfusion imaging (MPI); gamma cameras and the different types of motion present during MPI studies. The recent literature on patient and respiratory motion estimation and correction on the Discovery 530c dedicated solid state cardiac camera (DNM 530c) was summarised. Chapter 3 will explore the effect of motion on MPI on the DNM 530c. Chapters 4 and 5 will concentrate on estimation and correction of low frequency *patient motion* and chapters 6 and 7 will focus on estimation and correction of *respiratory motion* on the DNM 530c.

This chapter will start by discussing the effect of motion in the context of MPI, outlining a simple mathematical model to demonstrate the magnitude of motion that significantly affects myocardial perfusion images. A systematic phantom study will then be presented looking at the effect of *patient motion* on the DNM 530c and the results will be translated into the context of *respiratory motion*.

3.2 – Mathematical Model

This section presents a simple mathematical model demonstrating the impact of motion on MPI and identifying the dominant factors relevant to image interpretation. The wall of the left ventricle is thickest towards the base and becomes thinner towards the apex. The normal thickness of the myocardium of the left ventricle for an adult heart is 12-15mm, reducing to 1-2mm at the apex (Ho, 2009). Consider a short axis slice through the left ventricle, with the radial profile of radioactivity through the myocardial wall represented as a square function, figure 3-1a,b. The motion of the left ventricle due to cardiac contraction is approximately 10mm (Kovalski et al., 2009b) therefore when imaging the left ventricle over time, the image will be blurred due to cardiac motion, figure 3-1c. The image blurred over cardiac motion will also be convolved with the point spread function of the imaging

system, figure 3-1d. This very simple one-dimensional model excludes many factors such as reconstruction, scatter, attenuation and depth dependent resolution.

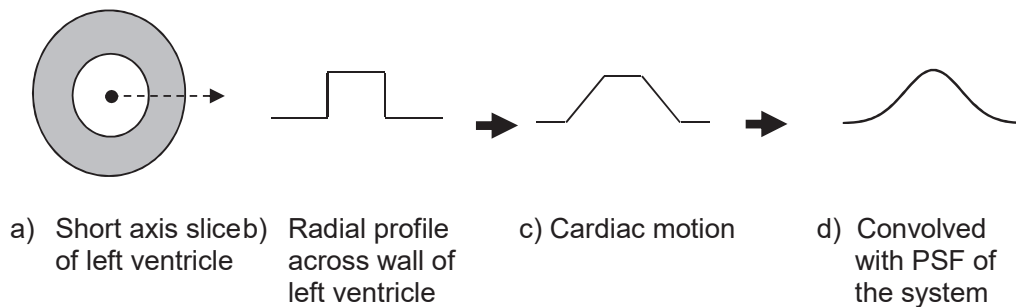


Figure 3-1 – (a) The radioactivity distribution in a short axis slice of the left ventricle, (b) a radial profile from the centre of the left ventricle can be approximated to a square function, (c) this is then blurred due to cardiac motion and (d) convolved with the point spread function of the imaging system. PSF – point spread function.

Quantitative Perfusion SPECT (QPS) described in section 2.3.5 segments myocardial perfusion images by generating radial count profiles, starting at the mid-myocardial surface. An asymmetric Gaussian curve is fitted to the count profile and the endocardial boundary is defined as 65% of the inner standard deviation, figure 3-2, (Germano et al., 1995).

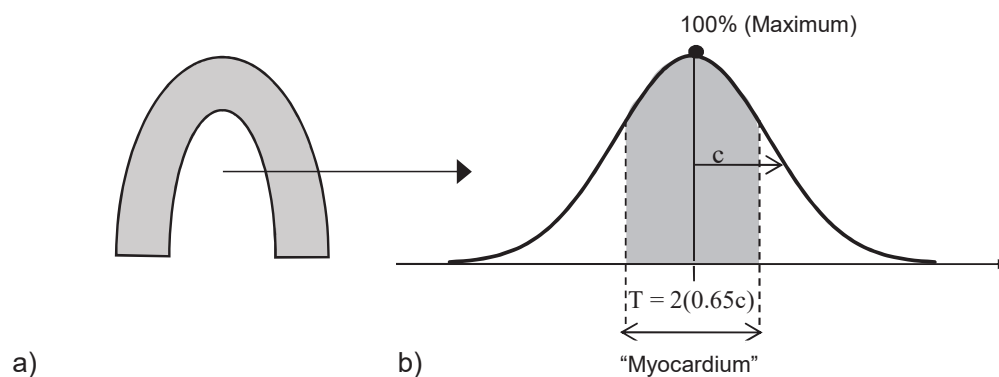


Figure 3-2 – (a) A long axis representation of the left ventricle, (b) Quantitative Perfusion SPECT segments of the endocardial boundary to define the myocardium using 65% of the inner standard deviation of a Gaussian fitted across the wall of the left ventricle, c - standard deviation of the Gaussian, T - myocardial thickness.

For the purpose of simplification this exercise will simplify the profile to a symmetrical Gaussian, centred on b as shown in figure 3-3a. The myocardial boundaries defined, and therefore the myocardial thickness measured, are estimated from a profile affected by the physiological myocardial thickness, along with the cardiac contraction and the resolution of the imaging system, figure 3-1. This will therefore be referred to as the “measured myocardial thickness”, to distinguish it from the true “physiological myocardial thickness”. The measured myocardial thickness, T , is related to the standard deviation of the Gaussian, c , through equation 3-1.

$$T=1.3c$$

Equation 3-1

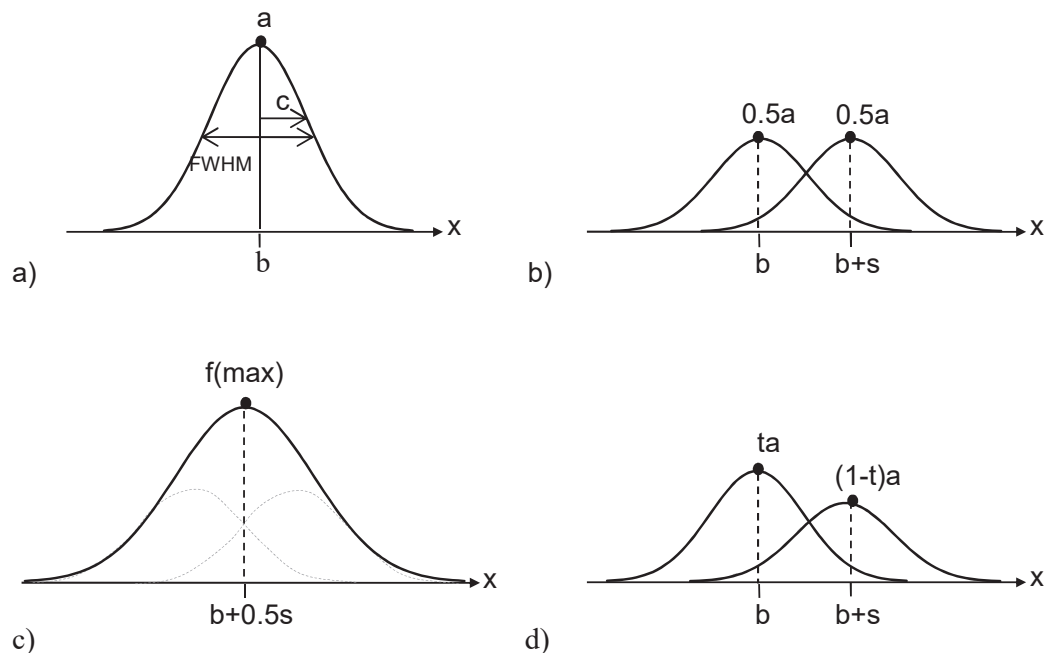


Figure 3-3 – (a) The profile of the left ventricle is simplified to a symmetrical Gaussian function, (b) motion half way through the scan can be simulated using two functions shifted relative to each other, (c) summing these functions models the left ventricle with motion imposed and (d) the model can be adapted to demonstrate motion for a proportion of the scan time. FWHM – full width half maximum, c – standard deviation, a – maximum of the Gaussian, t – scaling factor representing the percentage of the total time spent at the position, $f(\max)$ – maximum of the profile generated by summing two Gaussians, b – the x position of the maximum, s – magnitude of simulated motion.

The count profile, $f(x)$, can be described by equation 3-2, where a is the height of the Gaussian at the maximum point and b is the x position of the maximum point. The standard deviation of the Gaussian, c , is related to the FWHM through equation 3-3.

$$f(x) = a \exp \left[- \left(\frac{(x-b)^2}{2c^2} \right) \right] \quad \text{Equation 3-2}$$

$$\text{FWHM} = 2\sqrt{2\ln 2} \quad \text{Equation 3-3}$$

Patient motion can affect localised areas of the myocardium depending on the direction of the motion; with the magnitude of the resultant artefacts dependent on the proportion of the scan affected by motion. It is reasonable to assume that the most significant artefacts will occur if the heart spends 50% of the time at two separate positions, for example, if patient motion causes the heart to move position half way through the scan. In this situation the count profile in the direction of the motion could be represented by the sum of two equal Gaussian count profiles, one representing the first part of the scan and one shifted by a distance, s , representing the second part of the scan, equation 3-4, figure 3-3b.

$$f(x) = \frac{a}{2} \exp \left[- \left(\frac{(x-b)^2}{2c^2} \right) \right] + \frac{a}{2} \exp \left[- \left(\frac{(x-(b+s))^2}{2c^2} \right) \right] \quad \text{Equation 3-4}$$

When reporting myocardial perfusion images, the stress and rest images are displayed with the maximum value of the colour scale for each image, set to the maximum pixel value in the region of the myocardium. When motion is present this distributes the counts from the myocardium over a larger area, reducing the individual pixel values and making the counts in certain areas appear reduced, mimicking the appearance of perfusion defects. In this model the maximum count of the summed image, figure 3-3c, will be at $x = b + 0.5s$ (provided $|s| \leq \text{FWHM}$), simplifying the problem, equation 3-5.

$$f(\text{max}) = a \exp \left[- \left(\frac{0.25s^2}{2c^2} \right) \right] \quad |s| \leq \text{FWHM} \quad \text{Equation 3-5}$$

Using the cardiac colour scale (Kapur et al., 2002) discussed in section 2.3.5, myocardial regions with a maximum count <70% are typically classified as reduced perfusion. Therefore, motion artefacts become significant when $f(max) < 0.7$. The limit at which motion artefacts become significant, S_{lim} , is expressed by equation 3-6 and the variation of this limit with the measured myocardial thickness is shown in figure 3-4.

$$S_{lim} = \sqrt{\frac{-\ln(0.7)2c^2}{0.25}} \quad |s| \leq \text{FWHM} \quad \text{Equation 3-6}$$

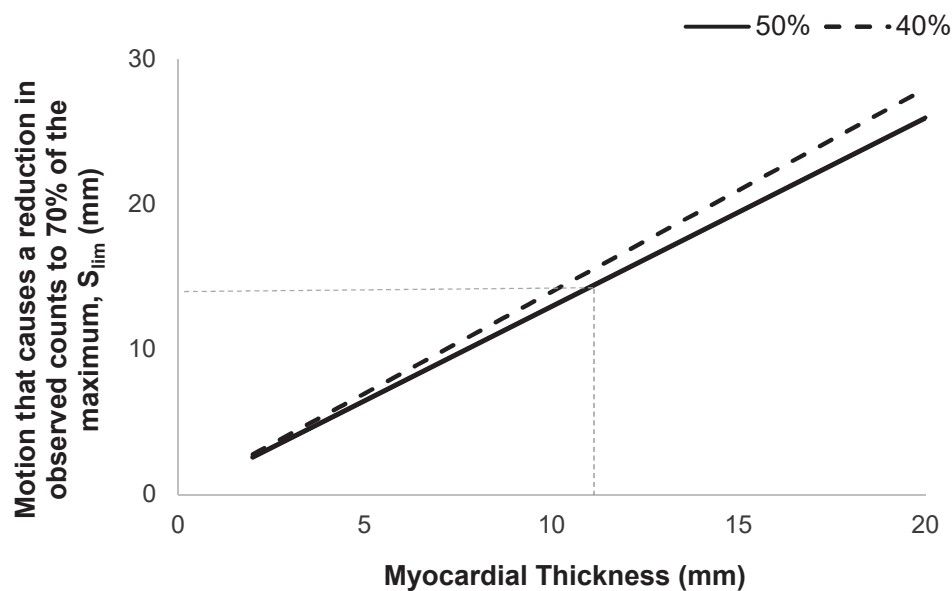


Figure 3-4 – The amount of motion, S_{lim} , required to reduce the maximum of two summed Gaussian profiles to 70% of the maximum without motion, as measured myocardial thickness increases. The grey dashed line represents a typical myocardial thickness as measured on a patient image on the DNM 530c. The percentage values represent the proportion of the acquisition time affected by motion.

The FWHM of a profile across the myocardium measured on the short axis slice of a patient image acquired on the DNM 530c was 5 pixels (20mm). This gives a value for the standard deviation, c , using equation 3-3 of 8.5mm, a measured myocardial

thickness, T , using equation 3-1 of 11mm and predicts significant motion artefacts, S_{lim} , using equation 3-6 for patient motion >14 mm. This is consistent with the limit of >13 mm quoted in the European Association of Nuclear Medicine (EANM) guidelines for Anger cameras (Hesse et al., 2005).

This is the case when motion occupies 50% of an acquisition however, the proportion of the scan affected by motion may be less than this. If the proportion of the scan affected by motion is expressed as a decimal t , then equation 3-4 can be re-written as equation 3-7, figure 3-3d.

$$f(x) = (1-t)a \exp\left[-\left(\frac{(x-b)^2}{2c^2}\right)\right] + ta \exp\left[-\left(\frac{(x-(b+s))^2}{2c^2}\right)\right] \quad \text{Equation 3-7}$$

When 50% of the scan is affected by motion, the maximum of the summed profile is at $b + 0.5s$, when $|s| < 2c$. When a proportion of the scan t is affected by motion this relationship becomes more complex, with the position of the maximum becoming a function of s , t and c . This can be modelled analytically by finding the position of the maximum, as the point when $f'(x)$ equals zero, equation 3-8, and calculating $f(x)$ at this position.

$$f'(x) = \frac{-(1-t)(x-b)a}{c^2} \exp\left(-\frac{(x-b)^2}{2c^2}\right) - \frac{ta(x-b-s)}{c^2} \exp\left(-\frac{(x-(b+s))^2}{2c^2}\right) = 0 \quad \text{Equation 3-8}$$

The limit for significant motion artefacts, S_{lim} , is higher when $<50\%$ of the scan time is affected by motion as the maximum count is dominated by the proportion of the scan time that is unaffected by motion. This results in the maximum count remaining $\geq 70\%$ regardless of the magnitude of the motion when $\leq 30\%$ of the acquisition is affected by motion. Figure 3-4 demonstrates the increase in S_{lim} for different measured myocardial thicknesses when 40% of the scan time is affected by motion. For the myocardial thickness measured from a patient study the limit for significant motion artefacts increases from >14 mm when 50% of the scan time is affected by motion to >15 mm when 40% of the scan time is affected by motion.

The model produced is a very simple 1 dimensional representation that assumes the myocardial boundary can be modelled by a symmetrical Gaussian. The dominant

factors that influence the effect of patient motion on the images have been identified as the measured myocardial thickness, which includes the effects of the point spread function of the imaging system and cardiac contraction, the magnitude of the patient motion and the proportion of the scan time affected by the motion. In reality there will be many other factors that will influence how patient and respiratory motion affects the images such as the type of camera, position and number of affected projections, attenuation, scatter, depth dependent resolution, sub-diaphragmatic activity and the reconstruction parameters. The model cannot be used to predict how much motion will be significant in patient studies or predict any differences between Anger cameras and the DNM 530c. The main difference between patient and respiratory motion will be the value of t , which will vary depending on the pattern of motion that is present.

3.3 – Statistical Analysis

Throughout the thesis statistical analysis is performed using the IBM SPSS statistics software version 21.0 for Windows (IBM Corp, Armonk, NY). Continuous data are expressed as maximum, minimum, mean and standard deviation values. Independent t tests, paired Students t tests and one-way ANOVA are used for the comparison of means. Linear association between continuous variables are assessed using the Pearson's correlation coefficient as described in table 3.1. Multivariate linear regression is performed to determine the association between multiple continuous variables. All statistical tests are two sided and P values <0.05 are considered statistically significant.

Pearson's Correlation Coefficient (r)	Descriptive Strength of Association
0	Poor
$0 > r \geq 0.20$	Very weak
$0.20 > r \geq 0.40$	Weak
$0.40 > r \geq 0.60$	Moderate
$0.60 > r \geq 0.80$	Strong
$0.80 > r \geq 1.00$	Very strong

Table 3.1 – The look-up table used to describe the association between two continuous variables

3.4 – Labelling Convention

A parameter that will be discussed in depth throughout the thesis is the direction of motion and depending on the context this will use different conventions, as outlined below.

Motion Relative to the Detector: Motion along the axes of the projection images will be described as detector motion with y representing motion along the vertical plane of the detector and x representing motion along the horizontal plane of the detector, figure 3-5a.

Motion Relative to the Patient: Motion along the planes of the patient will be described as being in the cranio-caudal, ventral-dorsal and lateral directions and these will be represented by Z, Y, X respectively, figure 3-5b.

Motion Relative to the Reoriented Axes of the Heart: Processing of myocardial perfusion images re-orientates the images of the left ventricle to give short axis, horizontal and vertical long axis images of the heart, section 2.3.1. Motion along these axes will be described as anterior-inferior, apical-basal and septal-lateral motion and these will be represented by Z, Y, X, figure 3-5c.

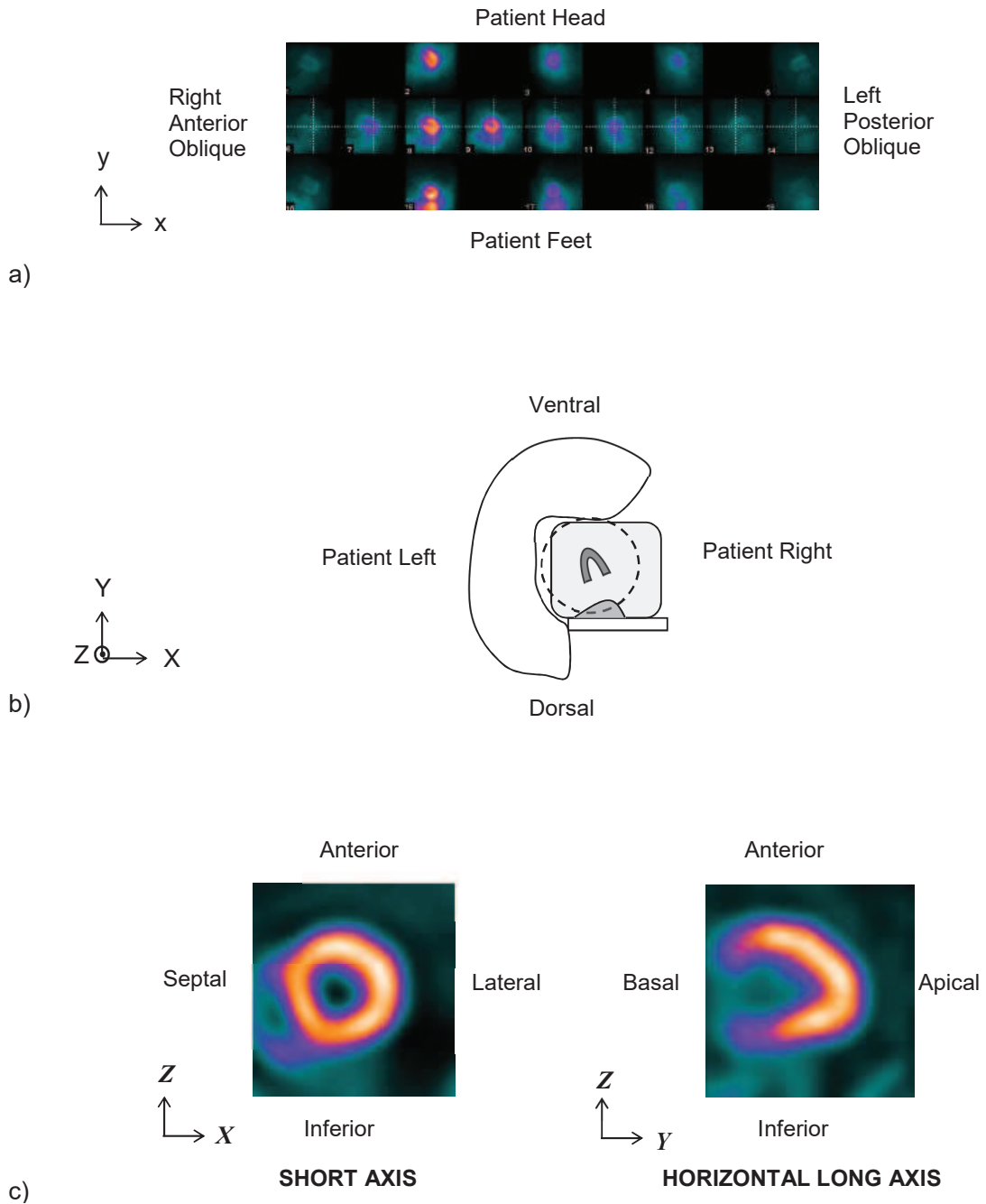


Figure 3-5 – The labelling convention used throughout the thesis, (a) relative to the plane of the detector, (b) relative to the planes of the patients, (c) relative to the plane of the heart.

3.5 – Clinical Imaging and Processing

Throughout the thesis the imaging and processing parameters adopted for phantom and patient studies were those used clinically. A two-day stress-rest protocol was used and if the stress scan was reported as normal the rest scan was not performed. A local diagnostic reference level (DRL) of 500MBq and image acquisition time of 6 minutes were used at the start of this work. During the course of this work, and as the result of a worldwide Tc^{99m} shortage, the local DRL was reduced to 400MBq and the imaging time was increased to 7.5 minutes. All the phantom work in this thesis was based on the former protocol, along with a majority of the patient acquisitions. The validation patients in section 7.5 were acquired using the latter protocol. This change in protocol during the study is unfortunate but unavoidable. The local DRL was adjusted based on patient weight. There was also a change in the stressing protocol during the study; adenosine and dobutamine were initially used and these were subsequently replaced with regadenoson.

All patients were positioned in the DNM 530c with the heart as close to the centre of the quality field of view (QFOV) as possible, taking into account physical restrictions due to body habitus. For rest scans, software on the acquisition workstation facilitates positioning of the heart in approximately the same position in the QFOV as for the stress study. Locally developed software performs automatic quality control following acquisition, measuring the shift in the heart position between the stress and rest studies. If this is >1cm then imaging is repeated. An energy window of $\pm 8\%$ centred on 140KeV was used.

Image data from the DNM 530c were reconstructed using the commercially available dedicated iterative reconstruction algorithm (Myovation for Alcyone, Xeleris workstation, GE Healthcare). The reconstruction parameters used were 50 iterations, regularization type Green's one-step-late algorithm (Alpha – 0.37, beta – 0.2) with a 3D Butterworth post filter (critical frequency 0.37, power 2). No attenuation correction was performed. The reconstructed voxel size of the images was 4×4×4mm.

Parts of this section are reproduced with permission of Springer from Redgate, Barber et al. (2016). © American Society of Nuclear Cardiology 2016.

3.6 – Phantom Simulation Patient Motion

The effect of patient motion on myocardial perfusion images acquired on Anger cameras is well documented. The European guidelines (Hesse et al., 2005) recommend that ≥ 2 pixels (13mm) of patient motion justifies motion correction. As discussed in section 2.5.1, it has been widely stated in the literature that patient motion artefacts will be reduced on the DNM 530c compared to Anger systems due to shorter imaging times, increased patient comfort and temporally consistent data. There is limited literature to support this statement. This theory is based on the increasing probability of patient motion with increasing imaging time and is true for imaging on the same system. However, there are major differences in the design of the DNM 530c compared to Anger systems and this does not take into consideration that short periods of motion on the DNM 530c will affect all projections and a greater proportion of the overall acquisition time, which may increase the number or severity of motion artefacts.

This section presents a systematic phantom study investigating the effect of motion on phantom images acquired on the DNM 530c. The dominant factors identified in section 3.2 were the measured myocardial thickness, magnitude of the patient motion and the proportion of the scan time affected by the motion. For phantom images the physical myocardial thickness is fixed and cardiac contraction cannot be simulated. The magnitude of patient motion will be varied. The proportion of the scan time affected will also be varied by simulating different types of patient motion. The effect of motion on the phantom images will be analysed both quantitatively and qualitatively, focusing on identification of the point at which the magnitude of motion may potentially affect interpretation of the images.

3.6.1 – Method

Phantom Activity: An anthropomorphic phantom (Data Spectrum) was used to simulate the activity distribution in a patient. The phantom has lung and liver compartments and a cardiac insert, which is a left ventricle with a length of 9.3cm, diameter of 6.1cm and myocardial thickness of 1.0cm, figure 3-6. To determine the

Parts of this section are reproduced with permission of Springer from Redgate, Barber et al. (2016). © American Society of Nuclear Cardiology 2016.

compartmental activities required to simulate data of similar quality to our patient images, the phantom was filled with 12MBq, 81MBq and 116MBq for the myocardium, liver and tissue respectively. These values were estimated from radioactivity concentrations suggested in the literature (Nichols et al., 2007), taking into account a local diagnostic reference level (DRL) of 500MBq. The phantom was scanned on the DNM 530c using the clinical protocol, section 3.5 and the counts per pixel in the myocardium, liver and background regions were compared to the average measurement from 10 patients with normal stress images.

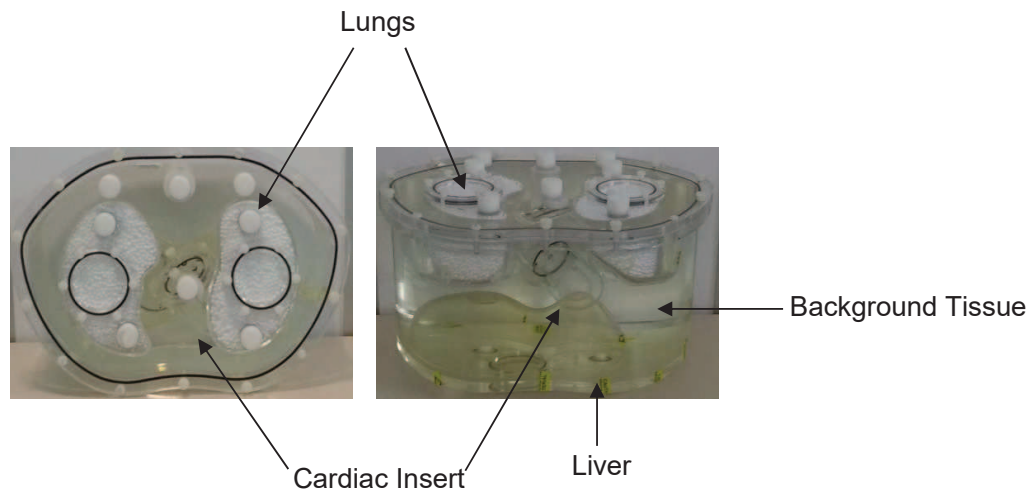


Figure 3-6 – The Data Spectrum anthropomorphic phantom used for the simulations.

It was determined that the phantom activities should be 8MBq, 41MBq and 64MBq in the myocardium, liver and background tissue respectively, giving a myocardium:liver:background activity concentration ratio of 12:6:1. This is similar to ratios quoted in the literature; 10:6:1 (Nichols et al., 2007) and 12:4:1 (Volokh et al., 2008). Phantom imaging was repeated using these activities and figure 3-7 shows that the patient and phantom images are visually comparable. The heart:background and heart:liver count ratios on the phantom images were 2.5 and 1.0, which are within 1SD of the average ratio measured on patient data, 2.7 +/- 0.5 and 1.3 +/- 0.6 respectively.

Parts of this section are reproduced with permission of Springer from Redgate, Barber et al. (2016). © American Society of Nuclear Cardiology 2016.

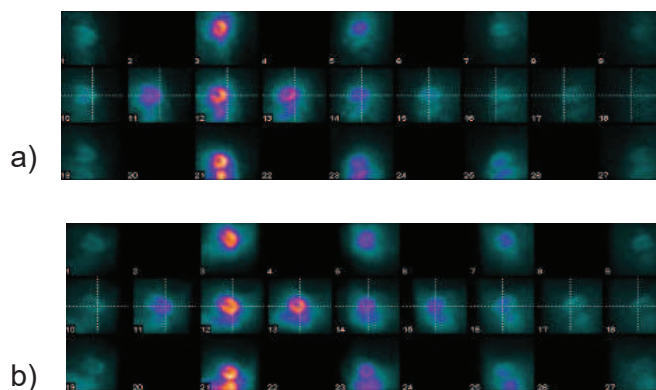


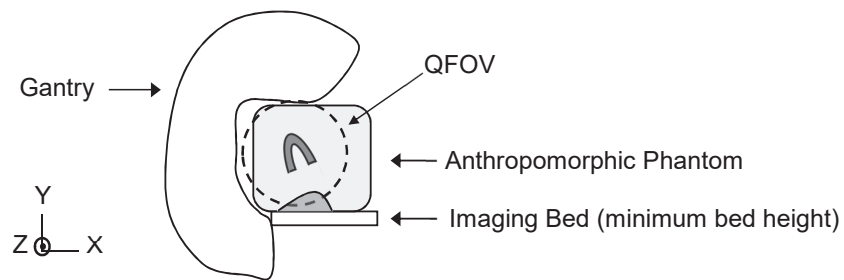
Figure 3-7 – Projection images of the heart from (a) a patient image and (b) the phantom image.

Phantom Acquisitions: Phantom images were acquired in list mode in the centre of the quality field of view (QFOV), as per the clinical protocol, section 3.5. A series of images were then acquired separately at different X and Z positions relative to the central position, figure 3-8a,b with Z representing a cranio-caudal offset along the axis of the patient and X representing lateral offset. Movement in the Y direction was restricted by the detectors and minimum bed height; therefore images were acquired at different Y positions, at a lateral position of 20mm, with Y representing a ventral-dorsal offset, figure 3-8c. Figure 3-8d shows how these images occupied the QFOV. Table 3.2 summarises the images that were acquired.

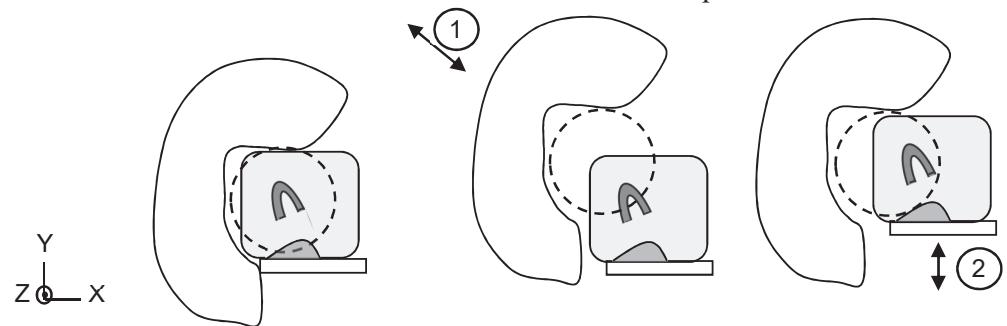
Direction	Position (mm)	Other Directions (mm)
Z	-20 , -15, -10 , -8, -6 , -5, -4 , -3, -2 , -1, 0 , 1 , 2, 3 , 4, 5 , 6, 8 , 10, 12 , 14, 16 , 18, 20	X = 0 Y = 0
X*	0 , 2, 4 , 6, 8 , 10, 12 , 14, 16 , 18, 20	Y = 0 Z = 0
Y**	-20 , -18, -16 , -14, -12 , -10, -8, -6, -4 , -2, 0	X = 20 Z = 0

Table 3.2 – Stationary images were acquired at different positions in the quality field of view. * Images could only be acquired one side of the central position as motion was restricted by the physical dimensions of the camera. ** Images were acquired at a lateral position of 20mm due to the physical restrictions of the camera. The bold numbers represent the images used to compile the normal database.

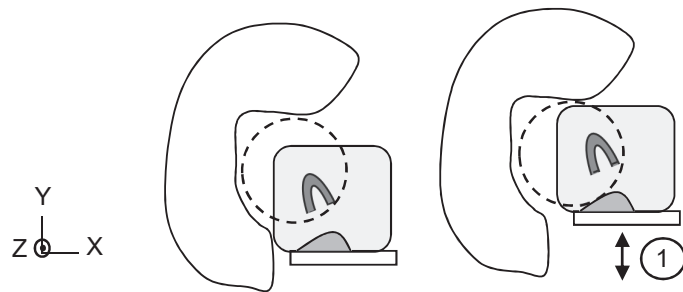
Parts of this section are reproduced with permission of Springer from Redgate, Barber et al. (2016). © American Society of Nuclear Cardiology 2016.



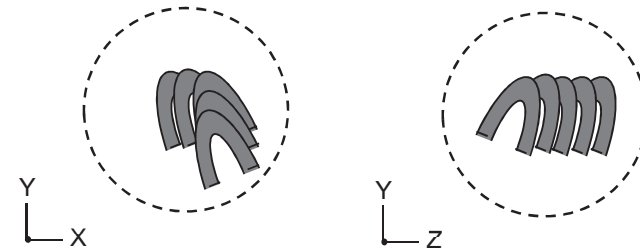
a) Z motion, imaging bed moved perpendicular to the plane of paper



b) X motion, (1) move gantry out, (2) move bed up



c) Y motion, (1) move bed up with heart at a lateral position of 20mm



d) The areas of the quality field of view where images were acquired

Figure 3-8 – Stationary phantom acquisitions acquired at different X, Y and Z positions. (a) Starting with the heart in the centre of the QFOV the imaging bed was moved in the Z direction (perpendicular to the plane of the paper). (b) Starting with the heart central in the QFOV the gantry is moved out (motion is approximately 45° to the X and Y axes); the gantry shift is calculated from the required X motion using Pythagoras Theory and the bed is then moved up by the same amount. This keeps the heart at the same Y position in the QFOV and changes the X position. (c) Starting with heart at an X position of 20mm the imaging bed was moved up to acquire images at different Y positions. (d) Demonstrates where all the images were acquired within the QFOV. QFOV – Quality Field of View.

Parts of this section are reproduced with permission of Springer from Redgate, Barber et al. (2016). © American Society of Nuclear Cardiology 2016.

Simulating Patient Motion: The patient motion considered here can be classified as;

- i. Creep, a gradual creep upwards in the position of the heart throughout the acquisition
- ii. Bounce, a single occurrence of returning motion
- iii. Step, non-returning motion (Wheat and Currie, 2004).

To ensure the counts in the images with simulated motion were representative of a 6 minute patient image, the list mode phantom data for each acquisition were reframed into 30s images. Step and bounce motion of magnitude 0 – 20mm were simulated by combining 30s images from different positions in the QFOV, figure 3-9a-d. Bounce motion was simulated for durations of 30 – 90s.

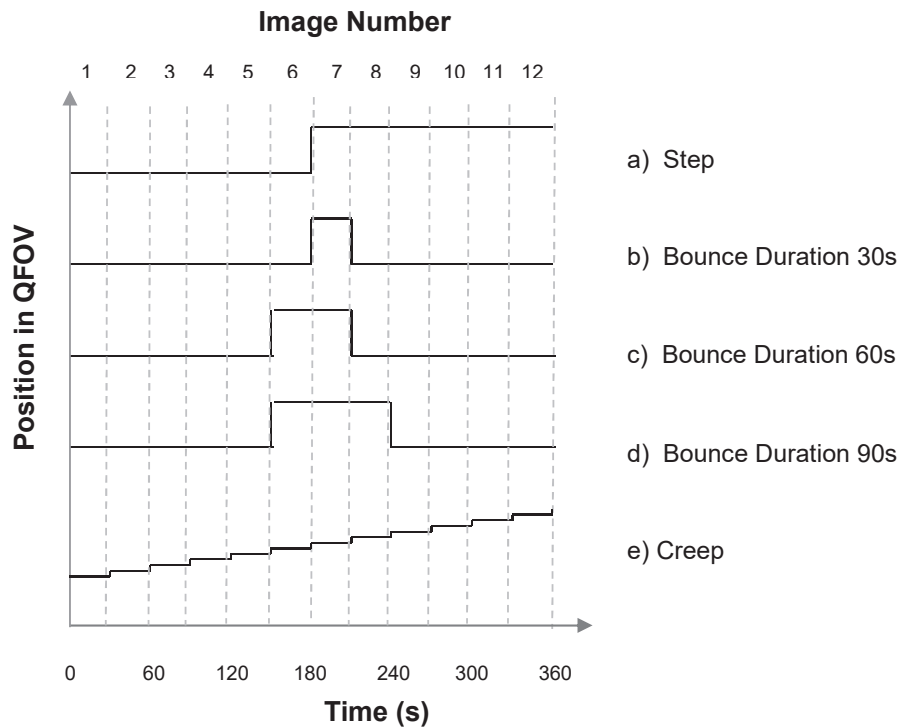


Figure 3-9 – Thirty second images from acquisitions at different positions in the quality field of view were added to simulate three types of motion; step, bounce (with three durations) and creep. The duration of the images was varied according to equation 3.9 to facilitate simulation of creep motion.

Parts of this section are reproduced with permission of Springer from Redgate, Barber et al. (2016). © American Society of Nuclear Cardiology 2016.

The list mode phantom data were also reframed into images of duration, d , calculated from equation 3.9, where t is the imaging time (360s), m is the magnitude of the simulated motion (0 – 20mm) and s is the step size (1 or 2 mm). Creep was then simulated by combining images of duration d , offset in 1 mm or 2mm steps, figure 3-9e. For example, to simulate creep motion of 2cm, eleven 32.7s images were added, starting with an image at -10mm and increasing in 2mm steps to +10mm.

$$d = \frac{t}{\left(\frac{m}{s} + 1\right)} \quad \text{Equation 3-9}$$

Direction	Motion	Magnitude of motion simulated (mm)
Z	Step	5, 10, 11, 12, 13, 14, 15, 16, 18, 20
	30s	5, 10, 15, 20
	Bounce 60s	5, 10, 15, 20
	90s	5, 10, 15, 20
	Creep	5, 10, 15, 20
X	Step	10, 12, 14, 16, 18, 20
	30s	10, 20
	Bounce 60s	10, 20
	90s	10, 20
	Creep	10, 20
Y	Step	10, 12, 14, 16, 18, 20
	30s	10, 20
	Bounce 60s	10, 20
	90s	10, 20
	Creep	10, 20

Table 3.3 – A total of 54 images with simulated motion were generated.

Parts of this section are reproduced with permission of Springer from Redgate, Barber et al. (2016). © American Society of Nuclear Cardiology 2016.

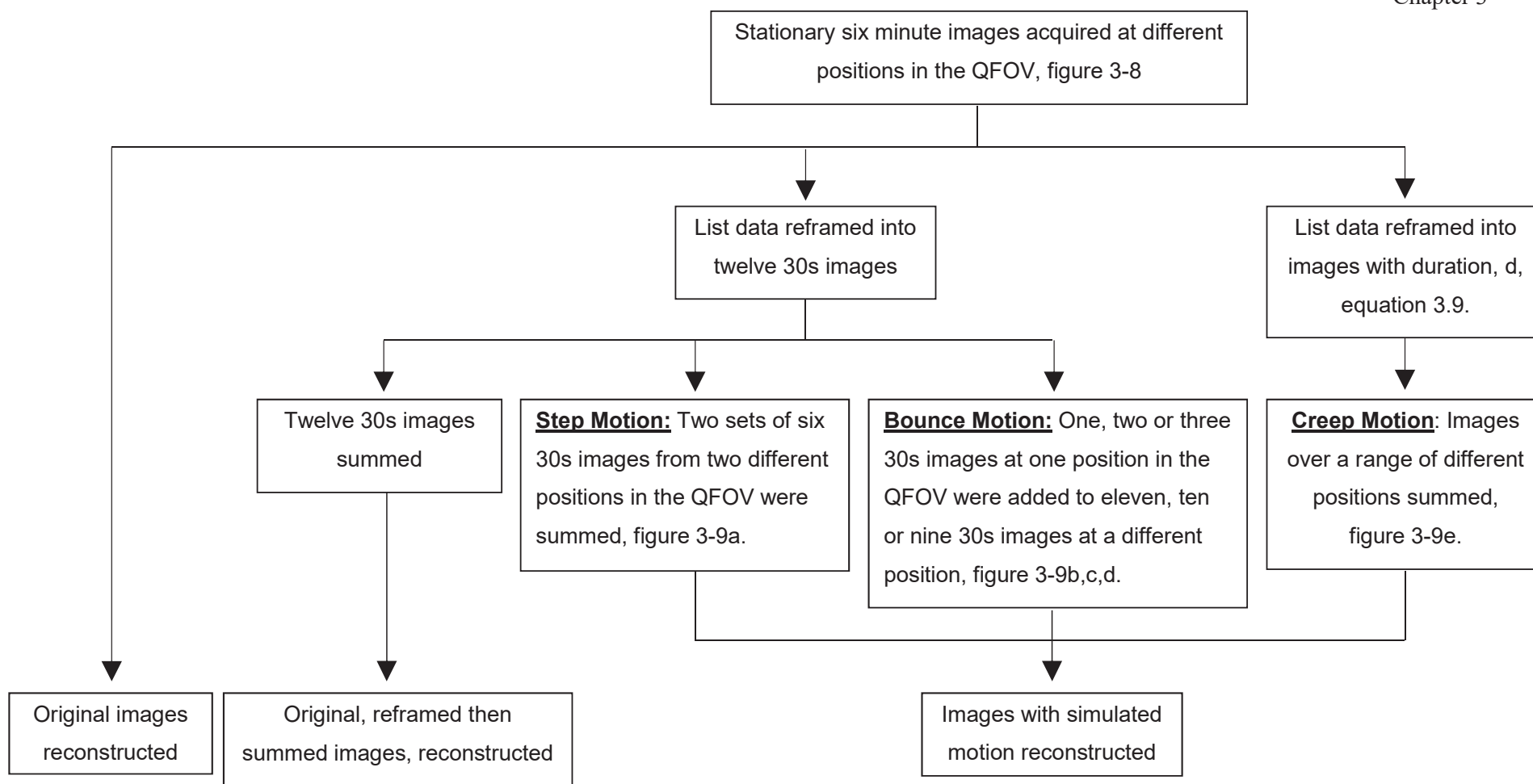


Figure 3-10 – Flow chart outlining how images acquired at different positions in the QFOV were combined to simulate phantom images with motion. The original images were reconstructed, and reframed, summed and reconstructed for comparison purposes.

In all instances the total imaging time for the summed image was 6 minutes. Motion in the Z direction was simulated evenly around the central position, for example 20mm Z step motion was simulated using images at +10mm and -10mm; however due to the limitations of the data acquisition, table 3.2, motion in the X and Y directions were simulated from the central position out towards the edge of the QFOV. A summary of all the simulated images used for data analysis is shown in table 3.3. The process described for simulation motion is summarised in figure 3-10.

Quantitative Analysis: The same mid short axis slice was selected from each of the reconstructed images and horizontal and vertical profiles were drawn. These were compared to show blurring of the myocardial wall due to motion. The improved quantification module of Quantitative Perfusion SPECT (PFQ, Cedars-Sinai Medical Centre, Los Angeles, CA) (Slomka et al., 2005), described in section 2.3.5, was used to compare the total perfusion deficit (TPD) for images with different degrees of simulated motion. It is known that the position of the heart in the QFOV can affect the perfusion pattern (Metherall et al., 2011; Hindorf et al., 2014; Timmins et al., 2015) and therefore stress and rest imaging need to be performed with the heart in approximately the same position in the QFOV; in Sheffield we aim for the difference in positioning to be ≤ 1 cm. For calculation of the TPD, a normal database of phantom images was compiled from a subset of the images acquired at different positions in the QFOV, table 3.2. The normal database was therefore representative of the expected variation due to reproducibility and positioning of the heart in the QFOV. A TPD limit of 5.5% has been used as the cut off for identification of significant perfusion defects in accordance with Slomka et al., (2005). Therefore, simulated motion on the phantom images that resulted in TPD values $>5.5\%$ were identified as significant artefacts. Images acquired at different positions in the QFOV that were not included in the normal database, were assessed against the normal database to ensure that the calculated TPD values for these normal images were within normal limits ($\leq 5.5\%$).

Qualitative Analysis: Pairs of images were processed as stress-rest studies; using images with 6–16mm simulated step motion as the stress study and the original images without motion as the rest study. To ensure differences in the images were due to motion and not due to the methodology of reframing and summing, the

Parts of this section are reproduced with permission of Springer from Redgate, Barber et al. (2016). © American Society of Nuclear Cardiology 2016.

original images, reframed and then summed were used as the rest study. Image registration was used to translate the stress and rest images into the same image space. These were then rotated through the same angles to obtain aligned short axis, horizontal long and vertical long axes images, reducing errors due to misalignment. The images were blindly assessed by 2 experienced reporters. The reporters were asked to score areas of perfusion on the stress study as 1 – normal, 2 – mildly reduced, 3 – moderately reduced, 4 – severely reduced and 5 – absent, based on a 17 segment model (Cerqueira et al., 2002). The reporters were presented with images displayed on a continuous colour scale and a discrete colour scale (ranges 100%–70%, 69%–50%, 49%–30%, 29%–10% and 9%–0%) (Kapur et al., 2002). Reporters were also asked to score segments as either 0 – No Reversibility or 1 – Reversibility and to record the scan quality (high, medium, low), confidence in the report (high, medium, low) and any relevant comments. JView, which is the in-house image viewing software routinely used in Nuclear Medicine (developed by Dr.P.Metherall, Clinical Scientist, Nuclear Medicine, Sheffield Teaching Hospitals NHS Foundation Trust), was adapted by Dr.P.Metherall to facilitate blinded reporting of myocardial perfusion images. This presented the images to the reporter in a random order and automatically recorded the responses of the reporter into a database. If there was disagreement between reporters, a joint reporting session was arranged and they were asked to reach a consensus decision on the presence of reversibility. Significant motion artefacts were defined as segments with a reversibility score of 1 and the severity of artefacts was defined as the corresponding perfusion score. Overall artefact extent was defined by the summed reversibility score multiplied by 5.9% (area of the heart covered by one segment of the polar plot) and the mean artefact severity was defined as the mean perfusion score for the reversible segments.

3.6.2 – Results

Visual Analysis: Figure 3-11 shows short axis slices for phantom simulations with no motion and motion in the X, Y and Z directions. This shows that motion artefacts are introduced into the anterior and inferior walls for cranio-caudal (Z) motion, in the septal and lateral walls for lateral (X) motion and in the antero-septal and infero-

Parts of this section are reproduced with permission of Springer from Redgate, Barber et al. (2016). © American Society of Nuclear Cardiology 2016.

lateral walls for ventral-dorsal (Y) motion. The severity of artefacts increases as the amount of motion increases.

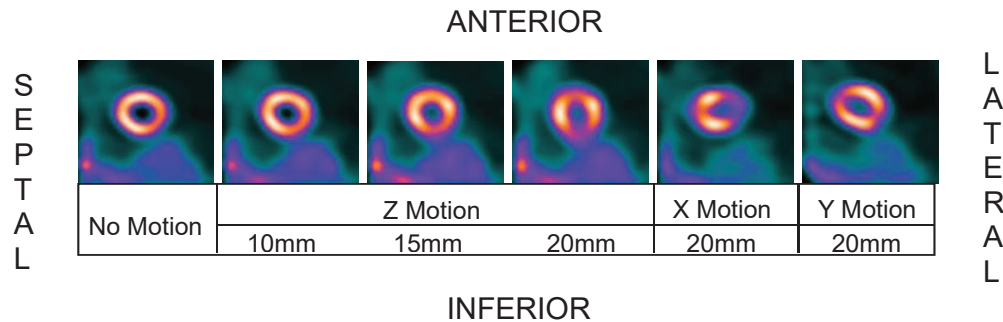


Figure 3-11 - Short axis images for different amounts and directions of simulated step motion.

Quantitative Analysis - Profiles: Figure 3-12a illustrates that for y profiles across short axis slices with simulated Z motion, the peaks of the profile decrease and the width of the profiles increase as motion increases. Figure 3-12b shows how the full width half maximum (FWHM) of the profiles increase as motion increases. This effect was most pronounced for step motion and similar for creep motion and 60s bounce motion. The effect became more pronounced as the duration of bounce motion increased from 30s to 90s.

Parts of this section are reproduced with permission of Springer from Redgate, Barber et al. (2016). © American Society of Nuclear Cardiology 2016.

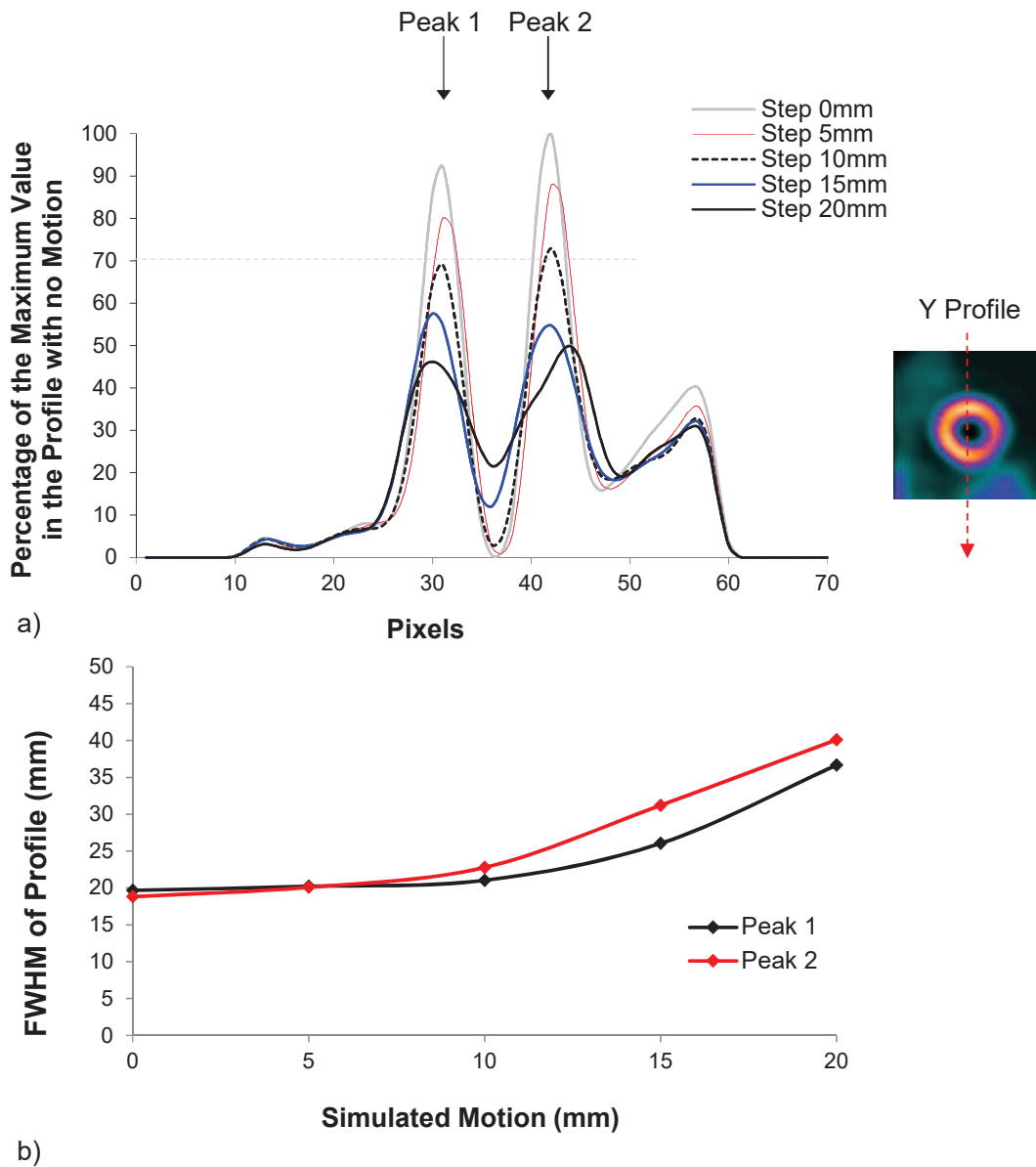


Figure 3-12 – (a) The y profiles for short axis slices and (b) the FWHM of the profiles for different amounts of Z motion. Note: the FWHM of peak 2 increases at a faster rate than peak 1 due to the close proximity to and reducing separation between the inferior wall and the sub-diaphragmatic activity as the magnitude of the motion increases.

Parts of this section are reproduced with permission of Springer from Redgate, Barber et al. (2016). © American Society of Nuclear Cardiology 2016.

Quantitative Analysis – TPD Values: A selection of images without simulated motion at different positions in the QFOV were used to build the normal database and the remaining images were used to test the database, table 3.2. The test set had an average TPD of 1% (Range 0 - 5%), validating that normal images processed using this technique have TPD values that fall below the limit of 5.5%. The TPD values for the phantom images with simulated motion are shown in figure 3-14 and polar plots associated with a selection of these are shown in figure 3-13. The polar plots show decreasing perfusion anteriorly and inferiorly and increasing TPD values as the magnitude of the motion increases.

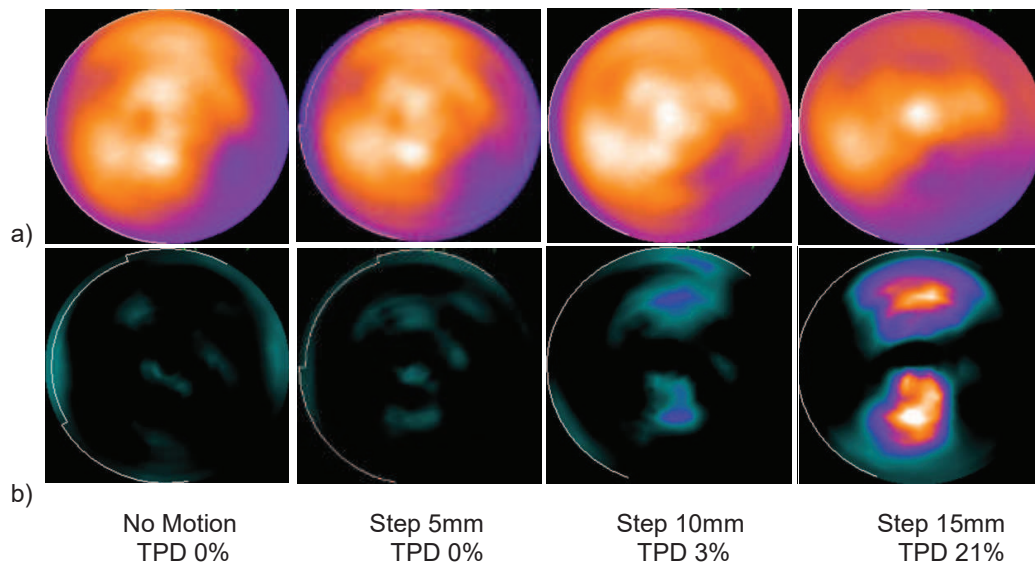


Figure 3-13 – Polar plots showing (a) uptake and (b) severity for different amounts of step motion in the Z direction.

Motion artefacts were most prominent for step motion and these were identified as being significant for step motion ≥ 11 mm. No significant motion artefacts were seen for any magnitude of 30s bounce motion. Motion artefacts increased as the duration of the bounce motion increased from 30s to 90s. The TPD values for motion simulated in the X and Y directions were slightly lower than for motion in the Z direction. There was no statistically significant difference between paired X – Y TPD results. Statistically significant differences were calculated between paired X – Z and Y - Z TPD results ($p = 0.034$ and $p = 0.013$).

Parts of this section are reproduced with permission of Springer from Redgate, Barber et al. (2016). © American Society of Nuclear Cardiology 2016.

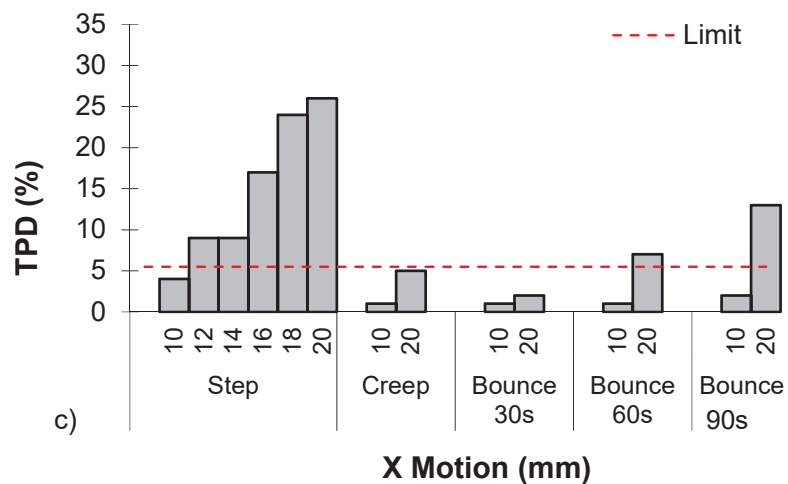
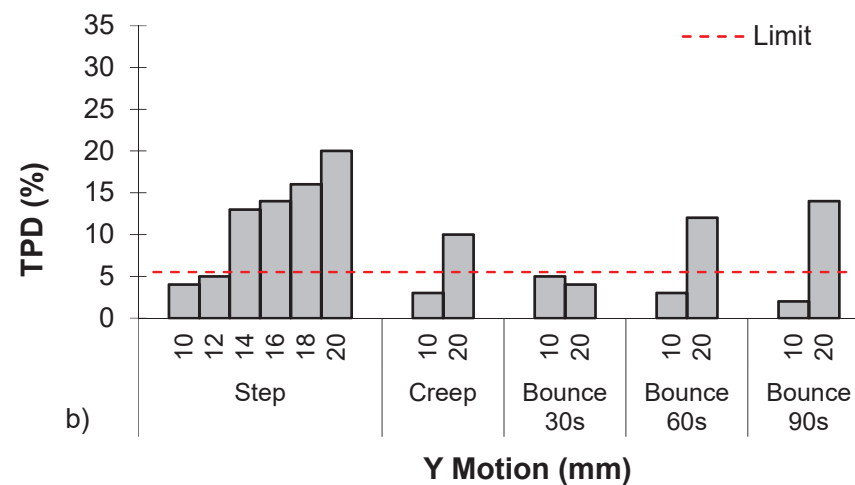
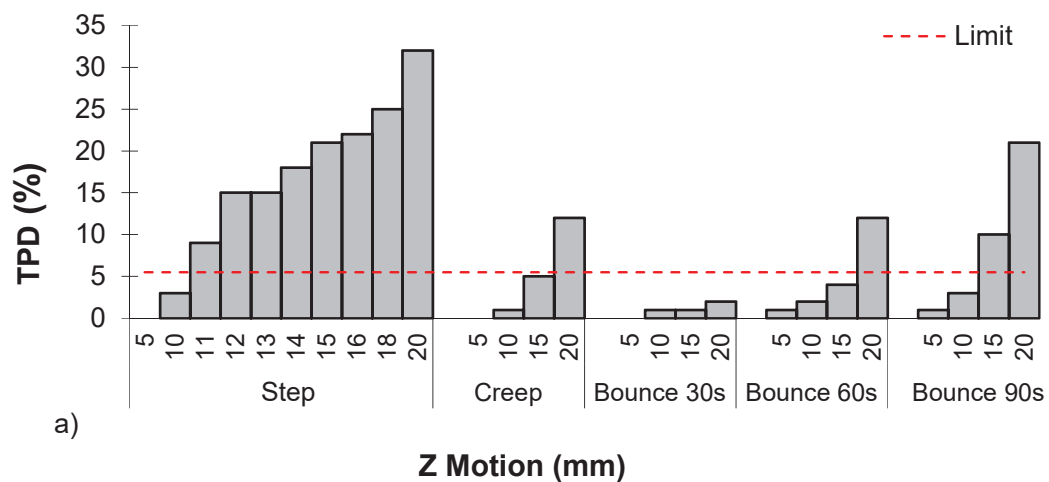


Figure 3-14 – The TPD values calculated for all the simulated images (a) Z direction, (b) Y direction and (c) X direction. The red horizontal dashed line on each graph represents the cut off limit of a $TPD \geq 5.5\%$ for the identification of motion artefacts; TPD values above this indicate significant patient motion artefacts.

Parts of this section are reproduced with permission of Springer from Redgate, Barber et al. (2016). © American Society of Nuclear Cardiology 2016.

Qualitative Analysis: Table 3.4 shows the artefact and mean severity scores for the individual reporters, along with the consensus reports. The consensus reports identified motion artefacts for ≥ 12 , ≥ 10 and ≥ 12 mm motion in the Z, X and Y directions respectively. Comments were recorded by the reporters that the basal infero-lateral wall / infero-lateral wall / lateral base appeared to improve on the stress scan compared to the rest scan in some instances, figure 3-15 and figure 3-16. All of the scans were reported as being high quality. Overall reporter confidence was approximately equally divided between medium and high; with reporter 2 having greater confidence in the reports than reporter 1.

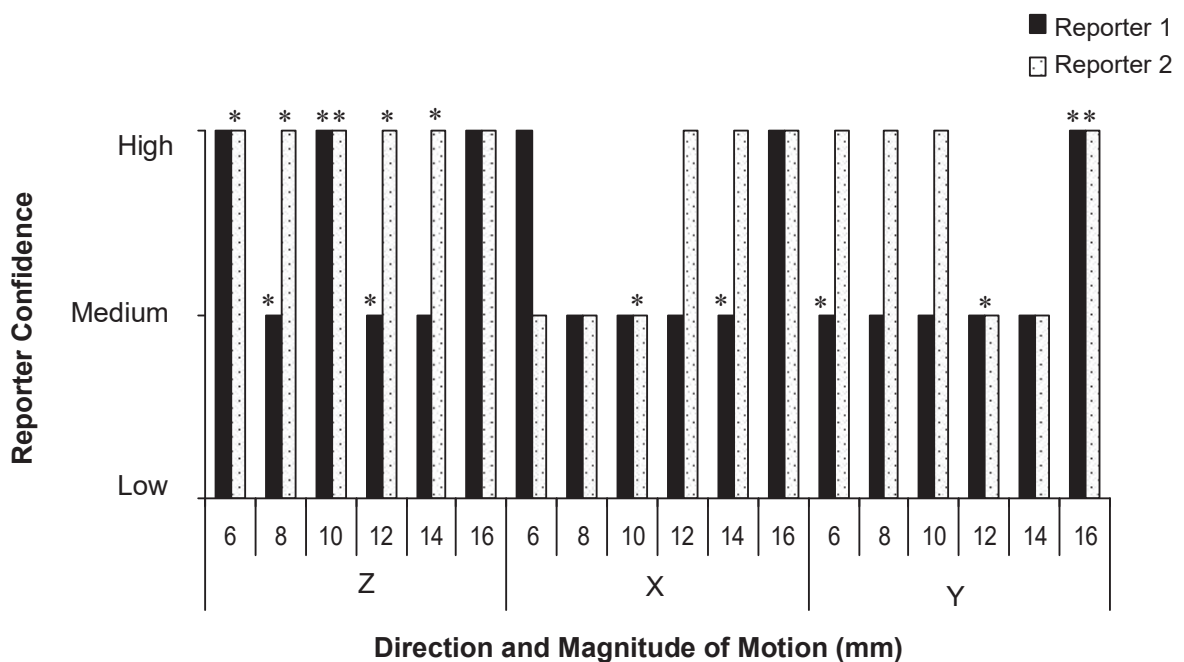


Figure 3-15 – Confidence in the report by both reporters for the different types of simulated motion. * Studies where the stress images appeared to have improved uptake in the basal infero-lateral region.

Direction	Step Motion (mm)	Artefact Extent (%)		Mean Artefact Severity Score (1-5)		Consensus Report Reversibility (Y/N)
		Reporter 1	Reporter 2	Reporter 1	Reporter 2	
Z	6	0	0*	-	-	
	8	0*	0*	-	-	
	10	0*	0*	-	-	
	12	0*	6*	-	2	Y
	14	6	12*	2	2	
	16	24	41	3	2	
X	6	0	0	-	-	
	8	0	6	-	2	N
	10	6	6*	2	2	
	12	18	18	2	2	
	14	12*	6	2	2	
	16	24	47	2	2	
Y	6	0*	0	-	-	
	8	0	0	-	-	
	10	0	0	-	-	
	12	6	6*	2	2	
	14	0*	6*	-	2	Y
	16	6	29	2	2	

*Table 3.4 – The artefact extent and mean severity scores calculated from blinded reporting of the images by 2 experienced reporters. * Studies where the stress images appeared to have improved uptake in the basal infero-lateral region. The shaded cells represent no consensus report required.*

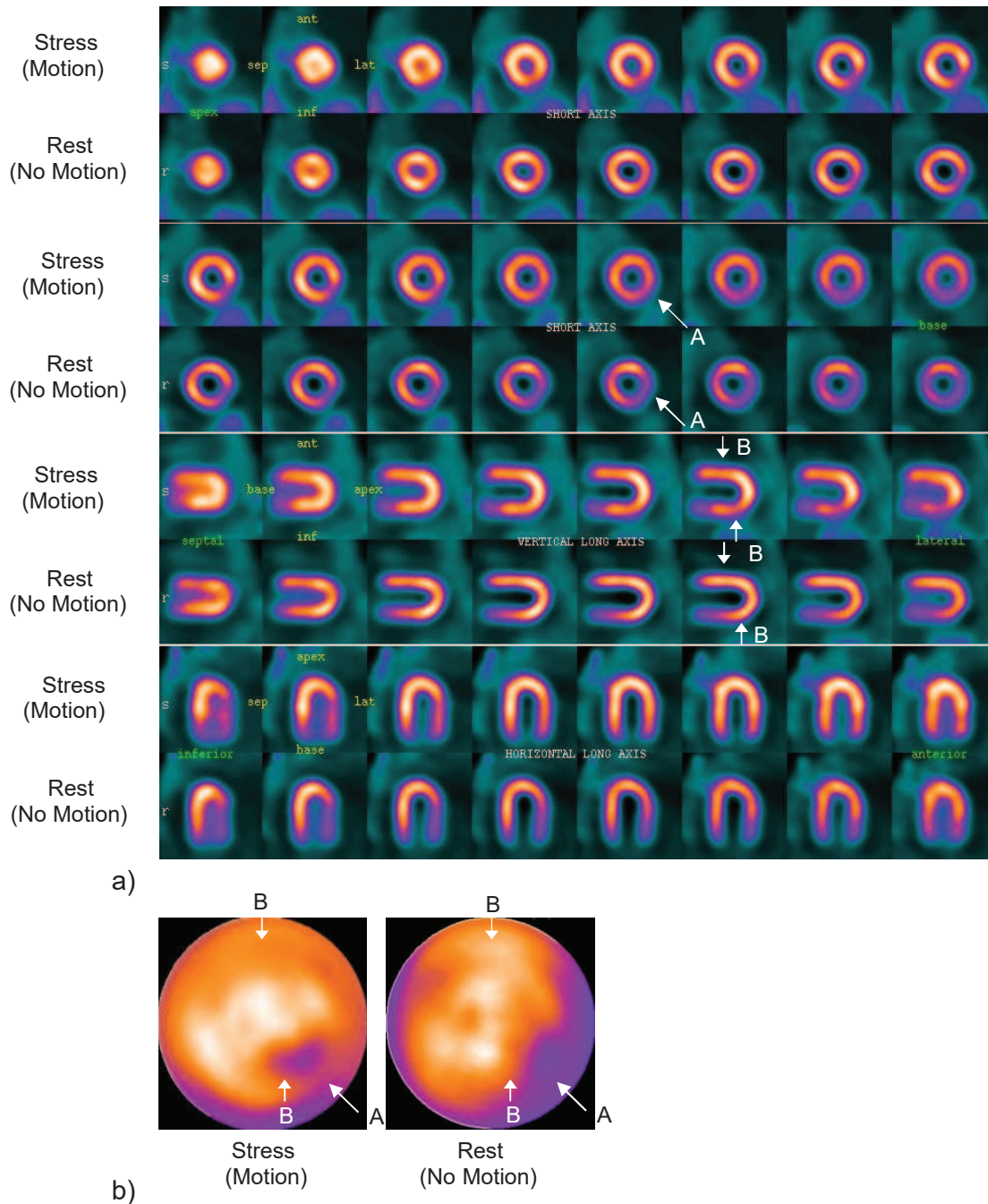


Figure 3-16 – (a) Myocardial perfusion imaging reporting screen and (b) polar plots for 12mm step motion in the Z direction. A - Improved basal infero-lateral perfusion at stress (with motion) compared to rest (no motion). B - Improved anterior and infero-apical perfusion at rest (no motion) compared to stress (with motion).

Parts of this section are reproduced with permission of Springer from Redgate, Barber et al. (2016). © American Society of Nuclear Cardiology 2016.

3.6.3 – Discussion

Quantitative comparison of the different types of motion has shown that step motion introduces the most significant artefacts, whereas bounce motion with a duration ≤ 30 s is insignificant (TPD $< 5.5\%$). For step motion quantitative analysis derived a cut off value for significant motion artefacts of ≥ 11 mm. TPD values were higher and therefore motion artefacts more significant in the Z direction. Arguably, this is because Z motion affects all the detectors, whereas motion in the X and Y directions will only affect detectors that are aligned with the direction of the motion. This is in agreement with results reported on a standard gamma camera, which showed that axial motion was more detectable than lateral motion (Cooper et al., 1992).

Qualitative results show that significant motion artefacts were identified on images with 10, 12 and 12mm motion in the X, Y and Z directions respectively. This is consistent with the limit of 11mm derived from quantitative assessment. Motion artefacts were preferentially identified in the X direction. This is in agreement with Salvadori et al., (2018) who observed that the DNM 530c was less vulnerable to motion in the Y direction compared to the X direction and the authors suggest that this is due to the asymmetrical geometry of the camera, with more detectors being affected by X motion than Y motion. Motion in the X direction mainly introduces artefacts into the lateral wall. There is less sub-diaphragmatic activity around the lateral wall compared to the anterior and inferior walls, which could make subtle artefacts in the region clearer to reporters. For example in figure 3-11 the lateral artefact for 20mm X motion appears clearer than the artefacts for 20mm Y and Z motion. A majority of the mean artefact severity scores were 3, showing that the artefacts introduced by motion were mainly mildly reduced. Artefact extent generally increased with increasing motion.

Combining both the quantitative and qualitative results, a limit for significant motion artefacts of ≥ 10 mm (2.5 reconstructed voxels) for the DNM 530c camera has been established. This takes into account motion in all directions. Patient motion is however predominantly in the Z direction (Matsumoto et al., 2001) and therefore a limit of ≥ 11 mm (2.75 reconstructed voxels) is suggested for motion in the cranio-caudal direction. This is slightly lower than the limit of ≥ 13 mm (2 pixels) that is used

Parts of this section are reproduced with permission of Springer from Redgate, Barber et al. (2016). © American Society of Nuclear Cardiology 2016.

for standard gamma cameras. It cannot be concluded from these results that motion on the DNM 530c is more significant than on Anger systems due to differences in the way these studies were performed. The literature relating to patient motion on Anger gammas consists of mainly Tl^{201} studies reconstructed with filtered back projection (FBP), table 2.4. It has been shown that motion artefacts are more significant for Tc^{99m} imaging (Kapur et al., 2002) and for iterative reconstruction techniques (Kovalski et al., 2007). The study that determined the limit of $\geq 13\text{mm}$ (2 pixels) simulated motion by shifting frames from normal motion free MPI studies (Cooper et al., 1992). The images will have therefore been affected by blurring due to cardiac contraction, which was not simulated in our study. These factors could credibly account for a 2mm difference in the results. The limits presented also coincide with the point where the FWHM of profiles across the myocardium start to noticeably increase, figure 3-12b.

Blinded reporting also identified areas of reduced perfusion that appeared to improve when motion was simulated on the images, figure 3-16. This is important, as motion could be present on the rest study and not the stress study and these could therefore be reported as reversible ischaemia. The phantom simulations represented normal myocardial uptake, which due to attenuation showed reduced perfusion infero-laterally towards the base. Improved perfusion at stress in this area was identified by the reporters for motion as low as 6mm and was more prominent for motion in the Z direction. This could be due to areas of reduced perfusion overlapping with adjacent areas of improved perfusion or increased overlap with the liver as the heart moves. A difference in the position of the heart in the QFOV $>1\text{cm}$ can alter the perfusion pattern between comparable images (Metherall et al., 2011). Therefore, infero-lateral wall differences could also be caused by apparent changes in the perfusion pattern as motion alters the position of the heart in the QFOV. Any areas of improved perfusion infero-laterally towards the base where motion is identified on the rest study should therefore be interpreted with caution.

There were many limitations to the study, as described in section 3.6.4, however the threshold of $\geq 10\text{mm}$ motion for $\geq 60\text{s}$ derived for significant motion artefacts provides a good starting point for the assessment of motion on patient studies. The limit of

≥60s is for an acquisition duration of 360s and to make this independent of the imagine duration should be quoted as ≥17% of the acquisition.

3.6.4 – Limitations

- **Simulation Method:** Motion was simulated by combining static images at different positions, however on patient studies motion could occur continuously throughout the study. Therefore, on patient studies there could be residual motion within the 30s images.
- **Normal Database:** The normal database consists of normal phantom studies and therefore does not include variations expected between normal patients. This may have underestimated the limit for significant motion artefacts derived using quantitative analysis.
- **Cardiac Motion:** Blurring due to cardiac contraction was not incorporated, which is a common limitation encountered with static phantom studies.
- **Normal Phantom:** Normal phantom studies were used. The improvements observed in the infero-lateral wall with motion raise the possibility that motion could improve the appearance of real perfusion defects. Systematic evaluation of this using the cardiac insert with defects was outside the remit of this thesis.
- **Activity outside the QFOV:** The phantom did not include gut activity, which has an influence in MPI. Also, the length of the anthropomorphic phantom limits activity outside the QFOV compared to a patient scan.
- **Image Quality:** Although the activity used in the phantom was determined to give similar quality images to patient studies, the scan quality was superior to patient studies due to the absence of other patient related factors such as cardiac motion and sub-diaphragmatic activity, as discussed above. The scan quality values were all high and the reporter confidence values were all medium or high.

3.6.5 – Conclusion

This section has provided an understanding of the types, magnitude and duration of patient motion that has a significant effect on myocardial perfusion imaging on the DNM 530c. Motion artefacts were visible for $\geq 10\text{mm}$ motion with a duration $\geq 17\%$ of the acquisition. Patient motion $\leq 30\text{s}$ of any magnitude did not introduce significant motion artefacts.

3.7 – Comparison to Mathematical Model

The mean FWHM of the inferior wall assessed on two slices (34 and 37) of phantom images with no motion was measured to be 20.5mm (range 19 - 22mm). Using the mathematical model in section 3.2 the percentage reduction in the peak value for different magnitudes and durations of motion, 50%, 8%, 17% and 25% of the acquisition, which equates to step motion and bounce motion 30, 60 and 90s in duration were modelled. From these data it is estimated that 15mm motion would cause significant motion artefacts on phantom studies when motion affects 50% of the acquisition time (step motion) and that 20mm of motion would not cause any significant artefacts when 8 - 25% of the acquisition is affected (bounce motion).

This is shown graphically in figure 3-17 demonstrating reasonable agreement between the mathematical model and the reduction in the peak value measured from profiles across the phantom images. For motion that occupies 50% of the scan the mathematical model slightly underestimates the reduction in counts and therefore overestimates the limit at which artefacts occur. For other durations of motion, the model generally lies between the values measured on two slices of the phantom images and is a good estimate of the phantom results. Considering the one-dimensional nature of the model, the assumption of independence of the profile from surrounding structures and omissions such as the reconstruction process, noise, scatter and partial volume effects, it is evident that although there are some differences between the model and phantom measurements, the model gives a simple but effective way in which to think about the effect of motion on myocardial perfusion images. Table 3.5 compares the limits determined from the mathematical model and profiles to TPD analysis and blinded reporting.

Parts of this section are reproduced with permission of Springer from Redgate, Barber et al. (2016). © American Society of Nuclear Cardiology 2016.

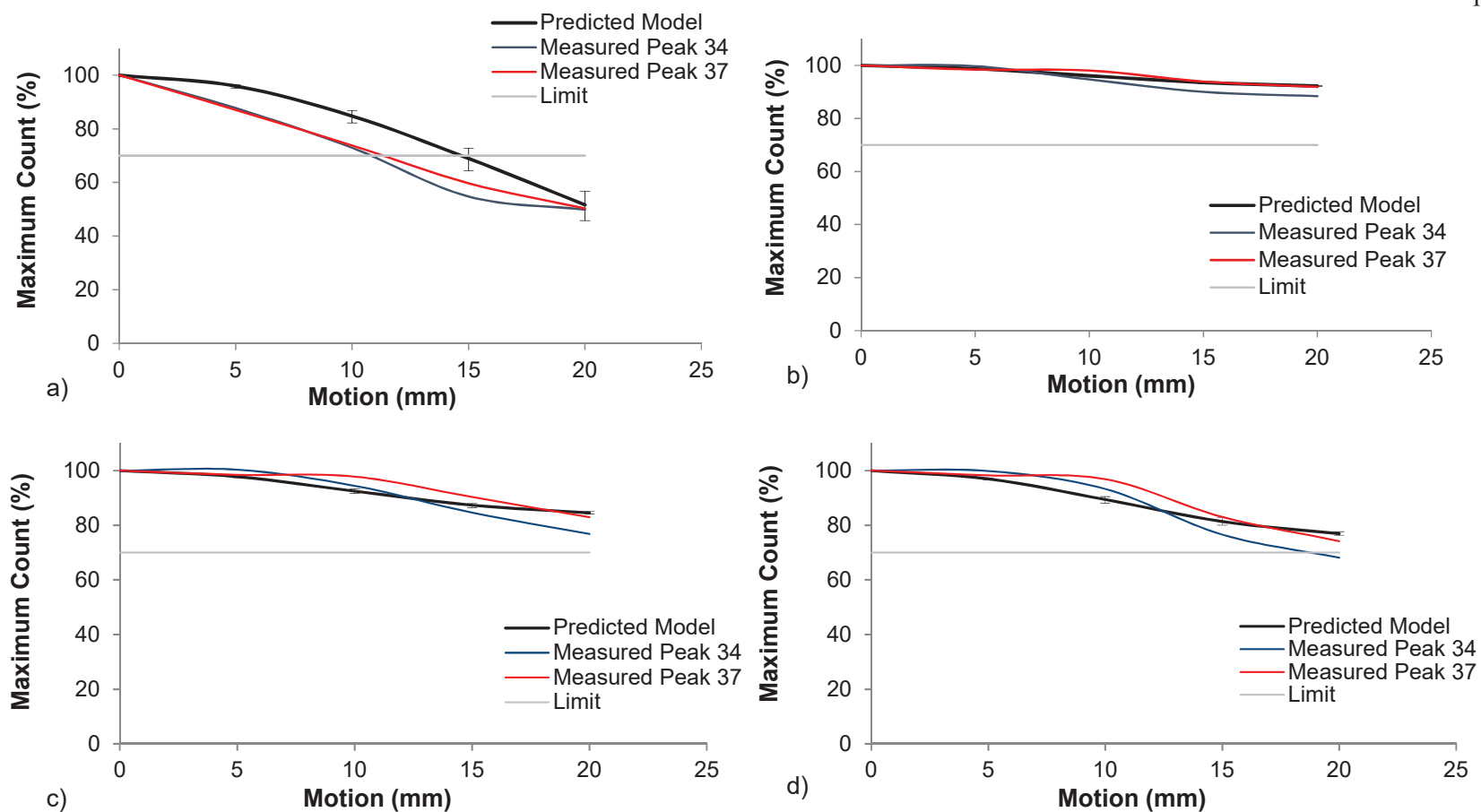


Figure 3-17 – The maximum of the profile expressed as the percentage of the maximum when no motion is present, for different durations of motion, calculated using the mathematical model and measured on phantom simulations. (a) 50% (b) 8% (c) 17% and (d) 25% of the acquisition affected by motion. A value for c of 8.7 was used for the model. The error bars are based on the variation in the FWHM measured on the phantom simulations. The red and blue lines represent the values measured on two different slices of the phantom image. The limit for significant motion artefacts, point at which the maximum count is 70%, is represented by the limit line.

Duration of Motion Expressed as the % Acquisition Time, (Description)	Motion that Results in Significant Motion Artefacts (mm)			
	Mathematical Model	Phantom Simulations		
		Profiles	TPD Analysis	Blinded Reporting
50 (step)	15	11 ⁺	11	10
25 (bounce 90s)	NMA	>20	12 ⁺	NM
17 (bounce 60s)	NMA	>20	16 ⁺	NM
8 (bounce 30s)	NMA	>20	>20	NM

Table 3.5 – The limit at which motion artefacts occur as determined by different methods. ⁺ - Linear interpolation was used to find limits that fell between acquired data points. >20 - Limit not reached for the measured range of 0 - 20mm. NM – Not measured. NMA – No motion artefacts as the maximum count never falls below 70% regardless of the magnitude of the motion.

For step motion the model and profile results are consistent with the results of the TPD analysis and blinded reporting. When motion occupies a shorter proportion of the acquisition time, there are some differences between the model, profile and TPD analysis. The limits for motion artefacts are generally lower for the TPD analysis compared to the model and profile values and although blinded reporting has not been performed, the TPD results agree with what is seen visually on the images. The model and profile are only making an assessment of the counts along one line of pixels across the wall of the left ventricle, whereas visual analysis is considering all the counts in the myocardium relative to the global maximum. The TPD analysis is comparing all the counts in the myocardium to a normal database. This is very different to reviewing the image in terms of the reduction in counts relative to the maximum, and includes local variations, such as the variation in the perfusion of the wall due to attenuation, position in the QFOV and noise. Considering the limitations of the model and profile analysis, the TPD values give a more realistic representation of the limits for significant motion artefacts.

3.8 – Respiratory Motion

The previous section undertook a systematic phantom study to investigate the effect of different types of patient motion on myocardial perfusion images acquired on the DNM 530c. The dominant factors determining the effect of motion were the magnitude and duration of the motion, which is broadly divided into step, creep and bounce motion. The results from section 3.6 can therefore be used to explore the effect of respiratory motion during MPI on the DNM 530c.

The graphs in figure 3-18a,c,e represent three types of cranio-caudal Z motion, step and creep patient motion, and respiratory motion approximated by a sine wave function. The signal is divided into five bins, with each bin representing 1/5th of the magnitude of the signal. The histograms in figure 3-18b,d,f represent the cumulative counts in each bin due to the amount of time spent by the heart at different Z positions. Motion artefacts will depend on the relative amplitude of the bins, which is equivalent to the counts in each bin. Motion concentrated equally at the extremes, figure 3-18a,b is equivalent to step motion. Step motion will introduce artefacts for a smaller motion displacement than evenly spaced creep motion, figure 3-18c,d due to an increase in the average motion across the study, even if the overall magnitude of motion (difference between the maximum and minimum positions) is the same. If respiratory motion is simplified to a sine wave function, figure 3-18e,f the relative distribution of the bins falls between step and creep motion; with the heart residing equally in the extreme bins for 30% of the imaging time.

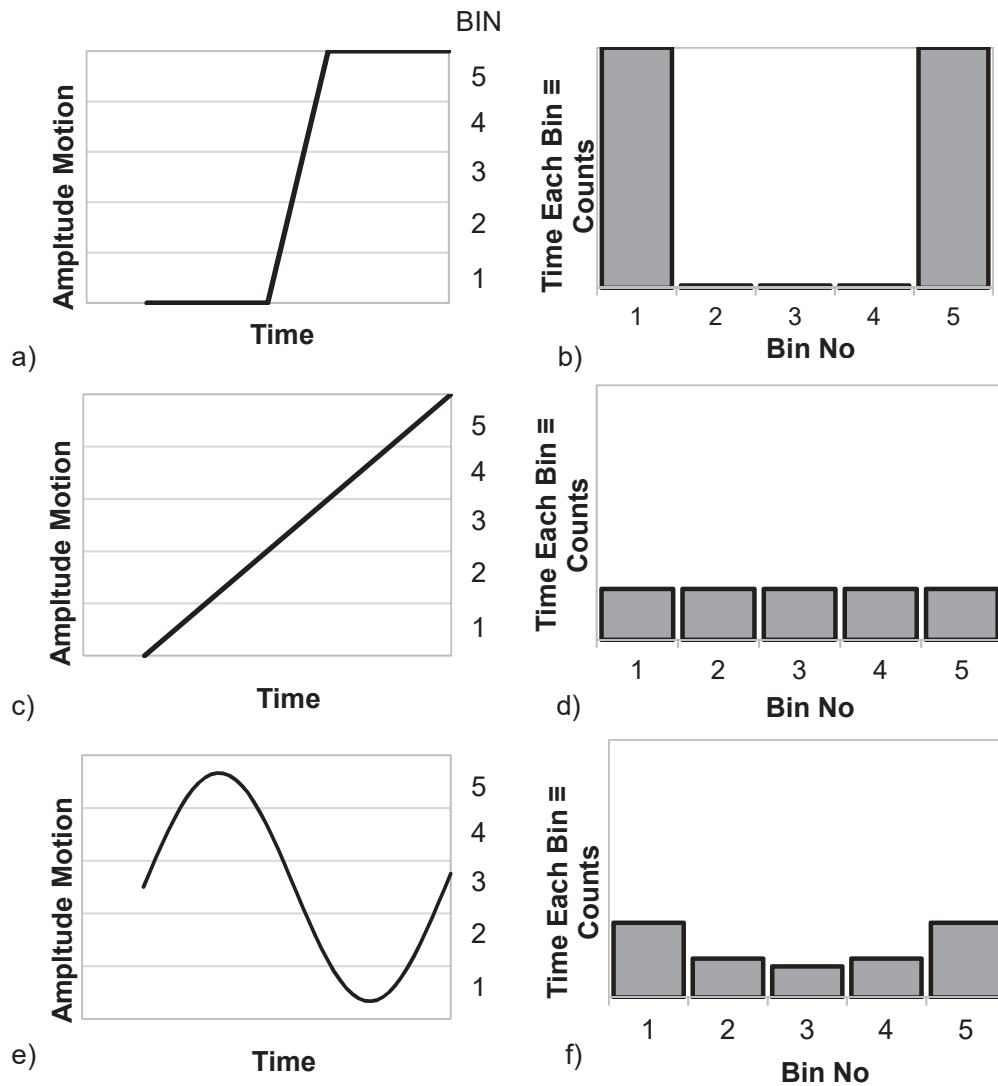


Figure 3-18 – A graphical representation of (a) step and (c) creep cranio-caudal (Z) patient motion, and (e) cranio-caudal respiratory motion. The histograms for (b) step, (d) creep and (f) respiratory motion represent the amount of time spent by the heart at different positions.

The limits determined for significant motion artefacts from the quantitative results in section 3.6, figure 3-14, were $\geq 11\text{mm}$ for step motion and $\geq 16\text{m}$ for creep motion (determined from liner interpolation between measured points). Therefore, as the distribution of motion between the bins from respiratory motion lies between step and creep motion, 12-13mm is a reasonable estimate of the magnitude of respiratory motion that would result in significant artefacts. The concept of the

duration of the motion is redundant for respiratory motion as motion is continuous. The respiratory pattern measured in patients has been shown to dominantly reside in the end–expiration phase (Kovalski et al., 2007) and therefore the distribution of time spent in each bin will vary between patients. The point at which artefacts are introduced will vary between patients depending on their individual respiratory pattern.

3.9 – Summary

This chapter has provided an understanding of the types and magnitude of motion that have a significant effect on myocardial perfusion imaging on the DNM 530c. Patient motion artefacts presenting as localised areas of reduced perfusion are significant on the DNM 530c for motion $\geq 10\text{mm}$ with a duration $\geq 17\%$ of the acquisition. The significance of any improvements in perfusion infero-laterally towards the base on images with motion should be interpreted with caution. This provides a guide for technologists and physicists performing quality control on MPI studies, indicating when to be concerned that motion could be having a negative effect on the images. Significant respiratory motion artefacts have been estimated to occur for cardiac displacements of 12 - 13mm resulting from respiratory effort.

4 – Motion Estimation on the Discovery 530c Dedicated Cardiac Camera

4.1 – Introduction

Chapter 3 assessed the magnitude of patient and respiratory motion that has a significant effect on myocardial perfusion images. On Anger cameras patient motion is assessed before the patient leaves the department, allowing motion correction to be performed and the scan repeated if necessary. Respiratory motion estimation and correction is not routinely performed following MPI on Anger cameras or the DNM 530c, despite evidence of this being advantageous (Buechel et al., 2010b; Ko et al., 2015). At the start of this study there was no software available to assess patient or respiratory motion on the DNM 530c. The techniques discussed in section 2.4.2 could not be directly applied without adaptations.

This chapter will introduce the techniques proposed for motion estimation and correction on the DNM 530c. Rather than adapting current algorithms, new approaches were taken to exploit the three-dimensional nature of the system. Simulations will be used to evaluate the proposed techniques.

4.2 – Motion Estimation Technique

Estimation of motion requires the position of the heart to be measured at specified time intervals throughout a study. Nyquist's theorem states that the minimum sampling frequency required to detect a signal should be at least twice the highest frequency in the signal. No standard frequency is cited as being suitable for characterising patient motion. Patient motion on Anger cameras is visualised between 30 second projections and therefore a sampling frequency of 30 seconds is pragmatically chosen for detection of significant patient motion. In contrast the average respiratory cycle is better defined and cited as 3 seconds (Bitarafan et al., 2008), suggesting that a sampling frequency of ≤ 1.5 seconds might be appropriate for respiratory motion.

A consistent method is used throughout this thesis for motion estimation. It involves dividing the acquisition into a time series of shorter images, registering all the images in the series to the first image in the series, then extracting and plotting the shifts required to align the images, figure 4-1. Two techniques can be used on the DNM 530c; registration of the projection images of the heart or registration of the reconstructed images. Both these techniques are described below.

Motion estimation using planar pinhole projection images involves the following steps, figure 4-2a,b,c. From this point onwards this will be termed the ***planar motion estimation technique***, as it determines motion for all three planes by combining the results from the planar images.

1. Image acquisition.
2. Data divided into a time series of images, with data over each time interval containing 19 projections of the heart.
3. Combine the images from each projection to produce 19 times series'
4. Register the images in each series, as described in figure 4-1, to determine the motion present on each series.
5. Correct the measurements for minification due to pinhole collimation, see section 4.3.
6. Combine the results from the detectors to estimate the motion present on the study.

Motion estimation using reconstructed images involves a similar workflow involving the following steps, figure 4-2a,b,d. From this point onwards this will be termed the ***three-dimensional motion estimation technique***, as it determines motion in all three planes from the three-dimensional reconstructed images.

1. Image acquisition.
2. Data divided into a time series of images, with data over each time interval containing 19 projections of the heart.
3. Reconstruct the data in each time interval to produce series of three-dimensional images.
4. Register the reconstructed images, as described in figure 4-1 to determine the motion present on the study.

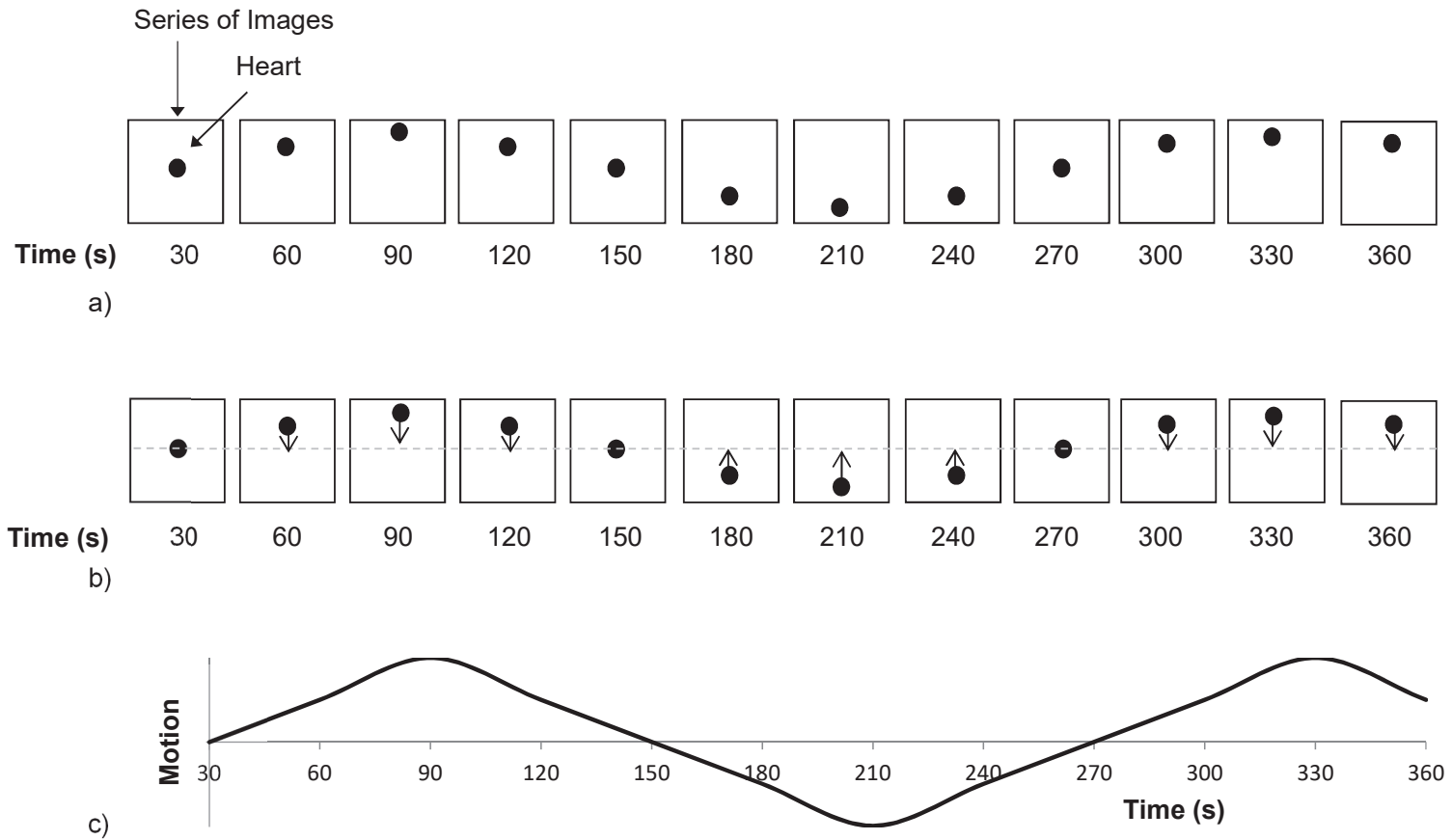


Figure 4-1 – A diagrammatic representation of the technique used for motion estimation throughout this thesis. (a) The myocardial perfusion image is divided into a time series of images; any shift in the heart (represented by the black dot) may be visualised between the images. (b) Each image in the series is registered to the first image in the series generating a registration mapping (black arrows). (c) The mappings from the registrations are extracted and plotted to estimate the motion present during the study.

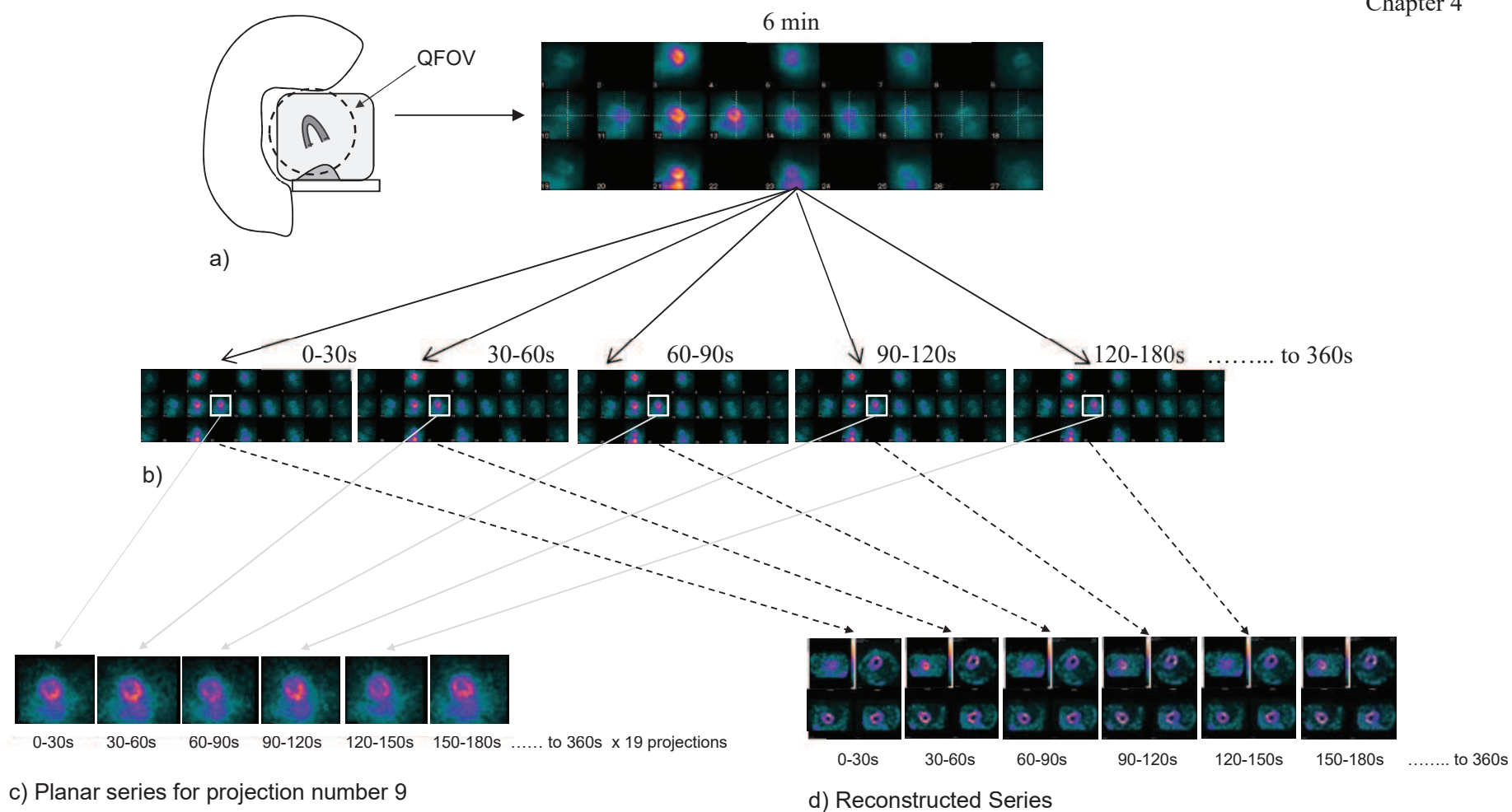


Figure 4-2 – (a) An image is acquired on the DNM 530c, resulting in 19 projection images of the heart. (b) The list mode data is divided into a time series, with 19 projections of the heart associated with each time interval. (c) The images from each projection are combined to give 19 time series or (d) the images at each time point are reconstructed to give a series of three-dimensional images over time. Motion on the images (planar or three-dimensional), is then assessed as described in figure 4-1.

4.3 – Pinhole Collimation

The ultimate aim of motion estimation is measurement of the shift of the heart during the study to determine if motion is likely to have had a detrimental effect on the images. A key design feature of the DNM 530c is that the pinhole collimators minify the image of the heart onto the detectors, as described in section 2.3.6. The *planar motion estimation technique* described in section 4.2 therefore includes correction for minification, as the motion of the heart measured on the detectors is a scaled measure of the true shift of the heart. The shift measured from reconstructed images using the *three-dimensional motion estimation technique* is a direct measure of the true shift of the heart. This section will estimate the scaling factors required to convert measurements made using the *planar motion estimation technique* into the true shift of the heart.

4.3.1 – Minification

Minification of the heart will depend on the pinhole-to-detector distance (PDD) and heart-to-pinhole distance (HPD), (GE Healthcare, Alcyone Technology White Paper), figure 4-3a. Therefore, for a fixed movement of the heart (hx), the measured movement of the heart on the detector (dx) will depend on the PDD and HPD, figure 4-3c. These are related through equation 4.1. Therefore, measurement of the true shift of the heart from the planar pinhole projection images requires a scaling factor to be calculated for each detector.

$$ScalingFactor = \frac{HPD}{PDD} = \frac{hx}{dx} \quad \text{Equation 4-1}$$

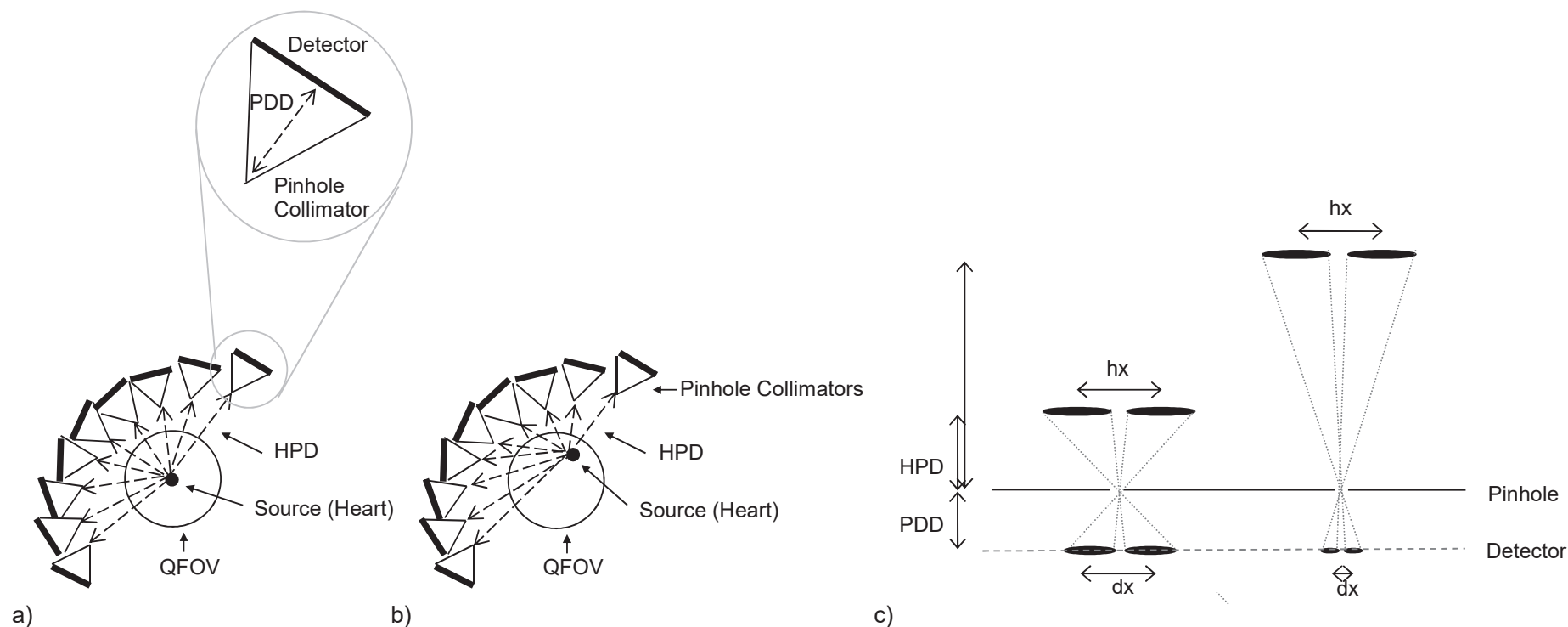


Figure 4-3 - (a) A schematic diagram showing the heart-to-pinhole distance (HPD) and pinhole-to-detector distance (PDD). (b) The HPD changes as the position of the heart changes in the QFOV. (c) The shift of the image of the heart measured on the detector (dx) will depend on the true shift of the heart (hx) and the ratio of the HPD to PDD; in this example the shift of the heart is the same but the HPD and hence the shift of the image on the detector is different.

4.3.2 – Determination of Scaling Factors

Anthropomorphic phantom images, as described in section 3.6.1, were acquired at the centre of the QFOV and offset in the Z direction by 10, 20 and 30mm. Scaling factors were calculated for all 19 detectors, by registering the offset images to the central image and calculating the ratio of the applied shift (hx) to the measured shift (dx), equation 4.1.

The calculated scaling factors and associated errors for all the detectors are shown in table 4.1.

Detector	1	2	3	4	5	6	7	8	9	10
Scaling Factor:										
Mean	2.54	3.27	3.62	3.24	3.51	2.60	2.51	2.55	2.67	2.78
SD	0.18	0.12	0.23	0.39	0.15	0.13	0.02	0.04	0.04	0.10
Error HM (mm)	0.7	0.4	0.6	1.2	0.4	0.5	0.1	0.2	0.1	0.4
Detector	11	12	13	14	15	16	17	18	19	
Scaling Factor:										
Mean	2.79	2.79	2.62	2.74	2.77	2.83	3.15	3.22	2.96	
SD	0.06	0.10	0.11	0.04	0.04	0.10	0.04	0.04	0.24	
Error HM (mm)	0.2	0.4	0.4	0.1	0.1	0.4	0.1	0.1	0.8	

Table 4.1 – The mean and standard deviation of the scaling factors calculated to convert the shift measured on planar detector images into the true shift of the heart. Error HM is the error on a true heart motion of 10mm that would be introduced due to measurement uncertainties in the calculated scaling factor based on a 1SD error.

4.3.3 – Assumption of Central Positioning

The scaling factors calculated in table 4.1 assume that the heart is positioned in the centre of the QFOV. However, the HPD and therefore the scaling factor is dependent on the position of the heart in the QFOV, figure 4-3b. The clinical technologists aim to position the heart in the centre of the QFOV, however patient

body habitus can result in off-center positioning. Figure 4-4 demonstrates how positioning of the heart in the QFOV can vary between patient images.

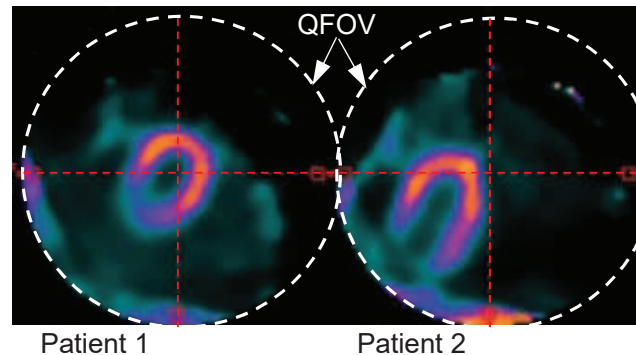


Figure 4-4 – Transaxial images of the heart for two patients showing the variation in the position of the heart in the QFOV.

The assumption made throughout this thesis is that the factors calculated in table 4.1 are applicable across the QFOV. Anecdotally, most patients can be positioned centrally or close to centrally and there are only a few patients with larger body habitus' where positioning is difficult and the heart is close to the edge of the QFOV. Additional errors due to positioning are therefore only expected to affect a limited number of patients.

4.3.4 – Conclusion

Scaling factors have been calculated that can be used to convert shifts measured using the *planar motion estimation technique* into the true shift of the heart. The average scaling factor across all detectors was 2.90 ± 0.12 .

4.4 – Initial Evaluation of Motion Estimation Technique

The techniques proposed for motion measurement were outlined in section 4.2, figure 4-1 and figure 4-2. This section illustrates the ability of the Sheffield Image Registration Toolkit (ShIRT) to register both planar and reconstructed myocardial perfusion images for the purpose of motion estimation. The capacity of ShIRT to

Parts of this section are reproduced with permission of Springer from Redgate, Barber et al. (2016). © American Society of Nuclear Cardiology 2016.

recover the shift between images will depend on the noise in the image and smoothing operations can help this. For the same reason it should be easier to detect patient motion, measured between images with frame durations of 30s, than respiratory motion where frame durations $\leq 1.5s$ are required.

4.4.1 – Sheffield Image Registration Toolkit

The Sheffield Image Registration Toolkit (ShIRT), appendix A, is utilised for registration of the images. The main ShIRT commands are shown below, with the words in bold representing user specified inputs. The command line involves the following syntax:

```
ShIRT Register Fixed fixed Moved moved Mask mask FixedSmooth nf
MovedSmooth nm NodeSpacing n Mapform mapform MutualInformation
```

- **fixed**: This is the image that remains fixed in space
- **moved**: This is the image that is warped to match the fixed image
- **mask**: A mask defined on the fixed image identifies the pixels that will be used to determine the registration mapping.
- **nf, nm**: This is a number specifying how many applications of a 1-2-1 smoothing filter should be applied on the fixed (nf) or moved (nm) image prior to registration.
- **n**: This is the node spacing. A node is a point on the fixed image that is mapped onto a point on the moved image. The node spacing is the distance between these nodes in pixels. Other points in the mapping are determined by tri-linear interpolation between these nodes.
- **mapform**: The types of registration that can be performed. The options are translation only, rigid (translation and rotation), affine and non-linear.
- **Mutual Information**: The default cost function for the registration is based on sum of squares. Mutual Information is an alternative cost function.

These parameters will be referred to throughout the thesis to describe the registrations that have been used.

4.4.2 – Method

The performance of ShIRT was evaluated using a 6 minute phantom image acquired with the heart in the centre of the QFOV as described in section 3.6.1, resulting in 19 projection images of the heart. The list mode data were divided into a time series of images. Ten series' were generated with frame durations of 1, 2, 3, 4, 5, 8, 10, 15, 20 and 30 seconds, figure 4-5. Motion was simulated on the data by the process described below. The ability of ShIRT to measure image shifts was assessed for planar images and reconstructed images.

- **Planar Images:** The images associated with projection number 9 were extracted from each series of images. All the images, apart from the first image in each series, were shifted by 1 – 8 pixels (2.5 – 19.7mm, pixel size 2.46mm). The shifted images were registered to the first image in the series. A simple registration (MapForm: Translation, NodeSpacing: 4, FixedSmooth: 2, MovedSmooth: 2) was used with a square mask around the heart specified on the fixed image. The registration mappings were compared to the known shift. The scaling factor calculated for detector 9 was used to convert the registration errors into values related to the true shift of the heart, allowing direct comparison with results from the reconstructed images.
- **Reconstructed Images:** The images in each series were reconstructed using the clinical parameters described in section 3.5. All the images, apart from the first image each series, were shifted by 1 – 8 pixels (4 – 32mm, pixel size 4mm). The shifted images were registered to the first image in the series. A simple registration (MapForm: Translation, NodeSpacing: 4, FixedSmooth: 2, MovedSmooth: 2) was used with a loose mask drawn around the heart on the fixed image. The shift from the mapping was extracted and compared to the known shift.

The performance of ShIRT for the registration of planar and reconstructed images was compared through calculation of the mean and standard deviation of the absolute errors on the final shift of the heart.

Parts of this section are reproduced with permission of Springer from Redgate, Barber et al. (2016). © American Society of Nuclear Cardiology 2016.

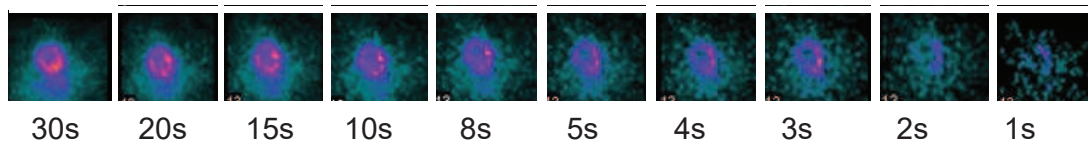


Figure 4-5 – Images from detector number 9 with different durations.

4.4.3 – Results

The mean absolute error for planar and three-dimensional techniques with different image durations is shown in figure 4-6.

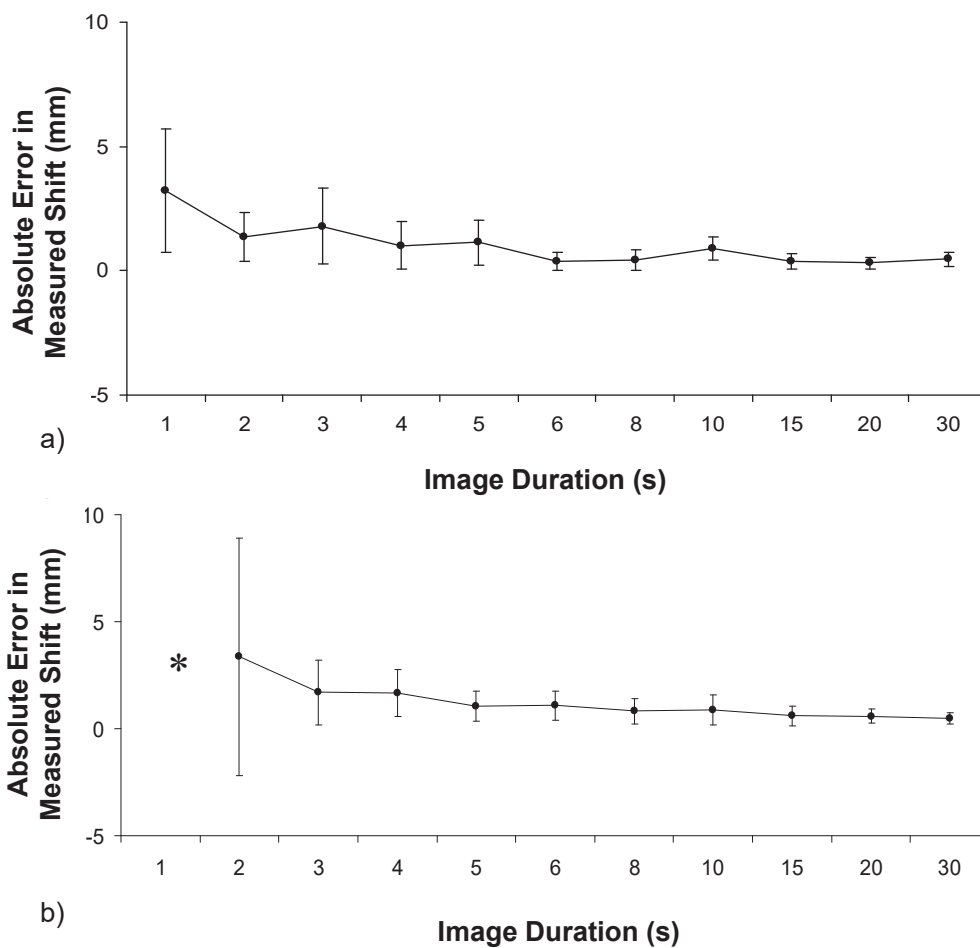


Figure 4-6 – The mean absolute error (± 1 SD) of the measured shift for (a) planar and (b) reconstructed images. * Due to the noise on the 1s images no sensible registration mask could be drawn.

Parts of this section are reproduced with permission of Springer from Redgate, Barber et al. (2016). © American Society of Nuclear Cardiology 2016.

4.4.4 – Discussion

Figure 4-6 clearly shows that for both the planar and three-dimensional techniques the errors on the measurement of motion increase as the duration of the images decrease. This is consistent with an increase in the noise on the images, as shown in figure 4-5. The mean absolute error represents the accuracy of the registration and exposes only systematic error. The standard deviation represents the precision of the registration and classifies the random error that is present. Although these are both important enabling the shift of the heart to be measured, for the proposed application it is the precision that is of most importance. If small systematic errors are present when measuring the shift of the heart, then these can be accounted for. However, if there are large variations in the error each time an image is registered, no meaningful estimation of motion can be made.

For 3 – 30s image durations the standard deviation values are similar, however for a 2s frame duration the standard deviation was larger for the three-dimensional technique compared to the planar technique. This is largely due to the fact that the reconstruction process inevitably increases the noise that is present on the images. Registration of reconstructed 1s images was not performed as the heart could not be visualised and therefore no sensible registration mask could be drawn.

Section 3.6 predicted that significant motion artefacts are introduced with $\geq 10\text{mm}$ motion, therefore it is motion of this order of magnitude that needs to be measured. The errors for both the planar or three-dimensional techniques when 30s images were registered were $< 1\text{mm}$ demonstrating that either technique could be used for patient motion estimation. For respiratory motion the errors for the planar registration technique were $3.2 \pm 2.5\text{mm}$ as measured from registration of 1s images. Errors of $3.4 \pm 5.6\text{mm}$ were measured when 2s images were registered using the three-dimensional techniques. Under these conditions this technique is not suitable for respiratory motion estimation.

4.4.5 – Conclusion

The method proposed in section 4.2 for the motion estimation on myocardial perfusion images is based on registration of images at different time points throughout the acquisition. The success of the technique is therefore largely dependent on the registration errors. A simple simulation has been performed to characterise these errors for different durations of planar and reconstructed images. Registration of 30s images, both planar and reconstructed, gave small errors (<1.5mm for 3SD) compared to the signal being measured (10mm), suggesting that either technique could be used for *patient motion* estimation. Registration of 1s planar images gave errors of the order of magnitude of the signal being measured (>10.7mm for 3SD) compared to a signal magnitude of 10mm. The suggested technique in its current form is therefore not suitable for *respiratory motion* estimation.

4.5 – Software Development

It has been demonstrated that registration of both 30s planar and 30s reconstructed images are sufficient to detect shifts $\geq 10\text{mm}$. These patient motion estimation algorithms were therefore adopted and software developed to implement both the planar and three-dimensional techniques. This section focuses on the details of the developed software, including the characteristics of the algorithms and their optimisation.

The primary workstation for processing nuclear medicine studies within the Nuclear Medicine Department at Sheffield Teaching Hospitals is the Link Medical workstation. ShIRT is executed via c-shell and offers a series of commands that can be activated from the command line on the Link Medical terminal. ShIRT also includes its own interpreter for its commands providing a rudimentary environment that can be used to combine ShIRT commands into ShIRT scripts. Linux scripts were developed in c-shell, with commands calling ShIRT scripts, to run specific functions to implement the method discussed in section 4.2.

Parts of this section are reproduced with permission of Springer from Redgate, Barber et al. (2016). © American Society of Nuclear Cardiology 2016.

4.5.1 – Planar Registration

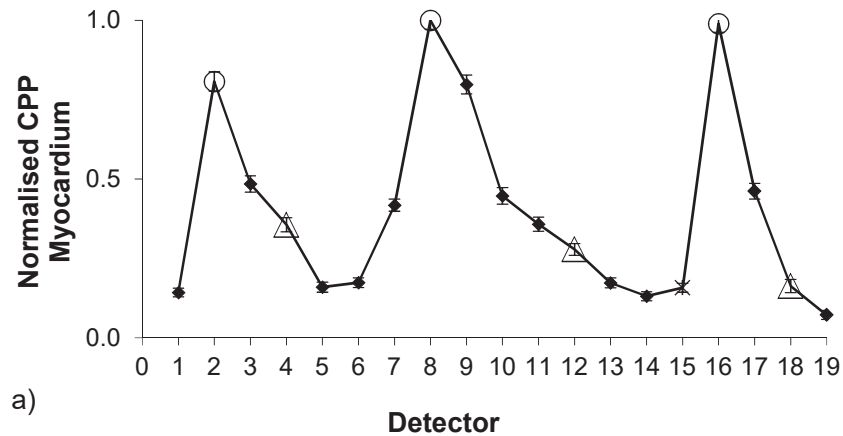
The registration parameters used for the demonstration of ShIRT in section 4.2 were optimised by varying the smoothing values between 0-4, the node spacing between 1-6 and using a variety of masks drawn around the heart at different distances from the edge of the myocardium. Registration of planar 30s images was performed and the errors in the registrations compared for the different parameters. The results showed that the errors on the technique are broadly insensitive to the registration parameters, differences due to smoothing were <0.4mm and differences due to node spacing were <0.9mm. The errors on the technique decreased slightly as the size of the mask increased, however clinically the mask size will be limited due to the need to exclude sub-diaphragmatic activity. A rigid registration with smoothing values of 1 and a node spacing of 4 provided the most encouraging results. Consequently, these were used, along with a loose mask drawn around the heart that excludes sub-diaphragmatic activity.

To enable motion to be estimated in all 3 dimensions, data from more than one detector needs to be analysed. To select which detector images to use, the background corrected counts per pixel in the phantom were calculated for each detector. This parameter varies between detectors due to the inherent design of the system. Images with the highest counts per pixel have the least noise and these were therefore preferentially selected for registration. The counts measured for each detector are shown in figure 4-7a. The images from detectors 15-19 were not selected as these suffer from additional sub-diaphragmatic activity overlapping the heart which may affect the results.

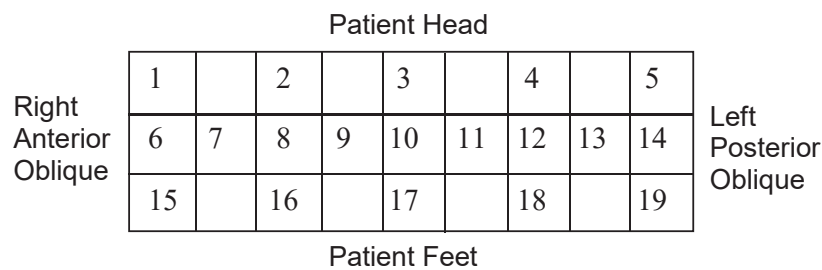
The convention adopted to describe motion in different planes was outlined in section 3.4. Z patient motion can be measured from the y translations on any detector, therefore the translations measured on the three detectors with the highest counts in the myocardium, 2, 8 and 9 were averaged. To measure Y patient motion the x translations from lateral images are required and therefore the translations from detectors 4 and 12 were averaged. To measure X patient motion the x translations from ventral images are required and therefore the translations from

detectors 8 and 2 were averaged. The detectors used for motion estimation are highlighted in figure 4-7c, with the numbering convention shown in figure 4-7b.

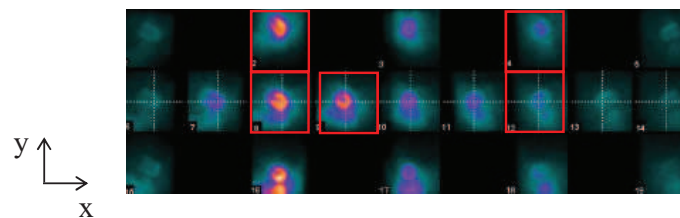
Averaging was performed by determining the motion curve for each detector, correcting for minification using the scaling factors in table 4.1 and then averaging the results at each time point. The motion of the heart was then calculated as the difference between the maximum and minimum points on the average curve.



a)



b)



c)

Figure 4-7 – (a) The background corrected counts per pixel (CPP) for each detector measured on phantom images and normalised to detector 8, Δ - lateral detectors, O - ventral detectors. (b) The numbering convention of detectors. (c) The detectors used for patient motion estimation are highlighted by red boxes.

Parts of this section are reproduced with permission of Springer from Redgate, Barber et al. (2016). © American Society of Nuclear Cardiology 2016.

4.5.2 – Three-Dimensional Registration

The parameters used for the three-dimensional technique were optimised by varying the smoothing values between 0-6, the node spacing between 1-6 and using a variety of masks drawn around the heart at different distances from the edge of the myocardium. A selection of registrations of reconstructed 30s images were performed and the errors on the registrations compared for the different parameters.

The results showed that the errors on the technique are broadly insensitive to the registration parameters; differences due to smoothing were <0.4mm and differences due to node spacing were <0.2mm. A loose mask was preferable. A rigid registration, smoothing values of 2 and a node spacing of 4 provided the most encouraging results. Consequently, these were used, along with a loose mask drawn around the heart that excludes sub-diaphragmatic activity. The motion during the study can be calculated as the difference between the maximum and minimum points on the motion curve. The error associated with this measurement will be a combination of the errors on each point³. In order to minimise measurement errors, motion on the study was determined by identifying the maximum and minimum points on the motion curve and then performing a second registration of the images at the maximum and minimum points to estimate the magnitude of the motion.

4.5.3 – Motion Correction

Motion correction was achieved in the software by adding the registered reconstructed images, to produce an image with patient motion removed.

4.6 – Summary

At the start of this study there were no methods of estimating patient motion on the DNM 530c. Two methods for motion estimation have been presented and it has been demonstrated that the errors are sufficient to measure patient motion. It has

³ Combination of errors states: $(\Delta a)^2 = (\Delta b)^2 + (\Delta c)^2$, where a represents the measurement of motion and b and c represent the errors on the points in the motion curve. In this situation the errors on b and c will be equal, therefore the error on a is $\sqrt{2}(\Delta b)$. If the maximum and minimum points on the motion curve are registered the error on the measurement of motion is Δb .

also been demonstrated that both techniques are not suitable for respiratory motion estimation. Due to the higher frequency of respiratory motion compared to patient motion, shorter image durations are required for motion estimation, which results in increased noise on the individual images and larger registration errors. Unlike Anger cameras where shifts measured on the detectors are equivalent to shifts of the patient, the pinhole collimation used by the DNM 530c results in scaled measures of motion. Scaling factors and their associated errors have been estimated for the centre of the QFOV for all detectors. From this point onwards these are assumed to be independent of the position of the heart in the QFOV. Software has been developed to implement these techniques, along with motion correction.

5 – Patient Motion Estimation and Correction: Phantom Validation and Patient Application

5.1 – Introduction

Section 4.2 introduced the method proposed to perform motion estimation. Section 4.4 evaluated the errors on the planar and three-dimensional techniques by shifting images that had already been acquired. The results were used to inform software development, however there are many factors that will influence motion estimation when motion is actually present on the imaging system. This chapter will therefore evaluate the performance of the patient motion estimation and correction techniques, using the developed software, when motion is simulated on a phantom study and apply these techniques to patient data to assess motion during clinical studies. The number of studies affected by patient motion is critical to provide an evidence base for departments performing MPI and for guidance documents. Incorporation into clinical practice will depend on the additional workload associated with motion estimation and correction balanced against the number of patients that will benefit.

5.2 – Phantom Evaluation

5.2.1 – Method

The planar and three-dimensional motion estimation techniques presented in the previous chapter, and the motion correction software, were applied to phantom simulations with motion in 5mm increments in the Z direction and 10mm increments in the X and Y directions for all types of simulated motion, step, creep and bounce, as described in section 3.6.

Parts of this section are reproduced with permission of Springer from Redgate, Barber et al. (2016). © American Society of Nuclear Cardiology 2016.

Error Assessment: The motion measured by the software was compared to the simulated motion, table 3.3, and the mean absolute errors were compared between the planar and three-dimensional techniques

Effect of Motion Correction: Section 3.6 characterised the effect of motion on phantom images both quantitatively, through calculation of the TPD value, and qualitatively, through blinded reporting of the images. Blinded reporting displayed images with simulated step motion as the stress study and the original (reframed and summed) images without motion as the rest study. Experienced reporters were asked to identify areas of reduced perfusion and reversibility. The quantitative and qualitative analysis was repeated for the simulations in table 5.1 after motion correction. The results were compared to the results from the images prior to motion correction to characterise the number of motion artefacts that are removed using this technique.

Direction	Motion	Magnitude of Motion Simulated (mm)
Z	Step	5, 10, 15, 20
	30s	5, 10, 15, 20
	Bounce 60s	5, 10, 15, 20
	90s	5, 10, 15, 20
	Creep	5, 10, 15, 20
X	Step	10, 20
	30s	10, 20
	Bounce 60s	10, 20
	90s	10, 20
	Creep	10, 20
Y	Step	10, 20
	30s	10, 20
	Bounce 60s	10, 20
	90s	10, 20
	Creep	10, 20

Table 5.1 – A subset of the phantom simulations discussed in section 3.6, table 3.3, were used to evaluate the errors on the motion estimation and correction software.

Parts of this section are reproduced with permission of Springer from Redgate, Barber et al. (2016). © American Society of Nuclear Cardiology 2016.

5.2.2 – Results

Error Assessment: Figure 5-1a shows the errors on the shifts measured by the patient motion estimation software in the Z direction. The mean absolute errors were 0.7 ± 0.4 and 0.6 ± 0.4 mm, and the maximum errors were 1.5 and 1.9 mm (which were both for 20mm creep motion), for the planar and three-dimensional techniques respectively. In the X direction, the errors were 0.1 ± 0.1 and 0.6 ± 0.5 mm with maximum errors of 0.2 and 1.6 mm for the planar and three-dimensional techniques respectively. In the Y direction the errors were 1.9 ± 1.5 and 0.9 ± 0.7 mm and the maximum errors were 4.1 and 2.3 mm for the planar and three-dimensional techniques respectively. Figure 5-1b shows the measured shifts plotted against the applied shifts for all the images with simulated Z motion. The average differences between the two methods (three-dimensional - planar) were -0.2 ± 0.6 , 0.1 ± 0.7 , and 1.3 ± 2.0 mm; and the maximum differences were -1.7, 1.6, and 4.0 mm in the Z, X, and Y directions, respectively. There was no statistically significant difference between the two methods in any direction ($P = .119$, $P = .542$, $P = .078$). The errors when no motion was present on the images were 0.1 ± 2.1 mm and -0.4 ± 1.2 mm for the planar and three-dimensional techniques respectively.

Motion Correction – Quantitative Analysis: Figure 5-2 shows the calculated TPD values before and after motion correction. The TPD values before correction varied between 0 and 32%, depending on the type and magnitude of the simulated motion. For 39/40 simulations the TPD values after motion correction were $\leq 5\%$. Figure 5-3a shows successful correction of the motion artefacts for 1.5mm Z step motion. For this study, motion correction reduced the TPD value from 21% to 1% and perfusion in the anterior and inferior wall visually improved after correction; this was characteristic of all the motion corrected studies. For 90s bounce motion of magnitude 20mm in the Y direction, the TPD value before correction was 14% and the TPD after correction was 7%; vertical long axis slices for this simulation are shown in figure 5-3b.

Motion Correction – Qualitative Analysis: On the images before application of the motion correction algorithm the consensus reports identified 10 studies that had motion artefacts, table 3.4. The motion correction algorithm visually removed 9/10 motion artefacts. The study that was not fully corrected was 12mm Z motion and this

Parts of this section are reproduced with permission of Springer from Redgate, Barber et al. (2016). © American Society of Nuclear Cardiology 2016.

was described as a “*small area of minor reversibility*”, figure 5-4a. The motion correction algorithm introduced one additional subtle artefact in the mid infero-lateral wall for 6mm Z motion, figure 5-4b. Table 5.2 shows that motion correction reduced the number of images where motion improved the appearance of the basal infero-lateral wall from 6 and 8 studies before motion correction to 2 and 4 studies after motion correction, for reporters 1 and 2 respectively. There were no instances where an infero-lateral difference was identified on the motion corrected image that was not identified by at least one of the reporters on the images prior to motion correction.

		Basal Infero-Lateral Wall on this Image Improved Compared to Image with no Motion			
		Image with Simulated Motion		Motion Corrected Image	
Direction	Step Motion (mm)	Reporter 1	Reporter 2	Reporter 1	Reporter 2
Z	6		Y		
	8	Y	Y		
	10	Y	Y		
	12	Y	Y		
	14		Y	Y	
X	10		Y		Y
	14	Y			
Y	6	Y		Y	Y
	12		Y		Y
	14	Y	Y		Y

Table 5.2 – Images identified as appearing to have improved perfusion at stress (simulated motion or motion corrected image) compared to the rest image (no motion).

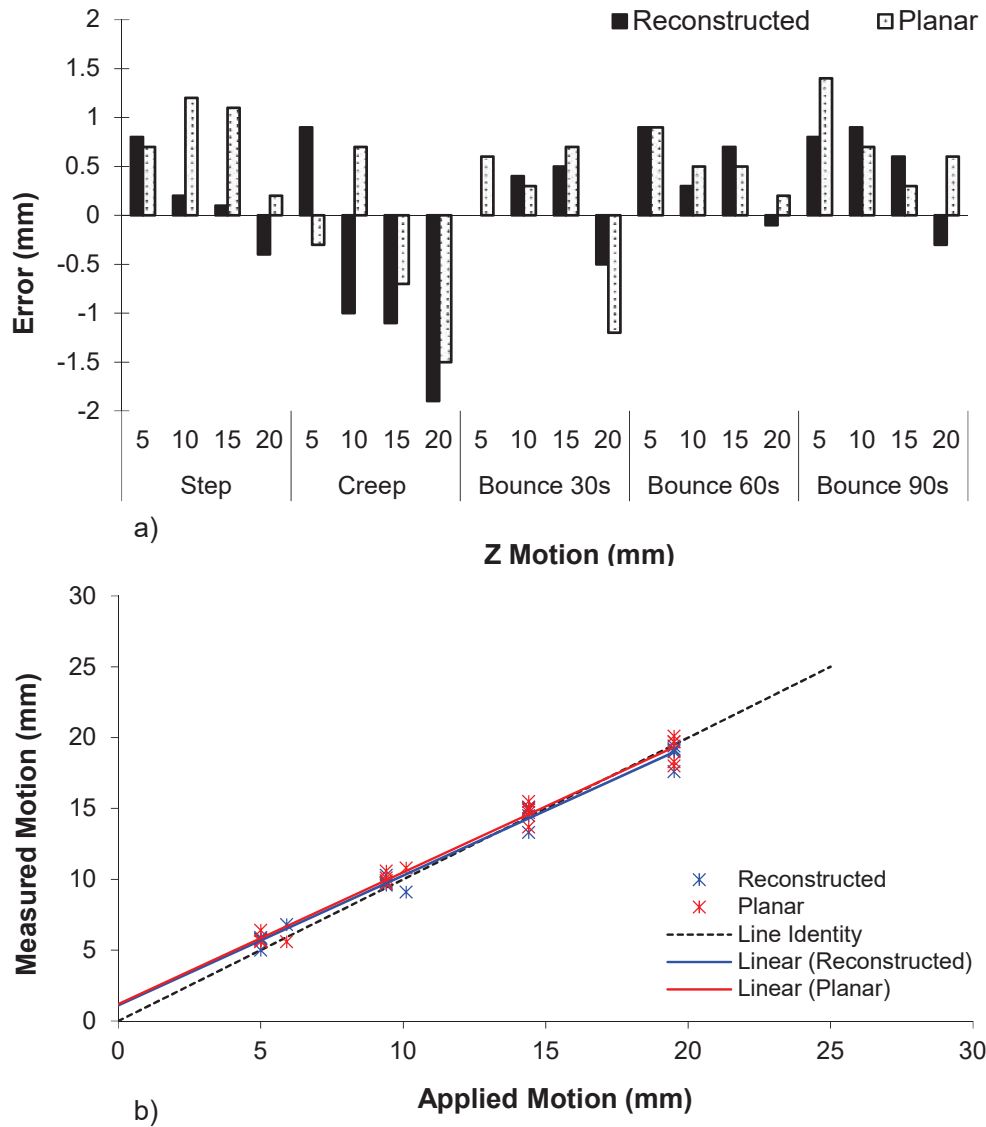


Figure 5-1 – (a) The errors on the measured Z motion on phantom simulations for the two methods of motion estimation and (b) the measured motion using both techniques plotted against the applied motion for simulations with Z motion.

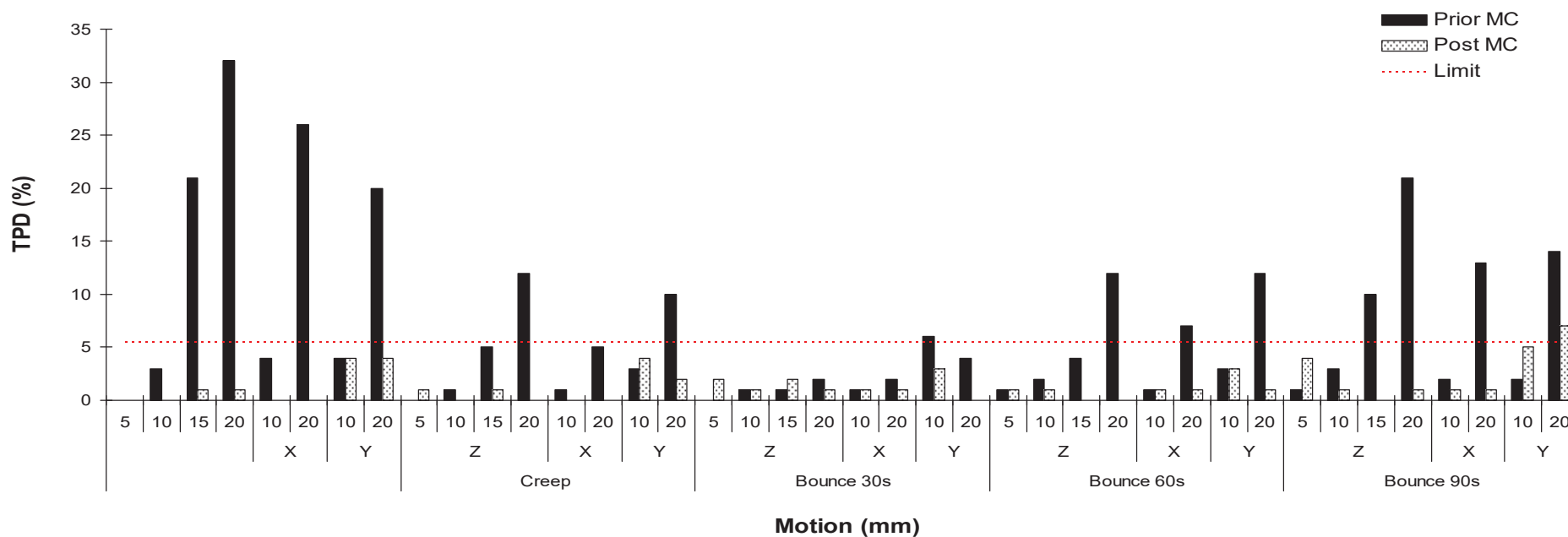


Figure 5-2 – The TPD values for the phantom simulations with motion, before and after application of the motion correction algorithm. --- Represents the cut off limit of a TPD $\geq 5.5\%$ used to identify significant motion artefacts. MC – motion correction.

Parts of this section are reproduced with permission of Springer from Redgate, Barber et al. (2016). © American Society of Nuclear Cardiology 2016.

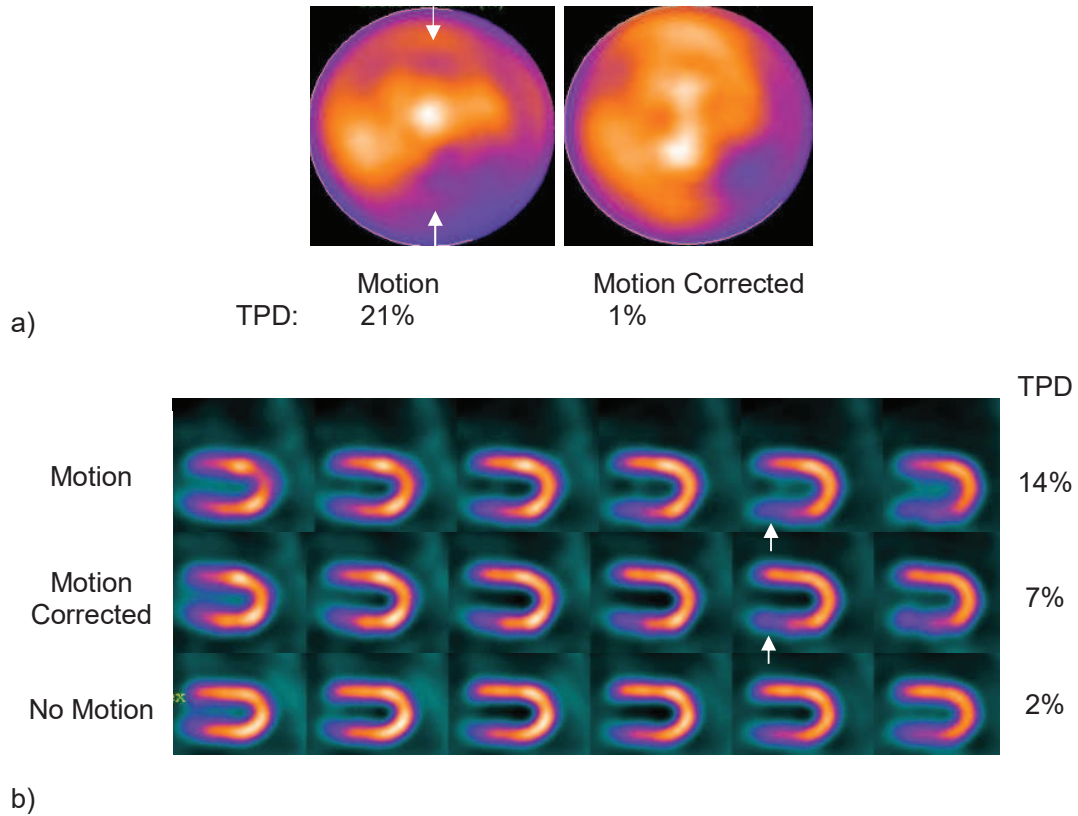


Figure 5-3 – (a) Polar plots for 15mm step Z motion, before and after motion correction, the arrows indicate motion artefacts that are corrected following motion correction. (b) Vertical long axis slices for 20mm Y 90s bounce motion, before and after motion correction, and the stationary acquisition acquired at the baseline Y position ($X = 20\text{mm}$, $Y = 0$, $Z = 0$). This is the only study where motion correction did not reduce the TPD value to $\leq 5.5\%$ and the images have residual motion artefacts on the motion corrected image in the inferior-basal wall, as indicated by the arrows.

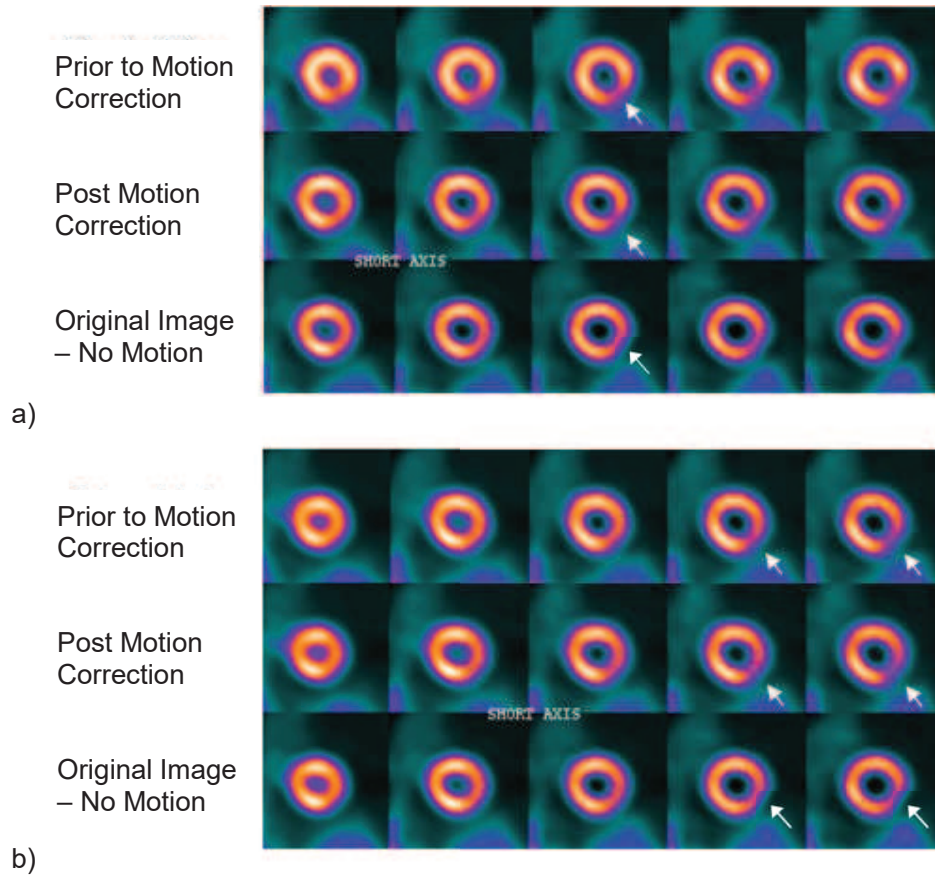


Figure 5-4 – (a) Phantom images with 12mm simulated Z motion before and after motion correction, the arrows highlight the area that was identified as a motion artefact; this was the only study where the artefact was not fully corrected by the motion correction software. (b) Phantom images with 6mm simulated Z motion before and after motion correction, compared to the phantom image with no motion; the arrows highlight the artefact introduced by motion correction (see the discussion for further analysis of this artefact).

5.2.3 – Discussion

To simulate Z motion the camera couch was moved, figure 3-8a. The indicative position of the couch is shown on the camera, however the actual couch position is stored in the image header. The values in the image header can therefore be used to calculate an accurate value for the simulated shift. The maximum difference

Parts of this section are reproduced with permission of Springer from Redgate, Barber et al. (2016). © American Society of Nuclear Cardiology 2016.

between the simulated shift, calculated from the indicative positions and actual position in the image header was 1mm. For X and Y motion the gantry and the bed were moved, figure 3-8b,c. The indicative gantry position and angle, and the indicative bed height are shown on the camera. The actual position and angle of the gantry are stored in the header, however the table height is not stored. Therefore, only errors on the Z and X motion give an accurate reflection of the errors on the technique; the errors calculated for the Y direction may include systematic errors due to the difference between the indicative bed height and actual height. In addition, when simulating motion in the X direction the heart may not have been returned to exactly the same Y position after the gantry was moved out. Z motion errors are the most relevant errors as patient motion has been found to be most dominant in the Z direction (Cooper et al., 1992). The absolute errors in the Z direction were 0.7 ± 0.4 and 0.6 ± 0.4 mm for the planar and three-dimensional techniques respectively, which are both sufficient to measure patient motion with an order of magnitude of 10mm.

Figure 5-1a shows the errors for each type of motion, demonstrating the largest negative errors for creep motion. The motion present on the study is calculated from the difference between the maximum and minimum points of the motion curve. If there are twelve 30s images in a scan, for step motion there will be 6 maximum points and 6 minimum points, all with associated measurement errors and the software will select the extreme maximum and minimum. For creep motion there will only be one point at the maximum and minimum points as the other points will lie in-between and the software can only select these two points. The overall effect of this is that the more maximum and minimum points the software has to select from, the higher the measured motion will be.

Combining all types of motion and plotting the motion measured against the magnitude of the motion shows that for both the planar and three-dimensional techniques, figure 5-1b, the measured motion is slightly larger than the simulated motion for motion <10mm, however in the range 10-20mm, which contains motion that can have a significant effect on MPI images, there is good agreement between the applied and measured shifts. The equation of trend lines fitted to the data between 10-20mm were $y = 0.92x + 1.1$ ($R^2 = 0.97$) and $y = 0.81x + 2.74$ ($R^2 = 0.90$) for the planar and three-dimensional techniques respectively.

Parts of this section are reproduced with permission of Springer from Redgate, Barber et al. (2016). © American Society of Nuclear Cardiology 2016.

No significant difference was found between the errors on the measured motion for the two methods of motion estimation. There are practical advantages and disadvantages between the planar and three-dimensional techniques. The planar technique has the advantage of being easy to use routinely, as no reconstruction is required and reframing the acquisition is straightforward. The three-dimensional technique involves reconstructing the reframed data which can only be done two images at a time, which could add a significant burden to the post processing workload of MPI studies, if applied to every patient passing through the department. The disadvantage of the planar technique is that additional errors are introduced due to the uncertainties associated with the scaling factors used to convert the measured shift into the true shift of the heart, table 4.1, section 4.3. The advantages of the three-dimensional technique are that the shifts measured from the registration are direct measures of patient motion, therefore the method does not require scaling factors and is independent of the position of the heart in the QFOV and motion correction can be performed at the same time. Once the series of images (planar or three-dimensional) have been transferred to the Link Medical workstation, the only manual intervention required for both techniques is the generation of registration masks to exclude sub-diaphragmatic activity. Both methods can provide a visual display of motion to support the measurements; for the two-dimensional technique this is a cine of the 30s reframed projection images and for the three-dimensional techniques this is a cine of the reconstructed 30s images.

The three-dimensional motion estimation technique has the potential to be fully automated, however this would involve adaptations that are not possible locally, but that could be made by the manufacturers of the system. Thirty second images could be reconstructed '*on the fly*' during the acquisition. The DNM 530c camera already has the capability to automatically reconstruct and transfer images. Also, standard cardiac processing, which is performed for every patient before they leave the department involves generation of a region around the heart. If this could be used as the registration mask, no additional regions would need to be generated by the operator.

It has been demonstrated both quantitatively and qualitatively that motion correction is successful on the phantom studies. The study where the TPD value was not

reduced to $\leq 5.5\%$ following motion correction was 20mm 90s Y bounce motion, figure 5-3b, which shows improved contrast of the LV cavity following motion correction, however when compared to an image at the baseline Y position with no motion there is some residual artefact remaining in the infero-basal wall. There was one instance where the motion artefact was still identified after motion correction, 12mm Z motion, figure 5-4a. Motion correction removed some of the blurring on the image as demonstrated by the improved contrast of the LV cavity, however it did not completely remove the infero-lateral motion artefact, which may in part be a result of differences in the perfusion pattern as the position in the QFOV changes, as Y motion had to be simulated closer to the edge of the QFOV due to the physical limitations of the camera. The difference was described as “a small area of minor reversibility” and in a clinical context this difference is unlikely to be significant. The case where the motion correction algorithm introduced a subtle artefact in the mid infero-lateral wall for 6mm Z motion, figure 5-4b, demonstrates the issue of consistent reporting for subtle differences. When reviewing the images together there does not appear to be any difference between the images prior to and post motion correction, with a subtle difference observed between these images and the original image. During randomised reporting, both reporters reported no significant difference between the original images and the images with motion. When the original images were compared to the post motion correction images one reporter identified a difference and one report concluded there was no significant difference, however at the consensus report it was agreed there was a subtle difference. This demonstrates that the software has not introduced an artefact it is just that there is a subtle, most likely clinically insignificant difference between the images that is at the limit of what reporters identify as significant. The reporters may have acclimatised to reporting good quality phantom studies during qualitative analysis of the images and it is doubtful whether this degree of difference would have been classified as abnormal on patient images.

The number of cases where the infero-lateral wall appeared improved on the stress image (with motion) compared to the rest image (no motion) reduced post motion correction, table 5.2. It is suggested in section 3.6.3 that infero-lateral differences could be due two things:-

- 1) Areas of reduced perfusion overlapping with adjacent areas of improved perfusion or increased overlap with the liver as the heart moves.
- 2) A change of the position of the heart in the QFOV as the patient moves.

Correction of these artefacts supports suggestion 1, as alignment of the images during correction will minimise overlap of the heart with adjacent structures. The fact that not all the artefacts are corrected supports suggestion 2 as any changes in the perfusion pattern due to the position of the heart in the QFOV would not be corrected by aligning the images.

5.2.4 – Conclusion

On phantom simulations the size of the errors for both the planar and three-dimensional techniques compared to the signal being measured enable successful estimation of patient motion on the DNM 530c. The motion correction technique successfully reduces the TPD values and visually reduces or removes motion artefacts.

5.3 – Application to Patient Studies

5.3.1 – Patient Cohort

Forty patient studies were selected for patient motion estimation. This group consisted of 15 females, average weight 81.8kg (range 60 - 115kg) and 25 males, average weight 91.1kg (range 71-136kg). Thirty-eight of the studies consisted of stress and rest imaging and two studies had normal stress images therefore negating the need to perform rest imaging. Fourteen studies were affected by sub-diaphragmatic activity and therefore underwent delayed repeat imaging. Of these, five studies had both the stress and rest imaging repeated, five studies had stress imaging repeated, three studies had rest repeated and one study had the rest imaging repeated twice. This resulted in a total of 20 repeat images. The stress images (original and 1 repeat) for patient 17 were excluded from the analysis as the

imaging time for the study had to be increased to compensate for an extravasated injection. This resulted in 96 MPI images, from 40 patients.

5.3.2 – Method

The planar and three-dimensional motion estimation techniques developed in chapter 4 were applied to the myocardial perfusion images. Chapter 3 demonstrated that $\geq 10\text{mm}$ of motion introduces localised reductions in perfusion that mimic true perfusion defects. Section 4.4 determined the errors on the registration of individual planar and reconstructed 30s images to be $0.5 \pm 0.3\text{mm}$ and $0.5 \pm 0.3\text{mm}$ respectively and chapter 5 determined the errors on the Z motion measurements by the final software, which combines measurements from different detectors, to be 0.7 ± 0.4 and 0.6 ± 0.4 mm for the planar and three-dimensional techniques respectively. Taking this into consideration any patients with measured motion $\geq 8\text{mm}$ using either technique were identified as having the potential for motion artefacts. These images were motion corrected and presented as a stress – rest study; the image with motion as the stress image and the motion corrected image as the rest image. Two experienced reporters were asked to identify differences between the studies and any differences were reported as significant motion artefacts.

5.3.3 – Results

The distribution of motion as measured using registration of reconstructed images is shown in figure 5-5a. For Z motion 61%, 35% and 3% of images had 0-4mm, 4 - 8mm and $\geq 8\text{mm}$ motion respectively. The results when motion was measured from the planar images were very similar with 59%, 34% and 4% of images having 0-4mm, 4 - 8mm and $\geq 8\text{mm}$ motion respectively. No images using either technique had $\geq 8\text{mm}$ motion in the X and Y directions. There is a statistically significant difference between motion measured in different directions as determined by one-way ANOVA ($P < 0.001$). Motion in the Z direction was significantly larger than motion in the X ($P < 0.001$) and Y ($P < 0.001$) directions. Motion in the Y direction was significantly larger than motion in the X direction ($P = 0.03$). The mean difference ($\pm 1\text{SD}$) between the Z patient motion measured using the two techniques was $-0.2 \pm 1.1\text{mm}$ and the maximum difference was 3.1mm. This was not statistically significant ($P =$

Parts of this section are reproduced with permission of Springer from Redgate, Barber et al. (2016). © American Society of Nuclear Cardiology 2016.

0.150). Figure 5.5b shows the motion measured using both techniques for a patient that did not demonstrate significant motion.

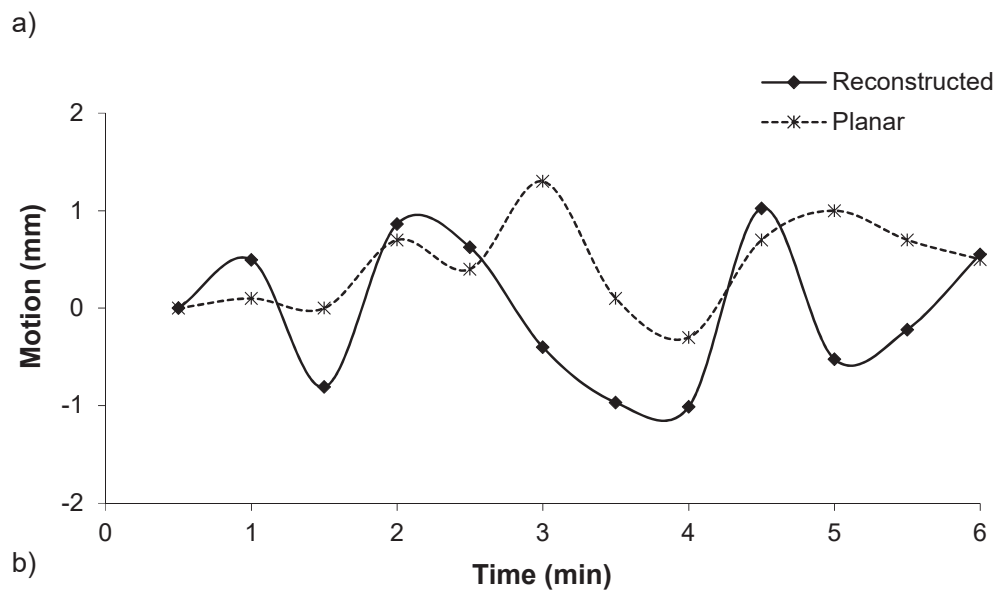
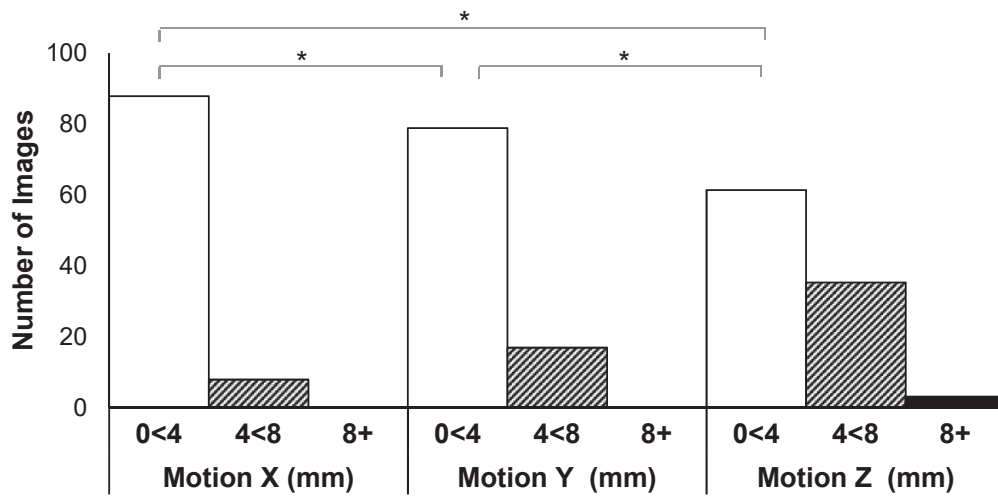


Figure 5-5 – (a) Motion measured on 96 patient images using the three-dimensional technique, * statistically significant difference and (b) motion measured for a patient that did not demonstrate significant motion.

Parts of this section are reproduced with permission of Springer from Redgate, Barber et al. (2016). © American Society of Nuclear Cardiology 2016.

Patient Study	Image	Direction	Planar Technique (mm)	Three-Dimensional Technique (mm)	Difference Identified between Image with Motion and Motion Corrected Image
6	Rest	Z	9.7	10.2	No significant difference
7	Rest	Z	10.7	10.3	Inferiorly and anteriorly
13	Stress	Z	9.1	12.2	Antero-basally
25	Stress	Z	9.0	6.7	No significant difference

Table 5.3 – The studies that were identified to have $\geq 8\text{mm}$ motion identified by either the planar or three-dimensional technique.

Four patient studies (10%) were identified as having at least 1 myocardial perfusion image (stress, rest or repeat) with $\geq 8\text{mm}$ motion. The motion measured on the images is shown in table 5.3. Graphs of the motion measured using both techniques and the motion and motion corrected images for all four patients are shown in figure 5-6, figure 5-7, figure 5-8 and figure 5-9. Analysis of the images by experienced reporters identified significant differences between the images with and without motion correction for 2 studies (5% of the cohort).

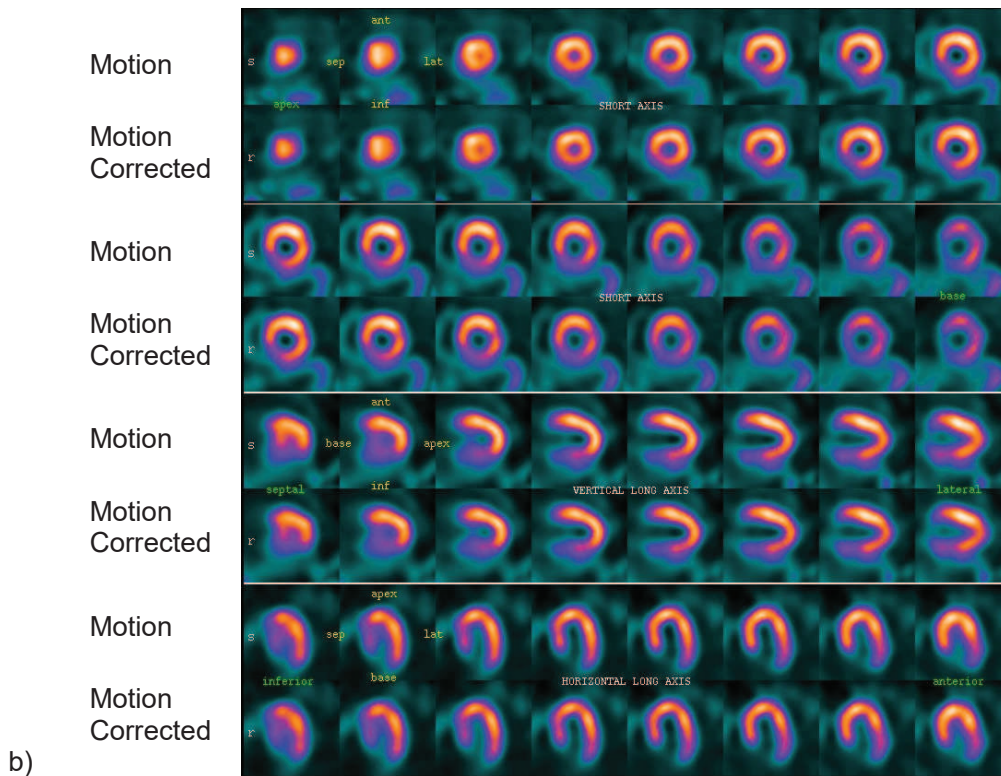
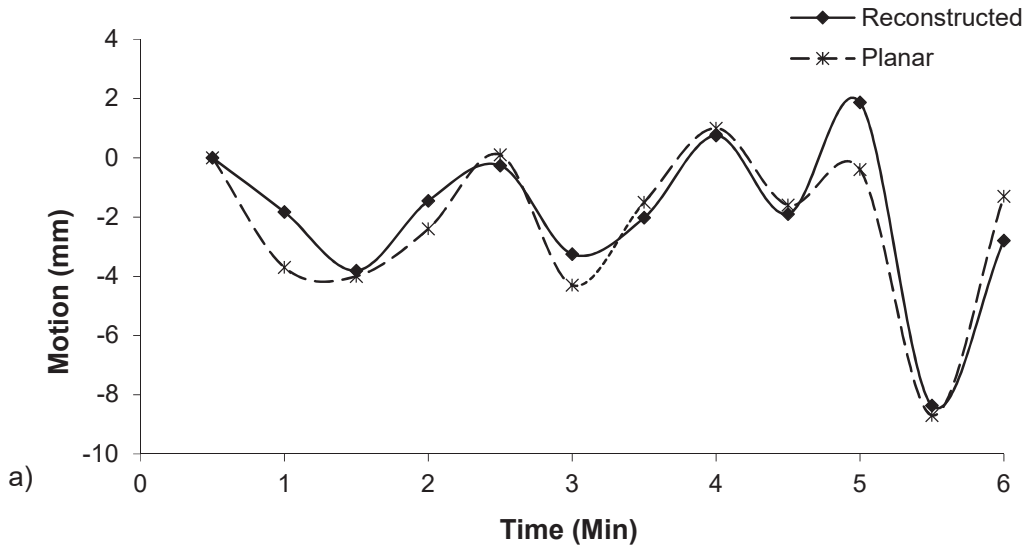
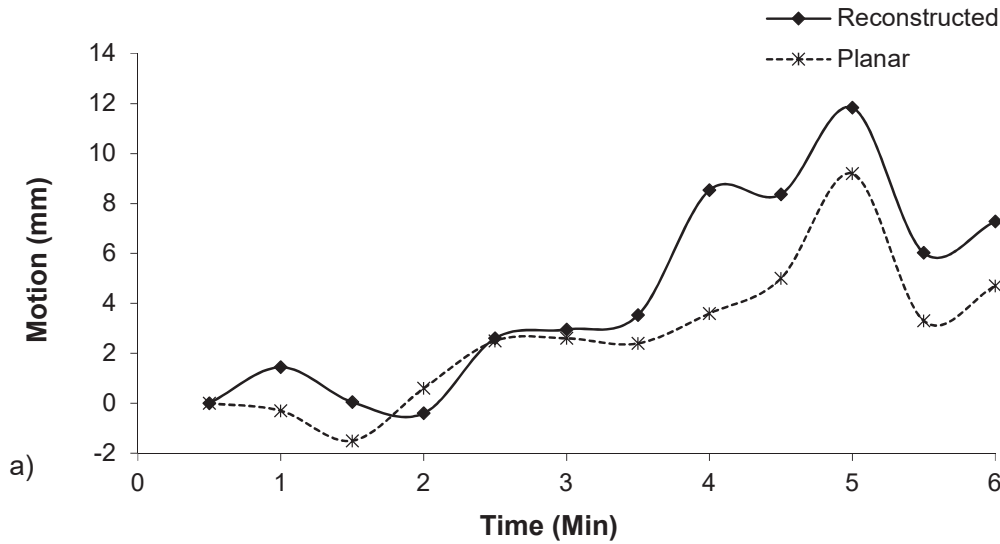
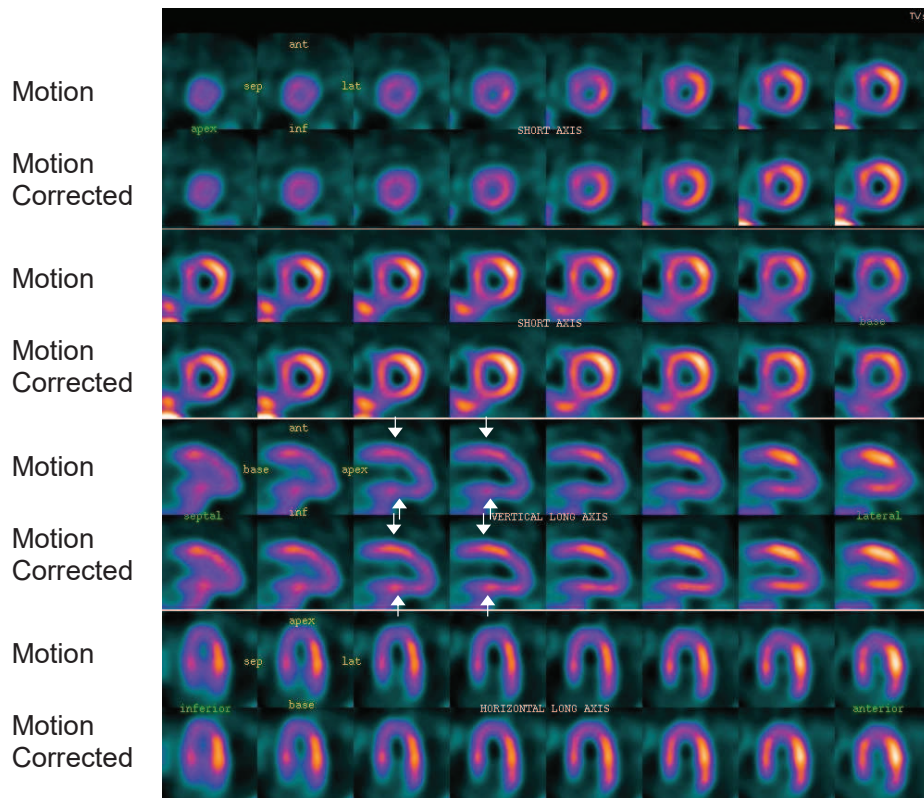


Figure 5-6 – Patient 6 rest study. (a) Motion measured in the Z direction using the planar and three-dimensional techniques and (b) a comparison of the motion and motion corrected images.

Parts of this section are reproduced with permission of Springer from Redgate, Barber et al. (2016). © American Society of Nuclear Cardiology 2016.



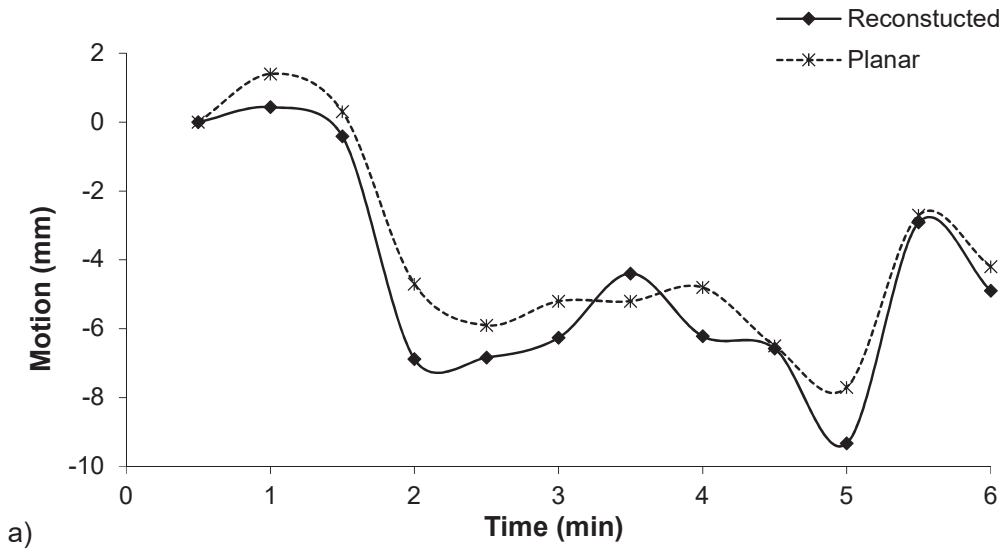
a)



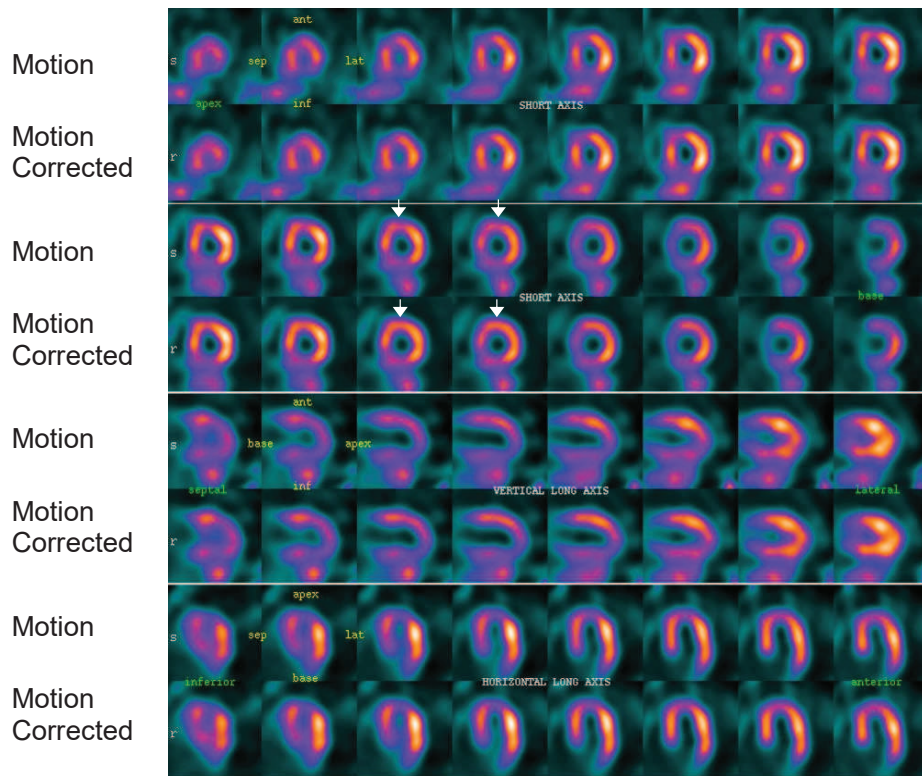
b)

Figure 5-7 – Patient 7 rest study. (a) Motion measured in the Z direction using the planar and three-dimensional techniques and (b) a comparison of the motion and motion corrected images, the arrows show areas of reversibility identified by the reporters.

Parts of this section are reproduced with permission of Springer from Redgate, Barber et al. (2016). © American Society of Nuclear Cardiology 2016.



a)



b)

Figure 5-8 – Patient 13 stress study. (a) Motion measured in the Z direction using the planar and three-dimensional techniques and (b) a comparison of the motion and motion corrected images, the arrows show areas of reversibility identified by the reporters.

Parts of this section are reproduced with permission of Springer from Redgate, Barber et al. (2016). © American Society of Nuclear Cardiology 2016.

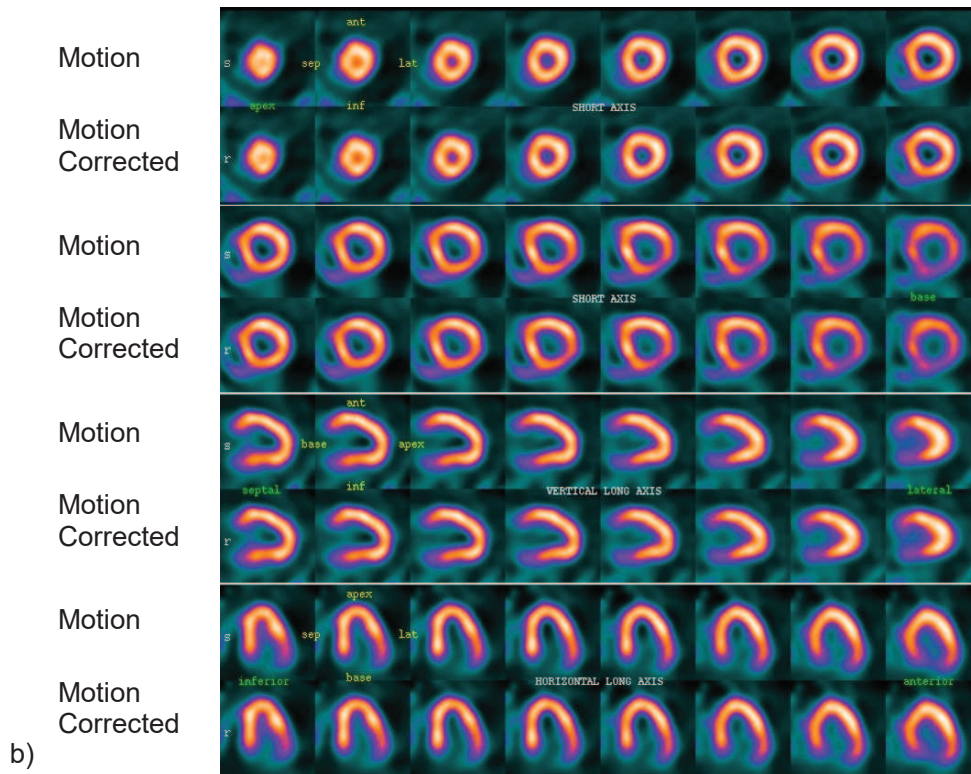
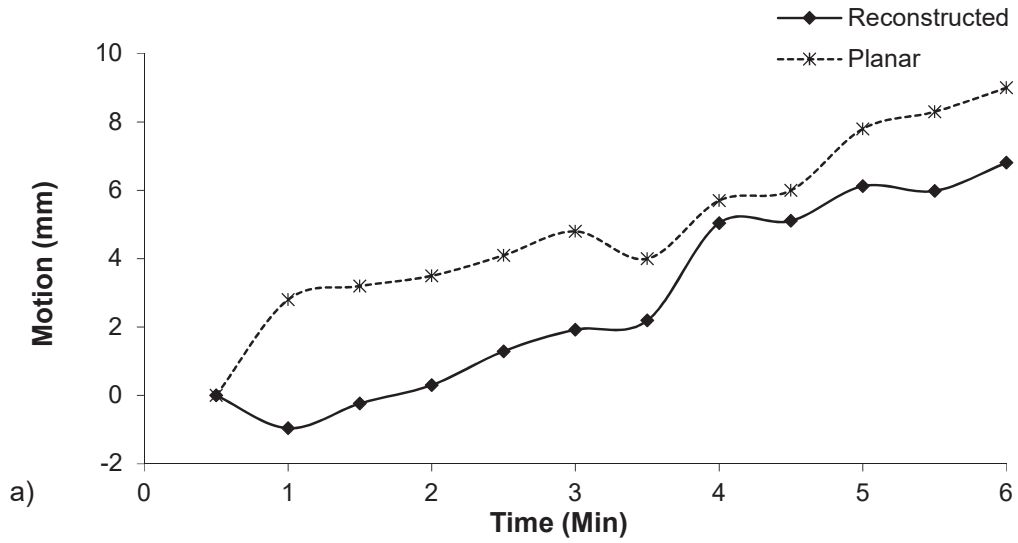


Figure 5-9 – Patient 25 stress study. (a) Motion measured in the Z direction using the planar and three-dimensional techniques and (b) a comparison of the motion and motion corrected images.

Parts of this section are reproduced with permission of Springer from Redgate, Barber et al. (2016). © American Society of Nuclear Cardiology 2016.

5.3.4 – Discussion

Applying the motion estimation techniques to patient data has shown that in our patient cohort motion only reaches magnitudes that can cause significant motion artefacts in the Z direction, figure 5-5. No significant motion (>8mm) was identified in the X and Y directions on any patient studies. It may therefore not be necessary to routinely assess motion in other directions. Only assessing Z motion would reduce the information available for review, simplifying the decision making process. However, 40 patients is not a large enough sample to conclude that motion in the X and Y directions will never occur and there is no disadvantage in terms of operator processing time to performing motion estimation in all three planes.

Four patients were identified as potentially having motion artefacts ($\geq 8\text{mm}$). There may appear to be discrepancies in the magnitude of the motion between the graphs, figure 5-6a, figure 5-7a, figure 5-8a and figure 5-9a, and table 5.3, for example, the motion measured on patient 13 using the three-dimensional technique was 12.2mm, however the difference between the maximum and minimum values on the graph, figure 5-8a, is 9.7mm. This is because the technique that registers the reconstructed images initially generates the curve and then performs a second registration of the images at the maximum and minimum points on the curve to determine the final measure of motion.

Out of these four patients, patient 6 and patient 25 had no significant differences between the images before and after motion correction. Figure 5-6a shows that the motion present on patient 6 resembles bounce motion approximately 30s in duration. The lack of motion artefacts for motion of this type is consistent with the results in chapter 3 which found that bounce motion $\leq 30\text{s}$ is insignificant. The reason no motion artefact was identified on patient 25, figure 5-9, is thought to be due to the actual motion being <10mm. A conservative limit of 8mm has been used to identify patients with potential artefacts and the motion measured was 9mm using the planar motion estimation technique and only 6.7mm using the three-dimensional technique, which suggests that the actual motion is <10mm and therefore insignificant.

Parts of this section are reproduced with permission of Springer from Redgate, Barber et al. (2016). © American Society of Nuclear Cardiology 2016.

The two studies where motion artefacts were identified had patterns of motion that affected multiple frames (≥ 60 s), figure 5-7a and figure 5-8a, again agreeing with the phantom simulation results in chapter 3 that found motion artefacts were significant for motion $\geq 17\%$ of the acquisition. After motion correction the perfusion appears improved anteriorly and inferiorly for these studies, which is consistent with motion artefacts expected from cranio-caudal patient motion (Kennedy and Strauss, 2016).

On patient studies the difference between the techniques for motion measured in the Z direction was 0.1 ± 1.5 mm, which is similar to the difference measured on the phantom simulations of -0.2 ± 1.1 mm. This was not statistically significant ($P = 0.150$). The phantom images were all central in the QFOV, whereas for patient studies there will have been a greater variation in position in the QFOV depending on the patient's body habitus.

The preferred technique for motion estimation routinely would be the three-dimensional motion estimation technique, due to direct measurement of motion and the ability to perform motion correction; however, the practical limitations of this have been discussed. There were no significant differences between the motion measured using the planar motion estimation technique and three-dimensional motion estimation techniques on the patient images and all the patients with significant motion artefacts were identified by both techniques. The planar motion estimation technique is therefore a suitable and practical alternative for measurement of patient motion. If the planar motion estimation technique were to be applied clinically, 10% of patients would be identified as having potential artefacts (≥ 8 mm) and no motion corrected image would be available. These patients could however be rescanned to get a motion free image. A rescanning rate of 1 in 10 patients should not add a significant burden to clinical scheduling. If motion was still present on repeat imaging, three-dimensional motion estimation could be applied or at the very least the reporting clinician would be aware of the presence of motion and could take this into account during reporting

It has been speculated in many review documents (Garcia and Faber, 2009) that patient motion will be reduced on this system due to increased comfort and shorter imaging times. A previous study demonstrated that 10% of patients imaged for 4

minutes on the DNM 530c have ≥ 12 mm patient motion, suggesting at least 10% of scans could have significant motion artefacts. This work has demonstrated that the proportion of our patients passing through the department that are affected by motion artefacts is 5%. This supports the need for routine assessment of patient motion on the DNM 530c system.

5.3.5 – Conclusion

In our patient population significant patient motion was identified in the Z direction only. A total of 10% of patients were identified as having significant patient motion (>8 mm) and the perfusion pattern of 5% of patients changed significantly due to motion artefacts.

5.4 – Summary

This chapter has applied the patient motion estimation and correction software developed in chapter 4 to phantom simulations and has demonstrated that the techniques can successfully estimate patient motion. It has also demonstrated that motion correction improves quantification and visually removes motion artefacts. The software was applied to 40 patient studies and 5% were found to have significant motion artefacts. Routine estimation and correction of patient motion is therefore recommended on the DNM 530c.

6 – Respiratory Motion Estimation and Correction Technique

6.1 – Introduction

Section 3.8 estimated that respiratory motion artefacts will be apparent for ≥ 12 -13mm by comparing simplistic histograms of step and creep motion to a sine wave approximation of the respiratory signal. Chapter 4 demonstrated using simulations that the patient motion estimation techniques were not suitable for respiratory motion. This chapter will adapt the patient motion estimation technique for respiratory motion.

6.2 – Initial Adaptations to the Patient Motion Estimation Techniques

Patient motion estimation was investigated using both planar and three-dimensional techniques. The advantage of using reconstructed images to assess motion is that this provides a direct measure of motion that is not dependent on the position of the heart in the QFOV. It also facilitates motion correction. However, reconstructing each of the 30s images increases the processing time. It has been suggested in section 4.2 that for respiratory motion estimation the data need to be divided into ≤ 1.5 s images; for a 360s scan this is a minimum of 240 images. Reconstruction of hundreds of images is impractical; therefore, the use of planar images only is the method of choice for respiratory motion estimation.

Image registration was evaluated for motion estimation in section 4.4. The mean error (± 1 SD) associated with the registration of planar 1s images was found to be 3.2 ± 2.5 mm. Adaptations of the technique were explored to attempt to reduce the errors on the technique to a level that would facilitate respiratory motion estimation. These are briefly summarised below.

- The y motion signals from an increasing number of detectors were combined to measure the cranio-caudal respiratory motion. This demonstrated a reduction in the errors on the technique when the results from up to 6 detectors were combined. The mean error ($\pm 1SD$) was reduced to 1.4 \pm 2.1mm.
- The duration of the fixed image was increased to improve the noise characteristics of the registration. This was first tested with a phantom image unaffected by motion, the mean error ($\pm 1SD$) was reduced to 0.7 \pm 1.2mm. However, when an image summed over the entire study was used as the fixed image, as would be the case in the clinical scenario, the success of the technique was negatively affected by motion on the fixed image. An iterative approach was taken to try to gradually remove the motion on the fixed image, however this was unsuccessful.

It was not possible to reduce the error using image registration alone to a level that would facilitate measurement of respiratory motion and it was concluded that an alternative approach was required.

6.3 – Motion Estimation using Principal Component Analysis

The original technique developed for patient motion estimation used image registration to measure the motion of the heart between the images. Image registration treats each image individually, registering pairs of images to get a motion measurement for each point on the signal. The errors in the technique increase as the duration of the images decrease, as shown in figure 4-6. An introduction to principal component analysis (PCA) is provided in appendix A. The advantage of using PCA for motion estimation is that the interdependence of the images is utilised. The component images, singular values and normalised coefficients are generated through consideration of the patterns across the entire series of images.

Principal component analysis of a series of $\leq 1.5s$ images will identify component images, singular values and normalised coefficients that best represent the data. Each component image is associated with a set of normalised coefficients. The first component image and normalised coefficients are representative of the mean of the data and will be referred to as the mean component image and mean normalised coefficients, and higher order component images and normalised coefficients are representative of the variance in the data and will be consecutively numbered (for example, the first two higher order components will be referred to as the first and second component images and normalised coefficients). It is expected that the first set of normalised coefficients will represent motion on the images, however the correlation of each set of coefficients to a known signal will be investigated. PCA for motion estimation could be implemented in two ways.

- Normalised coefficients could be directly attributed to respiratory motion on the study.
- The series of images could be regenerated from a subset from the principal components, effectively smoothing the data. Image registration could then be used to measure motion between the PCA smoothed images.

From this point onwards this will be referred to as the respiratory motion estimation technique, to distinguish it from the patient motion estimation techniques developed in the previous chapter. However, it is important to highlight at this point that the motion being measured is the motion of the heart during the study and this will be a combination of both patient and respiratory motion. Patient and respiratory motion may or may not be separated out into separate components by PCA analysis.

6.4 – Initial Evaluation of the Technique

To demonstrate how the proposed technique compares to using image registration to determine the motion signal a simple simulation was performed.

6.4.1 – Method

One projection of a static 360 second phantom acquisition was divided into 20s and 1s images. These images are shown in figure 6-1. Sinusoidal motion was imposed on the images by sequentially shifting the images by a number of pixels; the magnitude of the motion was equivalent to 2cm heart motion. The motion on the images was measured using three methods;

Method 1: Image Registration (IR): The shifted images were registered to measure the motion; this is the same technique that was used for patient motion estimation in chapters 4 and 5.

Method 2: Principal Component Analysis (PCA): The normalised coefficients were used as the motion signal.

Method 3 - Principal Component Smoothing with Image Registration (PCA+IR): The mean and first two principal components were selected to generate PCA smoothed images; these were registered to measure the motion on the images.

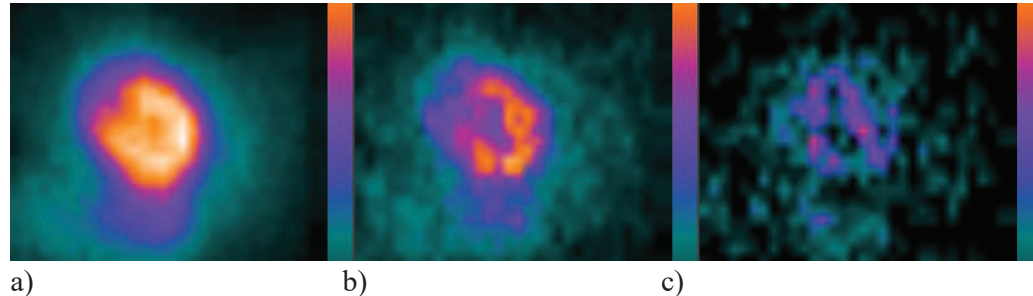


Figure 6-1 – Projection 8 of a phantom acquisition (a) 360s data, (b) 20s data and (c) 1s data.

PCA was implemented through ShIRT. The frequency of the simulated sinusoid remained constant relative to the number of images to avoid aliasing differences between comparisons (7 data points / cycle). The same region around the heart was used as the mask for image registration for the 1s and 20s images. The first image in the series was used as the reference image for registration. The units of measurement are different between methods; 1 and 3 measure the motion in mm

whereas the units for method 2 are arbitrary, therefore the signals were normalised to facilitate direct comparison and the mean square error (MSE) calculated to determine the extent to which the measured signal agreed with the simulated signal. For methods 1 and 3 the difference between the simulated and measured shifts was also calculated.

6.4.2 – Results

Figure 6-2 shows the mean, first and second normalised coefficients from the 20 second reframed images. Figure 6-3 shows the signal recovered using the three different methods for the 1 and 20 second reframed images; for method 2 the first normalised coefficients (C1) were used as the signal.

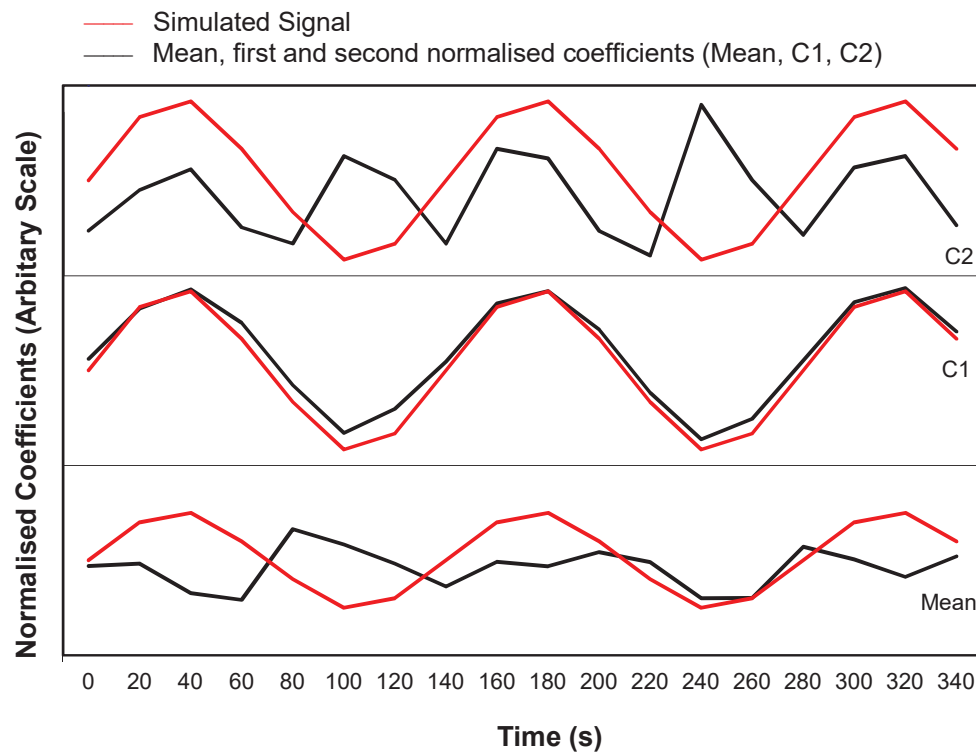


Figure 6-2 – The first 3 sets of normalised coefficients, mean, C1 and C2, generated from PCA analysis of 20s images from a phantom acquisition with simulated sinusoidal motion, compared to the motion that was simulated on the images. Note: the magnitudes of the signals have been displayed to allow comparison with the simulated motion.

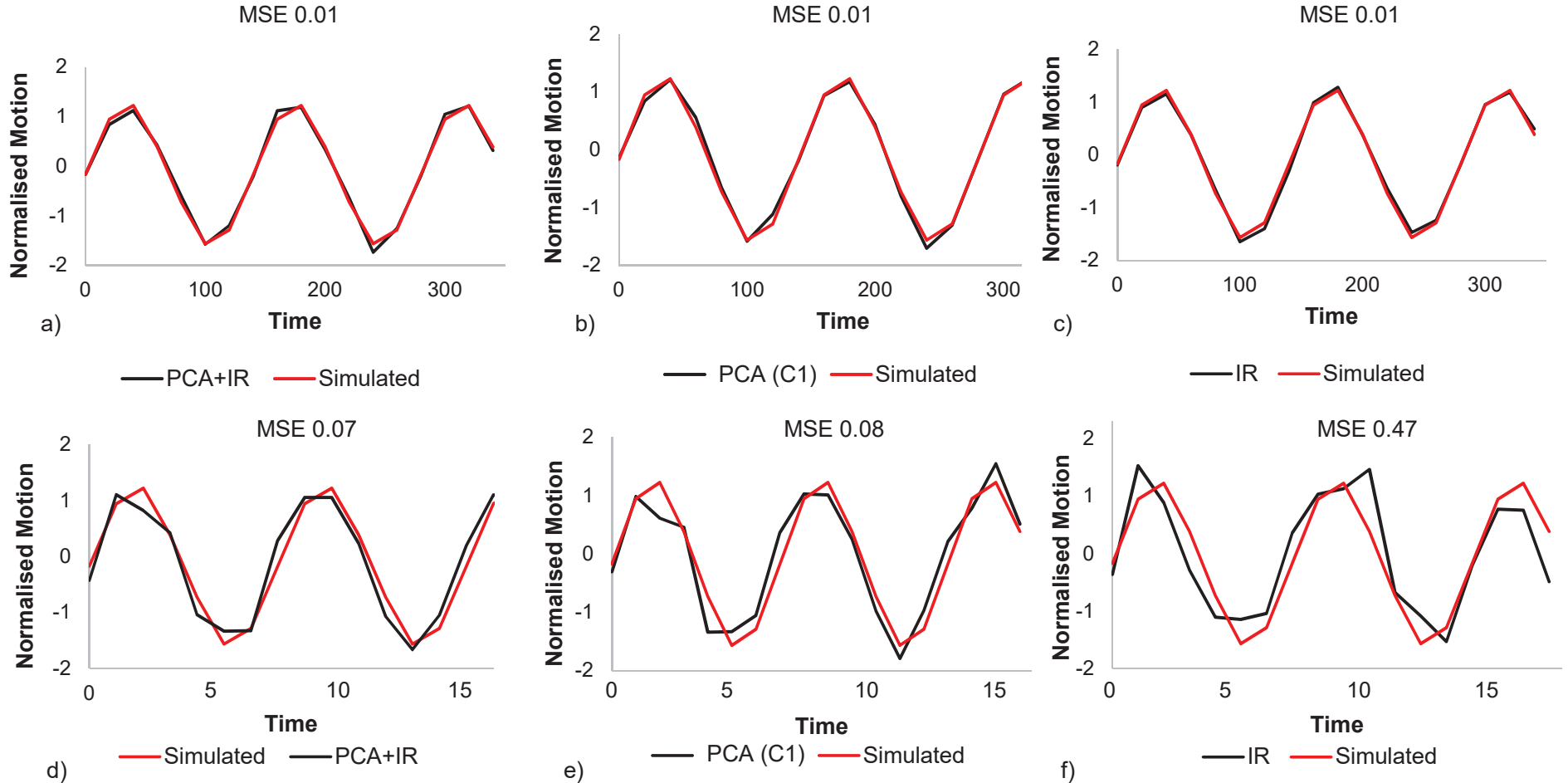


Figure 6-3 – The signals measured using three different techniques: Image Registration (IR), the first set of normalised coefficients from principal component analysis (PCA(C1)) and PCA smoothing of the images combined with image registration (PCA+IR), (a) PCA+IR 20s images, (b) PCA C1 20s images, (c) IR 20s images, (d) PCA+IR 1s images, (e) PCA C1 1s images and (f) IR 1s images. Note: only part of the signal from the 1s images has been included for comparison purposes.

6.4.3 – Discussion

Figure 6-2b indicates that the first normalised coefficients are measuring the variability of the signal due to motion on the images and these were therefore used for method 2, PCA(C1). Simple sinusoidal respiratory motion was simulated and it is not clear whether lower frequency patient motion superimposed on the signal would be measured by the same coefficient. Figure 6-3 shows that for the 20 second images which have good noise statistics, the errors from all the techniques are similar, 0.01, 0.01 and 0.01 MSE for IR, PCA(C1) and PCA+IR respectively. For 1 second images the errors from the techniques were, 0.47, 0.08 and 0.07 MSE for IR, PCA(C1) and PCA+IR respectively. The errors using the PCA techniques, PCA(C1) and PCA+IR, were significantly lower ($P < 0.01$) than the errors from image registration only. There was no significant difference ($P = 0.32$) between PCA(C1) and PCA+IR. The mean ($\pm 1SD$) absolute error was $2.0 \pm 1.4\text{mm}$ and $3.6 \pm 3.4\text{mm}$ for the PCA+IR and IR methods applied to the 1 second images respectively. This can be compared to an error of $3.2 \pm 2.5\text{mm}$ for image registration only in section 4.4 using a similar technique.

The advantage of using PCA(C1) is that respiratory motion, which could shift the images in three dimensions, would be represented by one signal, thus making full use of the information that is available. The advantage of using PCA+IR is that the direction of the motion relative to the heart can be determined and the magnitude of the motion can be measured. Based on the results from the 20s images there would be no advantage to changing the technique used for patient motion estimation to include PCA.

6.4.4 – Conclusion

This simple simulation has demonstrated a reduction in the errors on the measured signal when PCA is incorporated into the motion estimation technique. The PCA methods used the first set of normalised coefficients as the respiratory signal, PCA(C1), or generated PCA smoothed images and then registered these to measure the respiratory signal, PCA+IR. There was no significant difference in the errors on the signal between these two techniques. In the remainder of this chapter both techniques will be evaluated.

6.5 – Motion Correction Technique

To facilitate respiratory motion correction, after the respiratory signal has been estimated using the PCA methods the data will be binned based on the amplitude of the signal, figure 6-4. Once the images have been binned, each bin will be reconstructed and the reconstructed bins registered and then summed to give a motion corrected image.

6.6 – Software Development

The workflow proposed for respiratory motion estimation and correction is shown in figure 6-5 and compared to the workflows for the planar and three-dimensional patient motion estimation and correction. Patient motion was measured in the X, Y and Z directions. Respiratory motion estimation using PCA(C1) produces one motion signal. Respiratory motion has been measured to be 1.8, 2.3 and 9.1mm (Kovalski et al., 2007) and 0.4, 1.3 and 4.9mm (Shechter et al., 2004) for the X, Y and Z directions respectively and therefore respiratory motion presents predominantly in the cranio-caudal direction. Motion estimation using PCA+IR will therefore be limited to measuring motion in the cranio-caudal, Z, direction. The proposed techniques were implemented using workstations available in the department and the software was developed in c-shell, implementing ShIRT. Figure 6-6 shows the software developed and the steps involved in processing an MPI scan to correct for respiratory motion.

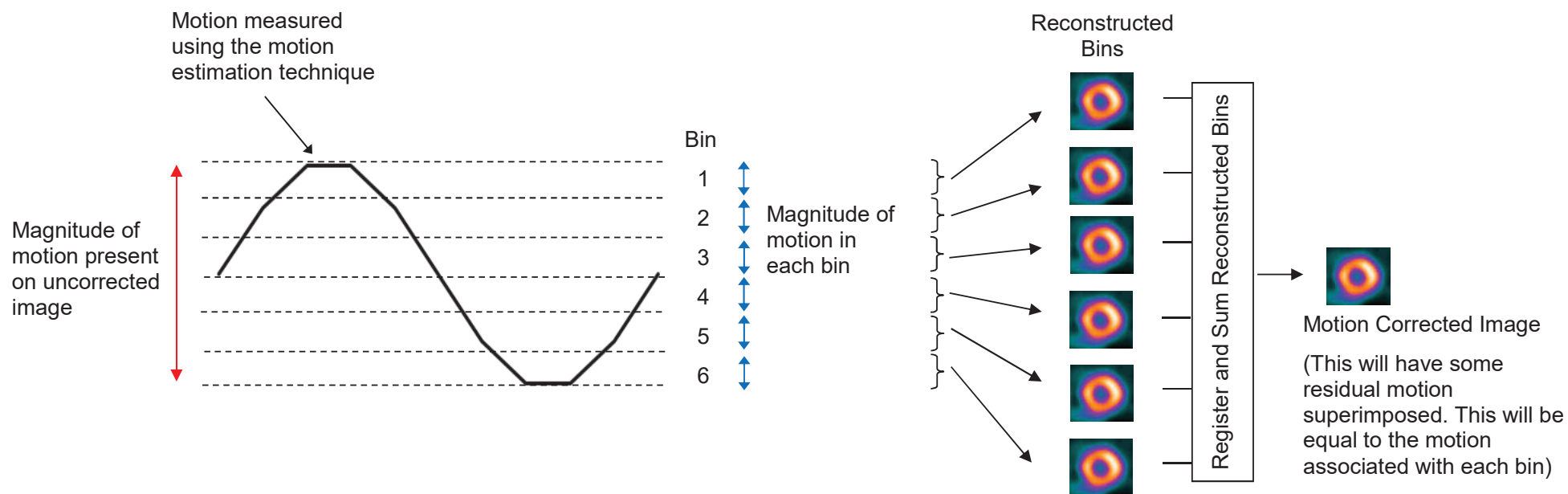


Figure 6-4 – A diagrammatic representation of the proposed motion correction technique. The motion curve is measured using the PCA+IR or PCA(C1) motion estimation technique. The data are then divided into bins based on the amplitude of the measured motion. The data from each bin are reconstructed. The reconstructed images are registered together to remove motion. PCA+IR – Principal component analysis smoothing with image registration, PCA(C1) – the first set of normalised coefficients from principal component analysis.

Myocardial perfusion image
list mode data (360s).

1. Divide each detector into a
series of 30s planar images.
(12 sets of 19 x 30s images)

Three-Dimensional Patient Motion Estimation and Correction

2. Reconstruct each set of 30s
images into a 3D image of the heart.
(12 x 30s 3D images)

3. Register the reconstructed images
to detect X, Y and Z motion.
(12 x 30s registered 3D images,
3 x motion signals)

4. Sum registered images to produce
a motion corrected image.
(1 x motion corrected 3D image)

Planar Patient Motion Estimation

2. Register the planar images
associated with each detector to
detect motion.
(19 x motion signals)

3. Average the signal from specific
detectors to detect X, Y and Z
motion.
(3 x motion signals)

Planar Respiratory Motion Estimation and Correction

1. Divide each detector into a series of planar 1s
images.
(360 sets of 19 x 1s images)

2. Detect respiratory motion from the planar 1s
images associated with each detector using the
motion estimation techniques.
(19 x motion signals)

3. Average the y signals from specific detectors.
(1 x motion signal)

4. Define n bins based on the amplitude of the
measured signal. Group the 1s images for each
detector according to which bin they fall in to
and sum the images for each bin.
(19 detector images x n bins)

5. Reconstruct the images in each bin into a 3D
image of the heart.
(n x 3D images)

6. Register and sum the 3D images to produce
a motion corrected image.
(1 x motion corrected 3D image)

Figure 6-5 – Flowchart showing the steps for planar and three-dimensional patient motion and planar respiratory motion estimation and correction. $PCA(C1)$ – 1st normalised coefficient from principal component analysis (PCA), $PCA+IR$ - Image registration of the PCA images.

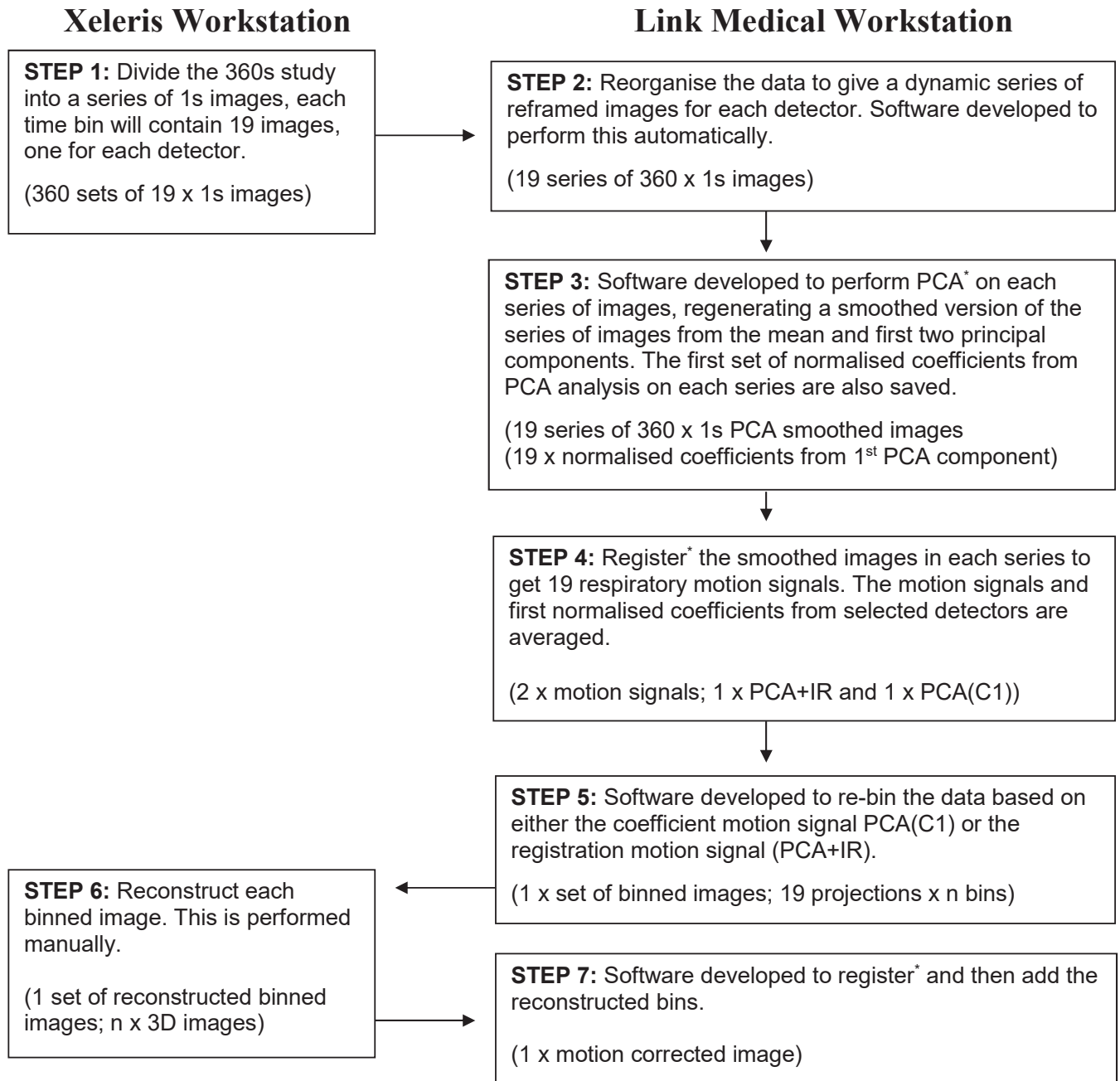


Figure 6-6 – The process of estimating and correcting for respiratory motion can be divided into seven steps performed on the Link Medical and Xeleris workstations.

* This was implemented through the Sheffield Image Registration Toolkit (ShIRT).

PCA(C1) – the first normalised coefficient from principal component analysis (PCA),

PCA+IR – Image registration of the PCA smoothed images.

6.7 – Optimisation of Technique: Phantom Acquisitions

This section will use dynamic phantom acquisitions to further evaluate and optimise the techniques and software in terms of aliasing, averaging the result over multiple detectors and the number of bins required for motion correction.

6.7.1 – Phantom

There are advantages to optimising the motion estimation technique using a dynamic phantom instead of simulating motion from static phantom images, as was performed in the initial assessment of the PCA technique, section 6.4. The DNM 530c is a three-dimensional imaging system and using a dynamic phantom incorporates the changing relationship between the position of the heart relative to the detectors as the phantom moves. It also results in residual motion being included in binned data and allows the software to be tested under the same conditions as it would be used for patient studies.

A platform designed to study respiratory motion during lung imaging (Darwesh et al., 2013; Darwesh et al., 2014) was used which simulates 1.5cm sinusoidal motion in three planes, figure 6-7a. The anthropomorphic phantom used in section 3.6, figure 3-6, was unsuitable for use on this system and therefore a cardiac insert was placed on the platform, figure 6-7b. A variable control altered the frequency of the platform movement between 5 and 25 cycles per minute. Three phantom MPI images were acquired as shown in table 6.1.

Acquisition	Activity (MBq)	Duration (s)	Cycles/Minute
1	200	60	20
2	4	360	20
3	4	360	0

Table 6.1 – The phantom acquisitions acquired using the moving platform. A frequency of 20 cycles/minute gives a respiratory cycle duration of 3s, representing the average respiratory frequency during myocardial perfusion imaging.

The high activity phantom, 200MBq, was acquired to limit the effect of noise on the results. The 4MBq acquisition had similar count statistics in the myocardium to a patient study. A stationary acquisition was acquired to give a reference image of the phantom without simulated respiratory motion.

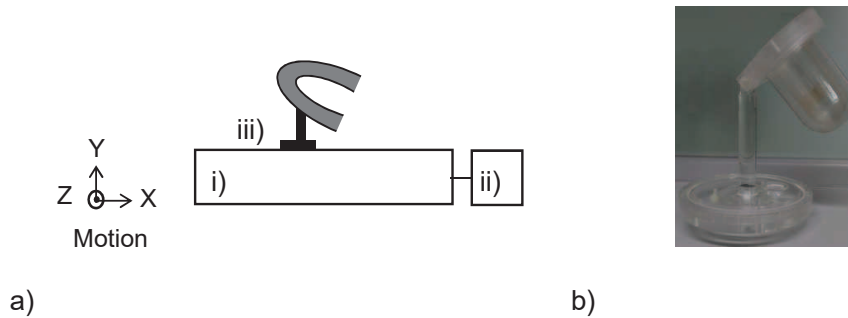


Figure 6-7 - (a) The moving platform (Darwesh et al., 2013) used to simulate motion in three dimensions, i - phantom drive system, ii - controls, iii - cardiac insert, and (b) the cardiac insert.

6.7.2 – Aliasing

This section investigates the maximum image duration that can be used to detect the respiratory signal whilst avoiding aliasing.

Method: The data from each detector for the 200MBq phantom acquisition were divided into five series; 15 x 4s images, 30 x 2s images, 60 x 1s images, 120 x 0.5s images and 240 x 0.25s images. The images from each detector for each time bin were reconstructed to give five series of three-dimensional images, with image durations of 4, 2, 1, 0.5 and 0.25s. The three-dimensional patient motion estimation technique was used to measure the motion on each series as this has demonstrated reasonable errors at a specified count level, chapter 4. The quality of a 0.5s image from the 200MBq acquisition gave approximately the same count statistics as the 30s acquisitions used for patient motion detection. The frequency of the motion signal was determined from the Fourier transform of the signal.

Results: The curves generated through registration of the reconstructed images and the associated frequency spectra are shown in figure 6-8. The frequency measured for each frame duration is shown in table 6.2.

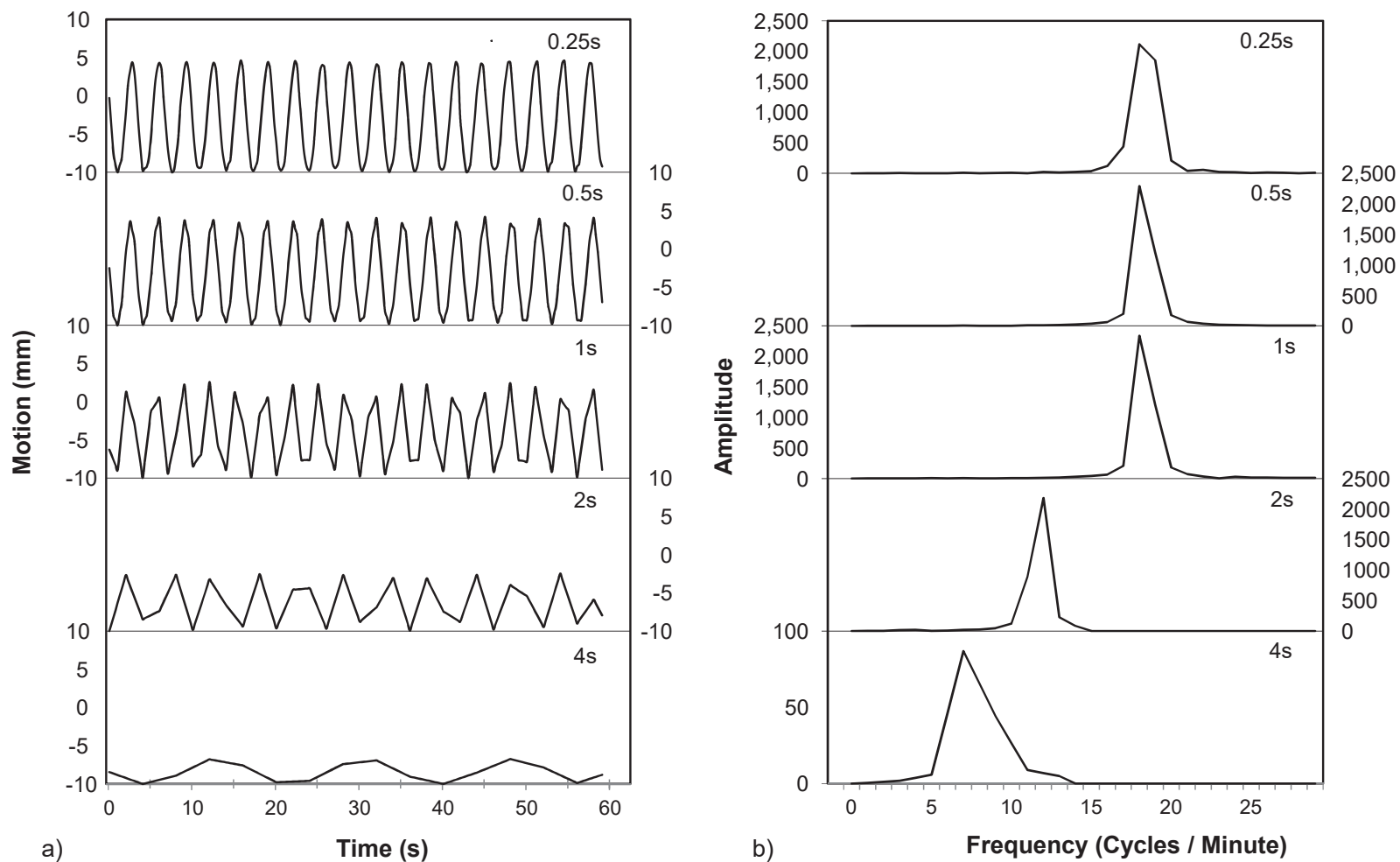


Figure 6-8 – (a) The signals generated for motion in the Z direction through registration of reconstructed images (three-dimensional patient motion estimation technique) for different image durations, (b) the Fourier transform of the signals.

Frame Duration (s)	Frequency (Cycles/Minute)
4	3.4
2	11.6
1	18.4
0.5	18.4
0.25	18.6

Table 6.2 – The frequency of the measured signal for different frame durations.

Discussion: The respiratory cycle stated for the phantom is 3s, which is equivalent to 20 cycles per minute. There is a difference between the stated frequency of the platform and the measured frequency of 18.6 cycles per minute. This may be due to variations between the stated and generated frequency of the phantom or a systematic measurement error. Aliasing is taking place for image durations ≥ 2 s, as demonstrated by signals with a lower frequency than expected. Using an image duration of 1s the sampling rate is sufficient to recover the frequency, however there is increased variability in the amplitude of individual peaks when compared to 0.5 and 0.25s images. The increased variability in the amplitude of the peaks is due to the sampling resolution not being fine enough to capture the maximum of each peak.

From these results it is recommended that a minimum frame duration of 0.5s is used for detection of the respiratory signal, as this will retain a margin of error to cover variations in respiration between patients. Applying Nyquist theory, section 4.2, an image duration of 0.5s would allow respiratory signals up to 60 cycles per minute to be detected, covering slow (10/minute), normal (20/minute) and shallow (40/minute) breathing (Marieb, 2004). Images 0.25s in duration could be used, however this would double the number of images required and increase the processing time.

6.7.3 – Motion Estimation: Optimisation

The initial evaluation of the PCA techniques, PCA(C1) and PCA+IR, simulated motion on one detector, section 6.4. The developed software determines a respiratory signal for each detector and then averages these to get a final motion

signal, figure 6-5. The respiratory signal detected may be improved by averaging over multiple detectors, however inclusion of detectors with lower count statistics may have a negative impact on the results. This section will investigate which detector signals should be averaged.

Method: The background corrected counts per pixel in the myocardium for each detector, normalized to detector 8, are shown in figure 6-9a and table 6.3. This can also be seen through comparison of the counts in the heart compared to the background figure 6-9b.

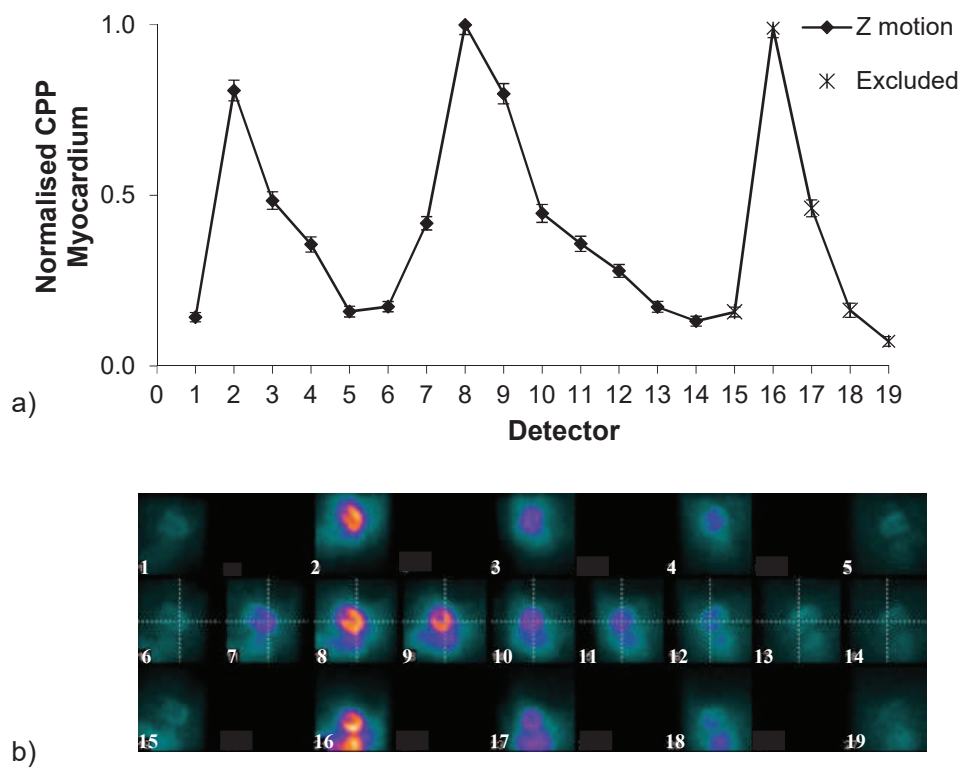


Figure 6-9 – (a) The counts per pixel (CPP) in the myocardium measured for each detector and normalized to detector 8, (b) the difference between the counts in the heart and background activity varies between detectors.

Detector	8	2	9	3	10	7	11	4	12	6	13	5	1	14
Normalised CPP	1.0	0.8	0.8	0.5	0.5	0.4	0.4	0.4	0.3	0.2	0.2	0.1	0.1	0.1
Simulation 1														
Simulation 2														
Simulation 3														
Simulation 4														
Simulation 5														
Simulation 6														
Simulation 7														
Simulation 8														
Simulation 9														
Simulation 10														
Simulation 11														
Simulation 12														
Simulation 13														
Simulation 14														

Table 6.3 – The grey boxes indicate the detectors averaged for each simulation. CPP - counts per pixel.

Motion signals from the 4MBq phantom generated using a 0.5s frame duration and both PCA techniques were compared when the results were averaged over different detectors. Averaging was performed as shown in table 6.3, starting with the detector with the highest counts per pixel and gradually increasing the number of detectors. This was performed with equal weight attributed to all detectors and with the images weighted based on their image quality. The images from detectors 15-19 were not included as they are often affected by sub-diaphragmatic activity. The normalised mean squared error (MSE) of all the signals was compared.

Results: Figure 6-10 shows the normalised MSE of the signal as the number of detectors included in the analysis increases.

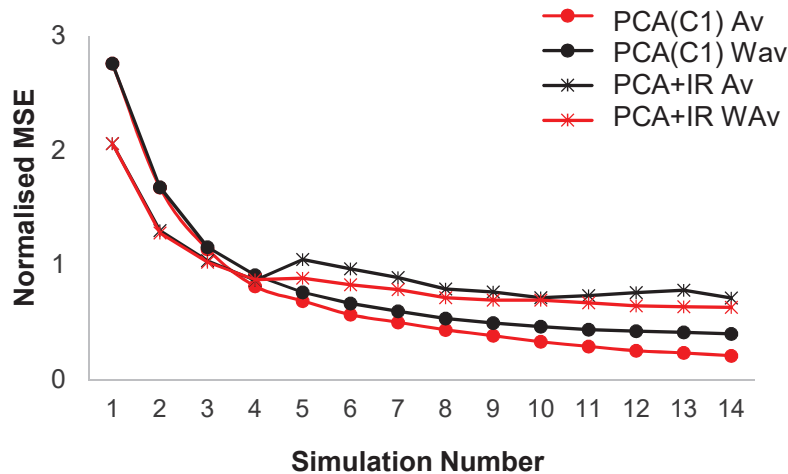


Figure 6-10 – The normalised MSE when the motion signal measured on multiple detectors is averaged. PCA(C1) – the first normalised coefficient from principal component analysis (PCA), PCA+IR - Image registration of the PCA smoothed images. Av – Average with equal weights applied to each detector, WAv – Weighted average determined by the counts per pixel measured in the myocardium.

Discussion: Figure 6-10 shows a sharp decrease in the normalised MSE error as the number of images averaged is increased. The degree of improvement reduces as the lower quality images are included.

PCA(C1) analysis shows higher errors initially, however after four images have been averaged the errors are reduced compared to PCA+IR. Weighting the images shows a slight further improvement. This may be a consequence of the data presented rather than the robustness of the technique. The normalised coefficients will be influenced by motion in all three directions, unlike image registration which measures motion in each direction separately. The phantom has equal motion in all three directions, however in patients the cranio-caudal component of respiration is significantly larger than the ventral-dorsal and lateral components (Shechter et al., 2004; Kovalski et al., 2007). Therefore, the contribution of the X and Y signals to the normalised coefficients may be reduced on patient data which may increase the errors on the technique. The difference demonstrated between the two techniques is

small. Therefore, considering the limitations of the perceived improvement for PCA(C1) and that there is value in estimating the magnitude of the motion from the measured signal, which can only be achieved through PCA+IR, the method of choice for the final software will be PCA+IR analysis. The PCA(C1) signal will be used to derive a quality index which will be described in section 7.6.

No disadvantage has been demonstrated to averaging over all detectors, however there is a risk that there could be a negative effect of including noisier images on patient studies where the image quality will be reduced compared to this simulation, due to the effects of attenuation, scatter and sub-diaphragmatic activity. Therefore, averaging over 5 detectors, 2, 3, 8, 9 and 10 will be used, as for PCA+IR there is only limited improvement after the signal from 5 detectors has been averaged. For PCA+IR there is a marginal improvement demonstrated using a weighted average over 5 detectors. On patient images the ratio of the counts per pixel in the myocardium between the detectors may vary depending in body habitus, therefore equal weight will be applied to the detectors.

6.7.4 – Motion Correction: Optimisation

Motion correction, figure 6-4, divides the amplitude of the respiratory signal into a number of bins. The optimum size of the bins is a trade-off between the count statistics of the bins and the residual motion on the corrected image. This section will investigate the optimum bin size.

Method: The respiratory signal was determined for the 4MBq acquisition using 0.5s frames, averaging the PCA+IR signal over detectors 2, 3, 8, 9, 10. The effect that changing the number of bins has on the success of motion correction was assessed. The magnitude of the respiratory signal was estimated to be 13.2mm, measured as the difference between the maximum and minimum points on the measured signal. The bin size required was determined from the magnitude of the motion divided by the number of bins. The data from the dynamic phantom acquisition were binned into 2, 4, 6, 8 and 10 bins. The binned images were reconstructed and registered to correct for motion, figure 6-5. Affine registration was used for motion correction as on patient data deformation of the heart, in the form of increased movement of the

inferior wall compared to the anterior wall, takes place during a respiratory cycle (Martinez-Moller et al., 2007). In addition, the amplitude of the respiratory signal was determined as the Z shift from registration of the reconstructed bins.

Results: Figure 6-11 shows three consecutive central short axis slices for a stationary phantom, the phantom with motion and motion corrected using different numbers of bins. Table 6.4 shows the motion measured from registration of the reconstructed bins.

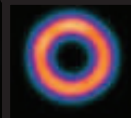

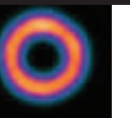
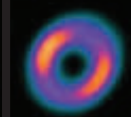
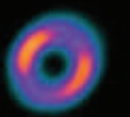
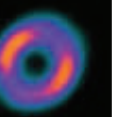


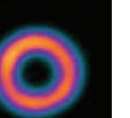


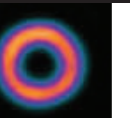
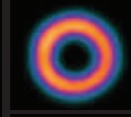

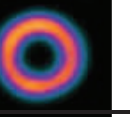
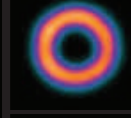

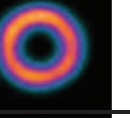
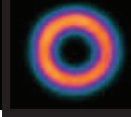
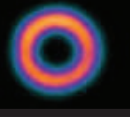
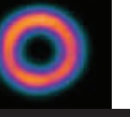
Short Axis Slice			
1	2	3	
			No Motion
			Motion
			Motion Corrected – 2 Bins Bin Size: 6.6mm
			Motion Corrected – 4 Bins Bin Size: 3.3mm
			Motion Corrected – 6 Bins Bin Size: 2.2mm
			Motion Corrected – 8 Bins Bin Size: 1.7mm
			Motion Corrected – 10 Bins Bin Size: 1.3mm

Figure 6-11 – Three consecutive central short axis slices of the phantom, with and without motion and motion corrected with different numbers of bins.

Number of Bins	Bin Size (mm)	Z Motion from Registration of Reconstructed Bins
2	6.6	9.3
4	3.3	12
6	2.2	12.9
8	1.7	13.6
10	1.3	13.6

Table 6.4 – The motion measured on the study from registration of the reconstructed binned data for different numbers of bins.

Discussion: Figure 6-11 shows that the artefacts introduced by motion are successfully removed by the motion correction technique for all the bin sizes used, with the corrected images resembling the image acquired without motion.

The magnitude of the motion was estimated to be 13.2mm from the difference between the maximum and minimum points on the measured signal. The motion measurement from registration of the reconstructed bins will be a more accurate reflection of the magnitude of the motion, as the count statistics of the images will be greatly improved. The magnitude of the motion measured from registration of the reconstructed bins is shown in table 6.4 and increases as the number of bins used increases. The motion measured plateaued at 13.6mm for bin sizes ≥ 1.7 mm. This indicates that the motion estimate of 13.2mm from the measured signal is reliable enough to be used to determine the bin size. This also highlights the advantage of the PCA+IR technique over the PCA(C1) technique, as the latter technique does not facilitate an estimate of the magnitude of the motion and therefore a fixed number of bins would need to be used for motion correction.

In the phantom study a 6.8mm bin size was sufficient to correct for motion. This is in agreement with Segars and Tsui, (2002) who found that respiratory artefacts are significantly reduced if the extent of respiratory motion within a bin is ≤ 1 cm during a gated time period. Using a nominal bin size of 5mm would allow for some errors in the estimated motion, without having excessive numbers of bins. Motion will not necessarily be a multiple of 5mm and it is preferable to have the bins of equal sizes

to minimise the chance of bins having poor count statistics, therefore the actual bin size was calculated by dividing the measured motion by 5mm and then rounding the number of bins. This results in studies with ≥ 8 mm motion being motion corrected; any studies below this threshold would be calculated to have one bin and therefore would not be corrected. As demonstrated in section 3.6 significant motion artefacts are not present for < 8 mm motion, therefore this method is consistent with the appearance of artefacts on the images.

6.7.5 – Conclusion

Dynamic phantom acquisitions have been used to confirm that the technique and software are working as expected and have enabled optimisation of factors such as image duration, averaging over detectors and the bin size used for motion correction.

6.8 – Summary

The technique used for patient motion estimation in chapter 4 was not robust enough to measure respiratory motion. Software has been developed to deliver an improved workflow for respiratory motion estimation and correction, figure 6-5 and figure 6-6. The improved technique incorporates principal component analysis (PCA) into the motion estimation technique. This can be implemented in two ways; using the first normalised coefficients from PCA analysis directly, PCA(C1) or using PCA to regenerate the data from the mean and first two principal components, effectively smoothing the data and then using image registration to determine the motion on the images, PCA+IR. This has been shown to significantly improve signal detection compared to techniques using image registration only. The software and technique were then validated and optimised using a dynamic phantom which determined that PCA+IR with a 0.5s frame duration should be used and the signals should be averaged with equal weight over detectors 2, 3, 8, 9 and 10. The technique for motion correction was also introduced and a bin size of 5mm determined for the successful removal of motion artefacts.

The phantom work clarified numerous issues but it also suffers from many limitations. For example, respiratory motion was simulated as periodic sinusoidal motion whereas on patient studies the cycle is biased more towards end expiration (Kovalski et al., 2007). Although the counts in the myocardium were similar to an average patient study, the image quality was significantly better than for patient images, as the effects of scatter, attenuation, cardiac motion, patient motion, sub-diaphragmatic activity and background were excluded, as shown in figure 6-12. Also, motion in the X and Y directions was much larger than would be expected in patients.

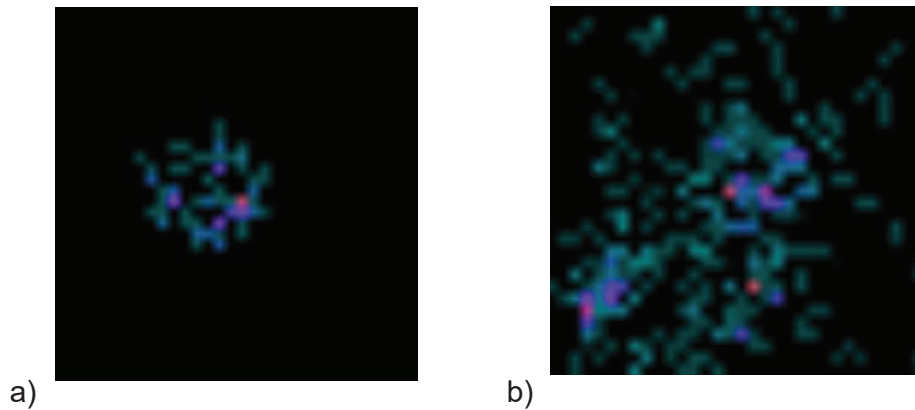


Figure 6-12 – Images 0.5s in duration from detector 8 of (a) the phantom acquisition and (b) a patient acquisition.

Together these may have improved the performance of the technique on the phantom studies compared to what might be expected of patient studies. Therefore, further validation of the technique will be undertaken on patient studies comparing the signal to that determined using an external motion measurement device.

7 – Respiratory Motion Estimation and Correction: Validation and Patient Application

7.1 – Introduction

Chapter 6 expanded the patient motion estimation technique to include principal component analysis and evaluated the proposed technique for respiratory motion estimation on phantom studies. This provided insight into how the technique works and optimised the processing parameters. This chapter will apply the technique to a cohort of patients, with a subset undergoing respiratory motion measurement with an external device.

7.2 – Patient Cohort

Forty-seven patient rest studies were selected to assess the potential of the respiratory motion estimation technique. The patients were selected to ensure reasonable quality images on which to evaluate the technique. The inclusion criteria were that the patient weight must be $\leq 100\text{Kg}$ and there must not be more than 2 adjacent segments of the heart based on a 9 segment model that have $>50\%$ reduction in counts. This group consisted of 26 females, average weight 77kg and 21 males, average weight 84kg. The final eight patients also consented to an extra myocardial perfusion acquisition, which was acquired after the clinical scan, using an external device as described in section 7.3, to record the respiratory signal. The imaging parameters used for the scans are as described in section 3.5. There were a total of 63 images acquired from this cohort, 47 clinical images, 8 repeat clinical images and 8 images acquired with an external device. The original clinical images are labelled PAT1 - PAT47, repeat clinical imaging is suffixed with a "R", for example PAT23R and the images acquired with an external device are suffixed with an "E", PAT40E – PAT47E.

7.3 – Respiratory Effort Transducer

Respiratory motion estimation using an external device to measure the respiratory signal was discussed in section 2.4.4. The external device used for this study was a respiratory effort transducer (Biopac Systems Inc) mounted on an elastic strap around the patient's thorax. This was connected to the MP45 data acquisition system which was connected to a computer, figure 7-1. The change in the thoracic circumference during respiration is measured by a transducer which converts this into an electrical signal (mV). The strap was placed around the patient's thorax at the point where motion was most apparent through visual assessment. The respiratory strap acquired data at 10Hz. The trace from the strap was observed until the respiratory signal stabilised and then the MPI scan was started. The signal was exported to Excel for comparison with the respiratory motion estimation technique.

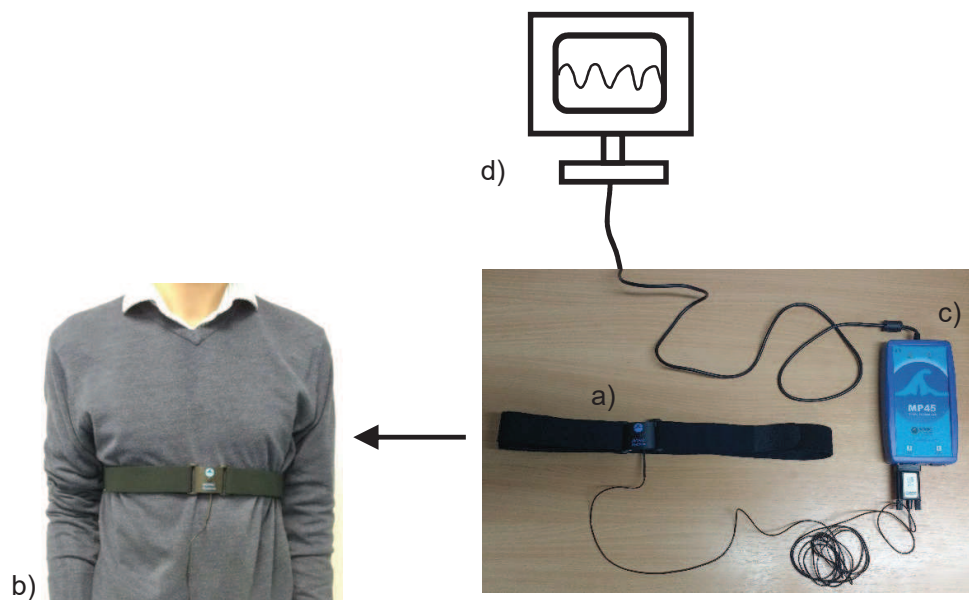


Figure 7-1 – (a) Respiratory effort transducer on an elastic strap, (b) the elastic strap and transducer are fitted around the thorax, (c) these are connected to a MP45 data acquisition system, (d) which is connected to a computer that displays the measured respiratory signal in mV.

The measurement from the transducer is not a gold standard measure of motion of the heart due to respiration, as chest motion may not necessarily correlate directly

with translation of the heart. However, this is a well-established method that has been shown to be effective for respiratory gating and was deemed a suitable method for benchmarking our data driven technique

7.4 – Signal Post Processing

Chapter 6 determined the optimum parameters for the respiratory motion estimation and correction software to be:-

- Image duration 0.5s
- Detection technique PCA smoothing combined with image registration, PCA+IR.
- Averaging with equal weight detectors 2, 3, 8, 9 and 10
- Bin size 5mm

The phantom study in chapter 6 was limited by the fact that respiratory motion was simulated using periodic sinusoidal motion. The value of investigating frequency domain post processing was therefore limited due to the narrow frequency spectrum of the signal. This section will therefore explore post processing on patient data.

7.4.1 – Method

Two patient images, PAT40E and PAT46E, acquired with an external device had clear respiratory motion detected by the software. The data from these two patients were processed using PCA+IR using 0.5 and 1 second images for comparison purposes. The signals obtained from 0.5s images were post processed using a Savitzky-Golay filter, using a range of values for the polynomial order (k) of 2 - 13 and for the frame length (f) of 5 - 15. The signals generated were compared, through calculation of the Pearson correlation coefficient, to the signal measured by the external device.

The signal from the external device is a measure of chest expansion and is therefore representative of the respiratory signal only. The signal measured by the respiratory motion estimation software represents motion of the heart and is therefore a measure of respiratory and patient motion combined. Therefore, prior to

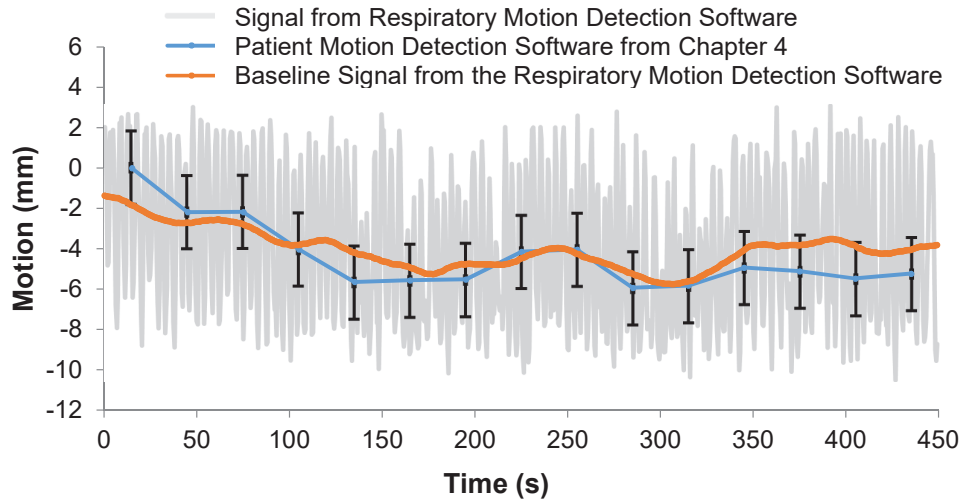
performing a comparison of the signals, patient motion was removed from the software signal by subtracting the baseline. The baseline was determined by two passes of a moving mean filter in Matlab, with window lengths of 60 and 30 data points respectively.

7.4.2 – Results

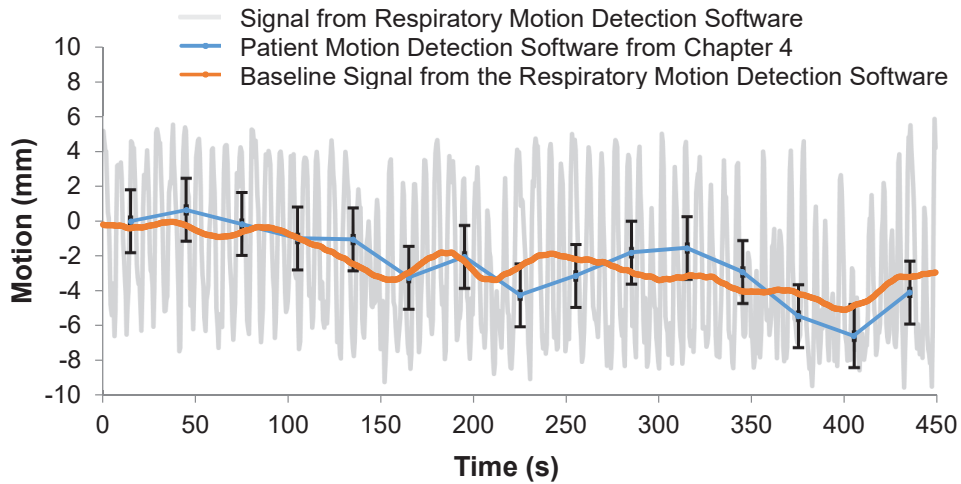
Figure 7-2 shows the signal from the motion estimation technique for both patients, along with the baseline signal and the patient motion signal measured using the patient motion estimation software generated in chapters 4 and 5. Figure 7-3 shows the effect of the Savitzky-Golay Filter ($k = 5$, $f = 7$) on the frequency spectrum of the signal. Table 7.1 shows the correlation coefficients calculated, with and without post processing.

Parameters		Pearson Correlation Coefficient
Image Duration (s)	Post Processing	
1	None	0.61
0.5	None	0.70
0.5	Savitzky-Golay Filter	0.76

Table 7.1 - The average Pearson correlation coefficient between the signal from the motion estimation technique (patient motion subtracted) and the external device.



a)



b)

Figure 7-2 – The signal detected by the respiratory motion detection software, the baseline signal after two passes of a moving mean filter and the patient motion signal measured using the software developed in chapter 4, (a) Patient PAT40E (b) PAT46E. The error bars represent the error measured on the patient motion signal in chapter 4 (mean error \pm 3SD).

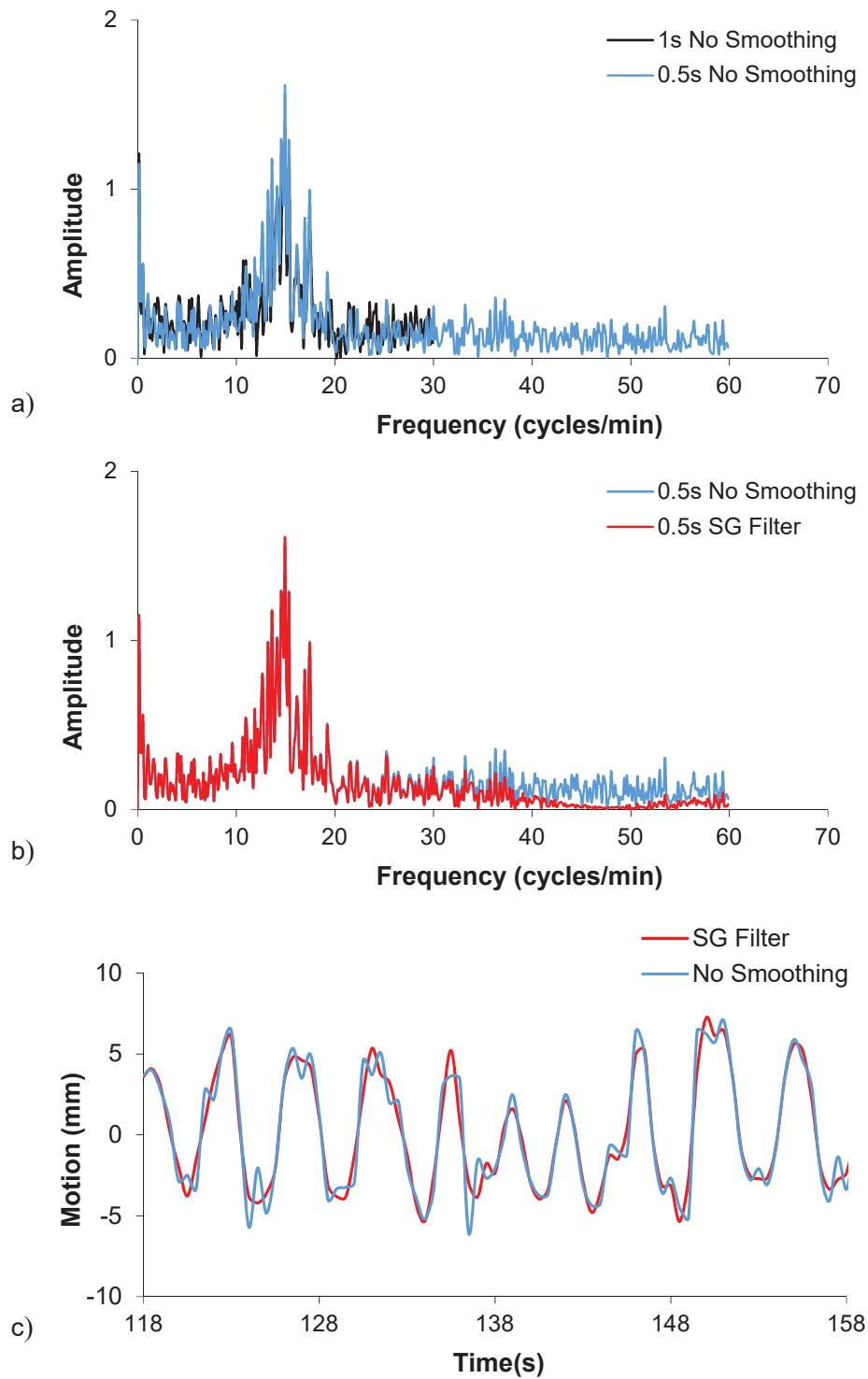


Figure 7-3 – The Fourier transform of the signal from PAT40E for (a) 1s and 0.5s images without post processing, (b) 0.5s images with and without post processing and a section of the signal from PAT40E with and without post processing. SG - Savitzky-Golay

7.4.3 – Discussion

Figure 7-2 shows that the baseline of the respiratory signal is in reasonable agreement with the patient motion signal determined independently by the software developed in chapter 4. Baseline subtraction is therefore considered a valid and straightforward method of removing patient motion from the signal. Baseline subtraction gives a more continuous representation of the patient motion signal without the discontinuities obtained with the method developed in chapter 4 and is therefore the preferred method.

The Savitzky-Golay filter was applied to the signal using different combinations of values for the polynomial order (k) and frame length (f). The signals were visually assessed and $k = 5$ and $f = 7$ selected as a compromise between smoothing lower frequency signals and maintaining the frequency of higher frequency components, for 0.5s images. Applying a Savitzky-Golay Filter to the signal derived from 0.5s images preserves frequencies up to 40 cycles/minute, which covers the physiological range of respiratory signals and attenuates higher frequencies which represent noise on the signal. Table 7.1 shows that using 0.5s compared to 1s images, and post processing the signal from 0.5s images with a Savitzky-Golay Filter improves the correlation with the external device.

7.4.4 – Conclusion

The signal from the respiratory motion detection software will be post processed with a Savitzky-Golay Filter with an order of 5 and a frame length of 7.

7.5 – Patient Validation

This section compares the signal from the motion estimation technique to the signal from the external device.

7.5.1 – Method

The eight patients described in section 7.2 that had an additional myocardial perfusion image acquired with an external device to measure the respiratory signal

were processed using the motion estimation technique. Patient motion was removed from the signal by subtracting the baseline, section 7.4. The remaining respiratory signal was then compared to the signal from the external device using the Pearson's correlation coefficient. The frequencies of both signals were determined from the maximum value of the Fourier transforms. Multiple measures of motion on each study were compared, as listed below and illustrated in figure 7-4 and figure 7-5.

Method 1: The magnitude of *respiratory motion* was determined by dividing the data into 8 bins based on the signal from the *external device*, then reconstructing and registering the bins⁴, figure 7-4a.

Method 2: The magnitude of the *patient and respiratory motion combined* was determined by dividing data into 8 bins based on the signal from the *motion estimation software*, then reconstructing and registering the bins⁴, figure 7-4b.

Method 3: The magnitude of the *patient and respiratory motion combined* was determined from the *motion estimation software*, as the difference between the maximum and minimum values of the signal, figure 7-4b.

⁴ Any bin that contained <3% of the acquisition (equivalent to 10s of imaging from a 360-minute scan) was excluded.

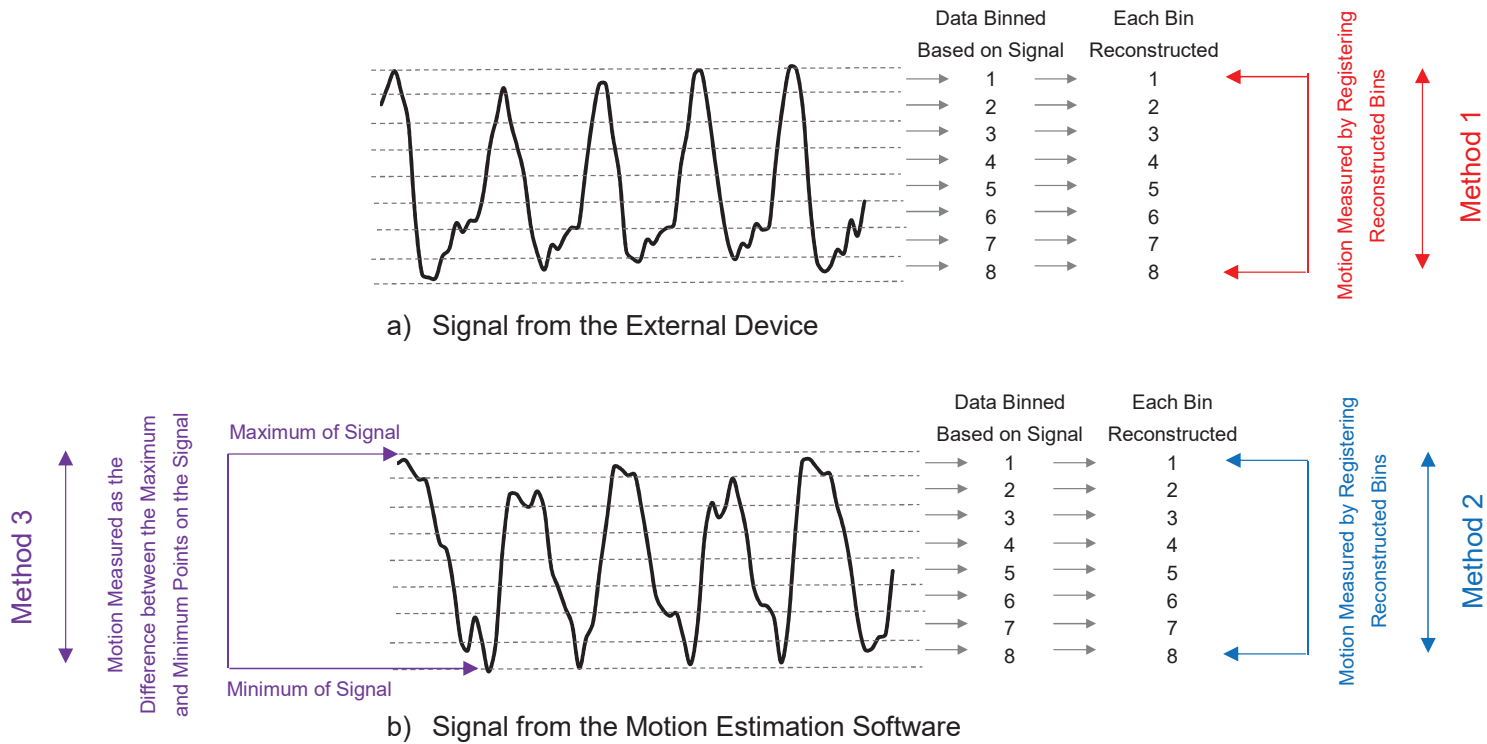


Figure 7-4 – (a) The magnitude of the respiratory motion was measured from the signal generated by the external device (method 1), (b) the magnitude of the respiratory and patient motion combined was measured from the signal generated by the motion estimation technique using methods 2 and 3.

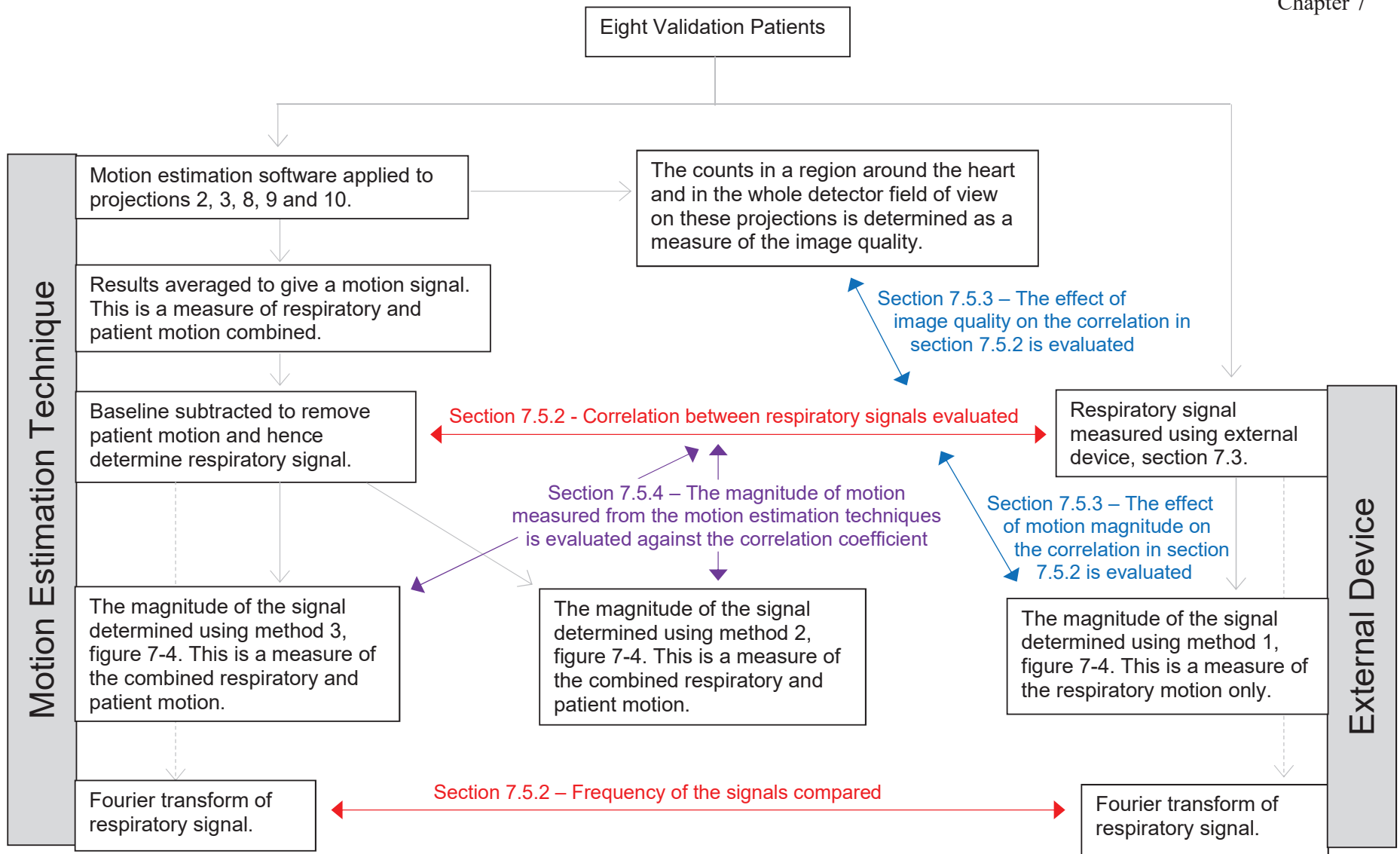


Figure 7-5 – A flowchart showing the processing steps (grey lines) and comparisons (coloured lines) made between the signals generated using the motion estimation technique and the external device.

The ability of the motion estimation technique to detect a signal may depend on the image quality. For all eight validation patients a region of interest was generated around the heart on detector images 2, 3, 8, 9 and 10. The average counts per pixel across the detectors for the whole field of view and within the region were calculated and compared between patients.

The results and discussion for this section will be divided into four parts; (1) correlation with the external device and comparison of the measured frequencies, (2) an exploration of weak correlations and (3) the magnitude of motion measured using the motion estimation technique, as outlined in figure 7-4. This will be followed by (4) an analysis of the frame duration that was used compared to the measured frequencies.

7.5.2 – Correlation with the External Device

Results: Figure 7-6, figure 7-7, figure 7-8 and figure 7-9 show the respiratory signals measured using the motion estimation software and the external device for PAT40E, PAT46E, PAT43E and PAT44E respectively. Figure 7-10 and figure 7-11 show the corresponding Fourier transforms. Table 7.2 shows the correlation coefficients, frequency and magnitude of motion measured for all eight patients.

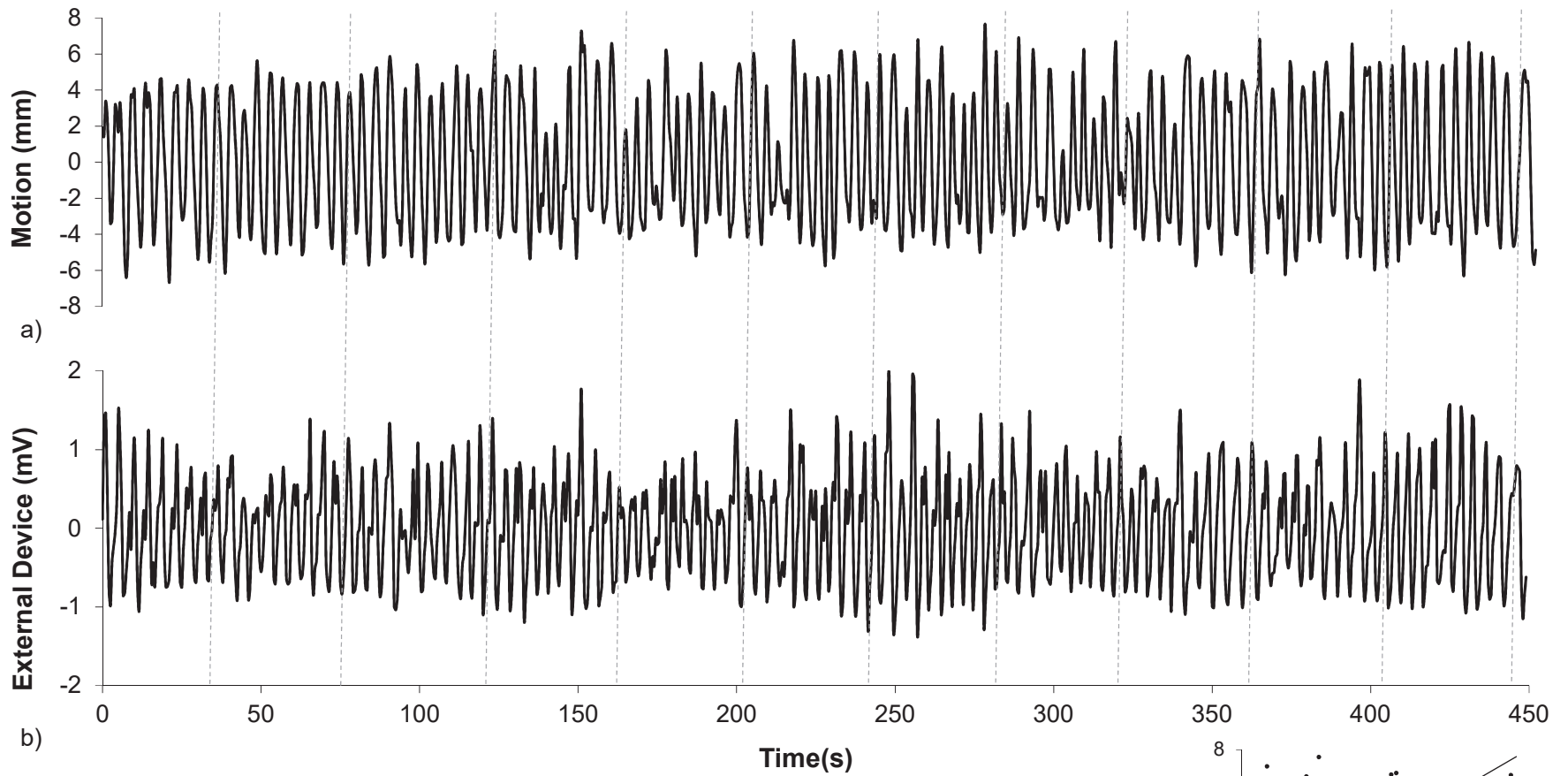
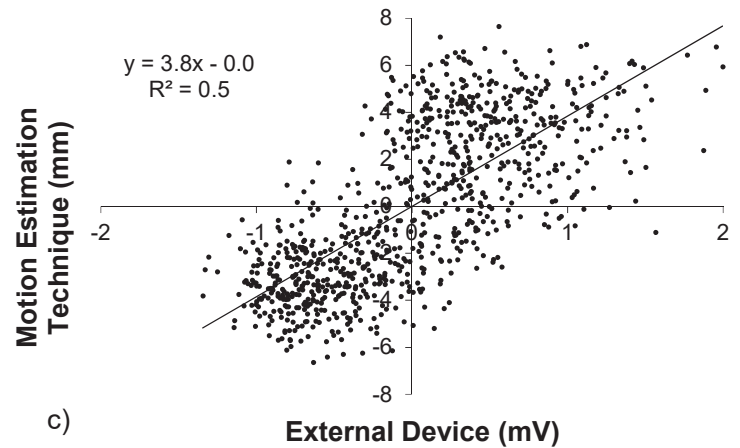


Figure 7-6 – A comparison of the respiratory signals from (a) the motion estimation technique and (b) the external device, for patient PAT40E. Regular markers have been added to aid comparison. (c) A correlation plot for both respiratory signals with a trend line added.



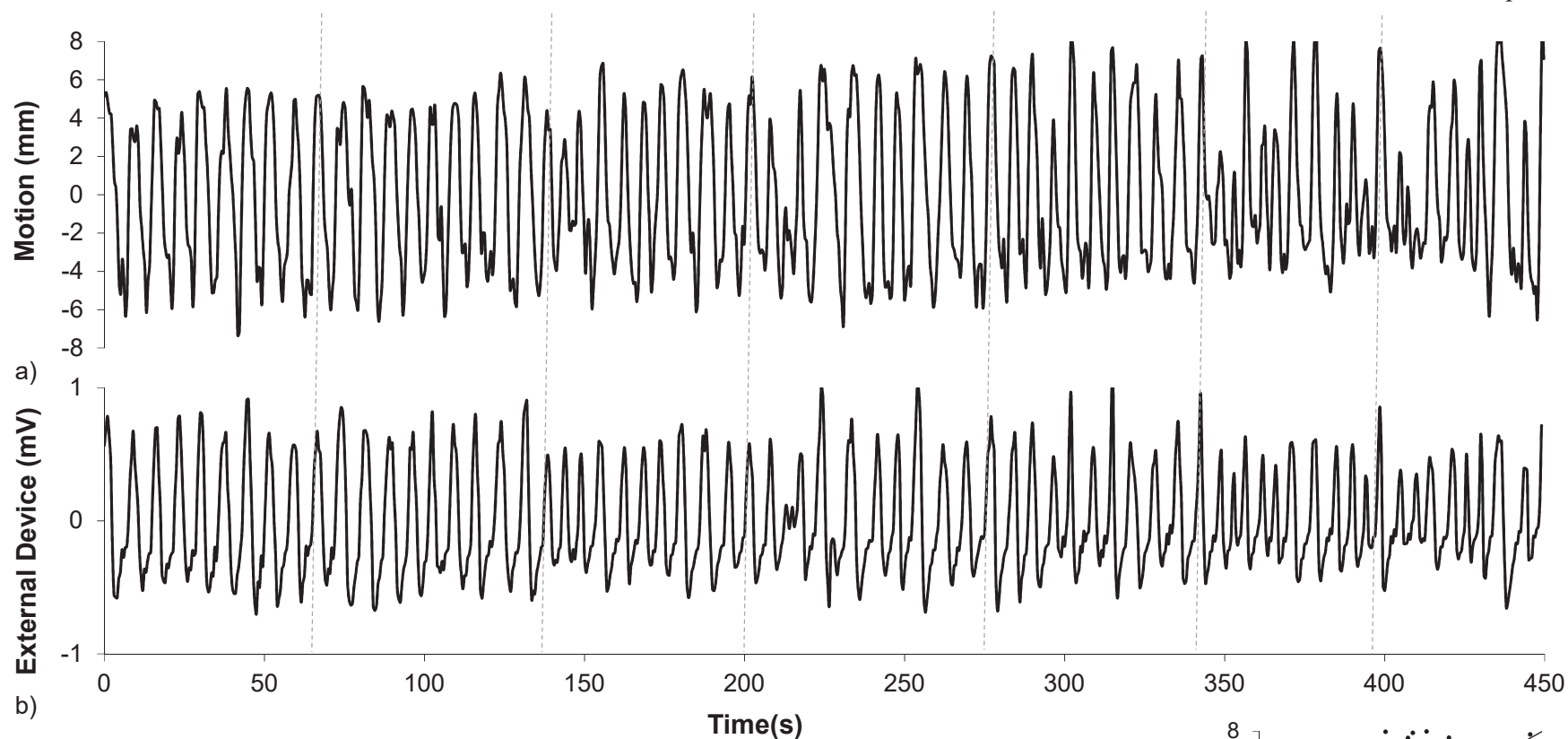
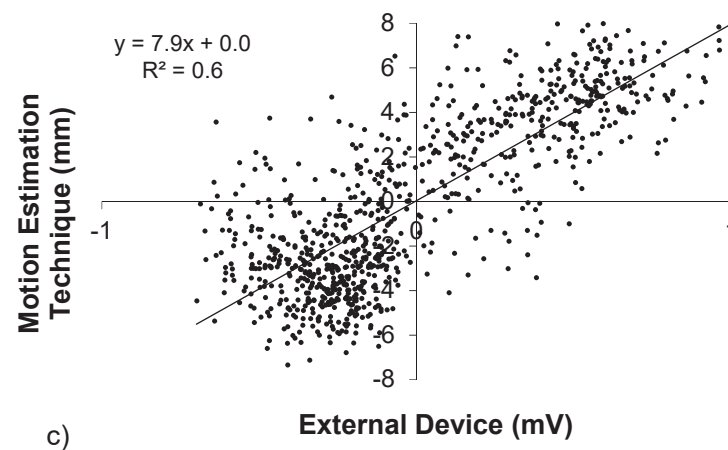


Figure 7-7 – A comparison of the respiratory signals from (a) the motion estimation technique and (b) the external device, for patient PAT46E. Regular markers have been added to aid comparison. (c) A correlation plot for both respiratory signals with a trend line added.



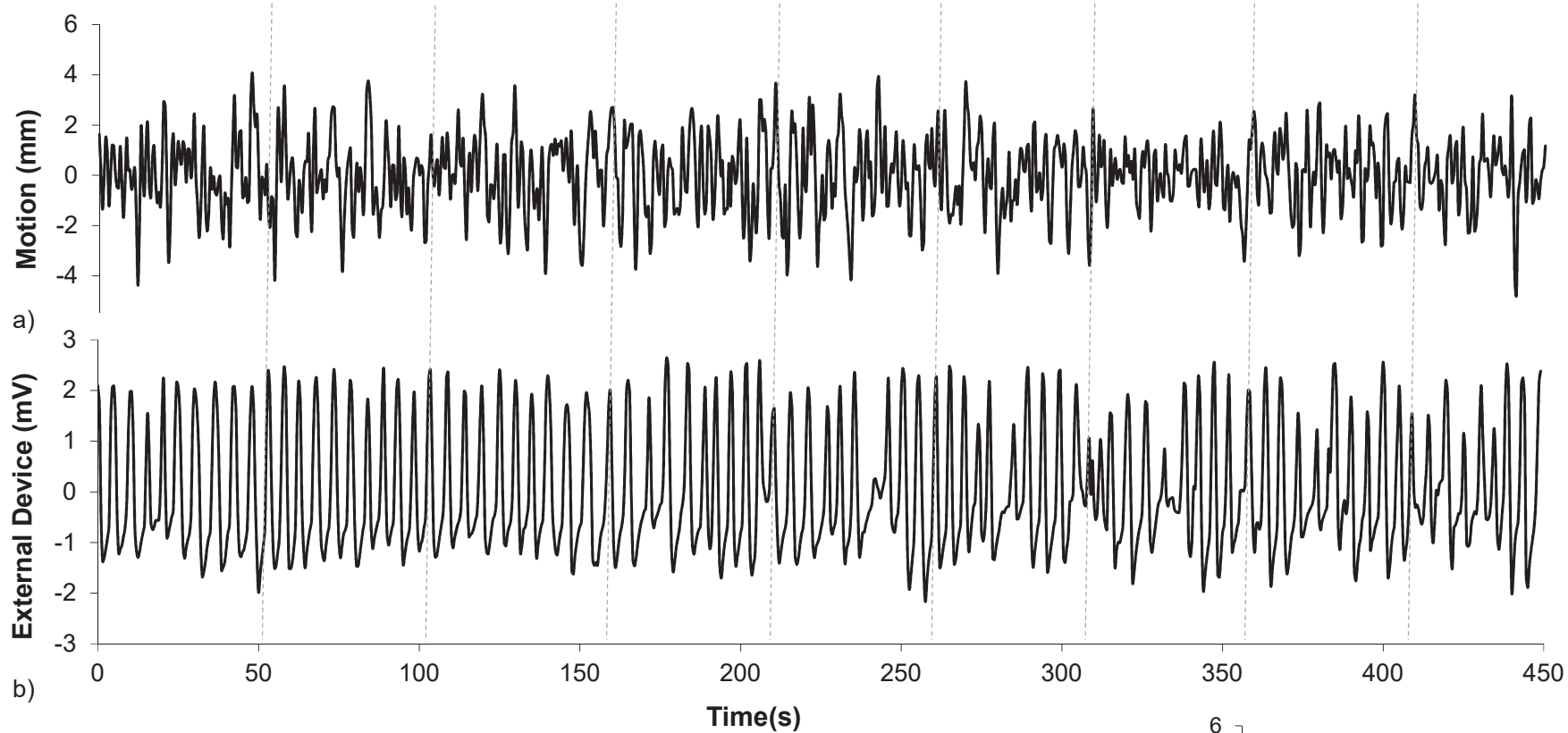


Figure 7-8 – A comparison of the respiratory signals from (a) the motion estimation technique and (b) the external device, for patient PAT43E. Regular markers have been added to aid comparison. (c) A correlation plot for both respiratory signals with a trend line added.

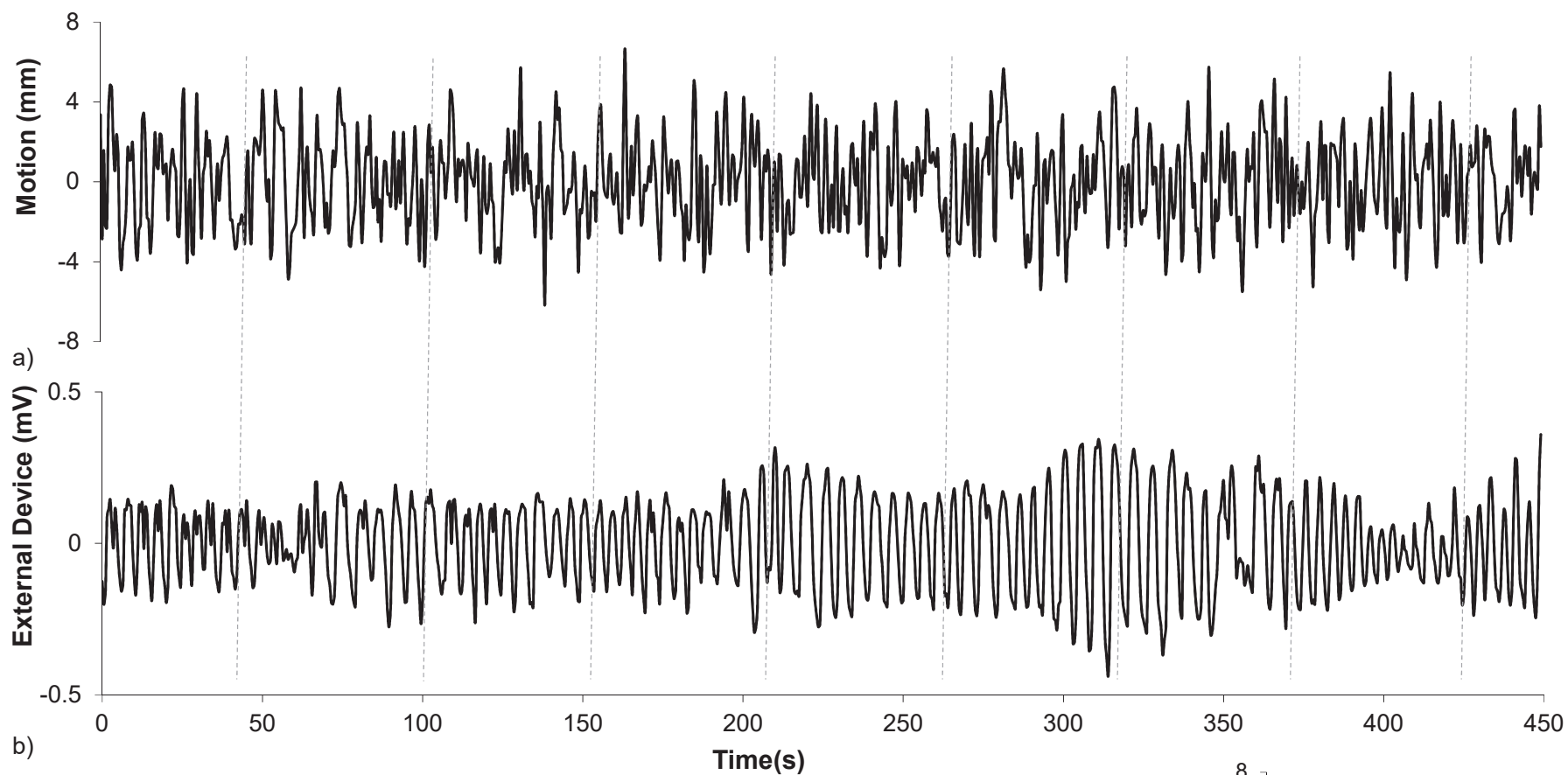
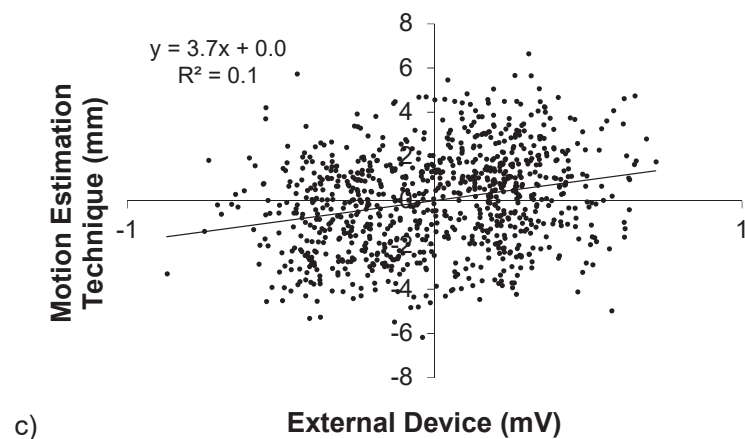


Figure 7-9 – A comparison of the respiratory signals from (a) the motion estimation technique and (b) the external device, for patient PAT44E. Regular markers have been added to aid comparison. (c) A correlation plot for both respiratory signals with a trend line added.



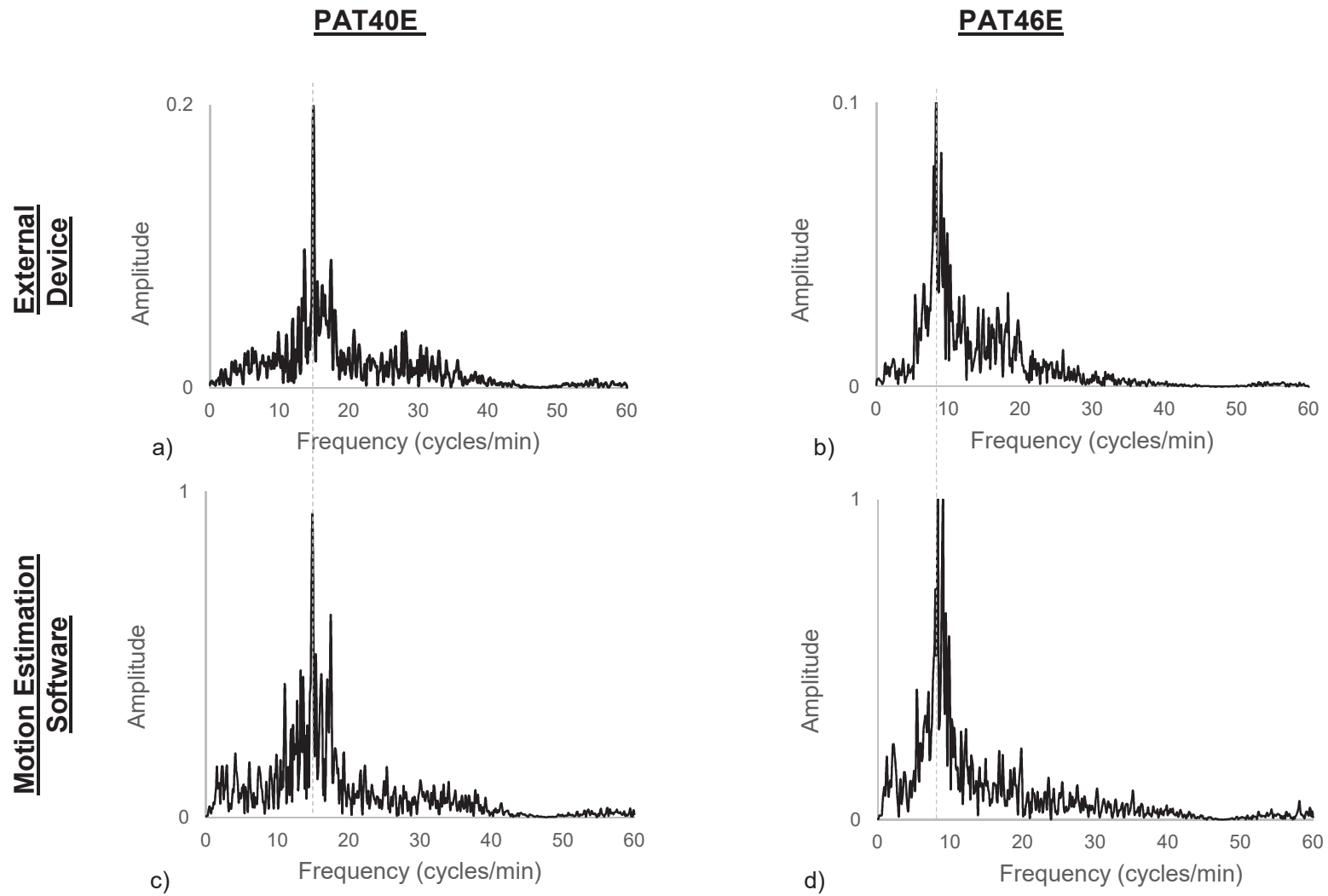


Figure 7-10 – Fourier transforms of the respiratory signals, (a) and (c) PAT40E from the external device and motion estimation technique respectively, (b) and (d) PAT46E from the external device and motion estimation technique respectively.

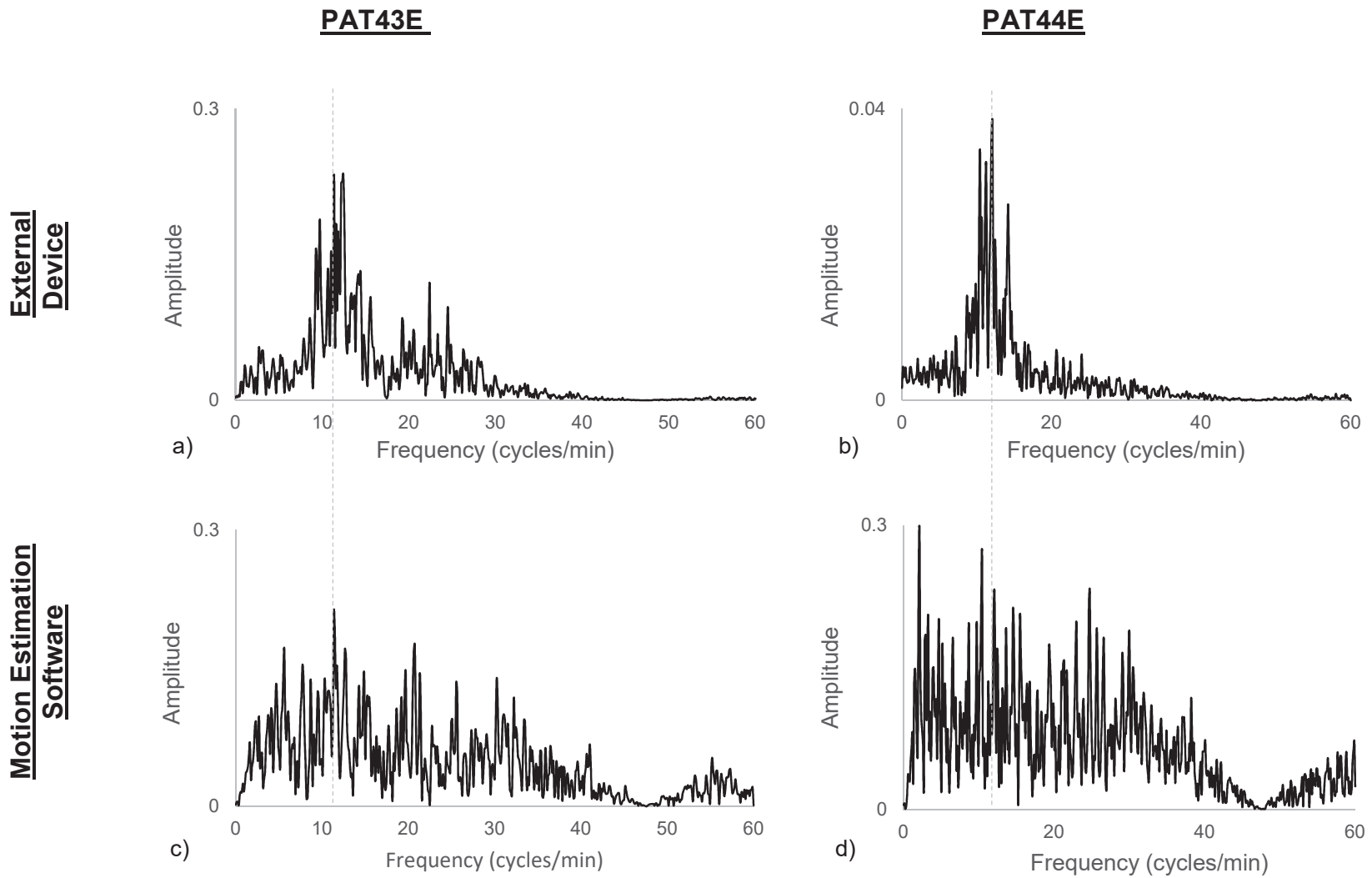


Figure 7-11 – Fourier transforms of the respiratory signals, (a) and (c) PAT43E from the external device and motion estimation technique respectively, (b) and (d) patient PAT44E from the external device and motion estimation technique respectively.

Patient Number (External Device)		40	41	42	43	44	45	46	47
Pearson's Correlation Coefficient		0.73	0.22	0.08	0.26	0.25	0.03	0.80	0.03
Significance, p.		<0.01	<0.01	0.02	<0.01	<0.01	0.36	<0.01	0.36
Frequency (Cycles/minute)	Motion Estimation Technique	14.8	4.1	21.0	11.4	2.1	20.6	8.3	15.7
	External Device	14.8	11.3	21.3	12.4	12.1	21.4	8.3	20.9
Motion (mm)*	(1) Respiratory Only (Method 1)	8.0	9.1	3.7	6.8	5.2	1.8	14.7	5.2
	(2) Respiratory and Patient (Method 2)	13	3.6 ⁺	0.3 ⁺	1.5 ⁺	6.2 ⁺	3.7 ⁺	14.5	1.4 ⁺
	(3) Respiratory and Patient (Method 3)	14.0	16.7 ⁺	15.8 ⁺	11.5 ⁺	14.6 ⁺	11.5 ⁺	15.6	14.7 ⁺

*Table 7.2 – The Pearson correlation coefficients, frequency and magnitude of motion for all eight patients. * Further details on the motion measurements are included in section 7.5.1 and figure 7-4. ⁺ The respiratory signal was not detected by the software, as demonstrated by no significant or a weak correlation with the external device, therefore these measurements are not a meaningful measure of the motion on the study.*

Discussion: There is a significant strong linear correlation between the respiratory signal and the external device for two patients, PAT40E and PAT46E. For these two patients the signals, figure 7-6 and figure 7-7, and the Fourier transforms of the signals, figure 7-10, were visually similar and the measured frequencies were identical.

Patient PAT42E and PAT43E demonstrated significant weak or very weak linear correlation with the external device, although the frequency of the signal from the software and external device were similar, table 7.2. Patients PAT41E and PAT44E demonstrated a significant weak correlation with the external device and different

frequency signals. A comparison of the signals for PAT43E and PAT44E, figure 7-8 and figure 7-9, show that the signals are not visually comparable. Comparison of the Fourier transform of the signals, figure 7-11, show that for PAT43E although the maximum frequency has been identified at the same point there are very different frequency distributions across the two signals. For both PAT43E and PAT44E the signal from the external device has a clear peak at approximately 12 cycles per minute, whereas the software signal has an almost relatively uniform distribution of frequencies. A similar appearance was observed for the signals and Fourier transforms for patients PAT41E and PAT42E. PAT45E and PAT47E did not demonstrate any significant linear correlation with the external device ($P > 0.05$).

These results indicate that for two out of the eight patients the software is correctly measuring the respiratory signal. In figure 7-6 and figure 7-7 the signals from the external device and motion estimation software are not identical. However, considering that these are measuring different physiologies (chest expansion due to respiration and heart motion due to respiration) they share a majority of features.

7.5.3 – No Significant and Weak Correlations

For the six patients that demonstrated no significant or weak correlations with the external device, this may be due to the following factors.

- Respiration having a minimal effect on the position of the heart, hence there being minimal heart motion to detect.
- The software not detecting the signal, possibly due to the image quality of the study

The respiratory motion of the heart was measured using method 1 and the counts per pixel in the heart and over the detectors were calculated as measures of image quality. The correlation between these measures of motion magnitude and image quality and the correlation between the motion estimation technique and external device were calculated.

Results: Figure 7-12 shows a very strong positive linear association ($r=0.82$, $P=0.01$) between the respiratory motion magnitude measured using method 1 and the correlation between the motion estimation technique and external device. There was no statistically significant linear association between the counts per pixel (over the detector or in the heart ROI) and the correlation between the motion estimation technique and external device, $r = 0.58$, $P = 0.13$ and $r = 0.29$, $P = 0.48$ respectively.

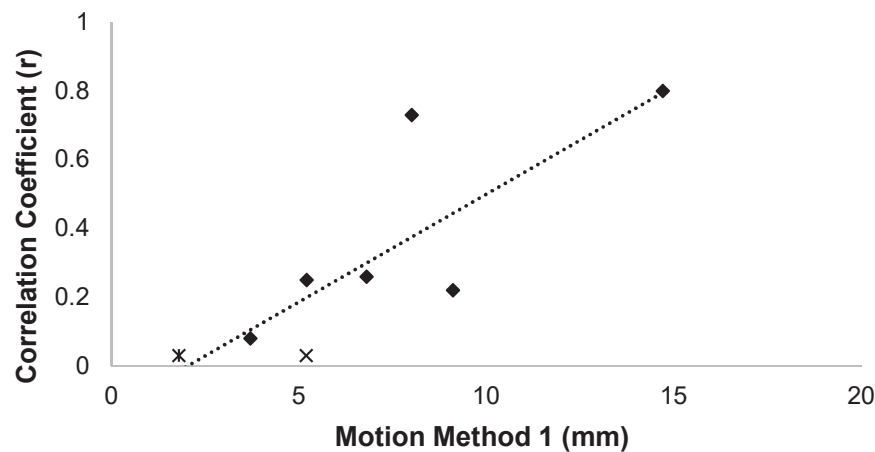


Figure 7-12 - The correlation between the motion estimation technique and external device, against the motion measured using method 1. Data for all patients are included. x - Insignificant correlation value.

Multivariate regression between,

- the motion of the heart measured using method 1 ($\beta = 0.71$, $P = 0.02$) and the counts per pixel over the detectors ($\beta = 0.37$, $P = 0.15$),
- the motion of the heart measured using method 1 ($\beta = 0.79$, $P = 0.03$) and the counts per pixel in the heart ROI ($\beta = 0.16$, $P = 0.54$),

determined that only the magnitude of the motion was a significant factor in the success of the motion estimation technique.

The images of detector 9 for PAT40E and PAT41E demonstrate the difference in the sub-diaphragmatic activity between the studies, figure 7-13.

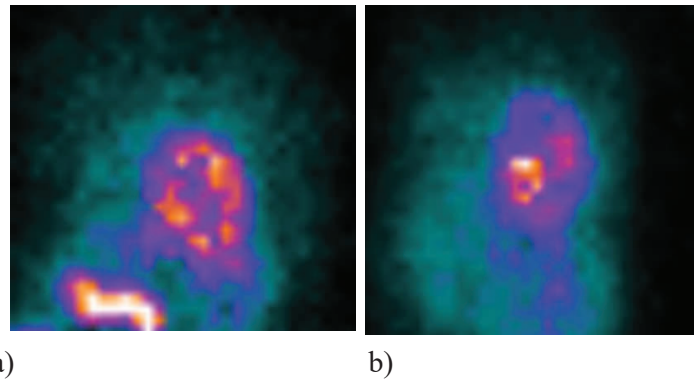


Figure 7-13 – The difference in sub-diaphragmatic activity between studies demonstrated on detector 9 for (a) PAT40E and (b) PAT41E.

Discussion: The positive association between the magnitude of the respiratory motion (method 1) and the correlation between the external device and motion estimation technique demonstrates that the smaller the displacement of the heart due to respiration, the more difficult it is to detect.

The lack of a significant association between the counts per pixel (in the heart ROI or over the detectors) and the correlation between the motion estimation technique and external device, and the multivariate analysis, suggests that successful detection of the signal does not depend on the counts in the study. However, it is expected that image quality should affect the success of the motion estimation technique. It may be that the variation in counts between the studies is not large enough to detect a relationship or that the sample size of 8 patients is too small. Eight patients was a practical number selected to validate the technique, however robust statistical analysis on the results was not envisaged. It may also be that the relationship between counts and successful motion estimation is more complex than the methods used, with the success of the technique depending on the distribution of the counts in areas of the image affected by respiratory motion. For example, the images of detector 9 for PAT40E and PAT41E, figure 7-13, show the difference in sub-diaphragmatic activity between the studies. The respiratory motion on these studies was 8.0 and 9.1mm respectively. The motion estimation technique did not successfully detect a signal for PAT41E. No sub-diaphragmatic activity was present on this study. On the PCA smoothed dynamic images for PAT40E the sub-

diaphragmatic activity demonstrated very clear respiratory motion and this may therefore have contributed to successful motion estimation for this patient.

7.5.4 – Motion Magnitude

The magnitude of the combined patient and respiratory motion was measured from the signal generated using the motion estimation technique, using method 2 and 3, figure 7-4 and table 7.2. These measures of motion are only meaningful if the motion estimation technique has successfully detected the signal.

When the motion signal was not detected by the software (as demonstrated by a poor - weak correlation coefficient) the motion measurement using method 2 was small (<6.2mm). When the motion signal is mainly noise, binning of the data based on this signal will be incorrect, with respiratory motion averaged across the bins resulting in minimal detectable motion between bins.

All the measurements of motion using method 3 were >11mm; this is a result of selecting the maximum and minimum values of the signal. For PAT40E and PAT46E, where the software correctly estimated the signal, motion using method 3 agreed with method 2 to within 1mm, showing that when the respiratory signal is successfully detected method 3 is reliable and can therefore be used as the basis for binning the data.

7.5.5 – Frame Duration

The largest respiratory frequency observed from the validation patients was 21 cycles/minute, range 8 – 21 cycles/minute, table 7.2, suggesting that a 1s frame duration would have been sufficient to measure respiratory motion for these patients. However, an eight patient sample is not large enough to draw any conclusions about the distribution of the respiratory frequencies over all patients undergoing MPI, and therefore no changes will be made to the technique and a 0.5s frame duration will be maintained.

7.5.6 – Summary

Below is a summary of the main points from this section.

- The respiratory signal was successfully detected for 2 out of the 8 validation patients and respiratory motion on these studies was $\geq 8\text{mm}$.
- There was no significant correlation with the external device for 2 out of the 8 validation patients and respiratory motion on these studies was $\leq 5.2\text{mm}$.
- Four studies had a weak or very weak correlation with the external device and out of these 3 had respiratory motion $\leq 6.8\text{mm}$.
- No correlation or a weak correlation with the external device is likely to be due to there being minimal heart motion to measure.
- PAT41E is an interesting case. Motion on this study was 9.1mm , however the software struggled to detect the motion signal. Although no significant association has been demonstrated between the count statistics of the study and the correlation between the technique and external device, anecdotally it has been suggested that there could be a more complex relationship between these two variables, based around the count density in regions affected by respiratory motion, such as sub-diaphragmatic organs as well as in the heart.

If this technique was implemented clinically, an external measure of motion would not be available and the only measures of the magnitude of motion would be method 2 and 3. These motion measurements are only reliable if the software has successfully detected the motion signal. Therefore, ideally there would be a quality measure that would indicate the quality of the measured signal and hence the reliability of the motion measurements.

7.5.7 – Conclusion

It has been demonstrated that the motion estimation technique can successfully detect the signal for respiratory motion $\geq 8\text{mm}$. For patients where the software was unsuccessful, this may be due to there being minimal heart motion to detect. PAT41E is the exception and may have been affected by the absence of sub-diaphragmatic activity.

7.6 – Quality Index

Motion correction should only be applied when the motion estimation technique has successfully detected the motion signal, as manipulation of the images with no benefit increases the risk of changing the images in a non-beneficial way. Additionally, the magnitude of the motion determined from the signal (method 2 and 3) is only reliable if the signal has been successfully detected. Therefore, a metric to identify the success of the technique is required.

Determining if the signal was respiration or noise was straightforward in the previous section as the signal from an external device was available for comparison, however in the clinical scenario this is not available and therefore signal quality may be much more difficult to evaluate. It can be difficult and subjective to determine through visual appearance alone if the signal is a true respiratory signal. This section will investigate the use of a quality index as an indicator of the quality of the signal.

7.6.1 – Method

It has been shown in section 6.4 that the first normalised coefficients are an alternative way of measuring the respiratory signal. Therefore, if there is a high correlation between the first normalised coefficients and the motion estimation technique, this might be indicative of a meaningful signal. If there is a low correlation, this would suggest that the signal is mainly noise. For the eight patients discussed in section 7.5, the first normalised coefficients from PCA analysis for detectors 2, 3, 8, 9 and 10 were averaged. The Pearson correlation coefficient between this average and the signal from the motion estimation technique was calculated. This correlation will be referred to from now on as the quality index. The

quality index was compared to the correlation that was measured between the motion estimation technique and the external device.

7.6.2 – Results

Figure 7-14 shows the correlation between the signal from the motion estimation technique and the average first normalised coefficients, termed the quality index, for PAT40E and PAT41E. Figure 7-14a demonstrates a significant strong linear correlation ($r = 0.96$, $P < 0.01$) for PAT40E, which demonstrated a significant strong linear correlation ($r = 0.73$, $P < 0.01$) with the external device. Figure 7-14b demonstrates a significant very weak correlation ($r = 0.08$, $P = 0.03$) for PAT41E, which demonstrated a significant weak correlation ($r = 0.22$, $P < 0.01$) with the external device.

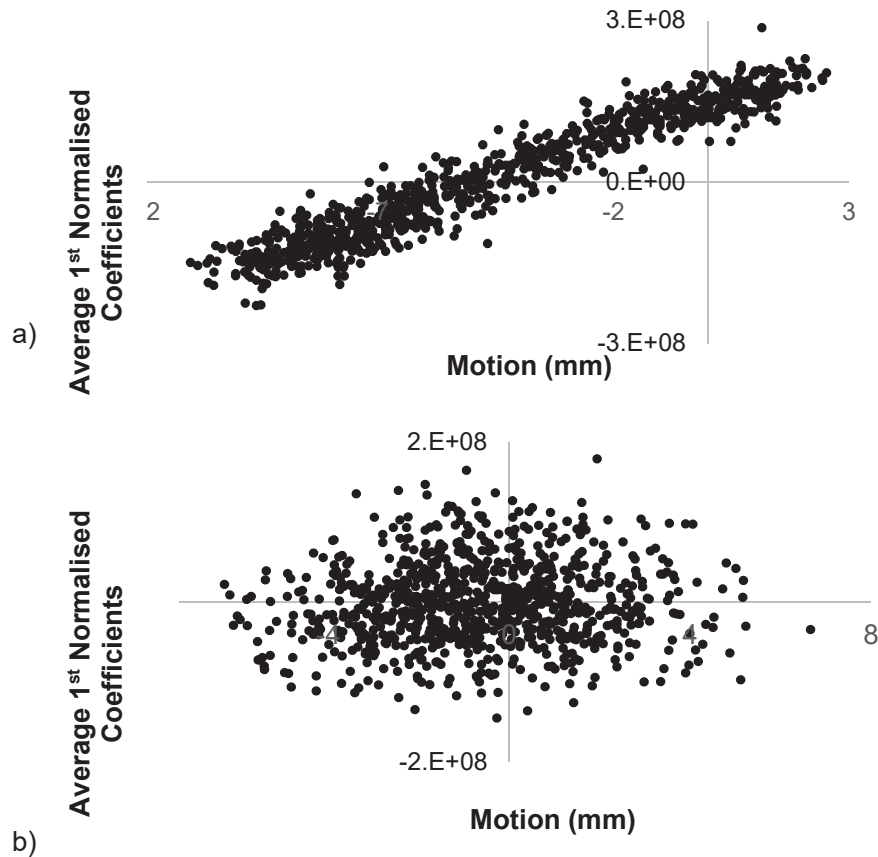


Figure 7-14 – The average first normalised coefficients against the signal from the motion estimation technique. (a) PAT40E, $r = 0.96$, $P < 0.01$ (b) PAT41E, $r = 0.08$, $P = 0.03$.

Figure 7-15 shows the values for the correlation between the motion estimation technique and external device, plotted against the quality index. Only values with significant correlations are included. Table 7.3 presents a look-up table between the quality index and the predicted correlation with the external device.

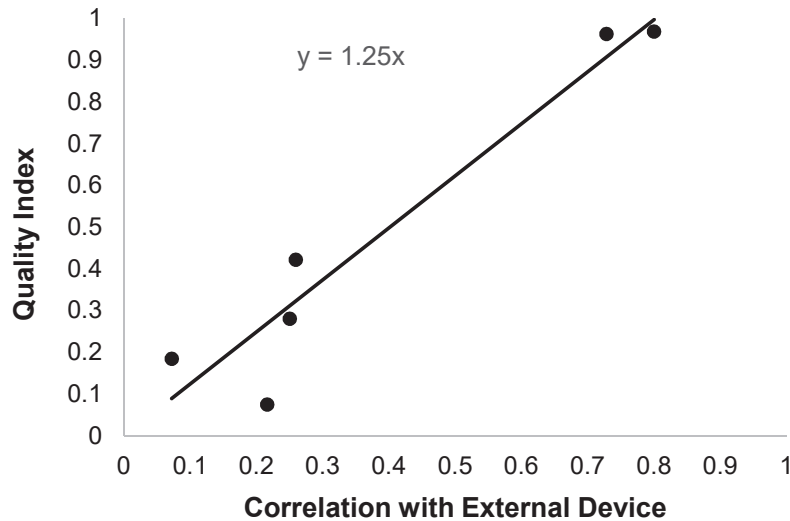


Figure 7-15 – The relationship between the external device and motion estimation technique correlation, and the quality index. Only values where both correlations were significant have been included.

Quality Index	Predicted Correlation with External Device
≤ 0.3	Very weak
$>0.3 \leq 0.5$	Weak
$>0.5 \leq 0.8$	Moderate
>0.8	Strong or very strong

Table 7.3 – The predicted correlation between the motion estimation technique and external device for different quality indices.

7.6.3 – Discussion

Figure 7-15 and table 7.3 demonstrate that the quality index can act as a surrogate for the correlation between the motion estimation technique and external device,

and it can therefore be useful for indicating if the measured signal is predominantly respiratory signal or noise. The quality index values were generally higher than the correlation between the technique and external device. This would be expected, as the normalised coefficients and signal from the motion estimation technique are based on the same parameter, motion of the heart, whereas the external signal is measuring chest expansion.

A cut-off limit to indicate a good quality signal is hard to define and it is doubtful that there is a discrete cut-off point between signal and noise; this is more likely to be a continuous scale where the level of noise in the signal gradually increases. No correlation coefficients with the external device were measured in the range 0.26 - 0.73, which is where any likely cut-off would lie. However, as a general rule if the quality index is >0.8 then a strong or very strong correlation with the external device is predicted and this is therefore a good measure of the respiratory signal. If the quality index is ≤ 0.5 a weak or very weak correlation is predicted and the measured signal is mainly noise.

7.6.4 – Conclusion

The quality index, which is the correlation between the average first normalised coefficients and the signal from the motion estimation technique, can be used as a surrogate for the correlation with the external device and therefore act as an indicator of the quality of the measured signal.

7.7 – Patient Application

Section 7.4 optimised the parameters for motion estimation and section 7.5 validated the technique against an external device. This section will apply the developed motion estimation and correction techniques as outlined in figure 7-16 to the cohort of patient studies described in section 7.2.

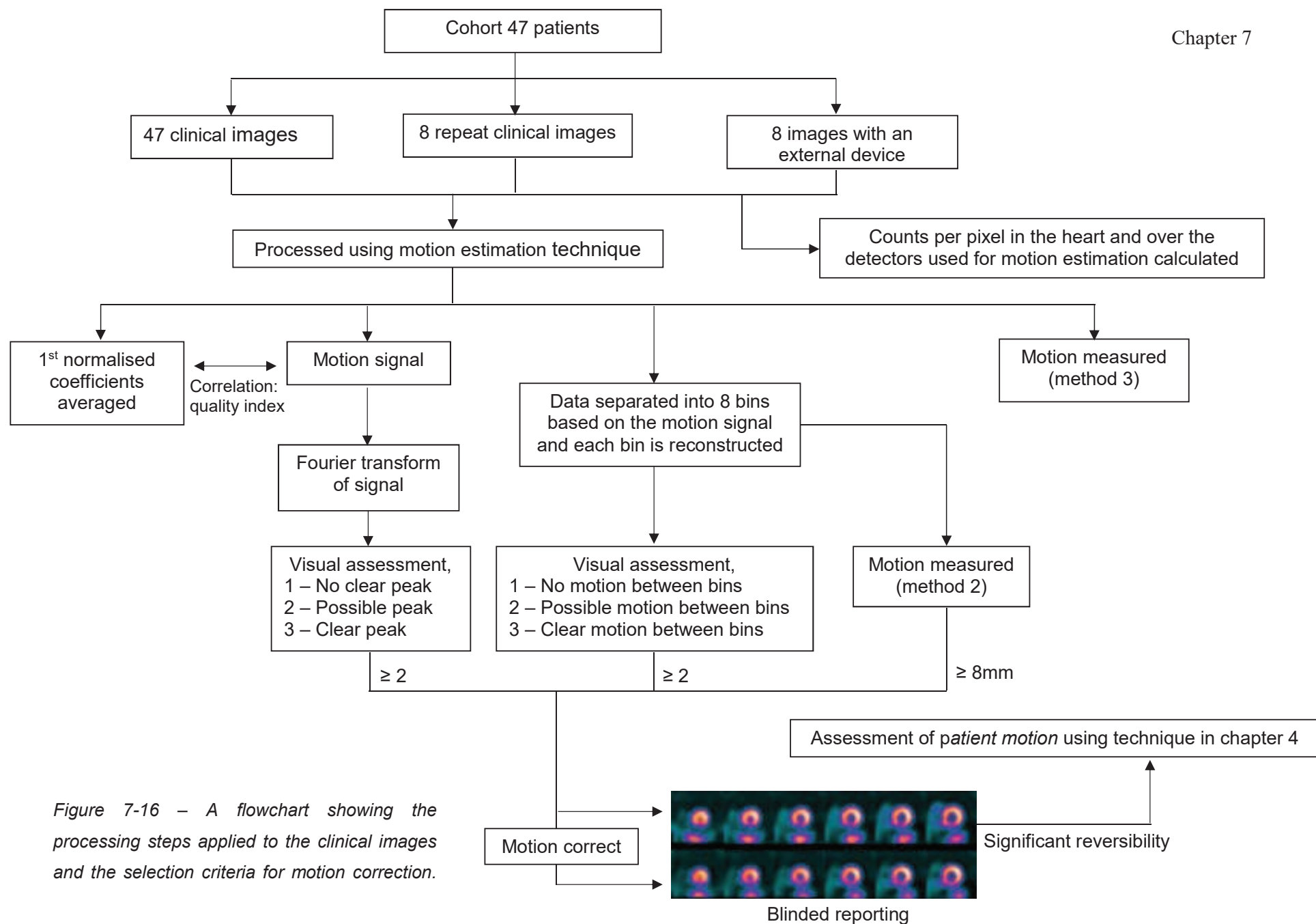


Figure 7-16 – A flowchart showing the processing steps applied to the clinical images and the selection criteria for motion correction.

7.7.1 – Image Processing

The respiratory motion estimation software using the parameters described in section 7.4 (0.5s images, averaging over detectors 2, 3, 8, 9,10 and post processing the signal with a Savitzky-Golay filter) was applied to 55 images acquired from 47 patients, section 7.2, including 47 original clinical images and 8 repeat clinical images. Motion on the study was determined using method 2 and 3 as described in section 7.5.1 and summarised below;

Method 2: The measured signal is divided into 8 bins, which are reconstructed and registered.

Method 3: The difference between the maximum and minimum values of the signal from the motion estimation technique.

The quality index for each study was determined as described in section 7.6 and the average counts per pixel across the detectors and within a region around the heart, were determined as described in section 7.5.

7.7.2 – Identifying Significant Motion

The Fourier transforms of the signals were reviewed and scored from 1 - 3, where; 1 – no clear peak, 2 – possible peak at a frequency in the physiological range for respiratory motion and 3 - clear peak. The eight reconstructed binned images generated to measure the magnitude of the motion using method 2 were reviewed as a dynamic image and motion visualised between the bins was scored on a scale of 1 - 3, where; 1 – no motion between bins, 2 – possible motion between bins and 3 – clear motion between bins.

To ensure that all images with respiratory motion were selected for motion correction, images were included if any of the criteria below were met.

1. Motion measured using method 2, $\geq 8\text{mm}$
2. A Fourier transform score of 2 or 3
3. A visual motion score of 2 or 3

A value of 8mm was selected as, due to the technique used to determine the bin size, motion <8mm would only generate one bin and motion correction would not be performed. Also, this was identified in section 5.3.2 as the value above which significant *patient motion* artefacts appeared. Due to the difference between the patterns of patient and respiratory motion, this is a very conservative estimate of the amount of respiratory motion that causes significant motion artefacts. The point above which respiratory motion artefacts become significant is more likely to be in the region of 12-13mm, as discussed in section 3.8. If a study was identified for motion correction by criteria 2 or 3 but the measured motion was <8mm, then the study was motion corrected using two equal sized bins.

7.7.3 – Blinded Reporting

All the selected images were then reconstructed and displayed as a stress-rest study, with the image prior to motion correction as the stress study and the image after correction as the rest study. These were blindly reported by two experienced reporters, who were asked to identify the location of any reversible defects and classify the significance of the reversibility as complete, partial or insignificant. Where the reporters disagreed, they were asked to reach a consensus decision. Studies were identified as having significant motion artefacts if reversibility was identified between the images. The eight additional images that were acquired with an external device were also assessed using the above criteria and images meeting the criteria were included for blinded reporting.

7.7.4 – Distinguishing Between Respiratory and Patient Motion Artefacts

For images where significant reversibility was identified, the images corrected for *patient motion* only using the software developed in chapter 4 and displayed in the same way, stress – no patient motion correction, rest – patient motion correction, were also reviewed for reversibility to determine if differences were due to patient or respiratory motion.

7.7.5 – Results

Table i, Appendix B, summarises the results for all the patients. Out of the 55 clinical images (excluding the validation patients), 53%, 18%, 18%, 7%, 2% and 2% had 0-4, 4-8, 8-12, 12-16, 16-20 and 20-24mm motion measured using method 2, figure 7-17. The motion measurement (method 2), Fourier transform score and visual motion scores are summarised in figure 7-18. Twenty-five clinical images were selected for motion correction, in addition to two validation images.

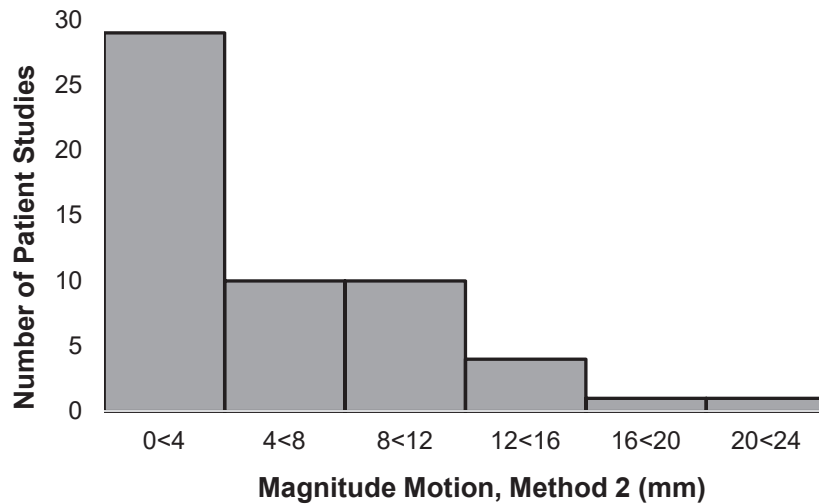


Figure 7-17 – The magnitude of respiratory motion across the 55 clinical images in the patient cohort. The measurements from the validation patients are not included.

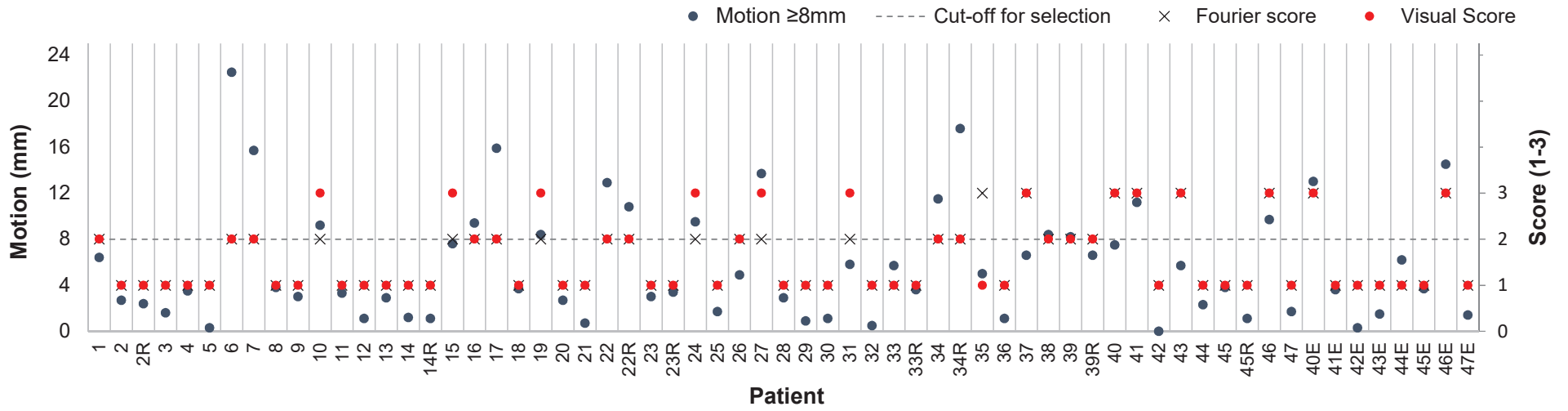


Figure 7-18 – The magnitude of the motion, the Fourier transform scores and visual motion assessment scores for 63 patient images, consisting of 47 clinical images, 8 repeat clinical images and 8 additional images acquired with an external device.

Out of the 25 clinical images identified for motion correction, five were reported as having visual differences between the images before and after respiratory motion correction by reporter 1, with the differences for three of these being classed as significant, table 7.4. Two were reported as having significant differences between the images before and after respiratory motion correction by reporter 2, table 7.4. The study where the reporters disagreed was jointly reviewed and the consensus was that the difference was “of doubtful clinical significance”. Out of the 2 validation patients that were identified for motion correction both reporters identified significant differences for one of these. None of these artefacts were identified on the images corrected for patient motion only and they can therefore be attributed to respiratory motion.

The three images where the reporters agreed on the presence of a significant difference before and after motion correction were PAT6, PAT17 and PAT46E. Figure 7-19, figure 7-20 and figure 7-21 show the images before and after motion correction, presented in the format of a stress-rest study for these three patients.

The data in figure 7-22 splits the magnitude of the motion and quality index measured into three categories;

1. Clinical images that did not meet the defined criteria for motion correction.
2. Clinical images that did meet the criteria but no differences were identified between the images before and after motion correction by the reporters.
3. Clinical images that did meet the criteria and a significant difference was identified between the images before and after correction by the reporters.

Motion measured using method 2 was <6, 5-18 and 16-23mm and method 3 was 5-18mm, 3-18mm and 15-19mm for categories 1, 2 and 3 respectively, figure 7-22a,b. The quality index values were 0.09-70, 0.35-0.94 and 0.81-0.96 respectively, figure 7-22c. Figure 7-23 shows the association between the quality index and counts per pixel over the detectors and in the region of the heart.

Patient	Reporter 1			Reporter 2			Consensus
	Reversibility	Location	Significance	Reversibility	Location	Significance	
6	Yes	Inferior Antero-basal	Partial Partial	Yes	Inferior Infero-lateral Anterio-basal	Partial Partial Complete	Reversibility
17	Yes	Infero-septal	Partial	Yes	Inferior Inferior-septal	Partial Partial	Reversibility
26	Yes	Inferior Infero-septal	Insignificant Insignificant	No	-----	----	No Reversibility
27	Yes	Inferior	Partial	No	-----	----	Changes in the anterior and inferior bases, of doubtful clinical significance
41	Yes	Infero-basal Antero-basal	Insignificant Insignificant	No	-----	----	No Reversibility
46E	Yes	Antero-lateral Infero-lateral	Partial Partial	Yes	Antero-lateral Inferior	Partial Partial	Reversibility

Table 7.4 - The images identified as having areas of reversibility by both reporters, the location of the reversibility and the significance.

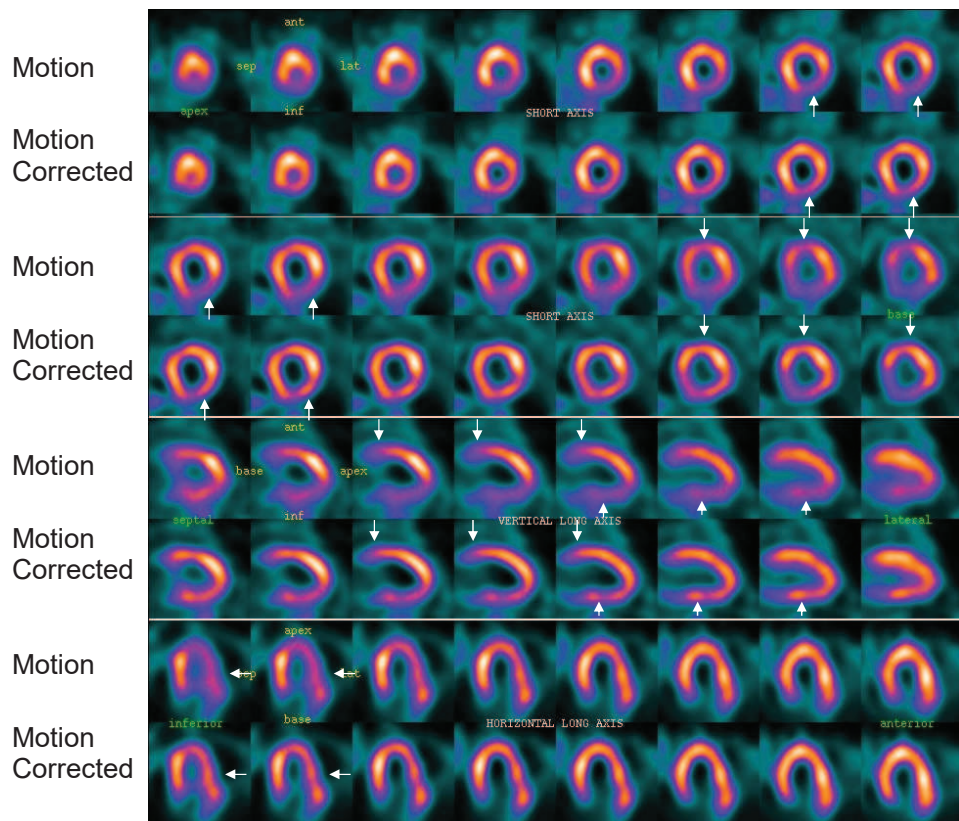


Figure 7-19 – The images for PAT6 corrected using data binned according to the motion estimation signal. The arrows represent areas of reversibility identified by both reporters.

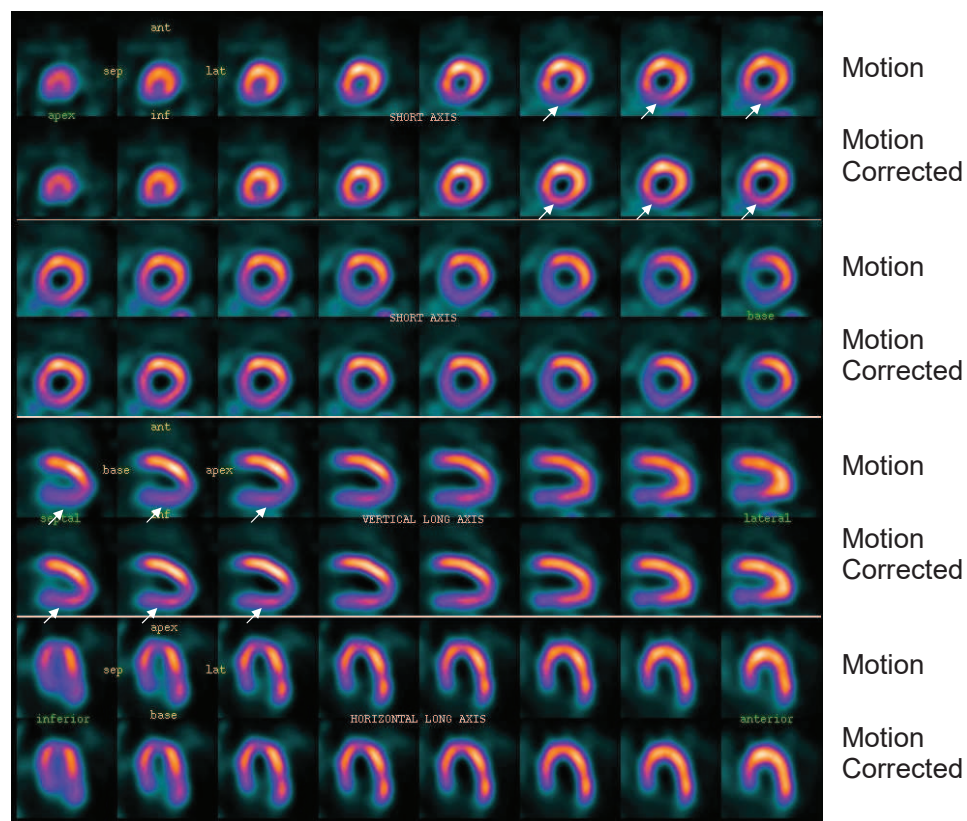


Figure 7-20 – The images for PAT17 corrected using data binned according to the motion estimation signal. The arrows represent areas of reversibility identified by both reporters.

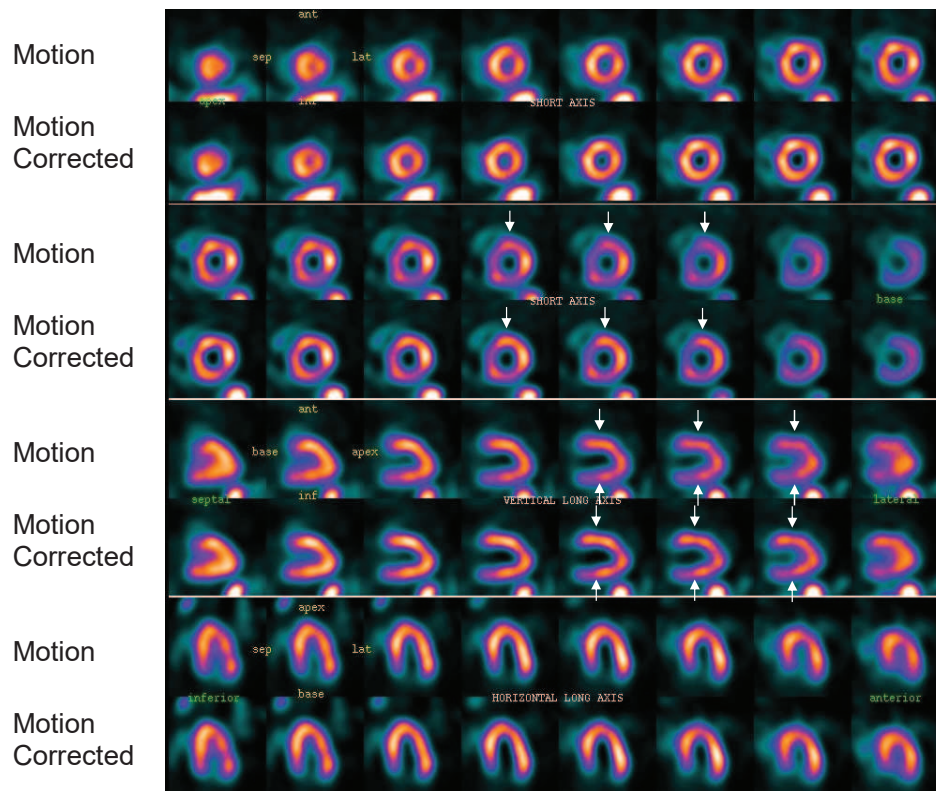
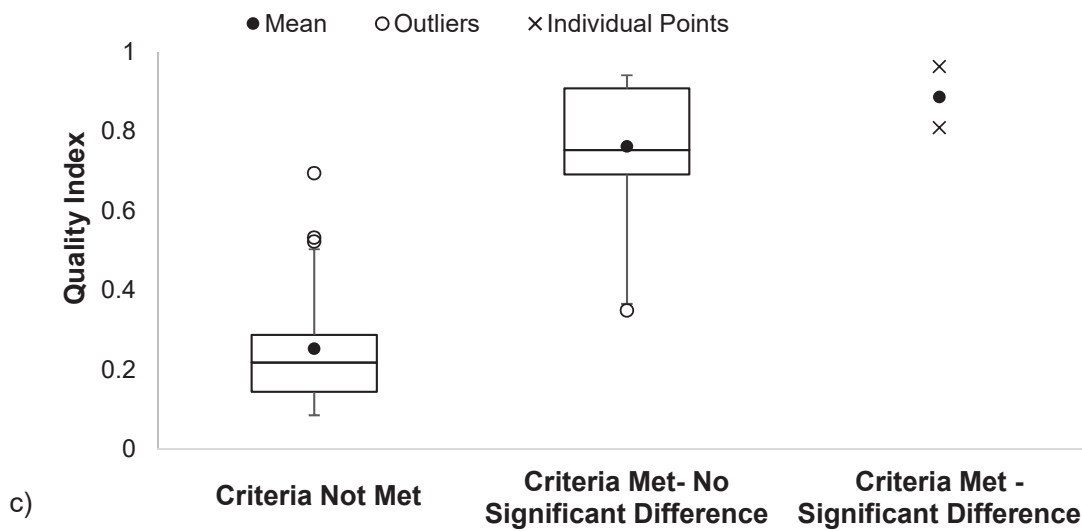
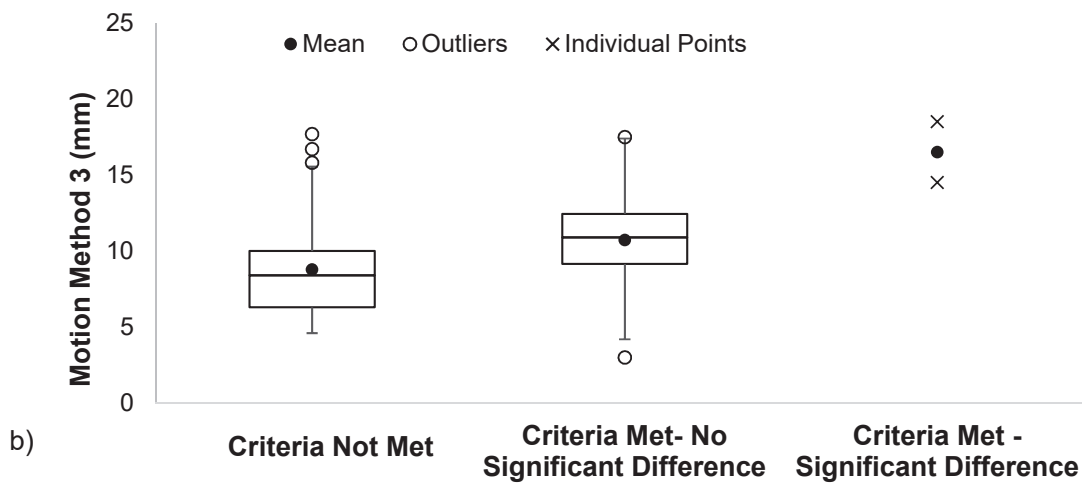
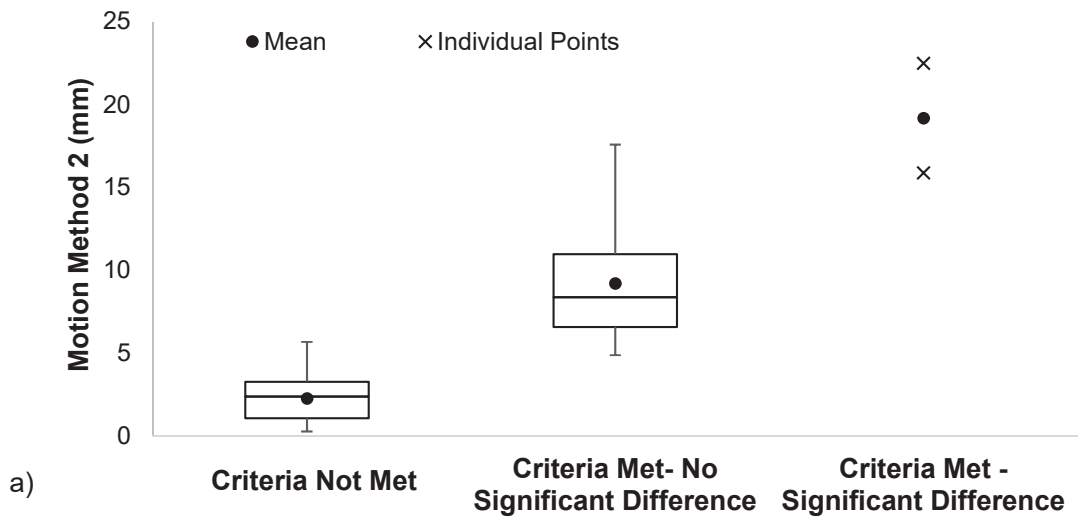


Figure 7-21 – The images for PAT46E corrected using data binned according to the motion estimation signal. The arrows represent areas of reversibility identified by both reporters



← Figure 7-22 – The (a) magnitude of motion measured using method 2, (b) magnitude of motion measured using method 3, (c) quality index, categorised according to images that did not meet the criteria for motion correction, as defined in figure 7-16, ($n = 30$), images that did meet the criteria but no significant difference was reported before and after motion correction ($n = 23$), and for images where a significant difference was identified between the images with and without respiratory motion correction by both reporters ($n = 2$). Values for the quality index that were not significant and patient data acquired using the external device have not been included.

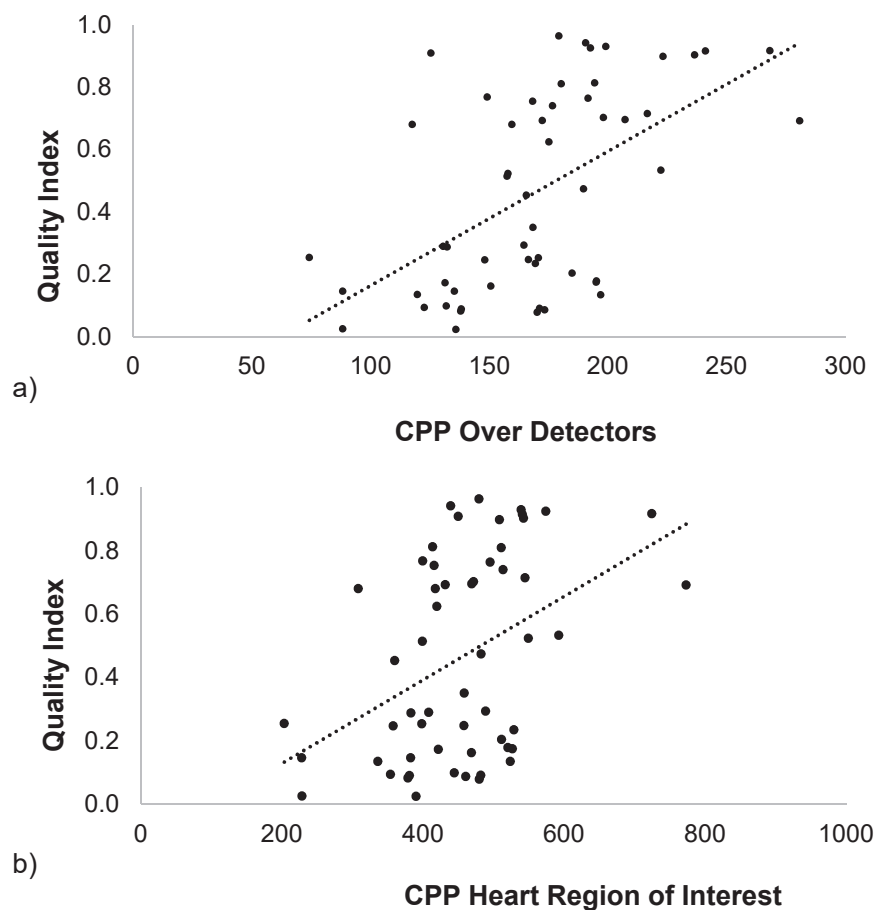


Figure 7-23 – The association between the quality index and the average counts per pixel across the detectors ($r = 0.56$, $P < 0.01$) and in a region around the heart ($r = 0.42$, $P = 0.01$), for the detectors used for motion estimation. CPP – counts per pixel.

7.7.6 – Discussion

Magnitude of Motion: The average respiratory motion across the clinical images was $5.8 \pm 5.0\text{mm}$ (range: 0 - 22.5mm). There was no significant association between the magnitude of motion and patient weight, gender and pharmaceutical used for stressing.

Identifying Significant Motion: Images with respiratory motion were identified if they met the specified criteria. All the images identified for motion correction met either criteria 2 or 3, section 7.7.2; there were no cases where the motion was measured to be $\geq 8\text{mm}$ but this was not identified either on the Fourier transform or visually between the reconstructed binned data. This demonstrates the appropriateness of the criteria for selecting images with motion.

Image Reporting: Two clinical images and one validation image were identified as having significant differences in appearance before and after motion correction. The areas affected were mainly the inferior and anterior walls. The stress – rest reports for these, figure 7-19, figure 7-20 and figure 7-21, all show areas of perfusion that appear improved after motion correction, suggesting that respiratory motion blurs the images and makes areas appear artificially reduced. The fact that these present in the anterior and inferior walls is consistent with respiratory motion being most prominent in the cranio-caudal direction (Kennedy and Strauss, 2016). These motion artefacts could potentially affect clinical interpretation. This demonstrates that for our patient cohort 2 out of 55 clinical images and 1 out of 8 validation images were affected by motion artefacts.

Indicators of Significant Motion: If this technique were to be implemented clinically then using the criteria presented to identify patients for motion correction would be onerous and subjective. An alternative measure is therefore required.

The motion measurement using method 2, figure 7-22a, shows a clear distinction between the three groups, mean ($\pm\text{SD}$) values, 2.3mm (± 1.3), 9.2mm (± 3.4) and 19.2mm (± 4.7) for group 1, 2 and 3 respectively. Using this motion measurement, a cut-off value to select images that are likely to have motion artefacts can be identified. A sensible cut-off is approximately 11mm, which is the third quartile of

group 2. This is less than the minimum magnitude of motion of 14.5mm that resulted in significant artefacts, thus allowing for a degree of error in the measurement, however this excludes all the images that did not meet the selection criteria and 75% that did meet the criteria but did not have motion artefacts. Out of the patient cohort this would have identified 8 out of 55 of the clinical images for motion correction. The disadvantage of using motion measured using method 2 is that this involves additional processing to bin the data into 8 bins and then register these to get this measure of motion.

Measuring motion using method 3 does not require any additional processing as it is measured directly from the respiratory motion signal generated by the motion estimation technique, however, figure 7-22b shows that this is a less reliable method of identifying images with significant motion as there is overlap between all three groups.

The quality index, figure 7-22c, shows a clear separation between the images that do not meet the criteria and do meet the criteria for identifiable respiratory motion, mean (\pm SD) values, 0.25 (\pm 0.16) and 0.77 (\pm 0.17) respectively. The separation between the images that meet the criteria without and with significant motion artefacts is less defined, 0.77 (\pm 0.17) and 0.89 (\pm 0.11) respectively. Using a quality index of 0.70, which is the first quartile of group 2 to identify images for motion correction would have identified all the images with motion artefacts and 75% of the images with respiratory motion and no artefacts. Combining the criteria and selecting images with >11mm motion measured using method 2 and with a quality index >0.7 would have identified 7 images for motion correction, including all the images identified as having motion artefacts.

A degree of caution needs to be applied when defining criteria to identify images for motion correction as the sample size of group 3 is very small ($n=2$) and cannot be relied upon to be a clear representation of the range of values expected for respiratory motion artefacts. Therefore, using a quality index of 0.7 is a sensible cut-off value. This will identify images with respiratory motion as opposed to noise, however this is not too restrictive and does not risk excluding patients that may have respiratory motion artefacts. Out of this patient cohort, 17 out of 55 of the clinical

images would have been selected for motion correction. Motion of the selected patients would have been, mean (\pm SD), 11.6mm (\pm 4.3) and motion of the unselected patients would have been 3.2mm (\pm 2.4).

Image Quality: The overall counts in the images were similar, however the counts per frame for patients 1-39 were generally higher than that for patients 40-47, due to the clinical imaging protocol changing between recruitment of these patients. The protocol applied to patients 1-39 used 500MBq administered activity and 360s imaging time and the protocol applied to patients 40-47 used 400MBq administered activity and a 450s imaging time. This resulted in a reduction in the counts per 0.5s frame of 20% for patients 40-47. The ability of the software to detect the respiratory signal may therefore be reduced for these patients due to decreased count statistics in the individual frames.

On the validation patients, section 7.5, no significant association was found between the counts per pixel in a region around the heart and averaged over the detectors and the success of the motion estimation technique. In this larger sample of clinical patients, figure 7-23 shows that there is a moderate positive association between the quality index and the counts in the heart ROI ($r = 0.42$, $P = 0.01$) and over the whole detector ($r = 0.56$, $P < 0.01$), demonstrating that the robustness of the technique will depend on the administered activity and time of imaging after injection.

Frequency: The highest frequency of respiratory motion measured from the images that met the selection criteria was 22 cycles/minute, which is similar to the highest frequency measured from the validation patients of 21 cycles/minute, suggesting that 1s images would have been sufficient to detect the respiratory signal on the MPI images.

7.7.7 – Conclusion

Out of the clinical images 45% (25 images) were identified as having respiratory motion and 4% (2 images) were identified as having significant respiratory motion artefacts. One of the eight validation images had significant respiratory motion artefacts. The images with motion artefacts had ≥ 15 mm motion measured using

method 2. A quality index of ≥ 0.7 can be used as a conservative limit to identify images that would benefit from motion correction.

7.8 – Summary

A strong correlation has been demonstrated between the respiratory motion estimation technique and external device for two out of the eight validation patients. Significant respiratory motion artefacts were visually identified for one of these patients. When the respiratory signal was not recovered by the motion estimation technique, this was mainly a result of there being minimal heart motion to detect. It has been demonstrated that a quality index, calculated from the correlation between the average first normalised coefficients and the signal from the motion estimation technique, is a good metric for the quality of the motion estimation signal. A quality index of ≥ 0.7 provides a reasonable limit for identifying images for motion correction. Out of 55 clinical images 4% (2 images) were identified as having significant respiratory motion artefacts. Images with motion artefacts had $\geq 15\text{mm}$ motion measured using method 2, which divides the signal into 8 bins and registers the reconstructed bins to measure motion.

8 – Summary and Discussion

This work has addressed the issue of patient and respiratory motion during myocardial perfusion imaging on the DNM 530c. At the start of this thesis in 2010 it was assumed in many review articles that motion would be reduced on this system due to shorter imaging times. There was very little published literature on patient or respiratory motion on the DNM 530c and over the course of this work the published literature in this area has increased, as demonstrated by table 2.6 and table 2.7.

The summary and discussion will be divided into sections covering; (1) the effect of motion on MPI images, (2) patient motion estimation, (3) respiratory motion estimation, (4) motion correction, (5) application of the techniques to patient studies, (6) principal component analysis and (7) limitations.

8.1 – Effect of Motion

8.1.1 – Patient Motion

A mathematical model was initially presented, section 3.2, which identified the dominant factors for the introduction of MPI motion artefacts to be the magnitude of the motion, the percentage of the acquisition affected by motion and the measured myocardial thickness. Considering the scale of the assumptions made for this model the results were fairly consistent with the results of the phantom simulations, section 3.7. Many limitations still remain with the phantom study, including that motion was simulated post acquisition and not during the acquisition, the effects of cardiac motion were not included and the normal database did not incorporate physiological variations between patients, however limitations aside, this phantom study is the first to systematically review the effects of motion on the DNM 530c system.

Subsequently Kennedy and Strauss, (2016) and Salvadori et al., (2018) published similar phantom studies to assess the effect of patient motion on the DNM 530c, table 2.6. Kennedy and Strauss, (2016) simulated motion during the acquisition by pausing the acquisition and moving the phantom. This is preferred over the method

used in this thesis as the motion data are all contained within one list mode file which can then be reframed as required. The method used in this thesis combined reframed images post acquisition to simulate motion, limiting reframing for motion correction to the time intervals used to simulate the motion. Therefore, in our study there was no residual motion in the bins used for motion correction, which may have made the performance of our motion correction method appear improved compared to the performance that would be demonstrated in clinical practice. Salvadori et al., (2018) combined half time acquisitions to simulate motion, however motion in the X and Z directions was achieved by moving the phantom on a horizontal printed target. This may have resulted in less accurate simulated shifts compared to this study, however the technique enabled acquisitions to be performed in areas of the quality field of view that could not be obtained through movement of the bed and gantry alone.

A limitation of the work by Kennedy and Strauss, (2016) and Salvadori et al., (2018) is that scattering material and background activity were excluded. These will affect the appearance of motion artefacts, as attenuation results in non-uniform uptake in the myocardium and scatter reduces the image resolution. As images are displayed relative to the global maximum the visual effect of patient motion in areas affected by attenuation may be different for the same amount of motion than when attenuation is excluded. Kennedy and Strauss, (2016) simulated low noise phantom studies using 26MBq in the myocardial section of the cardiac phantom for a 5 minute acquisition. The activity used in this study was 8MBq in the myocardial section of the phantom for a 6 minute acquisition, which equates to 9.6MBq for a 5 minute acquisition. Considering that the counts detected by the phantom study in this thesis will also be reduced by attenuation, then the image quality obtained by Kennedy and Strauss, (2016) will be superior to in this study. Salvadori et al., (2018) used 10MBq in the myocardial section of the cardiac phantom, however the imaging time is not stated. Kennedy and Strauss, (2016) performed visual and quantitative TPD analysis, using a TPD limit for significant motion artefacts of >5%. It is not clear if the normal database used for the TPD analysis was generated from patient images or non-attenuation corrected phantom data; the former would reduce the sensitivity for detection of motion artefacts as it would take into account the variability between patients, which the phantom study presented in this thesis did

not include. Salvadori et al., (2018) analysed the images through comparison of segmental activities based on a 17 segment model, with abnormal segments defined as <65% uptake.

Considering the differences between the studies, the results obtained were consistent. In chapter 3 significant motion artefacts were detected for ≥ 10 mm motion for $\geq 17\%$ of the acquisition. Kennedy and Strauss, (2016) identified artefactual perfusion defects for > 10 mm motion and Salvadori et al., (2018) identified abnormal segments for ≥ 10 mm motion on the DNM 530c. Both Kennedy and Strauss, (2016) and Salvadori et al., (2018) only evaluated step motion and they were therefore unable to draw any conclusions on what percentage of the acquisition needs to be affected by motion to result in artefacts.

8.1.2 – Respiratory Motion

The dynamic respiratory motion phantom study performed in section 6.7 was useful for evaluation of the software and optimisation of the technique, however the motion of the platform was fixed and therefore no analysis could be performed on the magnitude of respiratory motion that introduces significant motion artefacts. Extrapolation of the results of the phantom study on patient motion, section 3.8, suggested that respiratory motion in the region of 12-13mm would introduce significant motion artefacts. Ko et al., (2015) performed a similar but more detailed dynamic phantom study using a moving platform that simulated sinusoidal motion in a cranio-caudal direction with magnitudes of 2.5 - 25mm in 2.5mm intervals and reported significant visual and quantitative image deterioration when motion was ≥ 15 mm. The limit for motion artefacts in patients may vary from these values as respiratory motion does not typically follow a sinusoidal pattern but has a dominant end expiratory phase (Kovalski et al., 2007).

8.2 – Patient Motion Estimation

At the start of this study there were no commercial or published methods available for patient motion estimation and correction on the DNM 530c. The techniques for patient motion estimation presented in this thesis, using five projections to determine

three motion vectors, were first presented Redgate et al., (2012) and then published as a full paper Redgate et al., (2016).

Two alternative methods of patient motion estimation and correction on the DNM 530c have also been proposed. The manufacturer of the system has released motion estimation and correction software (MDC for Alcyone, Xeleris workstation, GE Healthcare) that tracks the centre of mass within a region around the heart on five projections. Van-Dijk et al., (2016) evaluated this software on phantom and patient studies, simulating motion in a similar way to Kennedy and Strauss, (2016), pausing the acquisition and moving the table every 20s. The activity used was similar to the activity used in the phantom simulations in this study. Attenuation and scatter were also simulated by placing the insert inside a Jaszczak phantomTM, however background and liver activity were not included. Table 8.1 compares the errors measured for the techniques developed in this thesis to the errors measured by Van-Dijk et al., (2016) for the MDC for Alcyone software.

Direction	Mean (\pm 1SD) Absolute Errors on the Technique (mm)		
	Planar Technique	Three-Dimensional Technique	MDC as Evaluated by Van-Dijk et al., (2016)
Cranial-caudal	0.7 \pm 0.4	0.6 \pm 0.4	0.8 \pm 0.6
Lateral	0.1 \pm 0.1	0.6 \pm 0.5	1.1 \pm 0.8
Ventral-Dorsal	1.9 \pm 1.5	0.9 \pm 0.7	1.1 \pm 0.8

Table 8.1 - The mean absolute errors for the patient motion estimation techniques developed in this thesis compared to the mean absolute errors measured by Van-Dijk et al., (2016).

It is not clear whether Van-Dijk et al., (2016) evaluated the errors from the indicative values displayed during the acquisition or from the values saved in the image header. Taking this into consideration, the errors measured by Van-Dijk et al., (2016) are similar to the techniques developed in this thesis. The advantage of the techniques presented in this thesis are that they supply the user with a measurement of the overall motion, which allows a quick assessment of the

significance of the motion to be made through comparison to a conservative limit, such as the limit of $\geq 8\text{mm}$ that was used in the patient analysis in chapter 5. This can be determined visually from the graph presented by the motion detection and correction software (MDC for Alcyone, Xeleris workstation, GE healthcare) evaluated by Van-Dijk et al., (2016), however it makes the process of deciding whether motion correction is required more subjective.

Kennedy and Strauss, (2016) also present motion estimation and correction techniques for the DNM 530c. The data are reframed into 10s images and the change in the centre of mass is calculated for each projection, however no region of interest is generated around the heart on the projection images to exclude sub-diaphragmatic activity. If the sub-diaphragmatic activity is also affected by motion then this technique will benefit as there will be more information present from which to derive the shifts of the heart, however if the sub-diaphragmatic activity is not affected by the motion or the relationship between the magnitude of the motion of the heart and sub-diaphragmatic activity is non-linear then this may introduce errors into the motion estimation technique.

In this thesis the aim of patient motion estimation was to evaluate motion in all three orthogonal planes separately, therefore 2 projections were averaged in the ventral-dorsal and lateral directions. Three projections were averaged for cranial-caudal motion. As the errors using this technique were low compared to the motion being measured, the improvement gained from averaging more projections for cranio-caudal motion was not investigated. The approach taken by Kennedy and Strauss, (2016) is that the motions in all planes are combined using equation 8.1 to get one measure of motion (P), where $x_{com}(t)$ and $y_{com}(t)$ are the location of the centre of mass in the x and y directions at time t and equally $x_{com}(0)$ and $y_{com}(0)$ are the centre of mass coordinates at t = 0 and k is the projection number.

$$P = \sqrt{\sum_{k=1}^{19} [x_{com}(t) - x_{com}(0)]_k^2 + [y_{com}(t) - y_{com}(0)]_k^2} \quad \text{Equation 8-1}$$

This is an interesting technique as it allows data from all projections to be utilised. For all projections the y direction is equivalent and equates to the cranio-caudal patient motion, however the motion vectors in the x direction on the detectors

consist of varying contributions of the lateral and ventral-dorsal motion vectors depending on the angle of the detector relative to the X and Y axes of the patient. This method therefore prioritises patient motion in the cranio-caudal direction, reducing the sensitivity of the technique to motion in the other planes.

The two techniques, the motion detection and correction software (MDC for Alcyone, Xeleris workstation, GE Healthcare) evaluated by Van-Dijk et al., (2016) and the technique proposed by Kennedy and Strauss, (2016), both measure motion on the projection images. There are no other studies in the literature that have used reconstructed images. The reconstruction process will increase the noise on the images and therefore it may be expected that the errors for this technique would be increased compared to planar techniques. However, for the count levels in our study this has not been demonstrated and no significant difference was found between the errors on the planar and three-dimensional techniques. One advantage of the three-dimensional technique, which also may explain why no increase in the errors was observed, is that estimating the motion between reframed reconstructed images utilises all the information available from the study, as opposed to rejecting 74% of the available data (14 out of 19 projections) as is the case for the planar technique presented in the thesis and the motion detection and correction software (MDC for Alcyone, Xeleris workstation, GE Healthcare), or suppressing the contribution of lateral and ventral-dorsal motion components as is the case for the technique by Kennedy and Strauss, (2016). Using reconstructed reframed data uses all the data to get motion in the three orthogonal directions and then, if an overall vector of motion is required, this can be calculated using equal contributions from all three planes. In addition, the three-dimensional technique measures the true shift of the heart, removing errors associated with scaling factors and positioning in the QFOV.

8.3 – Respiratory Motion Estimation

Chapter 6 adapted the motion estimation technique to include principal component analysis. This was implemented in two ways; (1) PCA smoothing the images which are then registered to measure motion and (2) using the first normalised coefficients as a surrogate for the respiratory signal. The former was adopted and the technique was optimised for respiratory motion estimation. The mean and the first two principal

components were used for PCA smoothing; this is consistent with work performed by Thielemans et al., (2011) who performed PCA analysis on PET data to determine the respiratory signal.

Since the start of this study other research groups have also published methods to address respiratory motion on the DNM 530c. Clerc et al., (2017) proposed using breath hold techniques, however the disadvantage of this technique is that it prolongs the imaging time and relies on patient compliance. Ko et al., (2015) and Daou et al., (2017b) both reframe the data into 0.5s images, with motion estimated from the centre of mass within a region around the heart for all detectors, and with the REGAT software respectively. The REGAT software is described as “a *data driven respiratory motion curve using a statistical method specifically adapted to handle low signal-to-noise ratio data*”, however no specific details of the technique can be found in the literature. The motion detection and correction software (MDC for Alcyone, Xeleris workstation, GE Healthcare) uses the same motion estimation technique that was used for patient motion; measuring the centre of mass of the counts in a region around the heart on five detectors. This technique was evaluated by Van-Dijk et al., (2016) using 1s reframed images.

There is variability in the reframed image duration used for respiratory motion estimation. All the studies apart from Van-Dijk et al., (2016) use 0.5s images, which is consistent with the approach that has been taken in this thesis. This is the Nyquist limit when the theoretical range of respiratory motion frequencies is considered. However, the frequencies measured for the patients selected for motion correction in this thesis were 10.9 ± 5.0 cycles/minute, with a maximum frequency of 22 cycles/minute, suggesting that 1s images could have been used. This is lower than the frequency of respiratory motion measured during MPI imaging in other studies; Ko et al., (2015) and Bitarafan et al., (2008) measured the mean respiratory frequency to be 17 and 18.5 cycles/minute respectively.

The technique proposed in this study is to use a quality index of ≥ 0.7 to determine if the respiratory motion estimation technique has successfully detected the respiratory signal. Ko et al., (2015) calculated the signal-to-noise ratio of the motion curve as the mean squared amplitude of the axial motion curve divided by the same

parameter for an area outside of the heart region of interest. Successful detection of a motion signal is indicated by a ratio >2 . There is no evidence presented to justify the choice of this limit, whereas the limit determined in this study is related back to the expected correlation with the external device and is therefore directly related to the quality of the measured signal. Using the signal-to-noise ratio as a quality measure will also depend on other variables such as physiological variations in the background activity. The limit by Ko et al., (2015) is related to a signal-to-noise level that would be expected to give good signal quality in a population of patients and some patients will vary from this criteria, whereas the quality index developed in this thesis is a patient specific indicator of the quality of the signal that only depends on how well the signal has been detected by the motion estimation technique.

Daou et al., (2017b) acknowledge that the performance of the technique will depend on the signal-to-noise ratio of the images, however no method of determining the quality of the signal for individual patients is presented. This is a critical component for ensuring that motion correction is not unnecessarily performed. The authors suggest that the critical threshold is not reached in any of the patient studies as there is no correlation between the counts in the study and the cranio-caudal respiratory motion measured through alignment of the binned data. However, in this thesis weak correlations were measured between the magnitude of the motion from alignment of the binned data and the counts per pixel in a region around the heart ($r = 0.34$, $P = 0.01$) and over the whole detector ($r = 0.39$, $P < 0.01$) respectively. However, a strong correlation was demonstrated between the quality index and the magnitude of the motion ($r = 0.77$, $P < 0.01$). This shows that demonstrating no correlation between respiratory motion and counts is not a good indicator that all the measured signals are good quality. Signals with good count statistics may have very little motion of the heart due to respiration and small motion measurements.

8.4 – Motion Correction

The same approach to motion correction has been taken in this thesis for both patient and respiratory motion; this is to register reconstructed bins to reduce the motion on the final summed image. The only difference between patient and respiratory motion is the counts in the bins and the number of bins. For patient

motion correction the number of bins is fixed and the counts in the bins are equal, as each bin is equivalent to 30s of data. For respiratory motion the number of bins depends on the magnitude of the measured motion and the counts in the bins depend on the pattern of the respiratory motion signal.

This method of motion correction is not ideal, as summing a series of reconstructed images is not the same as reconstructing the whole dataset, due to the non-linear reconstruction process. No work was performed to optimise the reconstruction parameters for the binned data to try to minimise this effect and this may have resulted in a difference in the image quality between the motion corrected image and an image reconstructed from the whole dataset. For both the patient and respiratory studies this effect was negated during blinded reporting by presenting the original image as the binned data summed and the motion corrected data as the binned data aligned and summed. Any differences identified between the images can therefore be attributed solely to motion. The original images reconstructed from the whole dataset were also reviewed by the author and the visual effect of summing reconstructed images appeared negligible. Figure 8-1 presents the results of preliminary analysis that was performed on this effect, where the phantom study was divided into an increasing number of reframed images, that were reconstructed and summed. No visual differences were observed and quantitative differences in the total perfusion deficit (TPD) value only presented for image durations ≤ 2 s.

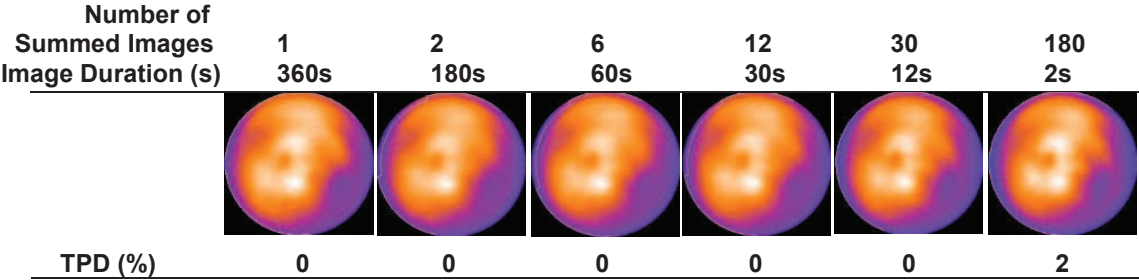


Figure 8-1 – Polar plots of a phantom study reconstructed from the whole dataset and through summing reconstructed images from data divided into different duration images. TPD - total perfusion deficit.

For respiratory motion the change in image quality due to binning and summing may be more pronounced if some bins have low counts, however this may be negated by the fact that there were generally less than half the number of bins for respiratory motion correction compared to patient motion correction. For respiratory motion any bins with <3% of the overall counts were rejected. This was a sensible limit based on the effect that these low count bins had on the motion measurement, however, if this method of motion correction were to be adopted then more work into the effect of adding low count reconstructed images and at what point these bins should be rejected would be required. Practically this method was only used to demonstrate the potential of the developed motion estimation techniques and if these were to be adopted then ideally they would be incorporated into more sophisticated motion correction methods.

A similar approach has been taken by Daou et al., (2017b) where rigid alignment was utilised to correct reconstructed respiratory gated bins. The work presented in this thesis used affine registration for respiratory motion correction. It has been demonstrated that non-linear motion of the left ventricle can occur during respiration with inferior wall motion being greater than anterior wall motion, therefore the technique in this study may provide improved motion correction compared to the technique by Daou et al., (2017b).

Kennedy and Strauss, (2016) did not convert respiratory motion measured on the detector into the true shift of the heart; instead they measured a motion index in pixels. Their approach to motion correction was to discard data with a motion index >2 pixels. This will reduce the counts and therefore image quality of the motion corrected image; the effect of this will depend on the proportion of the scan time with a motion index >2 pixels. In theory this could approach 50% of the acquisition. The motion correction technique presented in this thesis maintains the count statistics of the motion corrected image.

The approach taken by the motion detection and correction software (MDC for Alcyone, Xeleris workstation, GE Healthcare) is to incorporate motion correction into the reconstruction using a system matrix containing the measured motion. This is the preferred method of motion correction, but this can only be performed when all the details of the reconstruction and camera system are available. Ko et al., (2015)

divided the respiratory signal into eight respiratory gated bins and used the motion measured between these bins to generate a system matrix for incorporation into a reconstruction program that they designed, which incorporated motion compensation into the reconstruction process. It is not clear what assumptions had to be made about the DNM 530c configuration when designing this reconstruction program.

8.5 – Patient Studies

8.5.1 – Patient Motion

The mean (maximum) patient motion measured in this study was 1.9 (4.8), 2.5 (6.5), 3.8 (12.2) and 2.2 (4.7), 3.3 (6.8), 4.0 (10.7) mm in the lateral, ventral-dorsal and cranial-caudal directions for the three-dimensional and planar motion estimation techniques respectively. It was demonstrated that 10% of patients had ≥ 8 mm patient motion and in 5% of patients significant motion artefacts were observed. An abstract published by Kim et al., (2010) found 10% of patients had motion of ≥ 12 mm after 4 minutes imaging. Van-Dijk et al., (2016) measured the mean (maximum) patient motion using the motion detection and correction software (MDC for Alcyone, Xeleris workstation, GE Healthcare) to be 2.4 (5.4), 2.8 (5.7) and 3.4 (8.9) mm in the lateral, ventral-dorsal, and cranial-caudal directions respectively on 83 patient studies and visual analysis did not demonstrate any change in the diagnostic outcomes. This is consistent with the fact that the maximum motion that they measured was 8.9mm which is below the limit of ≥ 10 mm determined for significant motion artefacts in this study. It is not clear why motion was lower in their patient population. The imaging time used by Van-Dijk et al., (2016) was 8 minutes, therefore the lower instance of patient motion cannot be attributed to a shorter imaging time. This leaves a gap in the knowledge, with this study recommending that motion estimation and correction should form part of the routine quality assurance process following MPI acquisitions and Van-Dijk et al., (2016) concluding that there is limited value to motion correction. Kennedy and Strauss, (2016) presented one clinical example of motion affecting the quality of a patient study, figure 2-10, however motion in a cohort of patients was not evaluated.

When departments are deciding whether to take on the additional workload of performing motion estimation and correction, they will be basing this decision on the evidence of patient benefit. Therefore, more studies are needed to assess patient motion in different patient cohorts. With the advent of recent efforts to reduce the administered activity, particularly in the US and in some centres like our own due to previous Tc^{99m} shortages, there may be a trend over time towards reduced administered activity and longer imaging times. Therefore, a study, or perhaps multi-centre study, assessing the magnitude of patient motion on the DNM 530c for different image durations would be of real value, as the data could be extrapolated to centre specific protocols and referred to as protocols are changed.

8.5.2 – Respiratory Motion

Ko et al., (2015) identified 8.4% of scans as having respiratory motion ≥ 15 mm. Daou et al., (2017b) identified 55% of studies with >10 mm motion and 10% of studies with >15 mm motion. The results from this thesis are relatively consistent for ≥ 15 mm motion, with 16% and 8% of studies having ≥ 10 mm and ≥ 15 mm respiratory motion respectively.

Daou et al., (2017b) reported that motion impacted on the extent or severity of myocardial perfusion defects in 14% of all studies, 26% of studies with respiratory motion >10 mm and 60% of studies with respiratory motion >15 mm. The results from this study are consistent with 22% of studies with >10 mm motion and 50% of studies with >15 mm identified as having motion artefacts.

Both the magnitude of the motion and the number of patients affected by motion may have been underestimated by Ko et al., (2015) and in this thesis, as there is a subgroup of patients where motion tracking is poor quality (Ko, Wo et al SNR <2 , this study quality index ≤ 0.7) and there may therefore be patients in this subgroup where there is significant respiratory motion but this is not detected. It cannot be determined if this is the case for Daou et al., (2017b) and Van-Dijk et al., (2016) as no method of assessing signal quality was presented in these studies.

Out of the patient population assessed by Ko et al., (2015) there were twelve patients with patent coronary arteries from invasive coronary angiography; prior to motion correction six of these were abnormal scans and three of these become normal after motion correction. This demonstrates the diagnostic effect that motion has on MPI imaging. In contrast Van-Dijk et al., (2016) identified 9 patients where the visual SPECT interpretation changed following motion correction, however based on the agreement with FFR measurements they concluded that motion correction was of limited value as the diagnostic outcome improved in 4/9 cases but deteriorated in 5/9 cases. Although assessment of the effect of motion on the diagnostic outcome of MPI was beyond the scope of this study, it has been demonstrated that motion artefacts have been introduced by respiratory motion, suggesting that motion correction would be of benefit clinically. The current literature is inconclusive, therefore further studies to investigate the effect on diagnostic outcomes is warranted.

All the studies compared have the common advantage that no external respiratory motion tracking equipment is required and therefore these data driven techniques can be applied after the study has been acquired without any additional inconvenience for both the patient and technologist.

The main limitation of the studies by Ko et al., (2015), Daou et al., (2017b) and Van-Dijk et al., (2016) is the lack of comparison to an external tracking. A strong correlation has been demonstrated between the respiratory motion estimation technique and the signal from the external device on patient studies in this thesis and importantly studies where the motion estimation technique was unsuccessful could be identified and the reasons for this explored.

8.6 – Principal Component Analysis

Since the start of this study the use of principal component analysis for respiratory motion estimation has gained popularity in the literature. Sanders et al., (2015) used principal component analysis to determine a surrogate respiratory signal for myocardial perfusion imaging on an Anger camera. The signal was identified as the normalised coefficients with the largest singular value (first principal component). In

this study dimensionality reduction using Laplacian Eigenmaps was found to be more robust than PCA.

Principal component analysis is also being used in PET imaging, with the surrogate respiratory signal being determined from the first normalised coefficients (Thielemans et al., 2011; Thielemans et al., 2013; Manber et al., 2015; Bertolli et al., 2017). A good correlation was observed between this technique and an external device on patient data, with PCA proving to be the most stable technique over a range of count levels when compared to three other techniques including Laplacian Eigenmaps (Thielemans et al., 2013). A comparison of dimensionality reduction techniques for motion estimation on the DNM 530c was outside the scope of this thesis, however further investigation of other dimensionality reduction techniques would be warranted in future work.

One potential problem with the techniques outlined above is that if other factors influence the data (other types of motion or biological factors) it may not be clear which normalised coefficients to select (Thielemans et al., 2011). The work in this thesis measures motion through registration of images regenerated using a limited number of principal components and hence it is not limited to selecting one component of motion (one set of normalised coefficients). The surrogate respiratory motion signal will be an overall motion signal that encapsulates all the different types of motion contained within the selected components.

The polarity of the signal from principal component analysis may be inverted. In the above studies this has been corrected manually (Sanders et al., 2015) and through correlation with the external device (Thielemans et al., 2013). Automatic techniques have also been developed to determine the direction of motion from PCA analysis that do not require the respiratory signal to be measured using an external device (Bertolli et al., 2017). For the technique presented in this thesis the direction of motion is determined from registration of the images negating the need for additional processing to define the direction of the motion. The normalised coefficients for the technique presented in this thesis are used to calculate the quality index. Polarity of this signal was corrected through comparison to the external device for the validation patients and for the clinical patients the quality index was quoted as the

absolute value of the Pearson correlation coefficient, therefore ignoring any differences in polarity between the two signals. If a study has large motion contributions from other principal components the reliability of the quality index as a quality metric may be reduced.

8.7 – Limitations

The main limitation of the patient studies in this thesis is that motion artefacts were identified through visual differences between the motion and motion corrected images. These motion artefacts will have the potential to affect clinical interpretation, however this does not represent the diagnostic effect of the motion. Further work looking at the diagnostic effect needs to be undertaken to compare the stress and rest images, with and without motion correction, to see if motion would have changed the clinical outcome of the MPI study, and to compare the clinical outcome both with and without motion correction to clinical follow-up or outcomes from other modalities. The patient studies performed in the thesis also lacked quantitative assessment of perfusion before and after motion correction. Although TPD analysis was used in the phantom study, the normal database was generated from phantom acquisitions. Quantitative perfusion SPECT is not performed routinely at our institution and therefore the normal patient databases required to perform TPD analysis on clinical scans are not in place. This was however a pilot study to demonstrate the feasibility of the motion estimation technique and any further work looking at the diagnostic implications should include more robust quantification of the patient images.

9 – Conclusion and Further Work

9.1 – Conclusion

The research question posed at the start of this thesis was,

“To what extent does patient and respiratory motion introduce artefacts on myocardial perfusion imaging (MPI) on the Discovery NM 530c dedicated solid state cardiac camera (DNM 530c) and can the inherently 3D nature of this system be utilised for three-dimensional motion estimation and correction?”

Phantom images have demonstrated that patient motion artefacts presenting as localised areas of reduced perfusion are significant on the DNM 530c for motion $\geq 10\text{mm}$ that dominates $\geq 17\%$ of the acquisition. Two methods for motion estimation have been presented; one planar and one three-dimensional that utilise the three-dimensional nature of the DNM 530c system to estimate and correct for motion in three-dimensions. The mean absolute errors on the planar and three-dimensional techniques when applied to the phantom acquisitions were 0.7 ± 0.4 and $0.6 \pm 0.4\text{mm}$, and the maximum errors were 1.5 and 1.9mm respectively. Applying these techniques to patient studies demonstrated that 10% of patients had $\geq 8\text{mm}$ motion and 5% of patients had significant patient motion artefacts. The techniques used for patient motion were not robust enough for respiratory motion estimation. Incorporation of principal component analysis into the technique reduced the errors such that respiratory motion estimation was successful and also facilitated calculation of a patient specific quality index to indicate the quality of the detected signal. This was validated against an external device in 8 patient studies, with a strong correlation demonstrated for two patients. In a cohort of clinical images, 4% had significant respiratory motion artefacts. It has therefore been demonstrated that motion can introduce significant artefacts into myocardial perfusion images acquired on the DNM 530c and that these can be corrected with the proposed techniques. Further work investigating the diagnostic impact of motion in different patient cohorts is warranted.

As discussed at the beginning of this thesis, the ability of MPI to compete with other imaging modalities is declining especially following current changes to the National

Institute for Health and Care Excellence guidelines (NICE, 2017). Dedicated solid state gamma cameras present an opportunity, with improved spatial resolution and sensitivity to increase the competitiveness of MPI imaging. However, the resolution improvement offered by these systems cannot be realised until motion on MPI studies is resolved. There is therefore benefit in studies looking at correcting for patient, respiratory and cardiac motion, as a robust method of correcting for all types of motion would allow the potential resolution of these systems to be realised.

9.2 – Further Work

Further work following on from this thesis should include;

- Comparison of the robustness of the respiratory motion estimation technique developed in this thesis to the motion detection and correction software (MDC for Alcyone, Xeleris workstation, GE Healthcare).
- Assessment of the change in the diagnostic outcomes from patient and respiratory motion correction through assessment of low-likelihood and CAD patient groups. Preferably across different imaging protocols with different administered activities and imaging times.
- Investigation of possible improvements to the technique, which could include an assessment of other dimensionality reduction techniques, such as Laplacian Eigenmaps, or combining the data from all projections into one matrix for principal component analysis.
- Assessment of the robustness of the technique, in terms of the percentage of patients where the motion estimation technique produces a good quality signal, by performing a comparison of the signal from the external device to the motion estimation technique in a larger patient cohort, ideally for both supine and prone imaging.
- Development of the technique to include correction for cardiac contraction to get a motion frozen image of the left ventricle.

- Investigation of the feasibility of adapting the technique as a method of motion estimation and correction for dynamic SPECT, such as coronary flow reserve studies.
- Adaptation and application of the respiratory motion estimation technique to other nuclear medicine studies, for example lung perfusion imaging.

References

Aarsvold, JN, Galt, JR, Nye, JA, Grammens, FD and Glass, ZA (2012). "The Quality Field of View of a Discovery 530c." 2012 IEEE Nuclear Science Symposium and Medical Imaging Conference Record (NSS/MIC): 3551-3555.

Abdelnour, AF, Nehmeh, SA, Pan, T, Humm, JL, Vernon, P, Schöder, H, Rosenzweig, KE, Mageras, GS, Yorke, E, Larson, SM and Erdi, YE (2007). "Phase and Amplitude Binning for 4D-CT Imaging." Physics in Medicine and Biology, **52**(12): 3515.

Ackerman, MJ and Banvard, RA (2000). "Imaging Outcomes from the National Library of Medicine's Visible Human Project." Computerized Medical Imaging and Graphics, **24**(3): 125-126.

Agostini, D, Marie, P-Y, Ben-Haim, S, Rouzet, F, Songy, B, Giordano, A, Gimelli, A, Hyafil, F, Sciagrà, R, Bucerius, J, Verberne, HJ, Slart, RHJA and Lindner, O (2016). "Performance of Cardiac Cadmium-Zinc-Telluride Gamma Camera Imaging in Coronary Artery Disease: A Review from the Cardiovascular Committee of the European Association of Nuclear Medicine (EANM)." European Journal of Nuclear Medicine and Molecular Imaging, **43**(13): 2423-2432.

Anagnostopoulos, C, Harbinson, M, Kelion, A, Kundley, K, Loong, CY, Notghi, A, Reyes, E, Tindale, W and Underwood, SR (2003). "Procedure Guidelines for Radionuclide Myocardial Perfusion Imaging." Nuclear Medicine Communications, **24**(10): 1105-1119.

Administration of Radioactive Substances Advisory Committee (ARSAC)
"Notes for Guidance on the Clinical Administration of Radiopharmaceuticals and Use of Sealed Radioactive Sources", Public Health England.

Arumugam, P, Harbinson, M, Reyes, E, Sabharwal, N, Tonge, C and Underwood, S (2012). "Procedure Guidelines for Radionuclide Myocardial Perfusion Imaging with Single-Photon Emission Computed Tomography (SPECT)." British Nuclear

Cardiology Society Guidelines Adopted by the British Cardiac Society, the British Nuclear Cardiology Society, and the British Nuclear Medicine Society, [online],

Available at:

http://www.bnms.org.uk/resources/3F9_MPS_procedure_guidelines_Final_12.pdf,
[accessed 16th October 2016].

Asit, PK and Hani, NA (2004). "Gated Myocardial Perfusion SPECT: Basic Principles, Technical Aspects, and Clinical Applications." Journal of Nuclear Medicine Technology, **32**(4): 179-187.

Barber, DC and Hose, DR (2005). "Automatic Segmentation of Medical Images using Image Registration: Diagnostic and Simulation Applications." Journal of Medical Engineering & Technology, **29**(2): 53-63.

Barber, DC, Oubel, E, Frangi, AF and Hose, DR (2007). "Efficient Computational Fluid Dynamics Mesh Generation by Image Registration." Medical Image Analysis, **11**(6): 648-662.

Barber, DC, Valverde, I, Shi, Y, Brown, A, Beerbaum and Hose, RD (2014). "Derivation of Aortic Distensibility and Pulse Wave Velocity by Image Registration with a Physics-Based Regularisation Term." International Journal for Numerical Methods in Biomedical Engineering, **30**(1): 55-68.

Barone-Rochette, G, Leclere, M, Calizzano, A, Vautrin, E, Céline, G-C, Broisat, A, Ghezzi, C, Baguet, JP, Machecourt, J, Vanzetto, G and Fagret, D (2015). "Stress Thallium-201/Rest Technetium-99m Sequential Dual-Isotope High-Speed Myocardial Perfusion Imaging Validation Versus Invasive Coronary Angiography." Journal of Nuclear Cardiology, **22**(3): 513-522.

Beach, RD, Pretorius, PH, Boening, G, Bruyant, PP, Feng, B, Fulton, RR, Gennert, MA, Nadella, S and King, MA (2004). "Feasibility of Stereo-Infrared Tracking to Monitor Patient Motion During Cardiac SPECT Imaging." IEEE Transactions on Nuclear Science **51**(5): 2693-2698.

- Ben-Haim, S, Kennedy, J and Keidar, Z (2016). "Novel Cadmium Zinc Telluride Devices for Myocardial Perfusion Imaging—Technological Aspects and Clinical Applications." Seminars in Nuclear Medicine, **46**(4): 273-285.
- Benz, DC and Buechel, RR (2016). "Moving Ahead with CZT Technology." Journal of Nuclear Cardiology, **23**(3): 527-528.
- Benz, DC and Buechel, RR (2017). "How to Stop Breathing: On the Matter of Getting Respiratory Motion Under Control." Journal of Nuclear Cardiology, **24**(5): 1608-1609.
- Benz, DC and Fuchs, TA (2016). "Breathless or Breathtaking: Respiratory Motion Correction." Journal Nuclear Cardiology, [online], Available at: <https://doi.org/10.1007/s12350-016-0590-4>, [accessed 9th October 2016].
- Bertolli, O, Arridge, S, Stearns, CW, Wollenweber, SD, Hutton, BF and Thielemans, K (2017). "Sign Determination Methods for the Respiratory Signal in Data-Driven PET Gating." Physics in Medicine and Biology, **62**: 3204-3220.
- Bitarafan, A, Rajabi, H, Gruy, B, Rustgou, F, Sharafi, AA, Firoozabady, H, Yaghoobi, N, Malek, H, Pirich, C, Langesteger, W and Beheshti, M (2008). "Respiratory Motion Detection and Correction in ECG-Gated SPECT: A New Approach." Korean Journal of Radiology, **9**(6): 490-497.
- Bitarafan, A, Rajabi, H, Rastgou, F, Firoozabady, H, Yaghoobi, N, Malek, H, Langesteger, W and Beheshti, M (2015). "Influence of Respiratory Motion Correction on Quantification of Myocardial Perfusion SPECT." Journal of Nuclear Cardiology, **22**(5): 1019-1030.
- Bocher, M, Blevins, IM, Tsukerman, L, Shrem, Y, Kovalski, G and Volokh, L (2010). "A Fast Cardiac Gamma Camera with Dynamic SPECT Capabilities: Design, System Validation and Future Potential." European Journal of Nuclear Medicine and Molecular Imaging, **37**(10): 1887-1902.

Boening, G, Byrne, CL, Gifford, HC, Feng, B, Bruyant, PP, Beach, RD and King, MA (2004). "Motion Correction for Cardiac SPECT using a RBI-ML Partial-Reconstruction Approach." 2004 IEEE Nuclear Science Symposium Conference Record (NSS/MIC): 2849-2853.

Botvinick, EH, Zhu, YY, O'Connell, WJ and Dae, MW (1993). "A Quantitative Assessment of Patient Motion and its Effect on Myocardial Perfusion SPECT Images." Journal of Nuclear Medicine, **34**(2): 303-310.

Bruyant, PP (2002). "Analytic and Iterative Reconstruction Algorithms in SPECT." Journal of Nuclear Medicine, **43**(10): 1343-1358.

Bruyant, PP, Gennert, MA, Speckert, GC, Beach, RD, Morgenstern, JD, Kumar, N, Nadella, S and King, MA (2005). "A Robust Visual Tracking System for Patient Motion Detection in SPECT: Hardware Solutions " IEEE Transactions on Nuclear Science, **52**(5): 1288-1294.

Buechel, R, Herzog, B, Husmann, L, Burger, I, Pazhenkottil, A, Treyer, V, Valenta, I, von Schulthess, P, Nkoulou, R, Wyss, C and Kaufmann, P (2010a). "Ultrafast Nuclear Myocardial Perfusion Imaging on a New Gamma Camera with Semiconductor Detector Technique: First Clinical Validation." European Journal of Nuclear Medicine and Molecular Imaging, **37**(4): 773-778.

Buechel, R, Pazhenkottil, A, Herzog, B, Husmann, L, Nkoulou, R, Burger, I, Valenta, I, Wyss, C, Ghadri, J and Kaufmann, P (2010b). "Real-Time Breath-Hold Triggering of Myocardial Perfusion Imaging with a Novel Cadmium-Zinc-Telluride Detector Gamma Camera." European Journal of Nuclear Medicine and Molecular Imaging, **37**(10): 1903-1908.

Buechel, RR, Husmann, L, Pazhenkottil, AP, Nkoulou, R, Herzog, BA, Burger, IA, Ghadri, JR, Wolfrum, M and Kaufmann, PA (2010c). "Myocardial Perfusion Imaging with Real-Time Respiratory Triggering: Impact of Inspiration Breath-Hold on Left Ventricular Functional Parameters." Journal of Nuclear Cardiology, **17**(5): 848-852.

Case, JA and Bateman, TM (2013). "Taking the Perfect Nuclear Image: Quality Control, Acquisition, and Processing Techniques for Cardiac SPECT, PET, and Hybrid Imaging." Journal of Nuclear Cardiology, **20**(5): 891-907.

Cerqueira, M, Allman, K, Ficaro, E, Hansen, C, Nichols, K, Thompson, R, Van-Decker, W and Yakovlevitch, MM (2010). "Recommendations for reducing radiation exposure in myocardial perfusion imaging." Journal of Nuclear Cardiology, **17**(4): 709-718.

Cerqueira, MD, Weissman, NJ, Dilsizian, V, Jacobs, AK, Kaul, S, Laskey, WK, Pennell, DJ, Rumberger, JA, Ryan, T and Verani, MS (2002). "Standardized Myocardial Segmentation and Nomenclature for Tomographic Imaging of the Heart." Circulation, **105**(4): 539-542.

Cho, K, Kumiata, S-i, Okada, S and Kumazaki, T (1999). "Development of Respiratory Gated Myocardial SPECT System." Journal of Nuclear Cardiology, **6**(1): 20-28.

Chowdhury, FU, Vaidyanathan, S, Bould, M, Marsh, J, Trickett, C, Dodds, K, Clark, TPR, Sapsford, RJ, Dickinson, CJ, Patel, CN and Thorley, PJ (2014). "Rapid-Acquisition Myocardial Perfusion Scintigraphy (MPS) on a Novel Gamma Camera using Multipinhole Collimation and Miniaturized Cadmium–Zinc–Telluride (CZT) Detectors: Prognostic Value and Diagnostic Accuracy in a 'Real-World' Nuclear Cardiology Service." European Heart Journal – Cardiovascular Imaging, **15**(3): 275-283.

Claudin, M, Imbert, L, Djaballah, W, Veran, N, Poussier, S, Roch, V, Perrin, M, Verger, A, Boutley, H, Karcher, G and Marie, PY (2016). "Routine Evaluation of Left Ventricular Function using CZT-SPECT, with Low Injected Activities and Limited Recording Times." Journal of Nuclear Cardiology, [online]. Available at: <https://doi.org/10.1007/s12350-016-0615-z>, [accessed 9th october 2016].

Clerc, OF, Fuchs, TA, Possner, M, Vontobel, J, Mikulicic, F, Stehli, J, Liga, R, Benz, DC, Grani, C, Pazhenkottil, AP, Gaemperli, O, Buechel, RR and Kaufmann, PA (2017). "Real-Time Respiratory Triggered SPECT Myocardial Perfusion Imaging

using CZT Technology: Impact of Respiratory Phase Matching between SPECT and Low-Dose CT for Attenuation Correction." European Heart Journal – Cardiovascular Imaging, **18**(1): 31-38.

Cooper, JA, Neumann, PH and McCandless, BK (1992). "Effect of Patient Motion on Tomographic Myocardial Perfusion Imaging." Journal of Nuclear Medicine, **33**(8): 1566-1571.

Crum, WR, Hartkens, T and Hill, DLG (2004). "Non-Rigid Image Registration: Theory and Practice." British Journal of Radiology, **77**(supplement 2): S140-S153.

Danias, PG, Stuber, M, Botnar, RM, Kissinger, KV, Edelman, RR and Manning, WJ (1999). "Relationship Between Motion of Coronary Arteries and Diaphragm During Free Breathing: Lessons from Real-Time MR Imaging." American Journal of Roentgenology, **172**(4): 1061-1065.

Daou, D, Kaci, N, Tawileh, M and Coaguila, C (2007). "Benefits of Coupling Respiratory (RE) and ECG Gating (GAT) to Myocardial Perfusion SPECT: MPI-REGAT Project (Abstract)." Journal of Nuclear Medicine **48**: 237P.

Daou, D, Sabbah, R, Coaguila, C and Boulahdour, H (2017a). "Applicability of Data-Driven Respiratory Motion Correction to CZT SPECT Myocardial Perfusion Imaging in the Clinical Setting: The Birth of an Old Wish." Journal of Nuclear Cardiology, **24**(4): 1451-1453.

Daou, D, Sabbah, R, Coaguila, C and Boulahdour, H (2017b). "Feasibility of Data-Driven Cardiac Respiratory Motion Correction of Myocardial Perfusion CZT SPECT: A Pilot Study." Journal of Nuclear Cardiology, **24**(5): 1598-1607.

Daou, D, Sabbah, R, Coaguila, C and Boulahdour, H (2017c). "Impact of Data-Driven Cardiac Respiratory Motion Correction on the Extent and Severity of Myocardial Perfusion Defects with Free-Breathing CZT SPECT." Journal of Nuclear Cardiology, [online], Available at: <https://doi.org/10.1007/s12350-017-0806-2>, [accessed 29th March 2017].

Daou, D, Tawileh, M, Khiar-Dechmi, A and Coaguila, C (2015). "Myocardial Perfusion Imaging with Conventional Gamma Camera: To what Level do Data-Driven, Video and Belt Respiratory Motion Curves Correlate?" Journal of Nuclear Medicine, **56**(supplement 3): 1798.

Darwesh, R, Clay, D, Hay, PD, Kalirai, C, Rassoulia, H, Pitiot, A and Perkins, AC (2013). "A Three Dimensional Drive System for use with Fillable Emission Phantoms for SPECT and PET Imaging." Physica Medica, **29**(6): 695-700.

Darwesh, RM, Shin, E, Morgan, PS and Perkins, AC (2014). "Improved Visualization of Perfusion Defects by Respiratory-Gated SPECT: a Phantom Simulation Study." Nuclear Medicine Communications, **35**(2): 189-196

Davies, SC, Hill, AL, Holmes, RB, Halliwell, M and Jackson, PC (1994). "Ultrasound Quantitation of Respiratory Organ Motion in the Upper Abdomen." The British Journal of Radiology, **67**(803): 1096-1102.

DePuey, GE (1994). "How to Detect and Avoid Myocardial Perfusion SPECT Artifacts." Journal of Nuclear Medicine, **35**(4): 699-702.

DePuey, GE (2012). "Advances in SPECT Camera Software and Hardware: Currently Available and New on the Horizon." Journal of Nuclear Cardiology, **19**(3): 551-581.

DePuey, GE (2013). "New Software Solutions for Cardiac SPECT Imaging." Current Cardiovascular Imaging Reports, **6**(4): 314-321.

DePuey, GE and Rozanski, A (1995). "Using Gated Technetium-99m-Sestamibi SPECT to Characterize Fixed Myocardial Defects as Infarct or Artifact." Journal of Nuclear Medicine, **36**(6): 952-955.

Dey, J and King, MA (2009). "Theoretical and Numerical Study of MLEM and OSEM Reconstruction Algorithms for Motion Correction in Emission Tomography." IEEE Transactions on Nuclear Science, **56**(5): 2739-2749.

Duvall, W, Croft, L, Ginsberg, E, Einstein, A, Guma, K, George, T and Henzlova, M (2011a). "Reduced Isotope Dose and Imaging Time with a High-Efficiency CZT SPECT Camera." Journal of Nuclear Cardiology, **18**(5): 847-857.

Duvall, WL and Henzlova, MJ (2015). "Nuclear Cardiology as it Should Look in the Twenty-First Century." Journal of Nuclear Cardiology, **23**(1): 21-23.

Duvall, WL, Slomka, PJ, Gerlach, JR, Sweeny, JM, Baber, U, Croft, LB, Guma, KA, George, T and Henzlova, MJ (2013). "High-Efficiency SPECT MPI: Comparison of Automated Quantification, Visual Interpretation, and Coronary Angiography." Journal of Nuclear Cardiology, **20**(5): 763-773.

Duvall, WL, Sweeny, JM, Croft, LB, Barghash, MH, Kulkarni, NK, Guma, KA and Henzlova, MJ (2011b). "Comparison of High Efficiency CZT SPECT MPI to Coronary Angiography." Journal of Nuclear Cardiology, **18**(4): 595-604.

Eisner, RL, Noever, T, Nowak, D, Carlson, W, Dunn, D, Oates, J, Cloninger, K, Liberman, HA and Patterson, RE (1987). "Use of Cross-Correlation Function to Detect Patient Motion During SPECT Imaging." Journal of Nuclear Medicine **28**(1): 97-101.

Esteves, FP, R., GJ, D., FR, Liudmila, V and V., GE (2013). "Diagnostic Performance of Low-Dose Rest/Stress Tc-99m Tetrofosmin Myocardial Perfusion SPECT using the 530c CZT Camera: Quantitative vs Visual Analysis." Journal of Nuclear Cardiology, **21**(1): 158-165.

Esteves, FP, Raggi, P, Folks, RD, Keidar, Z, Askew, JW, Rispler, S, O'Connor, MK, Verdes, L and Garcia, EV (2009). "Novel Solid-State-Detector Dedicated Cardiac Camera for Fast Myocardial Perfusion Imaging: Multicenter Comparison with Standard Dual Detector Cameras." Journal of Nuclear Cardiology **16**(6): 927-934.

Fiechter, M, Ghadri, J, Kuest, S, Pazhenkottil, A, Wolfrum, M, Nkoulou, R, Goetti, R, Gaemperli, O and Kaufmann, P (2011). "Nuclear Myocardial Perfusion Imaging with a Novel Cadmium-Zinc-Telluride Detector SPECT/CT Device: First Validation

Versus Invasive Coronary Angiography." European Journal of Nuclear Medicine and Molecular Imaging, **38**(11): 2025-2030.

Fitzgerald, J and Danias, P (2001). "Effect of Motion on Cardiac SPECT Imaging: Recognition and Motion Correction." Journal of Nuclear Cardiology, **8**(6): 701-706.

Friedman, J, Van Train, K, Maddahi, J, Rozanski, A, Prigent, F, Bietendorf, J, Waxman, A and Berman, DS (1989). ""Upward Creep" of the Heart: A Frequent Source of False-Positive Reversible Defects during Thallium-201 Stress-Redistribution SPECT." Journal of Nuclear Medicine, **30**(10): 1718-1722.

Garcia, E and Faber, T (2009). "Advances in Nuclear Cardiology Instrumentation: Clinical Potential of SPECT and PET." Current Cardiovascular Imaging Reports, **2**(3): 230-237.

Garcia, EV, Faber, TL and Esteves, FP (2011). "Cardiac Dedicated Ultrafast SPECT Cameras: New Designs and Clinical Implications." Journal of Nuclear Medicine, **52**(2): 210-217.

GE Healthcare, Alcyone Technology White Paper

Geckle, WJ, Frank, TL, Links, JM and Becker, LC (1988). "Correction for Patient and Organ Movement in SPECT: Application to Exercise Thallium-201 Cardiac Imaging." Journal of Nuclear Medicine **29**(4): 441-450.

Germano, G, Kavanagh, PB, Slomka, PJ, Van-Kriekinge, SD, Pollard, G and Berman, DS (2007). "Quantitation in Gated Perfusion SPECT Imaging: The Cedars-Sinai Approach." Journal of Nuclear Cardiology, **14**(4): 433-454.

Germano, G, Kavanagh, PB, Waechter, P, Areeda, J, Van-Kriekinge, S, Sharir, T, Lewin, HC and Berman, DS (2000). "A New Algorithm for the Quantitation of Myocardial Perfusion SPECT. I: Technical Principles and Reproducibility." Journal of Nuclear Medicine, **41**(4): 712-719.

Germano, G, Kiat, H, Kavanagh, PB, Moriel, M, Mazzanti, M, Su, H, Van Train, KF and Berman, DS (1995). "Automatic Quantification of Ejection Fraction from Gated Myocardial Perfusion SPECT." Journal of Nuclear Medicine, **36**(11): 2138-2147.

Giannopoulos, AA and Buechel, RR (2017). "A Further Step Towards Getting Cardiac Respiratory Motion Under Control." Journal of Nuclear Cardiology, [online]. Available at: <https://doi.org/10.1007/s12350-017-0835-x>, [accessed 13th January 2018].

Gimelli, A, Bottai, M, Genovesi, D, Giorgetti, A, Di Martino, F and Marzullo, P (2012). "High Diagnostic Accuracy of Low-Dose Gated-SPECT with Solid-State Ultrafast Detectors: Preliminary Clinical Results." European Journal of Nuclear Medicine and Molecular Imaging, **39**(1): 83-90.

Gimelli, A, Bottai, M, Giorgetti, A, Genovesi, D, Kusch, A, Ripoli, A and Marzullo, P (2011). "Comparison Between Ultrafast and Standard Single-Photon Emission CT in Patients With Coronary Artery Disease: A Pilot Study." Circulation: Cardiovascular Imaging, **4**(1): 51-58.

Goto, K, Takebayashi, H, Kihara, Y, Yamane, H, Hagikura, A, Morimoto, Y, Kikuta, Y, Sato, K, Taniguchi, M, Hiramatsu, S and Haruta, S (2014). "Impact of Combined Supine and Prone Myocardial Perfusion Imaging using an Ultrafast Cardiac Gamma Camera for Detection of Inferolateral Coronary Artery Disease." International Journal of Cardiology, **174**(2): 313-317.

Green, PJ (1990). "Bayesian Reconstructions from Emission Tomography Data using a Modified EM Algorithm." IEEE Transactions on Medical Imaging, **9**(1): 84-93.

Hand, AJ, Sun, T, Barber, DC, Hose, DR and Macneil, S (2009). "Automated Tracking of Migrating Cells in Phase-Contrast Video Microscopy Sequences using Image Registration." Journal of Microscopy, **234**(1): 62-79.

Heijenbrok-Kal, H., M, Fleischmann, KE and Hunink, M (2007). "Stress Echocardiography, Stress Single-Photon-Emission Computed Tomography and

Electron Beam Computed Tomography for the Assessment of Coronary Artery Disease: A Meta-Analysis of Diagnostic Performance." American Heart Journal, **154**(3): 415-423.

Henzlova, MJ and Duvall, WL (2016). "Which SPECT for Today, Which SPECT for Tomorrow?" Journal of Nuclear Cardiology, **23**(4): 803-806.

Henzlova, MJ, Duvall, WL, Einstein, AJ, Travin, MI and Verberne, HJ (2016). "ASNC Imaging Guidelines for SPECT Nuclear Cardiology Procedures: Stress, Protocols, and Tracers." Journal of Nuclear Cardiology, **23**(3): 606-639.

Herzog, BA, Buechel, RR, Katz, R, Brueckner, M, Husmann, L, Burger, IA, Pazhenkottil, AP, Valenta, I, Gaemperli, O, Treyer, V and Kaufmann, PA (2010). "Nuclear Myocardial Perfusion Imaging with a Cadmium-Zinc-Telluride Detector Technique: Optimized Protocol for Scan Time Reduction." Journal of Nuclear Medicine, **51**(1): 46-51.

Hesse, B, Tagil, K, Cuocolo, A, Anagnostopoulos, C, Bardies, M, Bax, J, Bengel, F, Busemann Sokole, E, Davies, G, Dondi, M, Edenbrandt, L, Franken, P, Kjaer, A, Knuuti, J, Lassmann, M, Ljungberg, M, Marcassa, C, Marie, PY, McKiddie, F, O'Connor, M, Prvulovich, E, Underwood, R and van Eck-Smit, B (2005). "EANM/ESC Procedural Guidelines for Myocardial Perfusion Imaging in Nuclear Cardiology." European Journal of Nuclear Medicine and Molecular Imaging, **32**(7): 855-897.

Hillel, P, Hanney, M, Redgate, S, Taylor, J and Randall, D (2011). "Assessing the Performance of a Solid-State Cardiac Gamma Camera Prior to its Introduction into Routine Clinical Service (Abstract)." Journal of Nuclear Medicine, **52**(supplement 1): 1937.

Hindorf, C, Oddstig, J, Hedeer, F, Hansson, M, Jögi, J and Engblom, H (2014). "Importance of Correct Patient Positioning in Myocardial Perfusion SPECT when using a CZT Camera." Journal of Nuclear Cardiology, **21**(4): 695-702.

Ho, SY (2009). "Anatomy and Myoarchitecture of the Left Ventricular Wall in Normal and in Disease." European Journal of Echocardiography, **10**(8): iii3-iii7.

Holland, AE, Goldfarb, JW and Edelman, RR (1998). "Diaphragmatic and Cardiac Motion During Suspended Breathing: Preliminary Experience and Implications for Breath-Hold MR Imaging." Radiology, **209**(2): 483-489.

Howard, BA, Roy Choudhury, K, Oldan, JD, Pagnanelli, RA and Borges-Neto, S (2016). "Difference in Appearance between Prone and Supine Myocardial Perfusion Images Obtained on a High-Efficiency Cadmium Zinc Telluride SPECT Camera." Nuclear Medicine Communications, **37**(5): 487-492.

Hutton, BF (2011). "Recent Advances in Iterative Reconstruction for Clinical SPECT/PET and CT." Acta Oncologica, **50**(6): 851-858.

Ireland, RH, Dyker, KE, Barber, DC, Wood, SM, Hanney, MB, Tindale, WB, Woodhouse, N, Hoggard, N, Conway, J and Robinson, MH (2007). "Nonrigid Image Registration for Head and Neck Cancer Radiotherapy Treatment Planning With PET/CT." International Journal of Radiation Oncology Biology Physics, **68**(3): 952-957.

Jansen, FP, Tsukerman, L, Volokh, L, Bleviss, I, Hugg, JW and Bouhnik, JP (2010). "Uniformity Correction using Non-Uniform Floods." 2010 IEEE Nuclear Science Symposium Conference Record (NSS/MIC): 2314-2318.

Kapur, A, Latus, K, Davies, G, Dhawan, R, Eastick, S, Jarritt, P, Roussakis, G, Young, M, Anagnostopoulos, C, Bomanji, J, Costa, D, Pennell, D, Prvulovich, E, Ell, P and Underwood, R (2002). "A Comparison of Three Radionuclide Myocardial Perfusion Tracers in Clinical Practice: The ROBUST Study." European Journal of Nuclear Medicine and Molecular Imaging, **29**(12): 1608-1616.

Karacalioglu, AO, Jata, B, Kilic, S, Arslan, N, Ilgan, S and Ozguven, MA (2006). "A Physiologic Approach to Decreasing Upward Creep of the Heart During Myocardial Perfusion Imaging." Journal of Nuclear Medicine Technology, **34**(4): 215-219.

Keegan, J, Gatehouse, P, Yang, GZ and Firmin, D (2002). "Coronary Artery Motion with the Respiratory Cycle During Breath-Holding and Free-Breathing: Implications for Slice-Followed Coronary Artery Imaging." Magnetic Resonance in Medicine **47**(3): 476-481.

Kennedy, JA, Israel, O and Frenkel, A (2014). "3D Iteratively Reconstructed Spatial Resolution Map and Sensitivity Characterization of a Dedicated Cardiac SPECT Camera." Journal of Nuclear Cardiology, **21**(3): 443-452.

Kennedy, JA and Strauss, WH (2016). "Motion Detection and Amelioration in a Dedicated Cardiac Solid-State CZT SPECT Device." Medical & Biological Engineering & Computing, **55**(4): 663-671.

Kim, A, Marvin, B, Ruddy, T and Wells, GR (2010). "Patient Motion on the GE Discovery CZT Camera: Investigating the Necessity of Motion Correction (Abstract)." Journal of Nuclear Medicine, **51**(Supplement 2): 2114.

Ko, C-L, Wu, Y-W, Cheng, M-F, Yen, R-F, Wu, W-C and Tzen, K-Y (2015). "Data-Driven Respiratory Motion Tracking and Compensation in CZT Cameras: A Comprehensive Analysis of Phantom and Human Images." Journal of Nuclear Cardiology, **22**(2): 308-318.

Konik, A, Mukherjee, JM, Johnson, KL, Helfenbein, E, Shao, L and King, MA (2011). "Comparison of ECG Derived Respiratory Signals and Pneumatic Bellows for Respiratory Motion Tracking." 2011 IEEE Nuclear Science Symposium and Medical Imaging Conference Record (NSS/MIC): 3925-3930.

Korin, HW, Ehman, RL, Riederer, SJ, Felmlee, JP and Grimm, RC (1992). "Respiratory Kinematics of the Upper Abdominal Organs: A Quantitative Study." Magnetic Resonance in Medicine, **23**(1): 172-178.

Kovalski, G, Israel, O, Keidar, Z, Frenkel, A, Sachs, J and Azhari, H (2007). "Correction of Heart Motion due to Respiration in Clinical Myocardial Perfusion SPECT Scans using Respiratory Gating." Journal of Nuclear Medicine, **48**(4): 630-636.

Kovalski, G, Keidar, Z, Frenkel, A, Israel, O and Azhari, H (2009a). "Correction for Respiration Artefacts in Myocardial Perfusion SPECT is more Effective when Reconstructions Supporting Collimator Detector Response Compensation are Applied." Journal of Nuclear Cardiology **16**(6): 949-955.

Kovalski, G, Keidar, Z, Frenkel, A, Sachs, J, Attia, S and Azhari, H (2009b). "Dual "Motion-Frozen Heart" Combining Respiration and Contraction Compensation in Clinical Myocardial Perfusion SPECT Imaging." Journal of Nuclear Cardiology, **16**(3): 396-404.

Lamata, P, Niederer, S, Nordsletten, D, Barber, DC, Roy, I, Hose, DR and Smith, N (2011). "An Accurate, Fast and Robust Method to Generate Patient-Specific Cubic Hermite Meshes." Medical Image Analysis, **15**(6): 801-813.

Lima, R, Peclat, T, Soares, T, Ferreira, C, Souza, AC and Camargo, G (2016). "Comparison of the Prognostic Value of Myocardial Perfusion Imaging using a CZT-SPECT Camera with a Conventional Anger Camera." Journal of Nuclear Cardiology, **24**(1): 245-251.

Lindner, O, Pascual, TNB, Mercuri, M, Acampa, W, Burchert, W, Flotats, A, Kaufmann, PA, Kitsiou, A, Knuuti, J, Underwood, SR, Vitola, JV, Mahmariyan, JJ, Karthikeyan, G, Better, N, Rehani, MM, Kashyap, R, Dondi, M, Paez, D and Einstein, AJ (2016). "Nuclear Cardiology Practice and Associated Radiation Doses in Europe: Results of the IAEA Nuclear Cardiology Protocols Study (INCAPS) for the 27 European Countries." European Journal of Nuclear Medicine and Molecular Imaging, **43**(4): 718-728.

Livieratos, L, Rajappan, K, Stegger, L, Schafers, K, Bailey, DL and Camici, PG (2006). "Respiratory Gating of Cardiac PET Data in List-Mode Acquisition." European Journal of Nuclear Medicine and Molecular Imaging, **33**(5): 584-588.

Livieratos, L, Stegger, L, Bloomfield, PM, Schafers, K, Bailey, DL and Camici, PG (2005). "Rigid-Body Transformation of List-Mode Projection Data for Respiratory Motion Correction in Cardiac PET." Physics in Medicine and Biology, **50**(14): 3313-3322.

Loong, CY and Anagnostopoulos, C (2004). "Diagnosis of Coronary Artery Disease by Radionuclide Myocardial Perfusion Imaging." Heart, **90**(supplement 5): v2-v9.

Mageras, GS, Yorke, E, Rosenzweig, K, Braban, L, Keatley, E, Ford, E, Leibel, SA and Ling, CC (2001). "Fluoroscopic Evaluation of Diaphragmatic Motion Reduction with a Respiratory Gated Radiotherapy System." Journal of Applied Clinical Medical Physics **2**(4): 191-200.

Manber, R, Thielemans, K, Hutton, BF, Barnes, A, Ourselin, S, Arridge, S, O'Meara, C, Wan, S and Atkinson, D (2015). "Practical PET Respiratory Motion Correction in Clinical PET/MR." Journal of Nuclear Medicine, **56**(6): 890-896.

Marieb, EN (2004). Human Anatomy and Physiology, . 4th edition, California, Benjamin / Cummings Science Publishing.

Martel A L, Froh M S, Brock K K, Plewes D B and C., BD (2007). "Evaluating an Optical-Flow-Based Registration Algorithm for Contrast-Enhanced Magnetic Resonance Imaging of the Breast." Physics in Medicine and Biology, **52**(13): 3803-3816.

Martinez-Moller, A, Zikic, D, Botnar, RM, Bundschuh, RA, Howe, W, Ziegler, SI, Navab, N, Schwaiger, M and Nekolla, SG (2007). "Dual Cardiac-Respiratory Gated PET: Implementation and Results from a Feasibility Study." European Journal of Nuclear Medicine and Molecular Imaging, **34**(9): 1447-1454.

Marwick, TH (2003). "Stress Echocardiography." Heart, **89**(1): 113-118.

Matsumoto, N, Berman, DS, Kavanagh, PB, Gerlach, J, Hayes, SW, Lewin, HC, Friedman, JD and Germano, G (2001). "Quantitative Assessment of Motion Artifacts and Validation of a New Motion-Correction Program for Myocardial Perfusion SPECT." Journal of Nuclear Medicine, **42**(5): 687-694.

McLeish, K, Hill, DL, Atkinson, D, Blackall, JM and Razavi, R (2002). "A Study of the Motion and Deformation of the Heart due to Respiration." IEEE Transactions on Medical Imaging, **21**(9): 1142-1150.

McNamara, JE, Pretorius, PH, Johnson, K, Mukherjee, JM and Dey, J (2009). "A Flexible Multicamera Visual-Tracking System for Detecting and Correcting Motion-Induced Artifacts in Cardiac SPECT Slices." Medical Physics, **65**(3): 1913-1923.

Mercuri, M, Pascual, TNB, Mahmarian, JJ, Shaw, LJ, Rehani, MM, Paez, DMD and Einstein, AJMD (2016). "Comparison of Radiation Doses and Best-Practice Use for Myocardial Perfusion Imaging in US and Non-US Laboratories: Findings From the IAEA (International Atomic Energy Agency) Nuclear Cardiology Protocols Study." JAMA Internal Medicine, **176**(2): 266-269.

Mester, J, Weller, R, Clausen, M, Bitter, F, Henze, E, Lietzenmayer, R and Adam, W-E (1991). "Upward Creep of the Heart in Exercise Thallium 201 Single Photon Emission Tomography: Clinical Relevance and a Simple Correction Method." European Journal of Nuclear Medicine and Molecular Imaging, **18**(3): 184-190.

Metherall, P, Redgate, S, Barber, D, Hillel, P, Tindale, W, Coates, R and Frisch, R (2011). "Minimising Artefacts Resulting from Stress-Rest Misalignment on a Solid State Dedicated Cardiac Gamma Camera (Abstract)." Journal of Nuclear Medicine, **52**(supplement 1): 1938.

Miao, TL, Kansal, V, Wells, G, R, Ali, I, Ruddy, TD and Chow, BJW (2015). "Adopting New Gamma Cameras and Reconstruction Algorithms: Do we Need to Re-establish Normal Reference Values?" Journal of Nuclear Cardiology, **23**(4): 807-817.

Mitra, J, McNamara, JE, Johnson, KL, Dey, J and King, MA (2007). Estimation of rigid-body and respiratory motion of the heart for SPECT motion correction. 2007 IEEE Nuclear Science Symposium Conference Record.

Mouden, M, Timmer, JR, Ottervanger, JP, Reiffers, S, Oostdijk, AHJ, Knollema, S and Jager, PL (2012). "Impact of a New Ultrafast CZT SPECT Camera for Myocardial Perfusion Imaging: Fewer Equivocal Results and Lower Radiation Dose." European Journal of Nuclear Medicine and Molecular Imaging, **39**(6): 1048-1055.

Mukherjee, JM, Hutton, BF, Johnson, KL, Pretorius, PH and King, MA (2013). "An Evaluation of Data-Driven Motion Estimation in Comparison to the Usage of External-Surrogates in Cardiac SPECT Imaging." Physics in Medicine and Biology, **58**(21): 7625-7646.

Mukherjee, JM, Johnson, KL, McNamara, JE and King, MA (2010). "Quantitative Study of Rigid-Body and Respiratory Motion of Patients Undergoing Stress and Rest Cardiac SPECT Imaging." IEEE Transactions on Nuclear Science, **57**(3): 1105-1115.

National Institute for Health and Care Excellence (NICE), "Assessing and Diagnosing Suspected Stable Angina", Available at: <https://pathways.nice.org.uk/pathways/chest-pain/assessing-and-diagnosing-suspected-stable-angina>, [accessed 11th November 2017}.

Nichols, KJ, Bacharach, SL, Bergmann, SR, Chen, J, Cullom, JS, Dorbala, S, Ficaro, EP, Galt, JR, Conaway, DLG, Heller, GV, Hyun, MC, Links, J and Machac, J (2007). "Instrumentation Quality Assurance and Performance." Journal of Nuclear Cardiology, **14**(6): 0-0.

Nishiyama, Y, Miyagawa, M, Kawaguchi, N, Nakamura, M, Kido, T, Kurata, A, Kido, T, Ogimoto, A, Higaki, J and Mochizuki, T (2014). "Combined Supine and Prone Myocardial Perfusion Single-Photon Emission Computed Tomography With a Cadmium Zinc Telluride Camera for Detection of Coronary Artery Disease." Circulation Journal, **78**(5): 1169-1175.

Oddstig, J, Hedeer, F, Jögi, J, Carlsson, M, Hindorf, C and Engblom, H (2013). "Reduced Administered Activity, Reduced Acquisition Time, and Preserved Image Quality for the New CZT Camera." Journal of Nuclear Cardiology, **20**(1): 38-44.

Oldan, JD, Shaw, LK, Hofmann, P, Phelan, M, Nelson, J, Pagnanelli, R and Borges-Neto, S (2016). "Prognostic Value of the Cadmium-Zinc-Telluride Camera: A Comparison with a Conventional (Anger) Camera." Journal of Nuclear Cardiology, **23**(6): 1280-1287.

Pitman, AG, Kalff, V, Every, B, Risa, B, Barnden, LR and Kelly, MJ (2005). "Contributions of Subdiaphragmatic Activity, Attenuation, and Diaphragmatic Motion to Inferior Wall Artifact in Attenuation-Corrected Tc-99m Myocardial Perfusion SPECT." Journal of Nuclear Cardiology, **12**(4): 401-409.

Pitman, AG, Kalff, V, Van Every, B, Risa, B, Barnden, LR and Kelly, MJ (2002). "Effect of Mechanically Simulated Diaphragmatic Respiratory Motion on Myocardial SPECT Processed with and without Attenuation Correction." Journal of Nuclear Medicine, **43**(9): 1259-1267.

Pretorius, PH, Johnson, KL and King, MA (2016). "Evaluation of Rigid-Body Motion Compensation in Cardiac Perfusion SPECT Employing Polar-Map Quantification." IEEE Transactions on Nuclear Science, **63**(3): 1419-1425.

Prigent, FM, Hyun, M, Berman, DS and Rozanski, A (1993). "Effect of Motion on Thallium-201 SPECT Studies: A Simulation and Clinical Study." Journal of Nuclear Medicine, **34**(11): 1845-1850.

Redgate, S, Barber, D, Al-Mohammad, A and Tindale, W (2013). "Using a Registration-Based Motion Correction Algorithm to Correct for Respiratory Motion during Myocardial Perfusion Imaging." Nuclear Medicine Communications, **34**(8): 787-795.

Redgate, S, Barber, DC, Fenner, JW, Al-Mohammad, A, Taylor, JC, Hanney, MB and Tindale, WB (2016). "A Study to Quantify the Effect of Patient Motion and Develop Methods to Detect and Correct for Motion during Myocardial Perfusion Imaging on a CZT Solid-State Dedicated Cardiac Camera." Journal of Nuclear Cardiology, **23**(3): 514-526.

Redgate, S, Fenner, J, Barber DC, Tindale WB, Al-Mohammad A, Fleming S and B., B (2012). "Detecting Patient Motion on a Solid State Multiple Pinhole Dedicated Cardiac Camera (Abstract)." The Journal of Nuclear Medicine **53** (Supplement 1): 2377.

Rosenthal, MS, Cullom, J, Hawkins, W, Moore, SC, Tsui, BM and Yester, M (1995). "Quantitative SPECT Imaging: A Review and Recommendations by the Focus Committee of the Society of Nuclear Medicine Computer and Instrumentation Council." Journal of Nuclear Medicine **36**(8): 1489-1513.

Salvadori, J, Petegnief, Y, Sabbah, R, Morel, O, Boulahdour, H, Karcher, G, Marie, P-Y and Imbert, L (2018). "Compared Vulnerabilities to Small Cardiac Motions between Different Cameras used for Myocardial Perfusion Imaging." Journal of Nuclear Cardiology, [online]. Available at: <https://doi.org/10.1007/s12350-017-1175-6>, [accessed 23rd January 2018].

Sanders, JC, Ritt, P, Kuwert, T, Vija, AH and Hornegger, J (2015). "Data-Driven Respiratory Signal Extraction for SPECT Imaging Using Laplacian Eigenmaps." 2015 IEEE Nuclear Science Symposium and Medical Imaging Conference Record (NSS/MIC).

Schillaci, O and Danieli, R (2010). "Dedicated Cardiac Cameras: A New Option for Nuclear Myocardial Perfusion Imaging." European Journal of Nuclear Medicine and Molecular Imaging, **37**(9): 1706-1709.

Segars, WP, Lalush, DS and Tsui, BMW (1999). The next generation MCAT: a realistic spline-based torso phantom. Proceedings of the First Joint BMES/EMBS Conference. 1999 IEEE Engineering in Medicine and Biology 21st Annual Conference and the 1999 Annual Fall Meeting of the Biomedical Engineering Society (Cat. N).

Segars, WP and Tsui, BMW (2002). "Study of the Efficacy of Respiratory Gating in Myocardial SPECT using the New 4-D NCAT Phantom." IEEE Transactions on Nuclear Science, **49**(3): 675-679.

Sharir, T, Brodtkin, B and Kovalski, G (2016). "Combined Assessment of Myocardial Perfusion and Left Ventricular Function by Nuclear Cardiology: The Value of High-Efficiency SPECT." Journal Nuclear Cardiology, **23**(6): 1262-1265.

Sharir, T, Pinskiy, M, Pardes, A, Rochman, A, Prokhorov, V, Kovalski, G, Merzon, K, Bojko, A and Brodtkin, B (2015). "Comparison of the Diagnostic Accuracies of Very Low Stress-Dose with Standard-Dose Myocardial Perfusion Imaging: Automated Quantification of One-Day, Stress-First SPECT using a CZT Camera." Journal of Nuclear Cardiology, **23**(1): 11-20.

Shechter, G, Ozturk, C, Resar, JR and McVeigh, ER (2004). "Respiratory Motion of the Heart from Free Breathing Coronary Angiograms." IEEE Transactions on Medical Imaging, **23**(8): 1046-1056.

Slomka, P, Berman, D and Germano, G (2010). "New Imaging Protocols for New Single Photon Emission CT Technologies." Current Cardiovascular Imaging Reports, **3**(3): 162-170.

Slomka, P, Dey, D, Duvall, WL, Henzlova, M, Berman, D and Germano, G (2012). "Advances in Nuclear Cardiac Instrumentation with a View Towards Reduced Radiation Exposure." Current Cardiology Reports, **14**(2): 208-216.

Slomka, P, Nishina, H, Berman, D, Akincioglu, C, Abidov, A, Friedman, J, Hayes, S and Germano, G (2005). "Automated Quantification of Myocardial Perfusion SPECT using Simplified Normal Limits." Journal of Nuclear Cardiology, **12**(1): 66-77.

Slomka, P, Patton, J, Berman, D and Germano, G (2009). "Advances in Technical Aspects of Myocardial Perfusion SPECT Imaging." Journal of Nuclear Cardiology, **16**(2): 255-276.

Slomka, PJ, Nishina, H, Berman, DS, Kang, X, Akincioglu, C, Friedman, JD, Hayes, SW, Aladl, UE and Germano, G (2004). "'Motion-Frozen' Display and Quantification of Myocardial Perfusion." Journal of Nuclear Medicine, **45**(7): 1128-1134.

Stathaki, M, Koukouraki, S, Papadaki, E, Tsaroucha, A and Karkavitsas, N (2015). "The Benefits of Prone SPECT Myocardial Perfusion Imaging in Reducing Both Artifact Defects and Patient Radiation Exposure." Arquivos Brasileiros de Cardiologia, **105**(4): 345-352.

Strauss, HW, Miller, DD, Wittry, MD, Cerqueira, MD, Garcia, EV, Iskandrian, AS, Schelbert, HR, Wackers, FJ, Balon, HR, Lang, O and Machac, J (2008). "Procedure Guideline for Myocardial Perfusion Imaging 3.3." Journal of Nuclear Medicine Technology, **36**(3): 155-161.

Suzuki, Y, Slomka, PJ, Wolak, A, Ohba, M, Suzuki, S, De Yang, L, Germano, G and Berman, DS (2008). "Motion-Frozen Myocardial Perfusion SPECT Improves Detection of Coronary Artery Disease in Obese Patients." Journal of Nuclear Medicine, **49**(7): 1075-1079.

Tanaka, H, Chikamori, T, Hida, S, Uchida, K, Igarashi, Y, Yokoyama, T, Takahashi, M, Shiba, C, Yoshimura, M, Tokuyue, K and Yamashina, A (2013). "Comparison of Myocardial Perfusion Imaging Between the New High-Speed Gamma Camera and the Standard Anger Camera." Circulation Journal, **77**(4): 1009-1017.

Thielemans, K, Rathore, S, Engbrant, F and Razifar, P (2011). "Device-Less Gating for PET/CT using PCA." 2011 IEEE Nuclear Science Symposium and Medical Imaging Conference Record (NSS/MIC): 3904-3910.

Thielemans, K, Schleyer, P, Marsden, PK, Manjeshwar, RM, Wollenweber, SD and Ganin, A (2013). Comparison of Different Methods for Data-Driven Respiratory Gating of PET Data. 2013 IEEE Nuclear Science Symposium and Medical Imaging Conference Record (NSS/MIC).

Timmins, R, Ruddy, TD and Wells, RG (2015). "Patient Position Alters Attenuation Effects in Multipinhole Cardiac SPECT." Medical Physics, **42**(3): 1233-1240.

Townsend, N, Bhatnagar, P, Wilkins, E, Wickramasinghe, K and M, R (2015). "Cardiovascular Disease Statistics, 2015 " British Heart Foundation:London, Available at: <https://www.bhf.org.uk/publications/statistics/cvd-stats-2015>, [accessed 2019th July 2016].

Townsend, N, Wickramasinghe, K, Bhatnagar, P, Smolina, K, Nichols, M, Leal, J, LuengoFernandez, R and Rayner, M (2012). "Coronary Heart Disease Statistics, 2012." British Heart Foundation: London, Available at:

<https://www.bhf.org.uk/publications/statistics/coronary-heart-disease-statistics-2012>, [accessed 2019th July 2016].

Townsend, N, Williams, J, Bahatnagar, P, Wickramasinghe, K and Rayner, M (2014). "Cardiovascular Disease Statistics, 2014 " British Heart Foundation: London, Available at: <https://www.bhf.org.uk/publications/statistics/cardiovascular-disease-statistics-2014>, [accessed 2019th July 2016].

Tsui, BMW, Segars, WP and Lalush, DS (2000). "Effects of Upward Creep and Respiratory Motion in Myocardial SPECT." IEEE Transactions on Nuclear Science, **47**(3): 1192-1195.

Udelson, JE and Hoffmann, U (2017). "The United Kingdom's National Institute for Health and Care Excellence Guideline on Chest Pain of Recent Onset: A United States Perspective." Journal of Nuclear Cardiology, **24**(5): 1535-1539.

Van-Dijk, JD, Van-Dalen, JA, Mouden, M, Ottervanger, JP, Knollema, S, Slump, CH and Jager, PL (2016). "Value of Automatic Patient Motion Detection and Correction in Myocardial Perfusion Imaging using a CZT-based SPECT Camera." Journal of Nuclear Cardiology, [online], Available at: <https://doi.org/10.1007/s12350-016-0571-7>, [accessed 9th October 2016].

Verberne, HJ, Acampa, W, Anagnostopoulos, C, Ballinger, J, Bengel, F, De-Bondt, P, Buechel, RR, Cuocolo, A, van-Eck-Smit, BLF, Flotats, A, Hacker, M, Hindorf, C, Kaufmann, PA, Lindner, O, Ljungberg, M, Lonsdale, M, Manrique, A, Minarik, D, Scholte, AJHA, Slart, RHJA, Trägårdh, E, Be-Wit, TC and Hesse, B (2015). "EANM Procedural Guidelines for Radionuclide Myocardial Perfusion Imaging with SPECT and SPECT/CT." Available at: http://www.eanm.org/publications/guidelines/2015_07_EANM_FINAL_myocardial_perfusion_guideline.pdf, [accessed 16th October 2016].

Volokh, L, Lahat, C, Binyamin, E and Blevis, I (2008). "Myocardial Perfusion Imaging with an Ultra-Fast Cardiac SPECT Camera - A Phantom Study " IEEE 2008 Nuclear Science Symposium Conference Record: 4636-4639.

Wallis, JW (1995). "Use of the Selective Linogram in Cardiac Tomography Quality Control." Journal of Nuclear Cardiology **2**(4): 303-308.

Wang, Y, Riederer, SJ and Ehman, RL (1995). "Respiratory Motion of the Heart: Kinematics and the Implications for the Spatial Resolution in Coronary Imaging." Magnetic Resonance in Medicine, **33**(5): 713-719.

Wheat, JM and Currie, GM (2004). "Incidence and Characterization of Patient Motion in Myocardial Perfusion SPECT: Part 1." Journal of Nuclear Medicine Technology, **32**(2): 60-65.

Wolff, SD, Schwitter, J, Coulden, R, Friedrich, MG, Bluemke, DA, Biederman, RW, Martin, ET, Lansky, AJ, Kashanian, F, Foo, TKF, Licato, PE and Comeau, CR (2004). "Myocardial First-Pass Perfusion Magnetic Resonance Imaging: A Multicenter Dose-Ranging Study." Circulation, **110**(6): 732-737.

Wolk, MJ, Bailey, SR, Doherty, JU, Douglas, PS, Hendel, RC, Kramer, CM, Min, JK, Patel, MR, Rosenbaum, L, Shaw, LJ, Stainback, RF and Allen, JM (2014). "ACCF/AHA/ASE/ASNC/HFSA/HRS/SCAI/SCCT/SCMR/STS 2013 Multimodality Appropriate Use Criteria for the Detection and Risk Assessment of Stable Ischemic Heart Disease: A Report of the American College of Cardiology Foundation Appropriate Use Criteria Task Force, American Heart Association, American Society of Echocardiography, American Society of Nuclear Cardiology, Heart Failure Society of America, Heart Rhythm Society, Society for Cardiovascular Angiography and Interventions, Society of Cardiovascular Computed Tomography, Society for Cardiovascular Magnetic Resonance, and Society of Thoracic Surgeons," Journal of the American College of Cardiology, **63**(4): 380-406.

Worden, NE, Lindower, PD, Burns, TL, Chatterjee, K and Weiss, RM (2015). "A Second Look with Prone SPECT Myocardial Perfusion Imaging Reduces the need for Angiography in Patients at Low Risk for Cardiac Death or MI." Journal of Nuclear Cardiology, **22**(1): 115-122.

Zakavi, SR, Zonoozi, A, Kakhki, VD, Hajizadeh, M, Momennezhad, M and Ariana, K (2006). "Image Reconstruction Using Filtered Backprojection and Iterative Method:

Effect on Motion Artifacts in Myocardial Perfusion SPECT." Journal of Nuclear Medicine Technology, **34**(4): 220-223.

Appendix A – Data Driven Motion Estimation

If two consecutive images are taken of an object, the imaging field of view remains constant but the object moves relative to the imaging plane; the image of the object will appear at a different location on the second image, figure i. An image is a matrix of pixel values that can be associated with a co-ordinate system to identify the location of the pixels. Movement between two images will change the co-ordinates of the image in the imaging plane. Mathematical techniques can be used to estimate the motion that has occurred between two images.

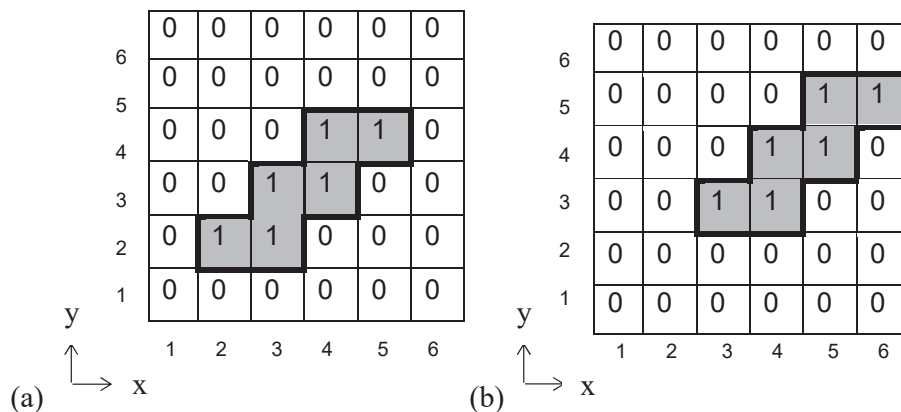


Figure i – A very simple representation of an image. The object is identified by pixel values of 1. The imaging plane consists of 36 pixels, with a coordinate system (x,y) that references the centre of the pixel, for example (1,1) is referencing the centre of the bottom left pixel. (a) original image, (b) a second image after the object has moved.

9.2.1 Centre of Mass

One method to estimate the shift of an object between two images is to calculate the centre of mass of the image, equation i, where x_{com} and y_{com} represent the position of the centre of mass in the x and y directions, N is the number of pixels, x_i and y_i are the x and y coordinates of the i^{th} pixel and m_i is the mass, or in the case of figure i, the pixel value, of the i^{th} pixel.

$$x_{com} = \frac{\sum_{i=0}^N x_i m_i}{\sum_{i=0}^N m_i} \quad y_{com} = \frac{\sum_{i=0}^N y_i m_i}{\sum_{i=0}^N m_i} \quad \text{Equation } i$$

In the example given in figure i the centre of mass calculated from equation i is $x = 3.5$, $y = 3$ for image a and $x = 4.5$, $y = 4$ for image b, therefore the difference in the centre of mass between the two images is $x = 1$, $y = 1$, indicating that there has been a shift in the position of the image in the x and y directions of magnitude 1 pixel. This is assuming translational motion with no deformation of the object.

9.2.2 Image Registration

An alternative method of determining the shift between the images is to use image registration, which moves a reference image, also termed the source, floating or moved image to match a target or fixed image. Image registration can be rigid which includes translations and rotations, affine which also includes scaling and shear, or non-linear which warps the reference image (with constraints applied) to match the target image (Crum et al., 2004).

Features in the image or the voxel values can be used to calculate a similarity measure or cost function between the two images. An iterative approach is taken to adjust the alignment of the images relative to each other to optimise the similarity measure, therefore minimising the differences between the aligned images. This results in a spatial transformation (mapping) that relates the points in the reference image to the corresponding points in target image.

The Sheffield Image Registration Toolkit (ShIRT) is an image processing software package focusing on image registration. The theory behind the ShIRT algorithm is described in the literature (Barber and Hose, 2005; Barber et al., 2007) and it has been evaluated for many medical applications (Ireland et al., 2007; Martel A L et al., 2007; Hand et al., 2009; Lamata et al., 2011; Redgate et al., 2013; Barber et al., 2014). The cost function (Q) used by ShIRT is based on the sum of squares differences between the two images, equation ii, where $m^T(a)$ is the moved image (m) mapped with the registration mapping (a) to the fixed image (f). If the images are completely mapped and in the absence of noise, the cost function would be zero.

$$Q = \sum_{AllVoxels} (f - m^T(a))^2 \quad \text{Equation ii}$$

Therefore, in the simple example in figure i, the sum of squares difference between the images is 4, if a transformation of y-1 pixels was applied to image b then the sum of squares difference between the images reduces to 3 and if a translation of y-1 and x-1 pixels is applied to image b there would be perfect alignment between the images and the sum of squares difference would be zero. This presents the basics of the cost function used by the registration algorithm, however registration of medical images is more complex than in this simple example. The registration algorithm identifies the minimum value of the cost function, however if a local minimum is identified instead of the global minimum then inaccuracies in the registration can arise. When applying ShIRT for image registration one parameter that is specified by the user is the node spacing for the registration. This user specified value is the minimum node spacing. To maximise the likelihood of finding the global minimum the software uses an iterative approach, starting with a course node spacing to perform global alignment of the images and then iteratively reducing the node spacing to the user specified minimum, using the transformation from the first registration as a starting point for the next registration. With no constraints any images could be aligned, however this does not mean that the alignment is useful or sensible, therefore a smoothness constraint is included in the cost function which imposes a degree of smoothing on the registration mapping.

9.2.3 Principal Component Analysis

The imaging plane in figure i has 36 pixels and the image is made up of 6 pixels. The locations of these pixels could be plotted as shown in figure ii(a) and represented as a $m \times n$ matrix, M , equation iii, where m is the number of variables and n the number of observations.

$$M = \begin{bmatrix} 2 & 3 & 3 & 4 & 4 & 5 \\ 2 & 2 & 3 & 3 & 4 & 4 \end{bmatrix} \quad \text{equation iii}$$

Principal component analysis reduces the data into new dimensions, termed principal components (PC), that minimise the variance of the data. The steps involved in computing the principal components, along with an example calculation for figure ii(a) are shown below;

Step 1: Normalise the data by subtracting the mean, figure ii(b), equation iv.

$$U = \begin{bmatrix} -1.5 & -0.5 & -0.5 & 0.5 & 0.5 & 1.5 \\ -1 & -1 & 0 & 0 & 1 & 1 \end{bmatrix} \quad \text{equation iv}$$

Step 2: Calculate the covariance matrix of the normalised data, equation v.

$$COV = \frac{1}{n-1}UU^T = \begin{bmatrix} 1.1 & 0.8 \\ 0.8 & 0.8 \end{bmatrix} \quad \text{equation v}$$

Step 3: Find the singular values, λ_i , and normalised coefficients, e_i , of the covariance matrix, equation vi and vii.

$$\lambda_1 = 0.1361, \quad e_1 = \begin{bmatrix} 0.6386 \\ -0.7695 \end{bmatrix} \quad \text{equation vi}$$

$$\lambda_2 = 1.7639, \quad e_2 = \begin{bmatrix} -0.7695 \\ -0.6386 \end{bmatrix} \quad \text{equation vii}$$

Step 4: The matrix P can now be defined, which contains the normalised coefficients as columns, ordered with the vector with the largest variance first, as defined by the singular values, equation viii.

$$P = \begin{bmatrix} -0.7695 & 0.6386 \\ -0.6386 & -0.7695 \end{bmatrix} \quad \text{equation viii}$$

Step 5: The original data can now be projected onto the new principal component axes, using equation ix, figure ii(c). The position of each point in this new coordinate system can be considered a linear combination of the original variables.

$$Q = P^T U \quad \text{equation ix}$$

Step 5: The original data can then be regenerated using a selected number of components from P, equation x, figure ii(d), taking into account the normalisation that was performed in step 1 through addition of the mean, μ .

$$U = PQ + \mu \quad \text{equation x}$$

The aim in this study is not to find the principal components of a single image but to find the components across a time sequence of images. If 720, 0.5s images are acquired, which is equivalent to a 360s myocardial perfusion scan, and each image contains 32 x 32 pixels, then the components can be derived. The data in each pixel can be thought of as a variable and each 0.5s image as an observation. A $m \times n$, 1024 x 720, matrix M can be produced and the singular values and normalised coefficients determined. Smoothed images can be generated at each time point by limiting the regenerated data to the first few components.

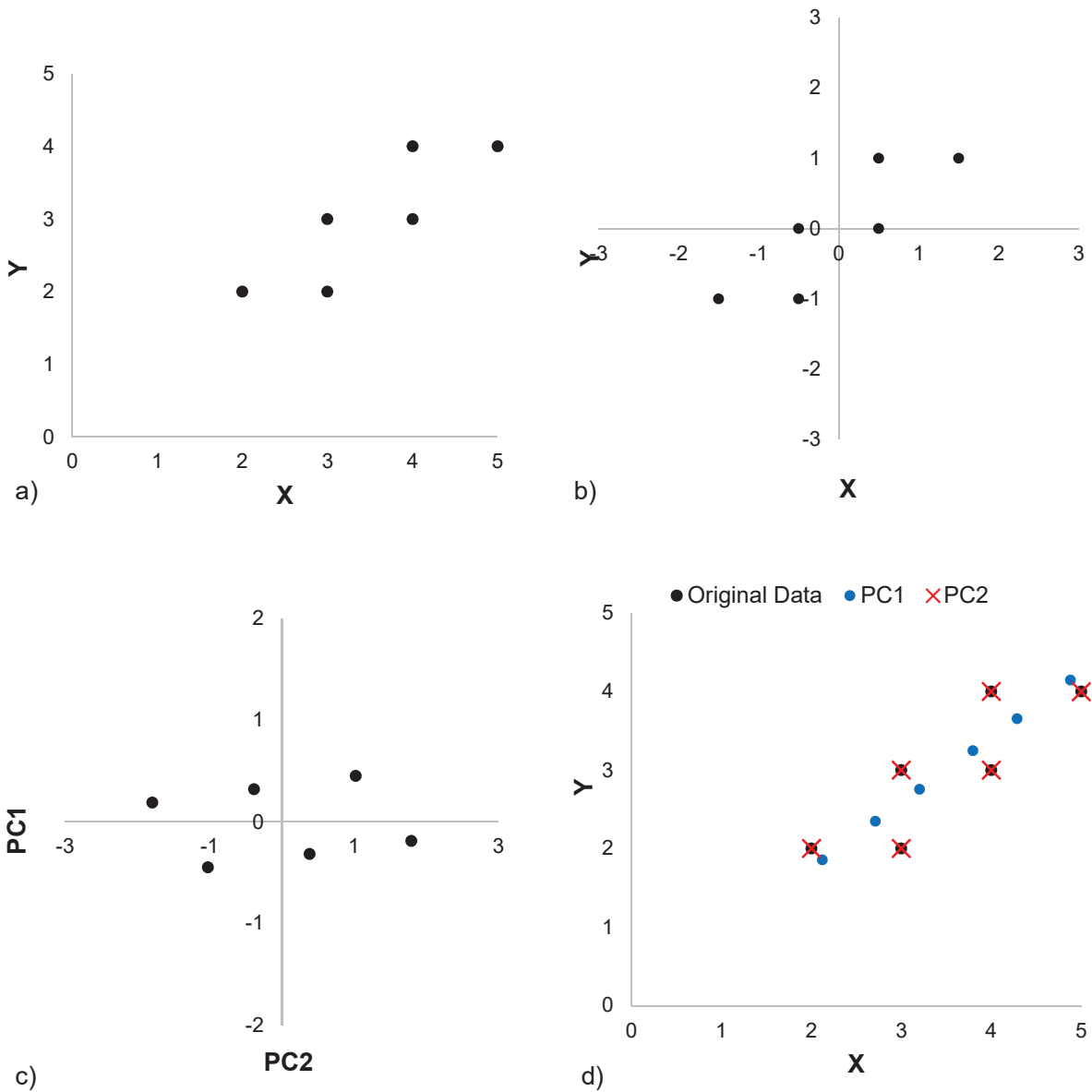


Figure ii – (a) The original data, M , (b) the data normalised by subtract of the mean, (c) the data projected onto the principal component axes, (d) the original data and data regenerated from the first and second components (PC1 and PC2).

Appendix B – Respiratory Motion Patient Results

Patient	Combined Patient and Respiratory Motion		Scores		Quality Index (Significance)		CPP Heart	Selected for Reporting	Positive Report
	Method 2	Method 3	Fourier	Visual					
1	6.4	6.6	2	2	0.68	(0.00)	418	Yes	No
2	2.7	15.5	1	1	0.15	(0.00)	228	No	No
2R	2.4	14.9	1	1	0.25	(0.00)	203	No	No
3	1.6	8.8	1	1	0.25	(0.00)	458	No	No
4	3.5	5.7	1	1	0.23	(0.00)	529	No	No
5	0.3	11.1	1	1	0.02	(0.54)	390	No	No
6	22.5	18.5	2	2	0.96	(0.00)	479	Yes	Yes
7	15.7	10.9	2	2	0.74	(0.00)	513	Yes	No
8	3.8	6.5	1	1	0.17	(0.00)	527	No	No
9	3	6.9	1	1	0.20	(0.00)	511	No	No
10	9.2	14.9	2	3	0.81	(0.00)	414	Yes	No
11	3.3	7.7	1	1	0.13	(0.00)	524	No	No
12	1.1	5.8	1	1	0.16	(0.00)	469	No	No
13	2.9	13.4	1	1	0.13	(0.00)	336	No	No
14	1.2	7.7	1	1	0.70	(0.00)	469	No	No
14R	1.1	7.2	1	1	0.45	(0.00)	360	No	No
15	7.6	9.1	2	3	0.76	(0.00)	495	Yes	No
16	9.4	9.3	2	2	0.77	(0.00)	399	Yes	No
17	15.9	14.5	2	2	0.81	(0.00)	511	Yes	Yes
18	3.7	8.6	1	1	0.52	(0.00)	549	No	No
19	8.4	11.2	2	3	0.69	(0.00)	431	Yes	No
20	2.7	4.6	1	1	0.25	(0.00)	358	No	No
21	0.7	10	1	1	0.29	(0.00)	408	No	No
22	12.9	11.8	2	2	0.90	(0.00)	508	Yes	No
22R	10.8	12.5	2	2	0.94	(0.00)	439	Yes	No
23	3	8.4	1	1	0.29	(0.00)	489	No	No

23R	3.4	8.8	1	1	0.17	(0.00)	422	No	No
24	9.5	9.2	2	3	0.90	(0.00)	542	Yes	No
25	1.7	9.5	1	1	0.25	(0.00)	398	No	No
26	4.9	9.0	2	2	0.69	(0.00)	773	Yes	No
27	13.7	17.5	2	3	0.70	(0.00)	471	Yes	No
28	2.9	4.7	1	1	0.18	(0.00)	520	No	No
29	0.9	4.7	1	1	0.15	(0.00)	382	No	No
30	1.1	9.7	1	1	0.08	(0.04)	480	No	No
31	5.8	11.1	2	3	0.62	(0.00)	419	Yes	No
32	0.5	17.7	1	1	0.03	(0.51)	228	No	No
33	5.7	5.5	1	1	0.47	(0.00)	482	No	No
33R	3.6	6.3	1	1	0.29	(0.00)	383	No	No
34	11.5	12.4	2	2	0.92	(0.00)	724	Yes	No
34R	17.6	16.5	2	2	0.93	(0.00)	539	Yes	No
35	5	9.2	3	1	0.09	(0.02)	482	Yes	No
36	1.1	5	1	1	0.53	(0.00)	592	No	No
37	6.6	6.5	3	3	0.51	(0.00)	399	Yes	No
38	8.4	9.2	2	2	0.93	(0.00)	574	Yes	No
39	8.2	10.4	2	2	0.72	(0.00)	544	Yes	No
39R	6.6	11.1	2	2	0.75	(0.00)	416	Yes	No
40	7.5	7.5	3	3	0.92	(0.00)	541	Yes	No
41	11.2	14.5	3	3	0.35	(0.00)	459	Yes	No
42	0.0	8.7	1	1	0.09	(0.01)	381	No	No
43	5.7	8	3	3	0.68	(0.00)	308	Yes	No
44	2.3	13.1	1	1	0.09	(0.00)	354	No	No
45	3.8	8.2	1	1	0.09	(0.01)	460	No	No
45R	1.1	9.9	1	1	0.08	(0.01)	378	No	No
46	9.7	14.3	3	3	0.91	(0.00)	450	Yes	No
47	1.7	10	1	1	0.10	(0.00)	444	No	No
40E	13	14	3	3	0.96	(0.00)	411	Yes	No
41E	3.6	16.7	1	1	0.08	(0.03)	376	No	No
42E	0.3	15.8	1	1	0.19	(0.00)	341	No	No
43E	1.5	11.5	1	1	0.42	(0.00)	296	No	No

44E	6.2	14.6	1	1	0.28	(0.00)	322	No	No
45E	3.7	11.5	1	1	0.15	(0.00)	367	No	No
46E	14.5	15.6	3	3	0.97	(0.00)	362	Yes	Yes
47E	1.4	14.7	1	1	0.01	(0.78)	382	No	No

Table i – The results from the respiratory motion patient cohort, section 7.2. The shaded rows represent images identified as having significant respiratory motion, defined by the criteria in section 7.7. Method 2 and Method 3 represent the measures of motion as described in section 7.5.1. CPP - counts per pixel.

Appendix C – Publications

Published work, conference proceedings and associated citations resulting from the work in this thesis are listed below.

Full Text Publications

Redgate S, Barber DC, Fenner JW, Al-Mohammad A, Taylor JC, Hanney MB, Tindale WB. A study to quantify the effect of patient motion and develop methods to detect and correct for motion during myocardial perfusion imaging on a CZT solid-state dedicated cardiac camera. *Journal of Nuclear Cardiology* (2016). 23(3): 514-526. Available at: <https://doi.org/10.1007/s12350-015-0314-1>.

Conference Proceedings

Redgate S, Fenner, JW, Barber DC, Tindale WB, Al-Mohammad A, Fleming S, Billingham B. Detecting patient motion on a solid state multiple pinhole dedicated cardiac camera. *The Journal of Nuclear Medicine* (2012). 53 (Supplement 1): 2377.

Redgate S, Barber DC, Fenner JW, Al-Mohammad A, Taylor JC, Hanney MB, Tindale WB. Correcting for patient motion on a solid state multiple pinhole dedicated cardiac camera. *European Journal of Nuclear Medicine and Molecular Imaging*, (2015). 42 (Supplement 1): S48.

Redgate S, Tindale WB, Fenner JW, Al-Mohammad A, Barber DC. Principal component analysis as a method of respiratory motion detection on a solid state CZT dedicated cardiac camera. *The Journal of Nuclear Medicine* (2016). 57(Supplement 2): 1969.

Redgate S, Tindale WB, Fenner JW, Al-Mohammad A, Barber DC. Respiratory motion correction of myocardial perfusion images on a solid state cardiac camera. *Nuclear Medicine Communications*, (2016). 37(5): 564.

Citations

Buck A, Decristoforo C. Highlights lecture EANM 2015: the search for nuclear medicines superheroes. *European Journal of Nuclear Medicine and Molecular Imaging* (2016). 43(10): 1910-1927. Available at: <https://doi.org/10.1007/s00259-016-3423-4>.

Benz DC, Buechel RR. Moving ahead with CZT technology. *Journal Nuclear Cardiology* (2016). 23(3): 527-528. Available at: <https://doi.org/10.1007/s12350-015-0321-2>.

van Dijk JD, van Dalen JA, Mouden M, Ottervanger JP, Knollema S, Slump CH, Jager PJ. Value of automatic patient motion detection and correction in myocardial perfusion imaging using a CZT-based SPECT camera. *Journal Nuclear Cardiology* (2016). Available at: <https://doi.org/10.1007/s12350-016-0571-7>.

Benz DC, Fuchs TA. Breathless or breathtaking: Respiratory motion correction. *Journal Nuclear Cardiology* (2016). Available at: <https://doi.org/10.1007/s12350-016-0590-4>.

Daou D, Sabbah R, Coaguila C, Boulahdour H. Impact of data-driven cardiac respiratory motion correction on the extent and severity of myocardial perfusion defects with free-breathing CZT SPECT. *Journal Nuclear Cardiology* (2017). Available at: <https://doi.org/10.1007/s12350-017-0806-2>.

Daou D. Dedicated cardiac CZT SPECT is steadily moving to achieve its destiny. *Journal Nuclear Cardiology* (2017). Available at: <https://doi.org/10.1007/s12350-017-1006-9>.

Salvadori J, Petegnief Y, Sabbah R, Morel O, Boulahdour H, Karcher G, Marie PY, Imbert L. Compared vulnerabilities to small cardiac motions between different cameras used for myocardial perfusion imaging. *Journal Nuclear Cardiology* (2018). Available at: <https://doi-org.sheffield.idm.oclc.org/10.1007/s12350-017-1175-6>.

Appendix D – Permissions

Figure 2-7 and Figure 2-9

Shelley Redgate
<mdq10sr@sheffield.ac.uk>

25/08/2017

to permissions@snmmi.org

I am currently writing my PhD thesis and would like to reproduce some images from two of your journal articles in my literature review. The details are below. Please could you advise if this is acceptable?

Effect of Mechanically Simulated Diaphragmatic Respiratory Motion on Myocardial SPECT Processed with and without attenuation correction, 2002, volume 43, no 9, 1259-1267. Figure 5.

Correction of Heart Motion Due to Respiration in Clinical Myocardial Perfusion SPECT Scans using Respiratory Gaiting, April 2007 volume. 48, number 4, 630-636. Part of figure 4.

Your help with this is greatly appreciated.

Best wishes
Shelley Redgate

PhD student
University Sheffield
UK
Email:mdq10sr@sheffield.ac.uk

Permissions permissions@snm.org via snmmi.onmicrosoft.com 19/09/2017

to me

Dear Shelley Redgate:

Thank you for your request to reprint material from a Society of Nuclear Medicine and Molecular Imaging (SNMMI) publication. Permission for this use has been granted under the following conditions:

1. Proper attribution is required with suggested verbiage as follows: This research was originally published in JNM. Author(s). Title. J Nucl Med. Year;vol:pp-pp. © by the Society of Nuclear Medicine and Molecular Imaging, Inc.
2. If used in a web-only publication (e.g, a web page), a link to the original article should be provided. Materials published in another medium that are additionally posted to the web should include a link if appropriate.

This permission applies only to materials to which SNMMI holds copyright. Materials

credited to outside sources are not original. In this case, the original rightsholders should be contacted for reprint permission. Copyright to material published by presenters at SNMMI Annual Meetings is retained by the original authors.

Mark Sumimoto

Editorial Project Manager

SNMMI | The Society of Nuclear Medicine and Molecular Imaging

phone: 703.652.6777 | fax: 703.708.9018

email: msumimoto@snmmi.org

www.snmmi.org

Figure 2-10

This Agreement between Ms. Shelley Redgate ("You") and Springer Nature ("Springer Nature") consists of your license details and the terms and conditions provided by Springer Nature and Copyright Clearance Center.

License Number	4277130803596
License date	Jan 27, 2018
Licensed Content Publisher	Springer Nature
Licensed Content Publication	Medical & Biological Engineering & Computing
Licensed Content Title	Motion detection and amelioration in a dedicated cardiac solid-state CZT SPECT device
Licensed Content Author	John A. Kennedy, H. William Strauss
Licensed Content Date	Jan 1, 2016
Licensed Content Volume	55
Licensed Content Issue	4
Type of Use	Thesis/Dissertation
Requestor type	academic/university or research institute
Format	print and electronic
Portion	figures/tables/illustrations
Number of figures/tables/illustrations	3
Will you be translating?	no
Circulation/distribution	<501
Author of this Springer Nature content	no
Title	CAMIRA: Correction Advances for Myocardial Imaging using Registration Algorithms
Instructor name	n/a
Institution name	n/a

Expected presentation date	Jan 2018
Portions	Figure 2, Figure 6, Figure 3
Requestor Location	Ms. Shelley Redgate Nuclear Medicine, I Floor, Royal Hallamshire Hospital, Sheffield Teaching Hospitals Sheffield,, South Yorkshire S10 2JF United Kingdom Attn: Ms. Shelley Redgate
Billing Type	Invoice
Billing Address	Ms. Shelley Redgate Nuclear Medicine, I Floor, Royal Hallamshire Hospital, Sheffield Teaching Hospitals Sheffield,, United Kingdom S10 2JF Attn: Ms. Shelley Redgate
Total	0.00 USD

Figure 2-11

This Agreement between Ms. Shelley Redgate ("You") and Springer ("Springer") consists of your license details and the terms and conditions provided by Springer and Copyright Clearance Center.

License Number	4196990712171
License date	Sep 27, 2017
Licensed Content Publisher	Springer
Licensed Content Publication	Journal of Nuclear Cardiology
Licensed Content Title	Data-driven respiratory motion tracking and compensation in CZT cameras: A comprehensive analysis of phantom and human images
Licensed Content Author	Chi-Lun Ko, Yen-Wen Wu, Mei-Fang Cheng et al
Licensed Content Date	Jan 1, 2014
Licensed Content Volume	22
Licensed Content Issue	2
Type of Use	Thesis/Dissertation
Portion	Figures/tables/illustrations
Number of figures/tables/illustrations	1
Author of this Springer article	No
Order reference number	

Original figure numbers	Figure 4
Title of your thesis / dissertation	CAMIRA: Correction Advances for Myocardial Imaging using Registration Algorithms
Expected completion date	Jan 2018
Estimated size(pages)	240
Requestor Location	Ms. Shelley Redgate Nuclear Medicine, I Floor, Royal Hallamshire Hospital, Sheffield Teaching Hospitals Sheffield,, South Yorkshire S10 2JF United Kingdom Attn: Ms. Shelley Redgate
Billing Type	Invoice
Billing Address	Ms. Shelley Redgate Nuclear Medicine, I Floor, Royal Hallamshire Hospital, Sheffield Teaching Hospitals Sheffield,, United Kingdom S10 2JF Attn: Ms. Shelley Redgate
Total	0.00 USD

Sections of Chapters 3, 4 and 5

This Agreement between Ms. Shelley Redgate ("You") and Springer ("Springer") consists of your license details and the terms and conditions provided by Springer and Copyright Clearance Center.

License Number	4196970377144
License date	Sep 27, 2017
Licensed Content Publisher	Springer
Licensed Content Publication	Journal of Nuclear Cardiology
Licensed Content Title	A study to quantify the effect of patient motion and develop methods to detect and correct for motion during myocardial perfusion imaging on a CZT solid-state dedicated cardiac camera
Licensed Content Author	Shelley Redgate, David C. Barber, John W. Fenner et al
Licensed Content Date	Jan 1, 2015
Licensed Content Volume	23
Licensed Content Issue	3
Type of Use	Thesis/Dissertation
Portion	Figures/tables/illustrations

Number of figures/tables/illustrations	11
Author of this Springer article	Yes and you are the sole author of the new work
Order reference number	
Original figure numbers	figures 1-7, tables 1-4
Title of your thesis / dissertation	CAMIRA: Correction Advances for Myocardial Imaging using Registration Algorithms
Expected completion date	Jan 2018
Estimated size(pages)	240
Requestor Location	Ms. Shelley Redgate Nuclear Medicine, I Floor, Royal Hallamshire Hospital, Sheffield Teaching Hospitals Sheffield,, South Yorkshire S10 2JF United Kingdom Attn: Ms. Shelley Redgate
Billing Type	Invoice
Billing Address	Ms. Shelley Redgate Nuclear Medicine, I Floor, Royal Hallamshire Hospital, Sheffield Teaching Hospitals Sheffield,, United Kingdom S10 2JF Attn: Ms. Shelley Redgate
Total	0.0 USD

This Agreement between Ms. Shelley Redgate ("You") and Springer ("Springer") consists of your license details and the terms and conditions provided by Springer and Copyright Clearance Center.

License Number	4196561144954
License date	Sep 26, 2017
Licensed Content Publisher	Springer
Licensed Content Publication	Journal of Nuclear Cardiology
Licensed Content Title	A study to quantify the effect of patient motion and develop methods to detect and correct for motion during myocardial perfusion imaging on a CZT solid-state dedicated cardiac camera
Licensed Content Author	Shelley Redgate, David C. Barber, John W. Fenner et al
Licensed Content Date	Jan 1, 2015
Licensed Content Volume	23

Licensed Content Issue	3
Type of Use	Thesis/Dissertation
Portion	Excerpts
Author of this Springer article	Yes and you are the sole author of the new work
Order reference number	
Title of your thesis / dissertation	CAMIRA: Correction Advances for Myocardial Imaging using Registration Algorithms
Expected completion date	Jan 2018
Estimated size(pages)	240
Requestor Location	Ms. Shelley Redgate Nuclear Medicine, I Floor, Royal Hallamshire Hospital, Sheffield Teaching Hospitals Sheffield,, South Yorkshire S10 2JF United Kingdom Attn: Ms. Shelley Redgate
Billing Type	Invoice
Billing Address	Ms. Shelley Redgate Nuclear Medicine, I Floor, Royal Hallamshire Hospital, Sheffield Teaching Hospitals Sheffield,, United Kingdom S10 2JF Attn: Ms. Shelley Redgate
Total	0.00 USD